Study and Optimisation of Wall Conditioning Methods on the Superconducting Stellarator W7-X

Andrei Goriaev

Doctoral dissertation submitted to obtain the academic degrees of
Doctor of Engineering Physics (UGent) and Doctor of Engineering Science (RMA)

Supervisors

Prof. Kristel Crombé, PhD* - Prof. Michael Van Schoor, PhD**

* Department of Applied Physics
Faculty of Engineering and Architecture, Ghent University

** Department of Physics
Polytechnic Faculty, Royal Military Academy

February 2022

GHENT
UNIVERSITY

RMA
Brussels
Royal Military Academy

Study and Optimisation of Wall Conditioning Methods on the Superconducting Stellarator W7-X

Andrei Goriaev

Doctoral dissertation submitted to obtain the academic degrees of
Doctor of Engineering Physics (UGent) and Doctor of Engineering Science (RMA)

Supervisors
Prof. Kristel Crombé, PhD* - Prof. Michael Van Schoor, PhD**

* Department of Applied Physics
Faculty of Engineering and Architecture, Ghent University

** Department of Physics
Polytechnic Faculty, Royal Military Academy

February 2022

ISBN 978-94-6355-566-1
NUR 961, 926
Wettelijk depot: D/2022/10.500/7

Members of the Examination Board

Chairs

Prof. Em. Hendrik Van Landeghem, PhD, Ghent University
Prof. Jan Leysen, PhD, Royal Military Academy

Other members entitled to vote

Timo Dittmar, PhD, Forschungszentrum Jülich, Germany
Prof. Marek Rubel, PhD, KTH Royal Institute of Technology, Sweden
Dirk Van Eester, PhD, Royal Military Academy
Prof. Geert Verdoolaege, PhD, Ghent University
Tom Wauters, PhD, ITER Organization, France

Supervisors

Prof. Kristel Crombé, PhD, Ghent University
Prof. Michael Van Schoor, PhD, Royal Military Academy

This project was done as a collaboration between the Max-Plank-Institute for Plasma Physics (IPP Greifswald, Germany), the Instutute of Energy and Climate Research (Plasma Physics IEK-4) Forschungszentrum Jülich (FZ-Jülich, Germany) and the Laboratory for Plasma Physics of the Royal Military Academy (LPP-ERM/KMS Brussels, Belgium).

This work has been carried out within the framework of the EUROfusion Consortium and has received funding from the Euratom research and training programme 2014-2018 and 2019-2020 under grant agreement No 633053. The views and opinions expressed herein do not necessarily reflect those of the European Commission.

Acknowledgments

This challenge has devoted a great effort and intense period of research and study, resulting in this PhD thesis. It was a long and complicated journey with many doubts, uncertainties and obstacles, nevertheless, giving an excellent opportunity to learn and work with many people involved without whom none of this project would be possible.

First of all, I wish to express my sincere gratitude to my supervisor Dr. Tom Wauters for all these years of guidance, advice, comments, debates and fruitful discussions in every aspect of the research process. I highly appreciate his significant effort in sharing his experience with me and his patience while explaining to me all the details even when I was stubborn and fully disagreed with him. It was a pleasure to get experience and have fun productively working together on different research projects.

I am incredibly grateful to Prof. Michael Van Schoor, my promoter in LPP-ERM/KMS, for organizing and supporting my work in the laboratory and extending my contracts to finish this PhD project. This work would not have been possible without Prof. Kristel Crombé, my promoter at Ghent University, continuously helping me with my annual reports and guiding me through a maze of administrative procedures. Moreover, I should also appreciate her assistance in organizing my PhD defence events.

I would like to thank a lot of colleagues from LPP-ERM/KMS, FZJ, KIPT, KTH and IPP Greifswald, in particular, the TOMAS team (Dr. Sören Möller, Prof. Marek Rubel, Dr. Per Petersson, Laura Dittrich, Sunwoo Moon, Dr. Yurii Kovtun, Daniel López-Rodríguez, Johan Buermans and Dr. Riccardo Ragona) for the successful development of the TOMAS project making possible to extend this work. I highly value your contribution to the progress of our international collaboration. I also want to thank Dr. Rudolf Brakel for organizing and supporting my work in IPP Greifswald during two experimental campaigns of W7-X.

My particular respect is to Dr. Fabrice Louche for always being young and curious about rock concerts, festivals and TV series discussing it during lunch

breaks, Dr. Anatoli Lyssoivan for his amazing "ski stories" told during long working sessions on TOMAS and Vincent Maquet for always coming to my office with a good mood and asking funny questions about my work.

Another important person was Marco Krause, who accommodated me Greifswald, helped me with the engineering aspect of the TOMAS project development and German language translations and was my travel buddy during the last years of my PhD studies.

I am entirely grateful to my Priority team (Dr. Alena Gogoleva, Dr. Egor Seliunin, Aleksandra Firstenko, Maria Kurepina, Natalia Egorova, Nina Elfimova, Dr. Yulia Zander and Dr. Mikhail Zander) for inspirational crazy travels and chatting in WhatsApp that allowed me to keep a positive attitude during the thesis writing process.

I am grateful to Irene Ortiz Samperio, my flatmate, for pleasant conversations, lovely coffee breaks and forcing me to learn Spanish during COVID-19 lockdowns at the final stage of this work.

Additionally, I would like to express deep respect to Pranay Valson for motivating me to stay in science. His unique example makes me passionate about fusion.

Finally, I would like to give special regards to my friends and family staying far away for always believing and motivating me to achieve better results.

Andrei Goriaev
Brussels, December 2021

Contents

Nederlandse samenvatting

Het totale energieverbruik in de wereld neemt toe. Het grootste deel van deze energie komt van de verbranding van fossiele brandstoffen, wat leidt tot een enorme uitstoot van broeikasgassen. Als alternatief kan kernfusie worden gebruikt om een schone, stabiele en duurzame energiebron te bouwen. Een van de belangrijkste opties om de reactanten in een kernfusiereactie op te sluiten, is magnetische opsluiting. De meest geavanceerde concepten voor magnetische opsluiting zijn de tokamak en de stellarator. Alle fusiemachines die tegenwoordig in gebruik zijn, zijn experimentele machines. DEMO wordt de eerste demonstratiereactor.

Het stellarator-concept wordt beschouwd als een mogelijk alternatief op lange termijn. Het Europese stellarator-programma richt zich op de wetenschappelijke exploitatie van de supergeleidende stellarator Wendelstein 7-X (W7-X). Eén van de uitdagingen van W7-X is de fysica van het randplasma en Plasma Surface Interacties (PSI) die verantwoordelijk zijn voor plasma onzuiverheden en brandstofrecycling. Wandconditionering in fusie-apparaten is een standaardhulpmiddel om de recycling van brandstof en onzuiverheden te beïnvloeden, waardoor de plasmaprestaties en de reproduceerbaarheid van ontladingen worden verbeterd. Het bedienen van W7-X vereist een strategie voor het conditioneren van de wanden. Dit is het onderwerp van dit doctoraat. Een strategie werd ontwikkeld door een experimentele optimalisatie uit te voeren van wandconditionering en door deze geïmplementeerde strategie op te volgen in elk van de operationele fasen van W7-X. De volgende technieken zijn relevant voor de operatie van W7-X in divertor-configuratie met plasmawand componenten (Plasma Facing Components – PFCs) van grafiet.

Bakken (Baking) is het proces waarbij hoge temperaturen worden gebruikt om vluchtige stoffen van de wanden van het vacuümvat te verwijderen om verdere migratie en verontreiniging van plasma's te voorkomen. Het is de meest gebruikelijke techniek om de hoeveelheid water te verminderen.

Plasma-geassisteerde (afvoer)wandconditionering is een methode gebaseerd op de mechanismen van door deeltjes geïnduceerde desorptie om onzuiverheden en brandstof uit PFCs te verwijderen. Gepulseerde ontladingsconditionering met een geoptimaliseerde werkcyclus kan maximale verwijdering bereiken terwijl retentie of herafzetting van het geïnjecteerde en aan de wand vrijgekomen gas wordt geminimaliseerd. Glow Discharge Cleaning (GDC) is gebaseerd op een zwak geïoniseerd plasma bij lage temperatuur, dat ontstaat door een spanningsverschil aan te brengen tussen één of meer kleine elektroden in het vacuümvat (anode) en de wanden van het vacuümvat (kathode). Het maakt verdere verwijdering van onzuiverheden mogelijk door het verminderen van metaaloxiden of hydrogenering van op koolstof gebaseerde oppervlakken na het bakken. De op radiofrequentie (RF) gebaseerde technieken zijn met name relevant voor fusiemachines met supergeleidende spoelen. Electron Cyclotron Wall Conditioning (ECWC) vertrouwt op een stroomloze ontlading die wordt geproduceerd door plaatselijke vermogensabsorptie bij de fundamentele EC-resonantie of de tweede harmonische ervan. ECWC-plasma is volledig geïoniseerd met een hoge elektronendichtheid en reinigt efficiënt het divertorgebied in stellarators. Ion Cyclotron Wall Conditioning (ICWC) koppelt RF-vermogen in het ion cyclotronfrequentie domein, aan zowel elektronen als ionen door voornamelijk botsingsabsorptie. ICWC-plasma's worden gekenmerkt door gemiddelde dichtheden en lage temperaturen met als doel een bekende en optimale lage energetische flux van neutralen naar de naar het plasma gerichte componenten te induceren.

Boronisatie is de meest gebruikelijke coatingmethode die typisch wordt toegepast via een GD in een mengsel met helium om zo amorfe dunne films die boor bevatten, af te zetten. Het maakt het mogelijk om zuurstofrecycling aanzienlijk te verminderen, metaalafgifte uit de vacuümvatwand te onderdrukken, lage-Z-onzuiverheidsconcentraties in het plasma te verminderen en de invloed van brandstofrecycling te minimaliseren. Een alternatieve methode om boorcoatings in realtime en in aanwezigheid van het magnetische veld aan te brengen, is gebaseerd op de injectie van boorpoeder.

Tussen 2015 en 2018 zijn de eerste drie experimentele campagnes (operationele fasen) OP1.1, OP1.2a en OP1.2b van de W7-X stellarator voltooid. De eerste fase, OP 1.1, werd uitgevoerd in de limiterconfiguratie. In OP1.2a en OP1.2b werd het apparaat voorzien van een divertor gemaakt uit grafiet. In OP1.1 werd het bakken van de wand uitgevoerd voorafgaand aan de plasma operatie. GDC werd gebruikt tussen experimentele dagen in de plasmaoperatiefase en ECWC werd gebruikt tijdens de experimentele dagen zelf. De beschikbare conditioneringstechnieken in OP1.2a waren bakken, GDC en ECWC. OP1.2 zorgde voor een lange GDC in waterstof, waardoor de hoeveelheid onzuiverheden aanzienlijk werd verminderd. Het volgen van GDC in helium maakte het mogelijk de wanden te ontdoen van resterende waterstof. In OP1.2b werd ook de toepassing van boronisatie toegankelijk. Voordat het eerste plasma werd gecreëerd, waren het bakken van de wand en GDC de minimaal vereiste voorwaarden om de experimenten te kunnen beginnen. Boronisatie en ECWC werden gebruikt tijdens de plasma-operatieperiode om respectievelijk de hoeveelheid zuurstof te verminderen en de waterstofrecycling te regelen.

Het bakken van de wanden van het plasmavat werd uitgevoerd in elk deel van OP1.2 nadat het vat was vacuüm gepompt, waarbij voornamelijk water werd verwijderd. Meer uitgebreide verwijdering van onzuiverheden werd waargenomen in OP1.2a. Het uitgassen van zware deeltjes werd onderdrukt. Het OP1.2b-bakken veranderde het restgasgehalte bij hogere massa's niet dramatisch.

Naast de initiële conditionering werd H_2-GDC tijdens de experimentele campagne ook wekelijks gebruikt om de wandcondities voor plasmaoperaties tot de eerste boronisatie verder te verbeteren. GDC in helium werd ofwel dagelijks uitgevoerd na waterstofplasma-experimenten of toepassing van H_2-GDC om de wanden te ontdoen van waterstof. GDC-parameters zijn geoptimaliseerd om een homogeniteit van de afvoer te bereiken, de reinigingsefficiëntie te maximaliseren en de erosie van PFCs te minimaliseren. Alleen voor H_2-GDC kon een betrouwbare opstart van het plasma worden bereikt. De plasma opstart in He-GDC was niet betrouwbaar en moest verder worden ontwikkeld. GDC in waterstof heeft een cumulatief effect op de verwijdering van onzuiverheden. Er is dus een bepaalde hoeveelheid H_2-GDC gevolgd door He-GDC vereist om betrouwbare plasma-werkingsomstandigheden te garanderen en een minimaal ontgassingsniveau van het waterstof te bereiken.

Drie boronisaties werden toegepast in een mengsel van di-boraan en helium met tussenpozen van een maand. Het proces van boronisatie werd van sessie tot sessie geoptimaliseerd. De eerste boronisatie onderdrukte het uitgassen van helium en breidde het plasma-operatievenster aanzienlijk uit in het dichtheidsbereik en de opsluitingstijden. De verbetering van de plasmaprestaties was te danken aan een significante vermindering van zuurstof en op zuurstof gebaseerde onzuiverheden. Een langdurig effect van boronisatie houdt verband met een lage ionen- en ladingsuitwisselingsflux naar de hoofdwand. De boorlaag wordt echter snel geërodeerd in de divertor.

Experimenten met boordruppelaars in OP1.2b waren bedoeld om de effectiviteit van de Probe Mounted Particle Injector (PMPI) te schatten. De positieve impact van de boorhoudende poederinjectie op de wandcondities is niet overtuigend. Een speciale reeks experimenten in een niet-geboroniseerd apparaat is nodig om de effecten van poederinjectie op wandconditionering adequaat te beoordelen.

Het belangrijkste conditioneringseffect van He ECWC in W7-X houdt verband met het reinigen van het divertorgebied. De techniek is geoptimaliseerd tot een routinetool voor dichtheidscontrole en een herstel van de plasmacondities na het plotse beëindigen van de ontlading door een te hoge straling. De volgende types He ECWC zijn ontwikkeld. "Single He recovery-ontladingen", dit zijn enkelvoudige ontladingen bij lage dichtheid en matig verwarmingsvermogen. “Pulstreinen” zijn reeksen van korte, lage tot gemiddelde vermogensontladingen met een vaste inschakelduur. Pulstreinen blijken efficiënter te zijn voor het verwijderen van waterstof. De pulstreinen zijn geoptimaliseerd door de pulslengte, het pulsinterval, het ingangsvermogen en de hoeveelheid gas. De toepassing van een geoptimaliseerde pulstrein maakt effectiever gebruik van de W7-X experimentele tijd. Vanwege boronisatie moest ECWC verfijnd worden voor de controle van brandstofrecycling.

De studie en optimalisatie van de wandconditioneringstechnieken die in W7-X werden toegepast, vereiste een aanzienlijke upgrade van de TOMAS-machine om het complexe multi-dimensionele beeld van de wandconditioneringstechnieken beter te begrijpen en de technieken voor te bereiden voor hun verdere toepassingen op W7-X. De experimenten met het bakken van de wand toonden aan dat deze techniek kan worden gebruikt om vastgehouden helium snel te verwijderen na wandconditionering in helium. De installatie van een W7-X-achtig GD-systeem in TOMAS maakte het mogelijk om de geassisteerde plasma opstart te bestuderen met behulp van een gelokaliseerde kortdurende injectie van argon. De invloed van het magnetische veld op de GD-homogeniteit en het onderzoek van onechte gebeurtenissen in GDC waren gericht op het reproduceren van erosie bij het opstart regime van GD (W7-X-achtige omgeving). De eerste pre-karakterisering van ECWC, ICWC en gemengde (ECWC+ICWC) plasma’s op TOMAS is gedaan met behulp van Langmuir Probes en Time-of-Flight Neutral Particle Analyzer als onderdeel van experimenten die wandconditionering en PSI-aspecten van deze technieken bestuderen. Eerste experimenten met het verwijderen van boor uit gecoate gepolijste grafietmonsters gemaakt van W7-X-tegels door He-GDC, dragen bij aan het begrijpen van de levensduur van de boorlaag in W7-X. Blootstelling van de met boor beklede grafietmonsters aan ICWC vereist aanvullende aanpassingen aan de machine.

De huidige conditioneringsstrategie voor de wand van W7-X bestaat uit twee fasen. De beginfase wordt uitgevoerd vóór het eerste plasma. Het begint met het 7 dagen bakken van het vacuümvat bij een gemiddelde PFC-temperatuur van 150 $^{\circ}\mathrm{C}$. De volgende stap is GDC. Eerst minimaal 9-10 uur GDC in waterstof met een druk van $\sim 4.5 \cdot 10^{-3}$ mbar en een anodestroom van 1.5 A. De laatste stap is een He-GDC van ongeveer 2 uur bij een neutrale gasdruk van $\sim 3.8 \cdot 10^{-3}$ mbar en een anodestroom van 1 A. De tweede fase is een reeks wandconditioneringstechnieken die routinematig worden toegepast tijdens plasmaoperatie. De boronisatieprocedure met een coatingfase van 3.5 - 4 uur moet maandelijks worden toegepast. In toekomstige campagnes kan echter een herziening van de boronisatiefrequentie nodig zijn. Verdere ontwikkeling van de boorpoederdruppelaar of een analoog moet worden overwogen om de levensduur van de boorcoating te verlengen. Om de brandstofrecycling gedurende een experimentele dag te regelen, kan voor elke ontlading de He ECWC-pulstrein worden gebruikt die is geoptimaliseerd voor toepassing in het geboroniseerde apparaat, met een pulslengte van 3 s, een pulsinterval van ongeveer 30 - 35 s, een ingangsvermogen van 2.1 MW, een gas instroom met een duur van 15 ms bij een constante stroom van 75 mbar · l/s. Het bewegen van de strikelines (i.e. de interacties gebieden met de wand in de divertor-regio) kan de divertortemperaturen boven 400 $^\circ\mathrm{C}$ houden tijdens de toepassing van de pulstrein, en versnelt zo de brandstofverwijdering en maximaliseert het getroffen divertorgebied.

Het werk dat in dit doctoraatsproject is gedaan, zal worden voortgezet tijdens toekomstige W7-X-operatiecampagnes. Daarnaast komen er nieuwe tools voor wandconditionering, waaronder een ICRH-systeem.

English summary

The total energy consumption in the world is increasing. Most of this energy comes from burning fossil fuels, leading to tremendous greenhouse gas emissions. As an alternative, nuclear fusion can be employed to build a clean, steady and sustainable energy source. One of the main options how to confine the reactants in a nuclear fusion reaction is magnetic confinement. The most advanced magnetic confinement concepts are the tokamak and the stellarator. All fusion devices in operation today are experimental machines. The DEMO device will be the first demonstration reactor.

The stellarator concept is considered as a possible long-term alternative. The European stellarator programme focuses on the scientific exploitation of the superconducting stellarator Wendelstein 7-X (W7-X). One of the W7-X challenges is edge plasma physics and Plasma - Surface Interaction (PSI) studies responsible for plasma impurities and fuel recycling. Wall conditioning in fusion devices is a standard tool to influence fuel and impurity recycling, improving plasma performance and discharge reproducibility. Operating W7-X requires a wall conditioning strategy, which is the topic of this PhD. The strategy is developed by performing an experimental conditioning optimization and by following up the implemented wall conditioning strategy in each of the operational phases of W7-X. The following techniques are relevant for W7-X operation in divertor configuration with graphite plasma-facing components (PFC)s.

Baking is the process of using high temperatures to remove volatile species from the walls of a vacuum vessel to prevent its further migration and contamination of plasmas. It is the most common technique to reduce the amount of water.

Plasma-assisted (discharge) wall conditioning is a method based on the mechanisms of particle-induced desorption to remove impurities and fuel from PFCs. Pulsed discharge conditioning with an optimized duty cycle can achieve maximum removal while minimizing retention or redeposition of the injected and wall released gas. Glow Discharge Cleaning (GDC) is based on a weakly

ionized low-temperature plasma, which is created by applying a voltage difference between one or more small electrodes inside the vacuum vessel (anode) and vacuum vessel walls (cathode). It allows further impurity removal by reducing metal oxides or hydrogenation of carbon-based surfaces after baking. Radiofrequency (RF) - based techniques are particularly relevant for fusion devices with superconducting coils. Electron Cyclotron Wall Conditioning (ECWC) relies on a current-less discharge produced by localized power absorption at the fundamental EC resonance or its second harmonic. ECWC plasma is fully ionized with high electron density and efficiently cleans the divertor area in stellarators. Ion Cyclotron Wall Conditioning (ICWC) discharges couple RF power in the ion cyclotron range of frequencies to both electrons and ions by collisional absorption mainly. ICWC plasmas are characterized by average densities and low temperatures aiming to induce a known and optimal low energetic flux of neutrals to the plasma-facing components.

Boronization is the most common coating method typically applied through a GD in a mixture with helium to deposit amorphous boron-containing thin films. It allows to significantly reduce oxygen recycling, suppress metal release from the vessel wall, reduce low-Z impurity concentrations in the plasma, and minimize an influence of fuel recycling. An alternative method to apply boron coatings in real-time and in the presence of the magnetic field is based on boron powder injection.

Between 2015 and 2018, the first three experimental campaigns (operational phases) OP1.1, OP1.2a, and OP1.2b of the W7-X stellarator have been completed. The first phase, OP 1.1, was performed in the limiter configuration. In OP1.2a and OP1.2b, the device was operated with a graphite divertor. In OP1.1, baking was performed prior to the plasma operation. GDC was used between experimental days during the plasma operation phase, and ECWC was employed during experimental days. The available conditioning techniques in OP1.2a were baking, GDC and ECWC. OP1.2 allowed for a long GDC in hydrogen, significantly reducing the amount of impurities. Following GDC in helium allowed depleting the walls from remaining hydrogen. In OP1.2b, the application of boronization also became accessible. Before the first plasma, the baking and GDC provided the minimum required conditions for starting physics experiments. Boronization and ECWC were used during the plasma operation period to reduce the amount of oxygen and control the hydrogen recycling, respectively.

The baking of the plasma vessel walls was performed in each part of OP1.2 after the vessel pump down, mainly removing water. More extensive removal of impurities was observed in OP1.2a. The outgassing of heavy species was suppressed. The OP1.2b baking did not dramatically change the residual gas content at higher masses.

Besides initial conditioning, H_2-GDC was also used weekly throughout the experimental campaign to further improve the wall conditions for plasma operations until the first boronization. GDC in helium was executed either daily after hydrogen plasma experiments or application of H_2-GDC to desaturate walls from hydrogen. GDC parameters have been optimized to achieve discharge homogeneity, maximize the cleaning efficiency, and minimize the erosion of PFCs. A reliable break-down could be achieved only for H_2-GDC. The break-down of He-GDC could be made only using a robust workaround and required further development. GDC in hydrogen has a cumulative effect on impurity removal. Thus, a certain amount of H_2-GDC followed by He-GDC is required to ensure reliable plasma operation conditions and provides a minimum hydrogen outgassing level for the physics program.

Three boronizations were applied in the mixture of diborane and helium with time intervals of one month. The process of boronization was optimized from session to session. The first boronization suppressed helium outgassing and significantly extended the plasma operation window in the density range and confinement times. The improvement of the plasma performance was due to a significant reduction of oxygen and oxygen-based impurities. A long-lasting effect of boronization is related to the low impinging ion and charge-exchange flux to the main wall. However, the boron layer is eroded quickly on the divertor target.

Boron dropper experiments in OP1.2b were intended to estimate the effectiveness of the Probe Mounted Particle Injector (PMPI). The positive impact of the boron-containing powder injection on wall conditions is inconclusive. A dedicated set of experiments in an un-boronized device is needed to adequately assess powder injection effects on wall conditioning.

The main conditioning effect of He ECWC in W7-X is related to the cleaning of the divertor area. The technique has been optimized into a routine tool for density control and recovery of the plasma conditions after radiative collapses. The following types of He ECWC were developed. “Single He recovery discharges” are single discharges at low density and moderate heating power. “Pulse trains” are sequences of short, low to medium power discharges with a fixed duty cycle. Pulse trains are found to be more efficient for hydrogen removal. The pulse trains have been optimized through the pulse length, pulse interval, input power and gas pre-fill. The application of the optimized pulse train uses the W7-X experimental time more effectively. Due to boronization, ECWC had to be more refined for fuel recycling control.

The study and optimization of the wall conditioning techniques applied in W7-X required significantly The study and optimization of the wall conditioning techniques applied in W7-X required significantly upgrading the

TOMAS device to understand better the complex multi-physics picture of the wall conditioning techniques and prepare them for further applications on W7-X. The baking experiments showed that it could be employed to remove retained helium after wall conditioning in helium quickly. The installation of a W7-X-like GD system in TOMAS allowed studying an assisted break-down using a localized short-time injection of argon. The influence of the magnetic field on GD homogeneity and the investigation of spurious events in GDC were aimed at reproducing erosion at the GD break-down regime (W7-X like environment). The first pre-characterization of ECWC, ICWC and mixed (ECWC+ICWC) plasmas on TOMAS has been done using Langmuir Probes and Time-of-Flight Neutral Particle Analyzer as part of experiments that study wall conditioning and PSI aspects of these techniques. First experiments on removing boron from coated polished graphite samples made from W7-X tiles by He-GDC contribute to understanding the boron layer lifetime in W7-X. Exposure of the boron coated graphite samples to ICWC requires additional device modifications.

The current wall conditioning strategy of W7-X comprises two phases. The initial phase is performed before the first plasma. It starts with 7 days of vacuum vessel baking at the average PFC temperature of 150 $^\circ\mathrm{C}$. The following step is GDC. First, at least 9-10 hours of GDC in hydrogen with a pressure of $\sim 4.5 \cdot 10^{-3}$ mbar and anode current of 1.5 A. The final step is $\sim$ 2 hours of He-GDC operated at a neutral gas pressure of $\sim 3.8 \cdot 10^{-3}$ mbar and an anode current of 1 A. The second phase is a set of wall conditioning techniques routinely applied during the plasma operation. The boronization procedure with a coating phase of 3.5 - 4 hours should be applied monthly. However, a revision of boronization frequency may be needed in future campaigns. Further development of the boron powder dropper or its analogue should be envisaged to extend the boron coating lifetime. To control the fuel recycling throughout an experimental day, the He ECWC pulse train optimized for application in the boronized device should have a pulse length of 3 s, a pulse interval of about 30 − 35 s, an input power of 2.1 MW, a gas pre-fill with a duration of 15 ms at the constant gas flow of 75 mbar · l/s 100 ms before each discharge. Applying strike lines sweeping and maintaining divertor temperatures above 400 $^\circ\mathrm{C}$ during the pulse train application enhances the fuel removal rate and maximizes the affected divertor area.

The work done in this PhD project will be continued throughout future W7-X operation campaigns. In addition, new tools for wall conditioning, including an ICRH system, will become available.

Publication in scientific literature of the main findings in the scope of this work

- A. Goriaev, T. Wauters, S. Möller, R. Brakel, A. Dinklage, K. Crombé, M. Van Schoor, “First results of W7-X-relevant conditioning procedures on the upgraded TOMAS device”, *44th EPS Conference on Plasma Physics* **Vol. 41F**, (2017)
- Tom Wauters, Andrei Goriaev, Arturo Alonso, Juergen Baldzuhn, Rudolf Brakel, Sebastijan Brezinsek, Andreas Dinklage, Heinz Grote, Joris Fellinger, Oliver P. Ford, Ralf König, Heinrich Laqua, Dmitry Matveev, Torsten Stange, Lilla Vanó, W7-X team, “Wall conditioning throughout the first carbon divertor campaign on Wendelstein 7-X”, *Nuclear Materials and Energy* **17**, (2018) 235–241
- A. Goriaev, T. Wauters, R. Brakel, H. Grote, M. Gruca, O. Volzke, S. Brezinsek, A. Dinklage, M. Kubkowska, U. Neuner, “Development of glow discharge and electron cyclotron resonance heating conditioning on W7-X”, *Nuclear Materials and Energy* **18**, (2019) 227–232
- A. Goriaev, T. Wauters, R. Brakel, S. Brezinsek, A. Dinklage, J. Fellinger, H. Grote, D. Moseev, S. Sereda, O. Volzke and W7-X team, “Wall conditioning at the Wendelstein 7-X stellarator operating with a graphite divertor”, *Physica Scripta* **T171**, (2020) 01406
- A. Goriaev, T. Wauters S. Möller, R. Brakel, S. Brezinsek, J. Buermans, K. Crombé, A. Dinklage, R. Habrichs, D. Höschen, M. Krause, Yu. Kovtun, D. López-Rodríguez, F. Louche, S. Moon, D. Nicolai, J. Thomas, R. Ragona, M. Rubel, T. Rüttgers, P. Petersson, P. Brunsell, Ch. Linsmeier and M. Van Schoor, “The upgraded TOMAS device: A toroidal plasma facility for wall conditioning, plasma production, and plasma–surface interaction studies”, *Review of Scientific Instruments* **92**, (2021) 023506

- Sunwoo Moon, Per Petersson, Per Brunsell, Marek Rubel, Andrei Goriaev, Riccardo Ragona, Sören Möller, Sebastijan Brezinsek, Dirk Nicolai, Christian Linsmeier, Yurii Kovtun and Tom Wauters, "Characterization of neutral particle fluxes from ICWC and ECWC plasmas in the TOMAS facility", *Physica Scripta* **96**, (2021) 124025

- Yu. Kovtun, T. Wauters, A. Goriaev, S. Möller, D. López-Rodríguez, F. Louche, K. Crombé, S. Brezinsek, A. Dinklage, D. Nicolai, Ch. Linsmeier, M. Van Schoor, J. Buermans, S. Moon, R. Ragona and P. Petersson "Comparative analysis of the plasma parameters of ECR and combined ECR + RF discharges in the TOMAS plasma facility", *Plasma Physics and Control Fusion* **63**, (2021) 125023

List of Abbreviations

CXRS charge exchange recombination spectroscopy. 56

DBM Low Iota magnetic field configuration. 50
DC GD Direct Current Glow Discharge. 40
DRGA diagnostic residual gas analyzer. 56

ECRH Electron Cyclotron Resonance Heating. 33
ECWC Electron Cyclotron Wall Conditioning. 34
EJM Standard magnetic field configuration. 50

FTM High Iota magnetic field configuration. 50
FWHM full width half maximum. 115

GD Glow Discharge. 29
GDC Glow Discharge Cleaning. 29

HEXOS extreme ultraviolet overview spectroscopy. 56
HFS High magnetic field side. 131

ICRF Ion Cyclotron Range of Frequencies. 35
ICRH Ion Cyclotron Resonance Heating. 35
ICWC Ion Cyclotron Wall Conditioning. 36
IPD Impurity Powder Dropper. 95

KJM High Mirror magnetic field configuration. 50

LCFS Last Closed Flux Surface. 42

LFS Low magnetic field side. 126

MPM Multi-Purpose Manipulator. 95

NBI Neutral Beam Injection. 52

PFC Plasma-Facing Component. 13

PHA soft-X-ray pulse height analysis. 56

PMPI Probe Mounted Particle Injector. 95

PSI Plasma Surface Interaction. 13

QMS squadrupole mass spectrometer. 56

RF Radio Frequency. 32

RGA Residual Gas Analyzer. 137

TDU Test Divertor Unit. 49

ToF NPA Time-of-Flight Neutral Particle Analyzer. 136

Z_{eff} Effective Plasma Charge. 56

Chapter 1

Introduction

> *Beware of the man who works hard to learn something, learns it, and finds himself no wiser than before. He is full of murderous resentment of people who are ignorant without having come by their ignorance the hard way.*
>
> Kurt Vonnegut, Cat's Cradle

At the beginning of the third decade of the twenty-first century, humanity is facing a tremendous challenge which can cause a global energy crisis and requires a boost of global technological progress. It is related to the production of green sustainable energy provided by reliable sources. This problem is essential for our future and can turn into a climate disaster in the long term if not enough care is taken. It is not new, and it did not appear suddenly. This problem has been being known for decades. However, one can feel that this topic is not enough explained and, consequently, is not well received by a broad audience. Despite these facts, the problem is very well described in many publications, reports, books, and other documents. Moreover, in most bachelor, master or PhD theses directly related to one or another aspect of energy development or distribution, it is mentioned as an introduction.

Nevertheless, this topic cannot be wholly ignored in the scope of this work since it is a premier reason why this work was done. A brief explanation of why everything described further is essential provides a smooth transition to the main topic of this PhD thesis. Thus, the overview of the current situation and its main aspects should be described here.

1.1 Why do we need clean sustainable energy?

Raising living standards, economic growth, and the world population's growth inevitably lead to increased energy consumption. It means that the currently used energy sources have to increase their capacity, or new energy sources should be successfully implemented. According to [1], at the end of 2020, around 70 % of the energy sources are based on fossil fuels such as oil, natural gas and coal. Despite positive progress in some countries whose economies have grown over the last decade, growth in energy use from fossil-fuel sources is still outpacing the rise of low-carbon sources and activities [2]. A major downside of the increase in energy production is an increase in greenhouse gases emission in the current circumstances. Carbon dioxide (CO_2) emissions from fossil fuels and industry comprise $\sim$ 90 % of all CO_2 emissions from human activities [3]. The emission of carbon dioxide, one of the greenhouse gases, is responsible for most climate change [4]. Even with a small exception of temporary reduction of the daily global CO_2 emission forced by unpredictable events like the COVID-19 confinement [5], the common trend shows an average growth of $\sim$ 1.1 % per year [6].

All these facts drive humanity to take major actions to prevent the further growth of greenhouse gas emissions and force the replacement of fossil fuel energy sources to avoid an unforeseen global energy crisis due to a limit of fossil fuel resources. Luckily, the first steps are already made. For example, the Paris climate agreement aims to hold global warming below 2 $^\circ\mathrm{C}$ and "pursue efforts" to limit it to 1.5 $^\circ\mathrm{C}$ [7]. The European Commission aims to reduce EU greenhouse gas emissions by at least 55 % by 2030, compared to 1990 levels, as a stepping stone to the 2050 climate neutrality goal [8]. Some other countries, like G20 countries, are planning to shift their energy politics towards the domination of alternative energy sources [9]. Thus, there is a well-established global need for sustainable low-carbon sources of electricity, especially for reliable and predictable power generation.

1.2 Low-carbon energy sources

Looking for low-carbon alternatives, the first that comes to the game is to check what is already available in the market. First of all, it is essential to choose sources that can successfully substitute fossil fuel on a large scale of energy production and in a relatively short time. Nuclear power and hydropower form the backbone of low-carbon electricity generation. Together, they provide three-quarters of global low-carbon generation [1].

1.2.1 Hydropower

Hydropower is a renewable energy source where electrical power is mainly derived from the energy of water moving from higher to lower elevations. This energy source requires no fuel and can respond almost instantaneously to changing electricity demand independent of the time of day or the weather. Hydropower is the leading source of renewable energy across the world (at the beginning of 2021). The technical potential for hydropower development around the world is much greater than the actual production. However, dams that are often used to generate electricity can have significant negative social and environmental impacts. Among them are disrupting river ecology, deforestation, losing aquatic and terrestrial biodiversity, releasing substantial greenhouse gases, displacing thousands of people, altering people's livelihoods, and affecting the food systems, water quality, and agriculture near them [10]. Moreover, not all regions in the world have considerable hydropower resources. It slows down the further development of the hydropower sector and requires innovative solutions that can move hydropower towards sustainable practices together with other renewable sources.

1.2.2 Nuclear power

Nuclear power is the second-largest source of low-carbon electricity today after hydropower, providing $\sim$ 10 % of the global electricity supply in 2020 [1]. The vast majority of electricity from nuclear power is produced by the energy released in a controlled nuclear fission reaction. In this reaction, the nucleus of an atom splits into two or more smaller, lighter nuclei. On the one hand, nuclear power is a carbon-free and sustainable energy source that provides enormous amounts of uninterrupted energy without direct pollution and greenhouse gas emissions. Nuclear power has relatively low fuel costs and can run at maximum capacity almost constantly [11].

On the other hand, several aspects pose potential threats to people and the environment. These include health risks, accidents and environmental damage from uranium mining, processing, transport and storage. Misuse of radioactive fuels or fuel waste can also be dangerous. However, the risks of storing waste are small and existing stockpiles can be reduced by using new recycling schemes [12]. Moreover, the complexity of nuclear reactors operations without proper handling can cause serious nuclear accidents. Among them, there are the Three Mile Island accident in the United States in 1979, the Chernobyl disaster in the Soviet Union in 1986 and the Fukushima Daiichi nuclear disaster in Japan in 2011.

As one can see, there is a long-running controversy about the advantages and disadvantages of using nuclear power [13]. Nevertheless, in advanced economies, like the German and Belgian ones, nuclear power has begun to fade, with plants closing and little new investment made, just when the world requires more low-carbon electricity [1].

1.2.3 Renewable sources

Renewable energy sources like sunlight, wind, rain, tides, waves and geothermal heat are naturally replenished on a much longer timescale than the human one. These energy sources are already available in the market and continue to grow strongly in the coming decade and beyond. Moreover, renewable energy technologies are getting cheaper through technological progress and the benefits of mass production and market competition [14]. Renewable electricity production from sources such as wind power and solar power is intermittent. It results in a limited capacity factor and requires either energy storage of capacity equal to its total output or backup power sources from hydropower, fossil fuels, nuclear power, or the development of a different energy source that is not yet available in the market.

1.2.4 Nuclear fusion

One of the promising solutions is to employ nuclear fusion, which is the source of energy radiated by the Sun and other stars. Nuclear fusion is a reaction of energy release due to the mass difference when two or more atomic nuclei fuse into different atomic nuclei and subatomic particles like neutrons. The same processes are proposed to build a steady and sustainable energy source, for example, based on the reaction between hydrogen isotopes (hydrogen fusion). The amount of fuel that is needed to run the reaction is tiny. If the fuel is not continuously replaced, the fusion reaction fades out. This makes a fusion power plant intrinsically safe [15]. In case of hydrogen fusion, a part of the fuel, tritium, is, indeed, radioactive. However, it has a relatively short half-life period (12.3 years for tritium) and can be quickly recycled and burned in a power plant.

The fusion reaction itself does not produce any radioactive waste. However, the radioactive neutron damage of fusion power plant components is inevitable due to its large energy ($\sim$14.06 MeV). In a reactor, this can be mitigated by deposition of their energy in the absorber (reactor blanket) to facilitate heat exchange and transfer to electricity-generating systems of a power plant [16].

The fuel of a fusion power plant is estimated to be less than 1 % of the total cost, while a few grams of fusion fuel can produce as much energy as tens of tons of fossil fuel. The major part is going to construction and maintenance [15]. Studies show that the nuclear fusion energy source shows that apart from being safe, clean and environmentally friendly, it can also be competitive with other sources in terms of costs. Furthermore, fusion and renewable technologies can co-exist with varying market shares without running into severe system incompatibilities [17]. A carbon-free power mix with fusion would be less expensive and more affordable [18].

These challenges are attractive despite the tremendous and complicated science and technology challenges for fusion [19]. The idea of realizing the controlled fusion power inspires many people, including the author of this PhD thesis. Thus, the rest of the introductory chapter is dedicated to the description of fusion mechanisms and recent achievements in fusion science and technology, smoothly flowing to the specialized topic of this work.

1.3 The idea behind nuclear fusion

The basic idea behind nuclear fusion-based energy sources is to employ liberated energy due to the mass difference between the reactants and products of the fusion reaction, which is well-known as a *mass defect*. It represents the difference of atomic binding energy between the nuclei before and after the reaction and is described by the famous Einstein' formula $E = mc^2$.

Nuclear fusion is the primary energy source of stars including the Sun. The energy production in the Sun contains stepwise conversion of four protons into a helium nucleus. The first reaction, which combines two protons to form deuteron, requires one of the protons to be converted into a neutron. That is the most challenging stage and much too slow to be employed on Earth. However, the second step of this chain, the reaction between proton and deuteron resulting in the production of helium-3 isotope, occurs much more quickly as well as other reactions which are more promising for application in fusion studies. For example,

$$D + D \to T + p,$$

$$D + D \to {}^3He + n,$$

$$D + T \to {}^4He + n,$$

$$D + {}^3He \to {}^4He + p.$$

Producing net energy by fusion on earth fusion is difficult. It is understood from the interplay of two opposing forces: the nuclear force, which combines nucleons, and the Coulomb force, which causes positively charged particles to repel each other. Since the nuclear force can overcome the Coulomb one only at a short-range, it takes considerable energy to force nuclei to fuse, even those of the lightest elements like hydrogen. In the Sun and other stars, the right conditions are provided by gravity. It prevents them from expanding and compresses the nuclei close enough to have a good statistical chance for fusion reactions to occur. However, gravity is a very weak force. Gravitational confined fusion works only when the mass is enormous. That is why this mechanism will not work in fusion applications on Earth. Thus, other ways of providing confinement should be found.

The components must be accelerated to a few 10's of keV are needed to overcome the Coulomb barrier making a hydrogen fusion reaction. Nevertheless, a fusion reaction has a certain probability of occurring. It is always measured in the form of a *cross section*. So, it makes sense to select a reaction that requires less energy and has a high probability, i.e. easier to achieve.

The cross-sections for the most probable fusion reactions are shown in Fig. 1.1. One can see that the most favourable reaction is D-T. It can be achieved with the highest probability at the lowest input energy. The scheme of this reaction is shown in Fig. 1.2. Providing the energy of 100 keV is not a problem for nuclei accelerators nowadays. However, since the cross-section of the D - T reaction is too small, only a tiny fraction of collisions result in a fusion event. Thus, most of the invested energy is lost in case of single collisions. Thus, to avoid it, one can think about an increase in the number of particles. In this case, it is better to use a mixture of deuterium and tritium gas and heat it to the required temperature. However, at these high temperatures, this gas will be fully ionized, transforming into plasma. At the same time, the temperature of the ions in fusion plasma is so high that no vessel can contain such plasma without damage to its wall material.

There are two main options how to keep high energetic ions far from vessel walls. The first option is called *inertial confinement*. Its principal mechanism is to compress the fusion reactants and then heat them quickly enough to ensure that fusion occurs before the reactants expand and their energy is lost at the walls. Another option is to use a magnetic field to guide charged particles along the field lines by the *Lorentz force*. Arranging the magnetic field lines in a proper configuration can prevent charged particles from collisions with the walls. It is the so-called *magnetic confinement*.

Both ways are pretty interesting, providing a lot of different technological and scientific tasks which are challenging for researchers and engineers.

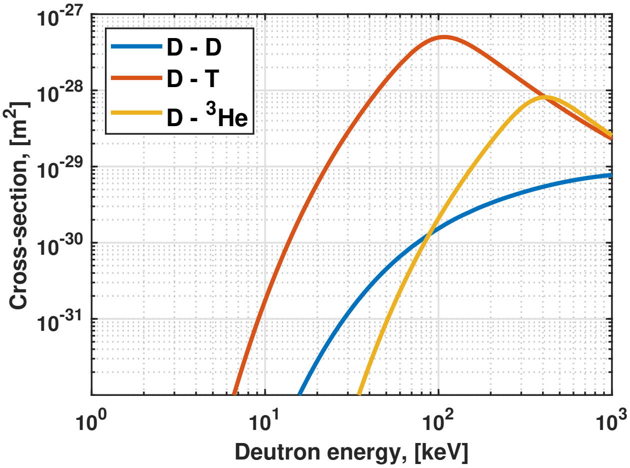

Figure 1.1: The cross section of fusion reaction for a range of energies of deuterons.

Nevertheless, for some unknown reasons, the author of this PhD work has chosen to do research in the field of magnetically confined fusion.

1.4 Magnetically confined fusion

Magnetic confinement fusion retains plasma via the collective behaviour of its free charge carriers and their interaction with magnetic fields so that the magnetic pressure should offset the plasma pressure. To achieve a successful arrangement, it has to meet the following criteria. The plasma must be in a time-independent equilibrium state. The equilibrium is macroscopically stable and features small plasma energy dissipation to the walls.

A plasma in stable equilibrium can be maintained indefinitely if the energy loss from the hot plasma is balanced by energy input. The energy can be provided by external sources or by the fusion products (e.g. alpha-particles). Ignition (in the case of D - T reaction) is achieved when alpha particle heating is sufficient by itself to make the fusion reaction self-sustaining. It is described by the *Lawson criterion*, which compares the rate of energy generated by fusion reactions within the fusion fuel to the rate of energy losses to the environment. Its extension into the "triple product" of the plasma density n, the energy confinement time τ_E, i.e. the inverse rate at which a system loses energy to its environment, and plasma temperature T, gives minimum

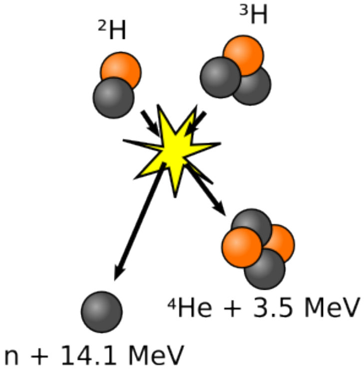

Figure 1.2: Fusion reaction of deuterium and tritium creating helium-4, freeing a neutron, and releasing 17.59 MeV as kinetic energy of the products.

required plasma parameters to obtain ignition. The condition for ignition is

$$nT\tau_E > 3 \times 10^{21} m^{-3} keV \cdot s. \qquad (1.1)$$

Ignition corresponds to infinite fusion energy gain factor Q which is given as the ratio of fusion power produced in a nuclear fusion reactor to the power required to maintain the plasma in a steady state. Q is also a measure of the fusion device performance. When $Q = 1$, so-called *breakeven* state, the fusion device can sustain a steady-state fusion reaction. A future fusion reactor should have predominant alpha particle heating meaning that $Q > 5 - 10$.

Another critical point, which can slow down the development of fusion power plants, is that the amount of available tritium is really small. Tritium does not occur naturally on Earth due to its radioactivity. Tritium will have to be manufactured as a fuel.

The key solution for fusion reactors is to use a so-called *lithium blanket*. It serves several purposes like shielding, cooling and tritium generation by absorbing neutrons produced by the fusion reaction. The latest is achieved according to two possible breeding reactions:

$$^6Li + n \rightarrow {}^4He + T,$$

$$^7Li + n \rightarrow {}^4He + T + n.$$

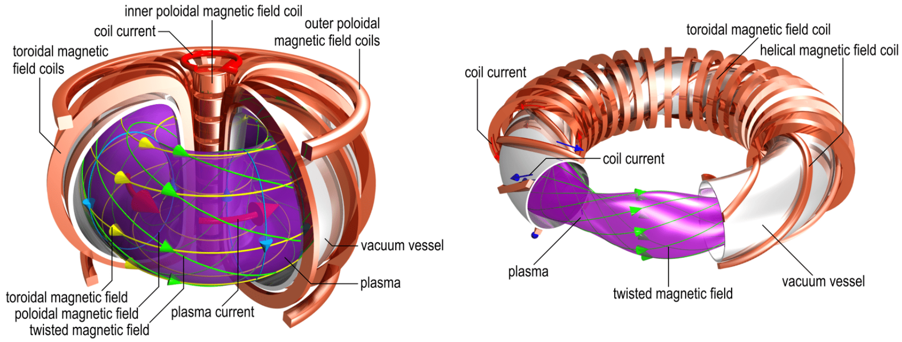

Figure 1.3: Schematic representation of tokamak (left) vs classical stellarator (right) [21].

1.4.1 Fusion devices

Many different types of magnetic configurations for plasma confinement have been devised and tested over decades. These may be grouped into two classes: open, linear configurations and closed, toroidal configurations.

Among others, the linear device configuration, where the strength of the magnetic field is increased at the ends, has become the earliest major approach to fusion power. In this configuration, charged particles approaching those ends slow down and most of them are reflected back. It is a so-called *magnetic mirror*. However, these magnetic mirrors cannot stop particles with dominantly parallel velocity, making them lost from the system. Various improvements, such as electrostatic plugging and additional plasma sections added behind the magnetic mirrors, were introduced to inhibit this leakage [20]. Even the invention of linear machines without requiring enormous magnets and power input did not prevent this field of research from giving the favour to toroidal devices.

The second group of magnetic configurations belongs to toroidal devices, which are highly developed nowadays. The most extensively investigated toroidal confinement concepts are *tokamaks* and *stellarators*. For both types of machines, it is essential to keep plasma in stable equilibrium. For this purpose, it is necessary to provide a twisted magnetic field that prevents charge separation and particle drifts.

The concepts of a tokamak and a classical stellarator are shown in Fig. 1.3. The total magnetic field in these devices is helical and wrapped around the torus. It consists of two components, $B = B_t + B_p$, a toroidal component B_t and a poloidal component B_p.

In a tokamak, the toroidal field is produced by coils that surround the toroidal vacuum chamber containing the plasma. The poloidal field is generated by a toroidal electric current that is forced to flow within the conducting plasma. It is typically done by a central solenoid which acts as a primary circuit in an improvised transformer while the plasma plays the role of the secondary circuit. Unfortunately, it cannot be used for a steady-state current making the plasma operation pulsed in tokamaks. However, this problem can be mitigated by using advanced techniques such as, for example, radiofrequency (RF) current drive [22] and neutral-beam current drive [23]. The outer poloidal field coils are used for positioning, shaping and stabilizing the plasma column.

In a classical stellarator, the magnetic field is produced by external coils only. Thus, the plasma current is essentially zero which, in turn, gives rise to the absence of toroidal symmetry. In the classical stellarator, a set of toroidal field coils produces the toroidal component of the magnetic field. Another set of coils is wound helically around the plasma, and it sits inside the toroidal field coils. The helical coils are arranged in pairs, with currents flowing in opposite directions in adjacent coils. Thus, their fields are cancelled in the torus centre. At the same time, it causes the toroidal field lines to twist at the outside edge. Modern stellarators use an optimized 3D-shaped modular coil set designed to simultaneously achieve high plasma performance, low currents and good confinement of energetic particles.

1.4.2 The next step devices

All fusion devices in operation are only experimental machines today. There are some critical stages to test the relevance of fusion power on a commercial scale to come to full-scale electricity-producing fusion power stations and future commercial reactors.

The first planned step is ITER [24]. It will be the world's largest tokamak, with a plasma radius of 6.2 m and a plasma volume of 840 m^3. ITER will demonstrate that a burning plasma can be created and sustained, generating up to 500 MW of fusion power. The planned injected power will be 50 MW corresponding to a fusion gain $Q = 10$ in the plasma. ITER is expected to achieve robust burning plasma regimes and test the conventional physics solutions for power exhaust. The ITER project will contribute to developing the scientific know-how for the plasma and some of the technology. The ITER planned successor, DEMO [25], will take fusion to the next level – a fully integrated science and technology demonstration of fusion. It is expected to be the first fusion reactor to produce electricity in an experimental environment. Its general goals are predictable power output of 300 – 500 MW of electricity to the grid, self-sufficiency in tritium, safety and environmental sustainability. While ITER is an international project, DEMO is seen as multiple national multi-phase plants [26].

1.4.3 EUROfusion Roadmap

To guide the fusion research in Europe aiming to be a key player in the fusion research market EUROfusion consortium was established. It unifies national fusion research institutes located in the European Union, the UK, Switzerland and Ukraine [27]. Nowadays, EUROfusion supports and funds fusion research activities on behalf of the European Commission's Euratom programme. Meeting the long-term need of fusion in time requires a strong programme in parallel with the construction and exploitation of ITER. The following steps are foreseen to achieve this goal for magnetic confinement fusion.

1. Technical demonstration of large-scale fusion power
2. Electricity delivered to the grid via a DEMOnstration fusion power plant (DEMO)
3. In parallel, a science, technology, innovation and industry basis to allow the transition from the demonstration fusion plant to affordable devices suitable for large scale commercial deployment
4. Large scale industrial production of fusion plants.

The European fusion roadmap addresses the first three of these goals, all in the context of the final goal (Fig.1.4). This plan leads to early conceptual design(s) of a European DEMO [28].

1.4.4 The role of stellarators

The stellarator is a possible long-term alternative to a tokamak fusion power plant. It is an integral part of the strategy to provide a sound basis for future fusion deployment, additionally supporting the ITER physics programme [27].

One of the main reasons for pursuing the stellarator line is their inherent steady-state capability and non - disruption (without a rapid loss of the stored thermal and magnetic energy) plasma, which are challenges for the tokamak. The European programme primarily focuses on the optimized stellarator Helias (Helical-Axis Advanced Stellarator) line to bring the stellarator

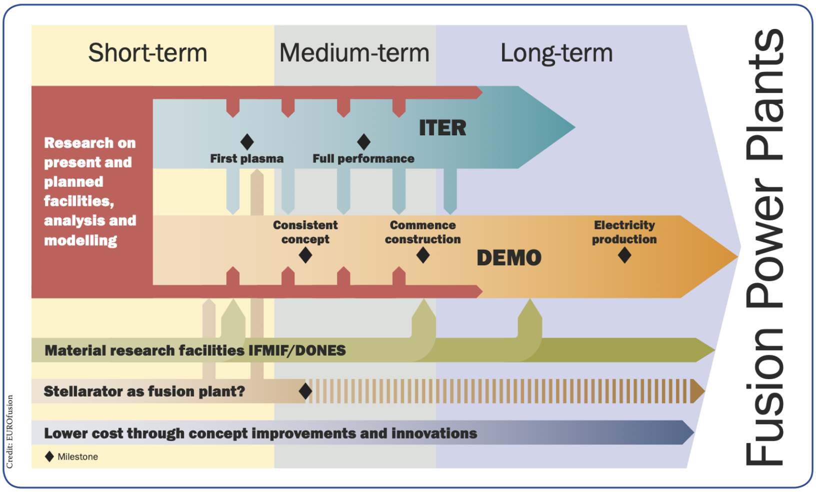

Figure 1.4: The European Roadmap in a nutshell [27].

configuration to maturity. This stellarator optimization approach is based on modular field coils. In the short term, the main priority of the European stellarator programme is the scientific exploitation of the superconducting stellarator Wendelstein 7-X (W7-X) [29]. The device is supposed to work under steady-state conditions demonstrating high-performance plasma scenarios.

The objective of W7-X is to demonstrate that the theoretically based optimization works in practice so that plasma properties that extrapolate to power plant requirements can be reached in a stellarator. Specifically, a triple product $(n \cdot T \cdot \tau_E)$ comparable to tokamaks of similar size should be achieved in conditions approaching a steady-state with up to 30 min of high-power operation [30]. W7-X also aims to show plasma parameters close to reactor parameters, e.g. plasma temperatures of more than 4 KeV and densities above 10^{20} m^{-3}, volume average normalized total plasma pressure of ≥ 5 % [31].

1.4.5 Technological and engineering challenges of fusion

The realization of fusion energy also has to face several particular challenges such as the development of plasma regimes of operation, development of an adequate solution for the large heat exhaust, production of neutral tolerant materials, research on tritium self-sufficiency, implementation of intrinsic safety measures, and combining all the fusion technologies into an integrated DEMO design [32].

The significant increase in discharge duration and plasma energy in a subsequent fusion reactor requires more power necessary to maintain plasmas at high temperatures. Part of this power has to be exhausted. It is done via plasma-facing components (PFCs) and exhaust systems which must be capable of withstanding the enormous heat and particle fluxes of a fusion power plant and at the same time allow as high performance as possible from the plasma. Thus, it will require an increased effort in edge plasma physics and Plasma - Surface Interaction (PSI) studies.

1.5 The problems of plasma - wall interaction

PSI in controlled fusion devices leads to significant surface modifications at the PFCs. These interactions comprise all processes involved in exchanging mass and energy between the plasma and the surrounding walls causing physical sputtering, chemical erosion, melting, evaporation or sublimation [33]. Moreover, PSI is responsible for two critical elements of high-performance operation: plasma impurities and fuel recycling [34].

1.5.1 Impurities

Besides all types of PFC damage mentioned above, another source of impurities is an exposure of the vacuum vessel to the air. Even after the initial pump down of the device, some of the species remain in the vessel. Additionally, occasional small leaks of the vacuum vessel can also significantly contribute to the amount of impurities. Layers of carbon and oxygen always cover surfaces even under ultra-high vacuum conditions. For example, oxygen at the walls is present in the form of adsorbed hydroxides, water, and various metal oxide compounds. Particles and radiation from the plasma bombard the walls, facilitating impurity species release (Fig. 1.5). The wall released impurities, often volatile neutrals, are partially evacuated from the chamber. Nevertheless, most of them are instantly ionized and transported along the magnetic field lines in the plasma edge until they get re-deposited at another surface location.

Plasma impurities cause two main effects related to high performance: the radiation of power and the dilution of the hydrogenic species. Furthermore, they can influence collision processes via Z_{eff}, and plasma resistivity, impacting plasma stability and global energy confinement [34]. The impurity radiated power increases strongly with Z. Different impurity atoms will radiate in different plasma regions according to their atomic number Z, various ionization and excitation potentials [35]. The ions with many electrons are

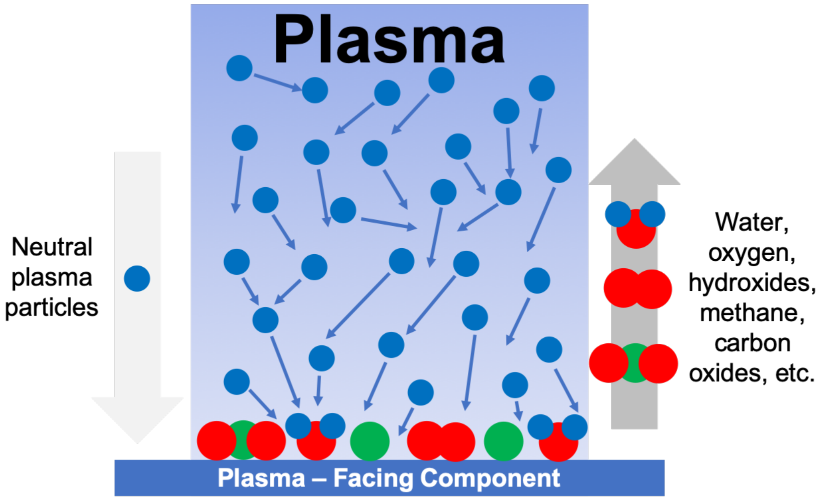

Figure 1.5: Impurity release scheme

responsible for energy radiated from the plasma core. It makes it challenging to reach ignition temperature and often lead to a plasma radiative collapse.

Plasma impurities also cause a dilution of the hydrogenic fuel. The nuclei of impurity atoms take the place of those from deuterons and tritons. The dilution cannot be counteracted by simply increasing the concentration of hydrogenic species due to the limit of the maximum achievable plasma density [36].

1.5.2 Fuel retention

Fuel recycling is the repeated interchange of hydrogen isotope species between the plasma and the wall (Fig. 1.6). Its appearance is different on metallic surfaces and ceramics such as graphite or boron and silicon containing layers. The fuel recycling can vary, depending on wall temperature and preloading, from a state in which the wall strongly absorbs plasma particles (wall pumping) to one in which hydrogen isotopes from the wall almost fully fuel the plasma and density control is impossible [34].

Fuel retention is one of the crucial points for the next step fusion devices, particularly for the long discharge operation. For example, the working guideline for the initial operation of ITER sets the limit of 700 g for the inventory of releasable tritium in the vacuum vessel [24, 37].

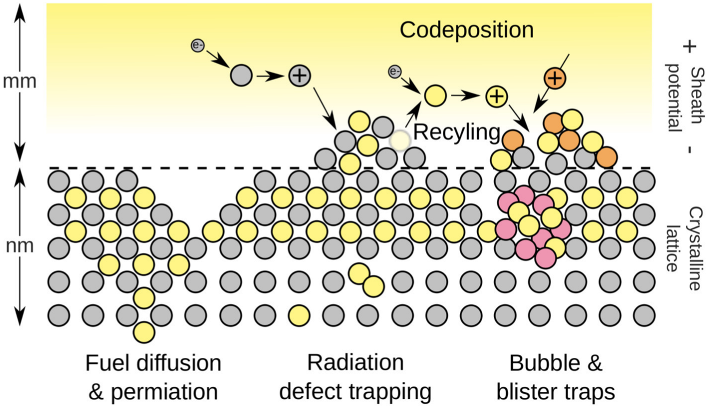

Figure 1.6: Fuel recycling and impurity redeposition scheme.

1.6 Wall conditioning

Wall conditioning in magnetic controlled fusion devices is a standard tool to influence fuel and impurity recycling, improve plasma performance and discharge reproducibility [34]. It allows controlling the surface state of plasma-facing components, easing plasma initiation and providing hydrogen isotopic ratio control. More specifically, conditioning techniques facilitate fusion device start-up and recovery from events such as disruptions in a tokamak, radiative collapses in a stellarator, or vacuum leaks. Conditioning accelerates the transition from plasma operations in one main plasma element, either a hydrogen isotope or helium, to another and provides access to advanced scenarios [38]. Wall conditioning usually occurs in the preparation of experimental campaigns, e.g. after vessel openings or during operation campaigns [39].

A number of wall conditioning techniques are applied for specific reasons and dependent on device types, operation stages, available plasma heating systems, other available equipment for wall conditioning, the material of PFCs, etc. Combining those methods forms an individual wall conditioning strategy for every nuclear fusion device in a particular configuration facilitating high-performance scenarios achievement and making device exploitation more time-efficient.

1.7 PhD thesis overview

This experimental PhD research project aims to study the conditioning methods applied in the superconducting stellarator Wendelstein 7-X. The first point of this work is to compare experimentally the conditioning effect of various wall conditioning techniques applied in W7-X in terms of removed gas, minimization of impurity content and subsequent W7-X plasma performance. Secondly, this thesis aims to give a comprehensive description of the conditioning mechanisms relevant to W7-X. The last point is to perform conditioning optimization to maximize effectiveness in PFC surface modification for the benefit of W7-X plasma performance while ensuring good and safe conditions of discharge operation. As a summary, this work aims to propose the wall conditioning strategy for the next operation phases of the superconducting stellarator Wendelstein 7-X.

In Chapter 2, the role of wall conditioning in the preparation and exploitation of fusion devices is discussed. A few models describing outgassing (thermal desorption and particle-induced desorption) are presented to understand the fundamental processes of fuel and impurity release. The chapter gives a detailed review of the wall conditioning techniques relevant for application in the superconducting stellarator W7-X operating in the divertor configuration with graphite PFCs. Typical wall conditioning techniques, such as baking, Glow Discharge Cleaning (GDC) and wall coating by boronization, are described. The new conditioning techniques working in presence of the nominal magnetic field, such as Electron Cyclotron Wall Conditioning (ECWC) and Ion Cyclotron Wall Conditioning (ICWC), are found to be highly relevant to superconducting fusion devices. All presented wall conditioning techniques are accompanied by an overview of the application experience in other fusion devices, giving a valuable hint for their application in W7-X. The importance of pulsed discharge conditioning is introduced to achieve the maximum pumped throughput of wall desorbed impurity or fuel flux. Finally, some experience of real-time wall conditioning techniques development is demonstrated to be applied in W7-X.

Chapter 3 is dedicated to the wall conditioning on the superconducting stellarator W7-X. The first part of the chapter is focused on the technical specification of W7-X and a brief description of the system and diagnostics relevant for wall conditioning studies. This part also includes a short description of the device upgrades and the achievements in the first operational phase OP1.1 (in 2016) carried out in the limiter configuration and two parts, OP1.2a (in 2017) and OP1.2b (in 2018), of the second operational phase, carried out in the uncooled divertor configuration. The second part of this chapter describes the application and analysis of wall conditioning techniques on W7-X. An overview of wall conditioning is given for each experimental campaign. An application of baking and GDC prior to the device operation is investigated. This part also shows the optimization of GDC as routine cleaning methods applied between experimental days. The critical role of boronization is emphasized in the way of achieving high densities. Approbation of the real-time wall conditioning by boron dropper experiment is analyzed by the impact on the plasma performance and impurity content. Different types of ECWC based on single discharges and multi-discharge sequences are analyzed by means of fuel removal efficiency. The remainder of the chapter is dedicated to the optimization of the selected ECWC type.

Chapter 4 introduces the upgraded TOMAS (TOroidal MAgnetized System) device [40], specially prepared to study wall conditioning, plasma start-up, and PSI to better understand the underlying physical processes. The first part of the chapter gives a detailed technical overview of the device, describes its engineering and research capabilities. Another part shows the contribution of wall conditioning and PSI studies on TOMAS, such as some aspects of baking and GDC, to W7-X wall conditioning optimization. The results of the first RF-plasma characterization are also presented in this chapter. The first PSI experiments on TOMAS aim to facilitate studies of the boronization lasting effect. Finally, future contributions of TOMAS and its corresponding modifications are discussed in the scope of further W7-X wall conditioning development.

In Chapter 5, the wall conditioning strategy is formulated for W7-X operating with uncooled graphite divertor based on the analysis results of wall conditioning experiments in OP1, OP1.2a and OP1.2b experimental campaigns together with the contribution of the studies on other fusion devices. The option of ICWC exploitation as a technique for regular wall conditioning is considered for application in future operation phases when the ICRH system [41] becomes available. It also aims to show a contribution of other fusion device experiences to ICWC studies for W7-X. The possible future improvements of the W7-X wall conditioning strategy are discussed, taking into account other upcoming device modifications and upgrades. It gives recommendations for further application of wall conditioning techniques in W7-X to provide the best outcome through high-performance plasma achievement and efficient device operation.

Chapter 6 is the conclusion. This chapters summarizes the results of experimental wall conditioning studies and findings in the frame of the given PhD project.

Chapter 2

Wall Conditioning

> *Theory and practice sometimes clash. And when that happens, theory loses. Every single time.*
>
> Linus Torvalds

The performance of present-day fusion devices depends strongly on the conditions of the plasma-facing components (PFCs), which can act as uncontrolled sources of impurities, through chemical and physical processes, and discharge gas, through recycling. Numerous wall conditioning techniques have been explored and developed to minimize these effects and allow operation with controlled density and low impurity concentrations.

A first big overview of different wall conditioning methods applied in fusion devices and their influence on plasma performance was given by J. Winter [34]. However, the permanent development of fusion technology, material science and commissioning of new fusion devices introduces new challenges for wall conditioning. Successful exploitation of fusion devices with superconducting coils demands new conditioning techniques that work in the presence of the nominal field. An overview of recent wall conditioning results in view of superconducting devices has been provided by T. Wauters [38]. Nevertheless, the application of any wall conditioning technique is individual for every fusion device, taking into account peculiarities of the device construction and exploitation. Thus, every fusion device should have its wall conditioning strategy.

This chapter gives a detailed review of the wall conditioning techniques relevant for application in the superconducting stellarator W7-X operating in the divertor configuration with graphite PFCs. The review contains the physics basis for wall conditioning, technical details of technique application and examples of the successful experience of these techniques' exploitation in other fusion devices.

2.1 Baking

Baking or bake-out in vacuum technology is usually the process of using high temperatures to remove by thermal desorption the volatile species from materials of inner walls of a vacuum chamber to prevent its further migration and contamination of fusion plasmas. Baking can be described as a forced acceleration of the process of outgassing. Outgassing means that molecules, which have been previously adsorbed during venting of the vacuum vessel, plasma operation or even component manufacturing, diffuse through the bulk of material of in-vessel components, arrive at its surface layer and desorb from it. The main consequence of this effect is that the outgassing molecules, which would be strong source of impurities in plasma operations, can be evacuated by the vacuum pumps.

In the case of an ideally pumped vacuum vessel (no leaks, no outgassing, no gas permeability) with initial pressure p_0 and without external gas introduction, the relation between pressure p and time t can be described as follows.

$$V\frac{dp}{dt} = -Sp(t) \tag{2.1}$$

or

$$p = p_0 \exp\left(-\frac{S}{V}t\right), \tag{2.2}$$

where V is the volume of the vessel and S is a volumetric pumping speed. The ratio $\tau_{ps} = V/S$ is considered to be a time constant. Thus, the p shows an exponential dependence on time.

In reality, only the initial phase of pumping corresponds to this exponential behaviour. Then, it is gradually changed to the asymptotic behaviour corresponding to a much slighter pressure decrease with a continuously increasing time constant τ_{ps}. It is usually due to the slow desorption of the gas adsorbed when the vessel is exposed to atmospheric pressure or plasmas. The desorption rate depends on the binding energies of the various gases to the surface, the surface material, the surface roughness and the surface temperature. It is generally observed that water dominates the outgassing in previously unbaked systems by more than 85 % [42]. The remaining outgassing species are H_2, CH_4, CO, and CO_2 for a clean system.

For water, but also for other molecules, there are two main mechanisms of adsorption. The first is physical adsorption, corresponding to a process where the fundamental interacting force between a surface and gas species is the Van der Waals force. The typical binding energies are below 0.4 eV [43]. The second mechanism is chemical adsorption which involves a chemical reaction between the surface and the gas. In this case the bond between the adsorbate and adsorbent is either covalent or ionic. The binding energies between the atoms and molecules of the vacuum material surface and the gas molecules range from 1 - 10 eV [44]. The amount of the adsorbed gas increases with the gas pressure at a constant temperature on a given surface [45].

A complete theory of adsorption/diffusion tends to be complex. This is due to the complexity of material surfaces and the many possible chemical reactions at the surfaces. For example, the metal surfaces inside a vacuum vessel are always covered with oxide or adsorbed oxygen. Thus, the first layer of adsorbed water is assumed to be formed as

$$H_2O + O \rightarrow 2OH.$$

The amount of water that is chemisorbed on the surface increases with increasing surface roughness. Outgassing follows then from the reverse process [46], as

$$2OH \rightarrow H_2O + O.$$

but, can occur as well from a recombination with hydrogen. Finally, the reduction of the metal oxides can also occur directly with hydrogen [47]. For example, the ferrous oxide reacts with molecular hydrogen as

$$FeO + 2H \rightarrow Fe + H_2O.$$

Adsorption models assume that molecular diffusion is either nonexistent or occurs sufficiently slowly that it only affects the outgassing rate at very long times [46].

To include outgassing the pressure balance, Eq. 2.1 should be extended to

$$\frac{dp}{dt} = -\frac{S}{V}p(t) + \frac{k_B T}{V}\frac{dN}{dt}. \tag{2.3}$$

The outgassing rate is often measured as the difference between desorption and re – adsorption rates. The outgassing term of Eq. 2.3 can be written as

$$\frac{dN}{dt} = \frac{dN_d}{dt} - \frac{dN_a}{dt}, \tag{2.4}$$

where N_d is a number of desorbed molecules assuming that the outgassing (re-adsorption) equilibrium is reached much faster than the pumping time, and N_a is a number of adsorbed molecules.

In the next section, two outgassing models for water are described for illustration. A first model assumes processes that occur at the surfaces, while the next model includes diffusion in the material into the rate determining equation.

2.1.1 Surface adsorption description for thermal desorption

This adsorption model assumes a quasi-static solution and that the adsorption is fully reversible. It means that the residence time of adsorbed molecules exchanging with the gas phase is short compared to a measured pressure change. The surface coverage can be expressed as a function of pressure by a suitable adsorption isotherm. One can describe it as the relation between the pressure and amount of adsorbed gas for monolayer adsorption. The distinct properties, development and potential applications of various adsorption isotherm systems are described in [45].

In this case, the outgassing term $\frac{dN}{dt}$ of Eq. 2.3 can be found by differentiating an appropriate adsorption isotherm, a function of the surface coverage $f(\theta)$. According to [46], for reversible adsorption, the surface coverage may be expressed as a function of pressure by a suitable adsorption isotherm which may be represented in general as

$$\theta = f(p) = \frac{N}{N_m}, \tag{2.5}$$

where m indicates monolayer coverage. For multiple adsorbed layers, the appropriate adsorption isotherm will vary for the outer layers [48]. Thus, Eq. 2.3 can be converted to

$$\frac{1}{p}\frac{dp}{dt}\left(1 - \frac{k_B T N_m}{V}\frac{d\theta}{dp}\right) = -\frac{S}{V}. \tag{2.6}$$

Due to the complexity of the surface, one can assume that the surface is heterogeneous and either (i) the distribution of energy is exponential amongst the adsorption sites or (ii) the distribution of energy decreases linearly with increasing coverage.

(i) corresponds to the so-called Freundlich isotherm and gives

$$\theta = kp^{\beta}, \tag{2.7}$$

where k and β are constants.

(ii) is related to Temkin isotherm and can be described as

$$\theta = A\ln(p) + B, \tag{2.8}$$

where A and B are constants.

After substitution of these isotherms into Eq. 2.6, one can get

$$p = C_1 p_0 t^{-\gamma}, \tag{2.9}$$

for the Freundlich isotherm and

$$p = C_2 p_0 t^{-1}, \tag{2.10}$$

for the Temkin isotherm, where C_1 and C_2 are constants dependent on T as $\sim \exp\left(\frac{-\Delta E}{k_B T}\right)$, ΔE is the activation energy, p_0 is the pressure at time 0.

Both approximations are only helpful over a limited range of coverage and cannot be a realistic representation of adsorption. Temkin isotherm is only valid in the middle range of coverage, while Freundlich isotherm cannot be used for heterogeneous surfaces. However, it shows the approximate pressure variation with time, most frequently observed for real systems. Indeed, some study indicates that the desorption rate follows the power law which, when the pumping speed is constant, corresponds to Eq. 2.9 [42]. The dependence of the measured rate on the pumping time τ_{ps} and the sticking probability is discussed in [49].

Numerous measurements of outgassing from metal surfaces show that the outgassing obeys a power law of where the exponent is typically near unity [50] which is similar to Eq. 2.10. However, in some cases, γ can be a function of the water vapour exposure during venting of the system, the surface material and roughness, and the physical properties of the passivation oxide layer on the surface. It should be noticed that the quantity of H_2O desorbed depends on the exposure duration as $\sim \log(t_0)$ and on the H_2O partial pressure during exposures as $\sim p_0^{0.25}$ [51].

2.1.2 Diffusion and surface recombination model for thermal desorption

Another model which can explain the outgassing behaviour of water takes into account diffusion in the surface. Fick's laws give the most common description of diffusion. The first Fick's law of diffusion can be written as

$$Q(x,t) = -D\frac{\partial U(x,t)}{\partial x}, \tag{2.11}$$

where D is a constant diffusion coefficient with the initial boundary conditions and U is the sorbed gas distribution near the surface of a vacuum vessel wall after venting for some time. According to [50], one can describe U as

$$U(x,o) = C_1 \exp\left(-\frac{x2}{\lambda^2}\right) + C_0, \tag{2.12}$$

where x is the distance from the surface, C_1 and C_0 are the density constants of the sorbed gas and λ is a length parameter giving the depth adsorbed molecules diffused into the chamber wall from a surface by the end of the venting period. Using Eq. 2.12 and taking into account that the outgassing rate should be corrected to the actual surface area, the solution of Eq. 2.11 is

$$Q(t) = f\sqrt{\frac{D}{\pi t}}\left(\frac{C_1\lambda^2/4D}{\lambda^2/4D + t} + C_0\right), \tag{2.13}$$

where f is the surface roughness factor representing the ratio of the actual surface area to the geometrical surface area, the second part of the right-hand side term determines the number of particles coming out of a unit surface area. The term $\frac{\lambda^2}{4D}$ represents the characteristic diffusion time. For example, this time does not exceed 10^2 s for stainless steel [50]. The typical time for outgassing, including the baking procedure, is usually several days.

Thus, the term $\left(\frac{\lambda^2}{4D}+t\right)^{-1}$ can be expanded as a Taylor series of $\frac{\lambda^2}{4Dt}$. The order expansion term gives

$$Q(t) = f\sqrt{\frac{D}{\pi t}}\left(\frac{C_1\lambda^2/4D}{t^{3/2}}+\frac{C_0}{t^{1/2}}\right). \tag{2.14}$$

The first term represents the diffusion-limited desorption. The second is the characteristic desorption rate for species distributed uniformly through the bulk typical for water vapour or hydrogen.

This model (Eq. 2.14) is valid for the constant diffusion coefficient D. However, the diffusion coefficient in solids is generally found to be well predicted by the Arrhenius equation at different temperatures T and thermal activation energies ΔE

$$D = D_0 \exp\left(\frac{-\Delta E}{k_B T}\right). \tag{2.15}$$

The bake-out procedure is usually done at a constant temperature of the flat top phase, and D_0 and ΔE are nearly constant within the same material layer. Thus, this model can be valid to describe the behaviour of outgassing in baking. Based on the asymptotic approximation, the conventional representation of Eq. 2.14 is

$$Q(t) = \frac{Q_0}{t^\gamma}, \tag{2.16}$$

where γ is the slope of $log(Q)$ versus $log(t)$ plot.

Values of γ vary in the range from 0.5 to 1.2 and indicate the type of material and outgassing mechanism [52]. For example, γ = 1.1 − 1.2 corresponds to the outgassing from clean/polished metal surfaces, γ = 1 is desorption from metal surfaces, γ = 0.5 − 0.7 indicates outgassing from porous surfaces and γ = 0.5 is diffusion-controlled outgassing from the bulk [52].

The outgassing rate can be easily converted to pressure at a constant pumping speed S as

$$p(t) = \frac{Q(t)A}{S}, \tag{2.17}$$

where A is the area of plasma vessel walls.

2.1.3 Baking experience in fusion devices

Baking, as shown by the temperature dependencies of the above equations, stimulates the outgassing of different species according to their binding energies [52]. Baking with temperatures of 100 – 500 °C are effective to remove water. Temperatures of $\sim$ 500 °C can be used to remove CH_4, CO and CO_2 and chemisorbed water. Baking at higher temperatures (up to 1000 °C for stainless steel) is mainly used to remove dissolved hydrogen from the material bulk. In general, bake out temperatures of up to 150 °C are sufficient for most ultra-high vacuum (UHV) applications.

Also, in fusion baking is the most common technique to support the pump down and reduce the amount of water by boosting the outgassing rate for a certain time, achieving a lower base pressure level. The PFCs of modern fusion devices are usually made of stainless steel, carbon, tungsten, and/or beryllium. With wall heating methods and peculiar properties of fusion device design, it determines the maximum available temperature or baking.

Below are some examples of baking temperatures of currently operated and soon to be exploited fusion devices. The first wall of TCV is routinely reconditioned using a vessel vacuum bake-out at 250 °C [53]. The maximum baking temperature of ASDEX Upgrade is limited to 150 °C due to the materials used for plasma diagnostics [54]. The initial JET conditioning cycle with an ITER-like wall contains the bake-out at 320 °C [55]. The integrated commissioning of the tungsten (W) environment in steady-state WEST tokamak included the impregnation and curing of the two in-vessel divertor coils, is performed at 180 °C, contributing to the baking of the vacuum vessel [56]. In the large helical device (LHD), baking is performed during intervals between the LHD plasma discharges. The baking temperature is below 95 °C because the wall is close to a superconducting magnet coil [57]. The vacuum vessel of JT-60SA is planned to be baked at up to 200 °C [58]. The baking temperature of the KSTAR PFCs, containing graphite and CFC tiles is set to 350 °C [59, 60]. The baking temperatures of the EAST vacuum vessel and PFCs are designed to be 250 °C and 350 °C, respectively [61]. Steady-state Superconducting Tokamak (SST-1) vacuum vessel adopts moderate baking at 110 ± 10 °C and the limiters baking at 250 ± 10 °C [62]. The vacuum vessel baking system of the DIII-D tokamak is used to heat the vessel walls and internal hardware to an average temperature of 350 °C to allow rapid conditioning of the vacuum surfaces [63]. For wall conditioning of T-15MD tokamak vacuum vessel, ohmic baking at the average temperature of 220 ± 20 °C is used [64, 65]. The strategy for ITER is to perform baking at 240 °C for the Be first wall and 350 °C for the W divertor [66].

2.2 Plasma - assisted wall conditioning

Plasma-assisted or discharge wall conditioning is another method to reduce outgassing further. This method is based on the mechanisms of particle-induced desorption. The principle and efficiency of discharge conditioning can be represented in the neutral pressure balance equations. In case the mean free path of the gas molecules is larger than the dimensions of the vacuum vessel, ignoring recombination in the plasma, the neutral pressure balance, initially given by Eq. 2.3, can be modified to

$$\frac{dp}{dt} = \frac{Q_s}{V} + \frac{Q_w}{V} - \frac{pS}{V} - (k_i + k_d)pn_e, \tag{2.18}$$

where p is gas partial pressure, Q_s and Q_w are the external injection and wall released gas flows, respectively, k_i and k_d are the total ionization and dissociation rate coefficients of the gas molecules. Based on the models proposed in [67, 68], the typical case for the neutral pressure balance can be described as a set of equations for partial pressures of the working gas (wg) and released impurities or fuel (im)

$$\frac{\partial p_{wg}}{\partial t} \approx \frac{Q_{wg}}{V} - \frac{p_{wg}S_{wg}}{V} - (1 - R_{wg})p_{wg}(k^i_{wg} + k^d_{wg})n_e, \tag{2.19}$$

$$\frac{\partial p_{im}}{\partial t} \approx -\frac{p_{im}S_{im}}{V} + c(t)Y_{im}p_{wg}(k^i_{wg} + k^d_{wg})n_e - (1 - R_{im})p_{im}(k^i_{im} + k^d_{im})n_e. \tag{2.20}$$

R is the PFC material-dependent total recycling coefficient of the particle flux to the wall. It is defined as a ratio between the particle flux to the wall Q_{tw} and the released particle flux Q_w. According to [68], the particle flux to the wall can be estimated as $Q_{tw}/V \approx (k^d + k^i)pn_e$.

Y_{im} is a global particle-induced removal yield of impurity and fuel species (D_2, H_2O, CO, etc). It represents the probability of a molecule being released per incident bombarding ion or neutral on the wall. The yield includes de-trapping, diffusion, desorption and depends on the PFC surface parameters, such as chemical composition, temperature, microstructure, etc., and the type and energy of bombarding particle. The released particle flux is expressed through the plasma (working gas) bombarding flux F as

$$Q_{im} = Y_{im}F, \tag{2.21}$$

where $F \approx p(k^i_{wg} + k^d_{wg})_{wg} n_e$. The coefficient $c(t)$ corresponds to the time-varying impurity concentration in the PFC.

Physical processes, that describe how the surfaces are loaded with particles and how species entering surface layers may be released, need to be included. It allows to investigate the advantage of particle-assisted wall conditioning compared to the models given above which describes only processes of outgassing. An interesting approach was proposed in Andrew's model for hydrogen retention in PFCs [69] and further extended and used for impurity outgassing modelling in [70]. The following couple of equations describe the interchange between deeply trapped atoms (t state) and loosely bound atoms or solution (s states).

$$\frac{\partial c_t}{\partial t} = -K_{ts} c_t + K_{st} c_s \left(1 - \frac{c_t}{c_0}\right), \tag{2.22}$$

$$\frac{\partial (c_t + c_s)}{\partial t} = K_r c_s^2. \tag{2.23}$$

The rate constants K_{ts} and K_{st} represent de-trapping from t into s and re-trapping, respectively. c_0 is the maximum limit of possible concentration c in state t. The gas release rate $K_r c_s^2$ occurs from the s state with the recombination rate K_r. If $c = c_t + c_s \approx c_t$ the following equation can approximate the outgassing rate

$$\frac{\partial (c)}{\partial t} \approx -K \frac{c^2}{\left(1 - \dfrac{c}{c_0}\right)^2}, \tag{2.24}$$

where $K = K_r \left(K_{ts}/K_{st}\right)^2 = \beta_0 exp\left(-\frac{2E}{k_B T}\right)$ with E being the potential energy difference between solution sites and traps.

To consider the possibility of atoms diffusing within the material, beyond the implantation layer and different processes on the PFC surface, Eq. 2.24 has to be extended, including another adjustable term

$$\frac{\partial (c)}{\partial t} \approx -K \frac{c^2}{\left(1 - \dfrac{c}{c_0}\right)^2} + C_{adj}. \tag{2.25}$$

C_{adj} can include the processes on the PFCs surfaces, such as material redeposition [69] and recombination on the surface [71]. A combination of transport and retention mechanism in PFCs and release mechanism from

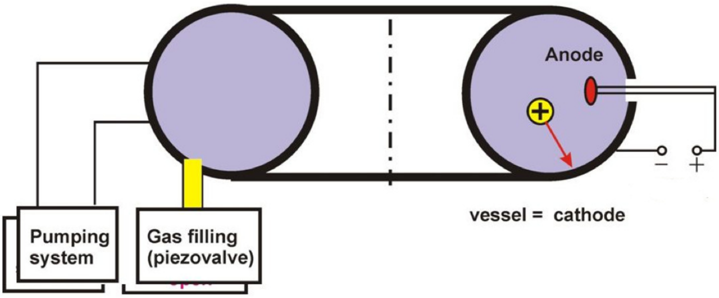

Figure 2.1: Scheme of GD in fusion devices

PFCs makes the typical impurities or fuel outgassing rate proportional to t^{-n} following from Eq. 2.25 [71]. For hydrogenic species, n is approximately 0.7, for example, observed in some fusion devices [72–74].

The properties (type of particles, energy spectrum and fluxes) of the particle-induced desorption are defined by the type of plasma used for this method.

2.2.1 Glow Discharge Cleaning

Glow Discharge Cleaning (GDC) is the most common particle-induced desorption method, beneficial for conditioning the vacuum vessel surfaces of fusion devices. This type of plasma can liberate much more highly-bonded carbon oxides and hydrocarbons than can be removed by baking. It is also suitable for cases when high-temperature baking is not possible.

Glow Discharge (GD) is weakly ionized ($n_e < 10^{16}$ m^{-3}) low temperature ($T_e < 10$ eV) plasma which is created by applying a voltage between the anode (positively charged electrode) and cathode (negatively charged electrode). In fusion devices, the walls of a vacuum vessel play the role of the cathode while one or more small electrodes inside the vacuum vessel serve as the discharge anode(s) (Fig. 2.1). The number of anodes, the size of anodes and their location usually depend on the inner wall shape and area, and the required discharge current uniformity at the walls [75]. The latter determines the homogeneity of ion fluxes towards the walls directly affecting the local cleaning process.

Two primary mechanisms determine the conditions for break-down and sustainment of direct current (DC) glow discharges. The first one contributes to a significant charge carriers' production through electron impact ionization, while the second corresponds to the cathode charge production through secondary electron emission [76]. Electron impact ionization describes the generation of ions by electron impact. It is empirically formulated via the so-called Townsend coefficient as

$$\alpha = Ap\exp\left(\frac{-Bpd}{V}\right), \tag{2.26}$$

where A and B are constants dependent on the gas composition [77], p is gas pressure, d is a gap between the anode and the cathode, and V is the applied voltage. Due to bombarding ions, secondary electron emission (γ) is defined as the ratio of electrons ejected per incident ion. To achieve break-down and make the glow discharge self-sustainable, the number of generated secondary electrons per initial electron should meet the minimum criterion

$$\gamma\left(\exp(\alpha d) - 1\right) = 1. \tag{2.27}$$

Based on these two equations, one can derive that the break-down voltage V_b is a function of the product of the gap and pressure pd

$$V_b = \frac{Bpd}{\ln(pd) + \ln\left(\frac{A}{\ln(1/\gamma) + 1}\right)}. \tag{2.28}$$

Eq. 2.28 represents the famous Paschen's curves. The Paschen curves have a characteristic minimum corresponding to optimal conditions for plasma formation for a given gas type. It should be noticed that for quasi-static conditions (slowly increasing voltage), the shape of the Paschen curves also depends on the electrode material [78]. It is also shown that the shift of the curves toward higher voltages and the change of the Paschen minima toward higher values of pd occur with the decreasing voltage rise time [79].

GD is a hollow cathode discharge in fusion devices due to the significant difference between cathode and anode sizes. Hollow cathode discharges break down at lower voltages and carry higher (one order of magnitude) than conventional glow discharges of similar dimensions and gas parameters [80]. GD is typically operated at a neutral gas pressure range of 10^{-3} –10^{-2} mbar. Some fusion devices use an assisted break-down that can be reliably achieved at GD operational pressures, usually lower by one order of magnitude. It allows avoiding spurious events such as arcing and an increase of metallic PFC erosion inside at high pressures. Moreover, it enables pulsed GD operations, starting and stopping the discharge for short periods to maximize removal while minimizing gas retention and sputtering. An assisted breakdown can be done by equipping the GD system with special devices like radio-frequency assisted glow discharge on TEXTOR [81] and KSTAR [82], an electron gun for DIII - D [83] or a separate starting electrode on ASDEX Upgrade [84].

The structure of the glow discharge at a steady-state regime is complex. It consists of several regions, such as anode sheath, bulk plasma and cathode sheath, which may have different physical phenomena depending on the discharge parameters. The physics of a hollow cathode discharge and its application as GDC in tokamaks are well described in [85–87].

The cathode sheath is characterized by a much larger ion density than the electron density. Due to the ion impact on the cathode, emitted secondary electrons are accelerated by the sheath towards the plasma core. At the same time, all ions move towards the wall. Thus, a significant potential fall and a large space charge are formed in front of the cathode. The ions accelerate towards the surfaces in the same cathode fall, releasing adsorbents through physical or chemically assisted sputtering. The ion current, therefore, determines the release rate of adsorbents from the surface.

These ions release at the same time secondary electrons. According to [85], a good estimate of the ratio of the total glow current I to the wall area A corrected for the secondary electron emission coefficient as follows:

$$\langle j_{wall} \rangle = \frac{I}{A(1+\gamma)}. \tag{2.29}$$

The current density is proportional to the plasma density that decays with increasing distance from the anode [38]. The non-uniformity of the profile has a consequence on the cleaning efficiency of the GD system. The locations where j_{wall} is minimum are sputtered at a lower rate during the cleaning sessions, forcing the duration of the treatment. The mitigation of the profile non-uniformity would hence allow shorter cleaning sessions [75].

GDC is one of the best-established techniques used in present-day fusion devices to remove impurities and fuel from PFCs. Many machines use GDC as a baseline wall conditioning technique. It allows to further deplete contamination layers on the wall surfaces after baking by reducing metal oxides or hydrogenation of carbon-based surfaces to reset the wall conditions between operation cycles and contribute to isotope change over in the PFC [38]. Neon glow discharge cleaning was first attempted in LHD instead of He glow discharge to remove hydrogen neutrals and control ion density [88]. JET with ITER-like-wall (ILW) uses GDC in hydrogen or deuterium before first plasma operation and for isotopic wall change over [55]. On EAST, typical

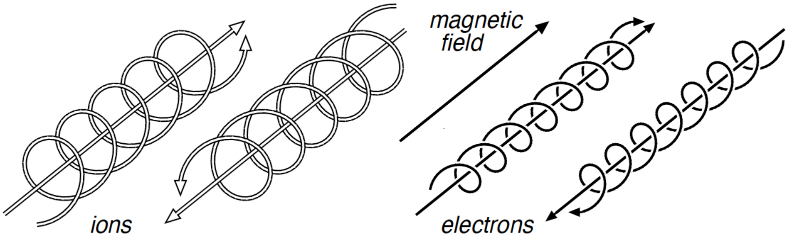

Figure 2.2: The gyration orbits of electrons and ions in a magnetic field

working gases for GDC are He or D_2. The GDC system could also be used for boronization [89]. The initial phase of KSTAR wall conditioning also includes GDC to be regularly performed as a standard wall cleaning procedure [90]. In the case of JT60-SA, the glow discharge cleaning is planned to prepare the device for exploitation and overnight to restore the wall conditions between experimental days [91]. GDC is one of the primary conditioning means to be used in ITER to prepare in-vessel component surfaces before machine start-up after venting and maintenance procedures [92, 93].

2.2.2 RF Wall Conditioning

GD operation even in small magnetic fields (a few mT) leads to the discharge localization becoming strongly inhomogeneous. At higher fields, GD fully stops. Fusion devices operating with superconducting magnetic field coils are restricted in the usage of the GDC due to their inability to (fast) cycle the magnetic field, on for operations and off for conditioning by GDC. It required the development of other techniques that do work in the presence of strong magnetic fields. Radio Frequency (RF) -based techniques appear to be compatible with magnetic fields and even need it to couple energy into the plasma. In this case, it is becoming commonplace to use the same RF - systems that are installed for plasma start-up and heating.

The motion of a charged particle in the presence of the constant magnetic field has a helix trajectory around the guiding center magnetic field line, as shown in Fig. 2.2.

The radius of gyration, or so-called Larmor radius, of the particle motion, is

$$r = \frac{(2mkT)^{1/2}}{|q|B}, \tag{2.30}$$

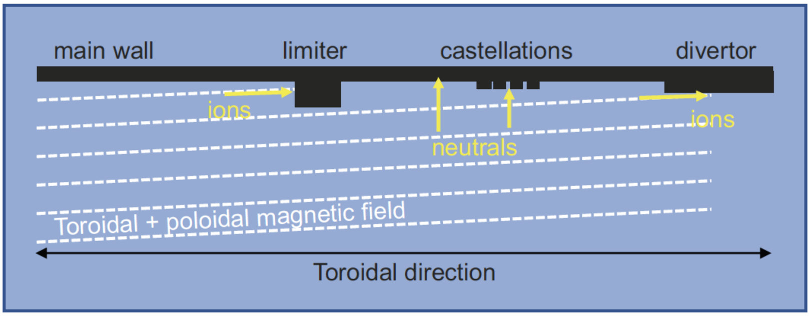

Figure 2.3: The typical surfaces in a magnetized toroidal plasma device and their interaction with the plasma flux flowing along the magnetic field lines (white dashed lines) [94]

where q is the particle charge and B is the value of the magnetic field. The frequency of the gyration, or cyclotron frequency, can be written as

$$\omega_c = \frac{qB}{m}, \tag{2.31}$$

where m is the mass of a particle.

Thus, the phenomenon of cyclotron resonance can be also employed to heat plasma by using electromagnetic waves with frequencies corresponding to the electron or ion cyclotron frequencies. Moreover, the RF power in the ion cyclotron range of frequencies can be coupled to both electrons and ions, e.g. by collisional absorption.

RF wall conditioning aims at inducing a known and optimal flux of particles to the plasma-facing components. These particle fluxes initiate the release of impurities or hydrogen isotopes. The preferred transport of charged particles along the magnetic field lines affects the intensity and properties of the conditioning flux for different wall components, as shown in Fig. 2.3.

2.2.2.1 Electron Cyclotron Wall Conditioning

Electron Cyclotron Resonance Heating (ECRH) is a plasma heating method using electromagnetic waves in the electron cyclotron frequency range and its low harmonics. The electron cyclotron frequency in the plasma is typically 28 to 170 GHz for modern tokamaks or stellarators.

Electron cyclotron waves can be absorbed by cyclotron damping if the relativistic resonance condition at the harmonic l is satisfied by electrons concerning the Doppler shift as

$$\omega = \frac{l\omega_{ce}}{\gamma} + k_{\|}v_{\|},$$

where ω_{ce} is the electron cyclotron frequency, $\gamma = (1 - v_{\perp}^2/c^2 - v_{\|}^2/c^2)^{-1/2}$ is the relativistic factor, $v_{\perp}$ and $v_{\|}$ are electron velocity components perpendicular and parallel to the magnetic field and $k_{\|}$ is the component of the wave vector $\boldsymbol{k}$ parallel to the magnetic field. The propagation of the waves in the electron cyclotron range of frequencies is determined by the dispersion relation that connects the index of refraction with the wave frequency, the electron plasma frequency, and the propagation angle between the wave vector and the magnetic field. The dispersion relation, including hot plasma effects plasmas, is given, for example, in [95].

A typical EC waves launcher imposes the initial direction and polarization of the wave. The direction of the wave outside the plasma determines the starting geometry for wave propagation in the plasma. The wave polarization at the plasma boundary determines which propagation mode is excited, the extraordinary (X-mode) or ordinary (O-mode) [95].

Electron Cyclotron Wall Conditioning (ECWC), or conditioning by ECRH plasma, relies on a currentless discharge, typically partially ionized, produced by localized power absorption at the fundamental EC resonance or its second harmonic. ECWC is generally operated at a neutral gas pressure range of 10^{-5} - 10^{-4} mbar. Localized power deposition in ECWC plasmas can affect discharge uniformity and the cleaning efficiency of ECWC [96]. The location and size of the plasma-wetted area are determined by the confining magnetic field [38]. A detailed description of the elementary processes in RF hydrogen-helium plasmas and charged particle and neutrals transport in tokamaks is given in [97]. Due to poor confinement, relatively low electron temperature (below 100 eV) and partially ionized plasma are obtained in tokamaks. The electron density range of tokamak ECWC plasmas is 10^{18} - 10^{19} m^{-3}.

The first review of ECWC studies was given in [67]. The following examples show the most recent part of extensive ECWC studies in the tokamak magnetic field configuration. Helium ECWC at the first harmonic for electron cyclotron resonance with the power of 100 to 300 kW was found as a good alternative for impurities removal and, however, less effective for deuterium wall desaturation in comparison to other wall conditioning techniques in TEXTOR [98]. Experiments on JT-60U showed that adding the horizontal field of 0.3 - 0.5 % of BT strength effectively extends He plasma (both with fundamental and second harmonic) with P_{ECRF}= 0.59 – 2.5 MW for wall conditioning toward the high field side from the resonant surfaces of ECH and make it homogeneous [99]. The helium ECWC plasmas were investigated in KSTAR using second harmonic heating and the fundamental heating at RF power of 200–300 kW and radial plasma extension by an additional poloidal field pattern to recover the device after disruptions [100]. The applicability of He ECWC with improved homogeneity (also by extending the discharge vertically and radially) was proven at the second EC harmonic to desaturate the carbon-based plasma-facing surfaces from deuterium in TCV in support of JT-60SA operation [96].

The suitability for wall coating and the use of pulsed EC plasma for wall conditioning were proven for the toroidal magnetic field configuration in TOMAS [101, 102].

In stellarators, ECRH plasma is fully ionized (T_e > 100 eV) with electron density above 10^{19} m^{-3} with strong surface interaction at the divertor strike lines [70]. Thus, ECWC on stellarators is more homogeneous poloidally plane and does not suffer from potentially high levels of non–absorbed ECRH radiation, unlike in tokamaks. ECRH conditioning plasmas in a stellarator are more efficient for cleaning the divertor area and are more similar to divertor conditioning by tokamak plasma rather than to ECWC in a tokamak [38]. Only a few tests with He plasma at P_{ECRF} = 0.9 – 1.4 MW, attempting to support the high ion temperature plasma production under the established magnetic field in LHD, were done, showing an apparent reduction of hydrogen content in plasma with an increase of the cumulated RF energy [103].

2.2.2.2 Ion Cyclotron Wall Conditioning

Ion Cyclotron Resonance Heating (ICRH) is a method that can directly heat ions via a resonant interaction between the plasma ions and radiofrequency waves launched in the plasma. The ion cyclotron range of frequencies (ICRF) can change power deposition from dominant ion to dominant electron by varying the chosen operational wave frequency and magnetic field or selecting a proper plasma composition. ICRF heating frequency in modern fusion devices can range from 20 MHz to about 100 MHz depending on the magnetic field and ion species used for plasma (Eq. 2.31).

To describe the propagation of waves in the ion-cyclotron range of frequencies (ICRF), one can use the differential equation for the waves, which can be excited in the ICRF, obtained from Maxwell's equations and the plasma permittivity tensor [104]. Recent advances in physics and technology of ion cyclotron resonance heating are given in [105].

ICRF uses well-established wave broadcast techniques to generate steady-state high power RF waves. The waves are transported from RF generators to an antenna system via conventional coaxial transmission lines. ICRH antennas are often built as boxes enclosing one or several central straps to which the high voltage is applied. The details of modern ICRH antenna design and matching are described in [106]. The antenna spectrum is determined by the phasing of the poloidal antenna straps., e.g. for monopole phasing, the parallel wave vector spectrum is concentrated around the longer wavelengths. For dipole phasing, it is around shorter wavelengths.

Based on the various heating mechanisms, there are different heating scenarios where the role of the plasma composition is essential. While these scenarios are well established, e.g. in [105], Ion Cyclotron Wall Conditioning (ICWC) plasmas have different mechanisms.

ICWC uses the standard poloidal strap ion cyclotron heating and current drive (ICRH&CD) antennas. The antennas are designed to couple the waves to dense ($n_e > 10^{19}$ m^{-3}) plasma, to initiate the discharge by the strong electric fields in the vicinity of the antenna [107] and to maintain the steady homogeneous RF plasma by coupling ICRF power to both electrons and ions, mainly via non-resonant processes [108]. The typical neutral operation pressure range is 10^{-5} – 10^{-4} mbar. Specific electron densities for low temperature ($T_e \approx$ 1 - 10 eV) ICWC plasmas are in the range of 10^{16} - 10^{18} m^{-3} when the standard ICRH heating settings are used [109]. ICWC is aimed at inducing a known and optimal particles flux to the plasma-facing components. Optimization of the particle flux also includes homogeneity improvement. Neutrals are the dominant flux component to the main wall. The high wall conditioning efficiency of ICRF discharges result from a significant flux of low energetic neutrals (10's of eV to a few keV) generated through charge exchange reactions of ions with background neutrals [109, 110]. That also shown in Sec. 4.2.3.4.

The first application of ICWC was made on the Uragan-3 stellarator to clean metallic surfaces by low-temperature hydrogen plasma [111]. Later, the utility of ICWC was shown by TEXTOR experiments dedicated to the efficient hydrogen desorption from the first wall at different conditions (power of 100-100 kW) of ICRF plasma in He and He + H_4Si gas mixtures [112]. Additionally, it was proven in Tore Supra, where high hydrogen removal rates were obtained in helium discharges, either in a continuous or pulsed operation mode, by injection of ICRF power in the range from 40 kW to 350 kW either in He or D_2 [113]. The first summary describing the state of the art of ICWC in terms of conditioning efficiency and plasma characterization for different fusion devices was presented in [67]. Later, numerous studies also confirmed the effectiveness of ICWC in various conditioning applications for tokamaks. JET

ICWC discharges have shown the ability to change the wall isotopic ratio of JET with carbon (C) -wall and JET with ITER-like-wall (ILW) within a limited number of discharges [110]. ICRF discharge cleaning with a toroidal field and an additional vertical field was carried out on EAST, showing that He discharge with injected ICRF power of 10 kW effectively recovered plasma performance quickly after a major disruption [114]. With inter-shot H_2/He ICWC, water was effectively removed from the metallic wall and inboard graphite tiles during the campaign in KSTAR [115]. Relatively clean plasmas (with a He content of more than 80 %) could be obtained by applying ICWC discharges upon changeover from D to He in the full-W ASDEX Upgrade [116].

In the case of ICWC studies in stellarators, wall conditioning using 50 kW of ICRF discharges in helium was successfully applied in the W7-AS stellarator to remove hydrogen from the vessel leading to improved density control [117]. In LHD, the first ICWC experiments, aiming at the hydrogen removal by CW ICRF discharges with up to 0.5 MW heating power, showed that the removal rate depends on the broad energy distributions of high-energy particles [118]. In later LHD studies, a series of repetitive $\sim$ 1 MW ICRF wall-conditioning discharge in He is found as an effective wall-conditioning technique for realizing high ion temperature plasmas by the hydrogen recycling decrease [119].

2.2.3 Pulsed discharge conditioning

The goal of wall conditioning is not only to desorb impurities or fuel from the wall but also to pump them out. That means that most desorbed species should be pumped out and not redeposited by conditioning plasmas on the vessel walls. When the particle flux to the wall is high enough, as for ECWC or ICWC, even a tiny percentage of the particles flux to the wall, which is permanently retained into the wall, can make the total retention or redeposition rate during the discharge be of the same order as the removal rate by the pumps.

According to [68], the out-pumped impurity flux $Q_p = pS$ can be written as a function of the total particle flux to the wall

$$Q_p = (1 - f)RQ_{tw}, \tag{2.32}$$

where f is the reionization probability which can also be estimated as

$$f = \frac{\tau_i^{-1}}{\tau_{ps}^{-1} + \tau_i^{-1}}. \tag{2.33}$$

$\tau_i = [n_e(k_i + k_d)]^{-1}$ is the characteristic effective time constant for ionization and dissociation.

The desorption process is limited by thermal diffusive transport of the molecules within the wall subsurface, which has large time constants (of the order of 1–10 s) [67]. The desorption continues after discharge termination with an exponentially decreasing rate. Thus, on the one hand, wall desorption and pumping can be achieved during the next seconds without plasma redeposition. On the other hand, retention is proportional to the plasma duration. As a result, maximizing removal while minimizing retention or redeposition of both the injected and wall released gas, $(1-R)$, can be achieved by pulsed discharge conditioning with an optimized duty cycle.

The high effectiveness of this method was proven by ICWC experiments on TEXTOR and TORE SUPRA [68]. The improvement of GDC efficiency can also be made by a discontinuous operation where the GD is intermittent. A purge phase during which the polluted gas is rinsed out of the vessel is added to start the next GD pulse with less dirty gas like it was done in ASDEX Upgrade [84]. However, the GD assisted break-down is required for this type of operation.

2.3 Wall coating

Oxygen plays a significant role in the operation of fusion devices containing graphite PFCs due to the high yield of CO formation and its volatility at room temperature. Low-Z wall coating is a fast and efficient way to reduce oxygen recycling by chemically binding it to stable solid oxides with low gettering. According to the comparison of the values of the enthalpy of the oxide's formation normalized to the number of oxygen atoms in the oxide for different wall coating elements, beryllium, lithium and boron were found as the suitable candidates for oxygen gettering among low-Z elements [120, 121].

Three main effects are observed following the application of the low-Z wall coating: suppression of (high-Z) metal liberation from the vessel wall, reduction of the low-Z impurity concentrations in the plasma, in particular of oxygen, and a positive influence on hydrogen recycling [120].

The release of the high-Z material from the metallic PFCs is reduced because the coating essentially covers the surfaces. The layer's lifetime on the first wall is dependent mainly, in stellarators, on the flux of charge exchange neutrals that hits its surface. The layer life-time on high heat flux areas such as divertor plates and limiters are much shorter since they are erosion dominated, see e.g. later in Sec. 3.3.6.

The reduction of oxygen follows similarly from covering (oxide) layers on the surfaces, but also from gettering of free oxygen by the active atoms B, Be or Li on the surface deposited coating layers, forming non-volatile oxides and the co-depositioning of oxygen with eroded coating material at deposition dominated areas. Reducing oxygen has as additional advantage that other impurity concentrations such as carbon, efficiently released by chemical erosion by oxygen, are reduced as well [122].

A hydrogen recycling reduction is achieved by increasing wall pumping rates. The latter is also due to the process of forming mixed layers occurring during erosion and redeposition in low–Z coated surfaces of tokamaks with graphite high heat flux components [120]. It means that a freshly deposited layer does not contain a lot of hydrogen. An elevated hydrogen isotope pumping happens during plasma exposure. Afterwards, fuel is additionally co-deposited with eroded coating material. For example, it has been shown that pure boron films store less hydrogen than layers that also incorporate carbon [34].

Thus, applying low atomic number (low-Z) wall coatings onto the PFC is a very effective method of wall conditioning, leading to much better plasma performance allowing to investigate advanced scenarios such as the high confinement modes of operation [38].

Be-coating is usually applied by the evaporation of beryllium as a pre-treatment before discharge execution. Beryllium plasma-spray coating technology can also be used for fusion applications [123]. However, Be-coating is not widespread due to the toxic effects of beryllium. Operation with beryllium PFCs is successfully shown in JET IWL featuring strongly reduced impurity concentrations and lower reliance on wall conditioning techniques for operations [124, 125]. Beryllium has been selected as the armor material for the first wall, baffle and limiter blanket modules ITER [126].

Lithium is primarily an oxygen getter compared to other low-Z materials. Therefore, a lithium film promotes large oxygen concentrations in the top layers of the surface. The increased oxygen concentration is responsible for the chemistry of fuel (e.g. deuterium) retention and sputtering, while lithium mainly plays the role of a catalyzer in this process [127]. The cost of it is a strong retention of large quantities of hydrogen isotopes in PFCs. Nevertheless, lithium is widely used as a wall coating material in TJ-II [128] and NSTX [129], reducing recycling, stabilizing the current-driven instabilities and improving energy confinement. Additionally, the ideas of using liquid lithium as a PFC [130] or lithium vapour for divertor detachment [131] also benefit the overall improvement of wall conditions.

There are some synergies between the lithium layer and the underlying boron-carbon in oxygen gettering. For example, the mixture of lithium and boron coating may reduce the frequency of wall conditioning and allow the glow discharge activation of the getter [132].

2.3.1 Boronization

Boronization, a deposition of amorphous boron or carbon-boron hydrogenated thin films (a-B/C:H), has been adopted by many fusion devices and has become a preferred conditioning method among low-Z coatings. The latest is due to a substantial decrease of effective plasma charge (Z_{eff}) and resistivity to chemical erosion [133].

Boronization is typically applied through plasma-assisted chemical vapour deposition using a GD in a mixture with a carrier gas. The molecules of the reactive gases are partly ionized in the glow plasma and accelerated in the cathode sheath onto the wall and limiters or divertor plates which are the discharge cathode. A DC GD with a helium carrier is most commonly used for boronization. There is a few boron hydrides (precursors), such as diborane (B_2H_6), deuterated diborane (B_2D_6) and decaborane ($B_{10}H_{14}$), used for boronization. The first two are highly toxic and explosive gases, while the last is a less toxic stable solid (at room temperature). Thus, the boronization procedure usually requires special equipment and operation procedures to ensure safe handling. A review of some characteristic features of the boronization process, properties of boron-containing films, and the influence of these features on tokamak discharges are given in [134].

Boronization of fusion devices containing graphite PFCs produces amorphous boron-containing carbon films (a-C/B:H) [120]. In addition, metals sputtered from the vessel components may also appear in the chemical composition of the coating at the beginning of the boronization process. Deposited layers have a well-defined composition that is homogeneous in depth. The coverage of the PFC surfaces by boron is usually not uniform due to the GD current density variation with the distance from the glow anodes [75]. Boron coatings with a thickness below 200 nm have very good adhesion to graphite and stainless steel surfaces. The further increase of the thickness leads to films delamination or detachment from the substrate.

The boron deposition rate is dependent on several variables such as gas mixture, pressure, gas flow rate, wall temperature and GD current density [134]. To obtain a good uniformity in the deposition film, the molecule of the precursor gas should be completely cracked. The average thickness of an amorphous deposited pure boron layer can be roughly estimated as

$$l = f_{cr} F_{prec} n_{mol} \frac{M_B Q_{inj}}{V_m \rho_l S}, \tag{2.34}$$

where f_{cr} is a cracking factor, F_{prec} is a fraction of the precursor gas in the mixture of carrier and precursor gases, n_{mol} is a number of boron atoms in a precursor gas molecule, M_B is the molar mass of boron, V_m is a molar volume of the ideal gas, Q_{inj} is an amount of the injected gas for boronization, ρ_l is an average density of an amorphous boron layer and S is a total area of the coated PFCs [135].

Besides the surface covering process, oxygen gettering occurs when the boron-containing surfaces are exposed to energetic particles as

$$4B + 3O_2 \rightarrow 2B_2O_3.$$

When the bombardment is stopped C/B:H surfaces appear to be chemically stable. Adsorbed (molecular) precursor gas on PFC surfaces also acts as a getter for oxygen [136].

In the case of using diborane as a precursor gas, additional oxygen gettering mechanism occurs. Diborane reacts preferentially with residual metal oxides on untreated metallic PFC surfaces

$$B_2H_6 + 3MO \rightarrow B_2O_3 + 3M + 3H_2.$$

The main procedure of boronization with diborane is always followed by a short GD in pure helium. It allows to crack the remaining diborane molecules and desaturate the surfaces from hydrogen isotopes.

The surface coverage of the coating is susceptible to erosion and redeposition processes during the plasma operation. At plasma-exposed areas, such as divertors and limiters, the boron layer can be completely eroded in a short time. The erosion rate at the main wall of a tokamak is typically less by one order of magnitude and appears lower in the case of stellarators [38].

The boronization was successfully performed in a He-GDC with 90 % He and 10 % B_2H_6 in W7-AS [137], ASDEX [138] and LHD [139] at room temperature vessel walls and in Tore Supra [140] at 200 °C of walls temperature. The thickness of the layer was up to 100 nm in these experiments. In some experiments, high wall temperature was used to enhance the desorption of hydrogen or deuterium and impurities and form better quality layers.

2.3.2 Active (real time) wall conditioning

Large fusion devices like LHD, EAST, KSTAR and W7-X push the limits of their operational space by extension of plasma durations and elevation of power throughputs. It will exhaust the transient effects of wall conditioning techniques that are currently used. It means either the design and engineering of the devices will have to guarantee most of the impurity and recycling control during the stable long flat top phase or new wall conditioning methods have to be developed to fulfil these requirements.

Alternative techniques to apply low-Z wall coatings applicable in the presence of the magnetic field turned out to be promising even without interrupting physics operations. The research of alternative ways of replenishing the low-Z coatings, in particular through injection of low-Z material in tokamak plasma discharges, using precursor gases or solid compounds, or by erosion of coated limiters, have shown that the most prominent example of in-shot deposition of low-Z coatings remains in experiments, where lithium and boron pellets injected in the early phase of plasma discharges [141].

The recently developed real-time technique is based on the proceeds of steady or pulsed low-Z powder (with grain sizes less than 1 mm) injections at calibrated rates [142]. The powder is delivered to the plasma gravitationally through a vertical drop. The majority of the injected granules is ablated within or just past the edge steep gradient region. Thus, effective penetration of powder granules in the main plasma, where they are entirely evaporated, depends on the plasma density. The created ions of injected material diffuse radially outwards, ending up deposited on the plasma-facing components. The coating occurs preferentially in the areas in contact with the Last Closed Flux Surface (LCFS). The distribution of the coating layer across the machine wall is expected to depend on the plasma scenario.

The most recently performed lithium and boron powder injection experiments show a good increase of plasma performance in real-time and improve overall wall conditions for subsequent discharges. For example, carbon and other higher Z impurities and radiated power levels were reduced with lithium powder injection in DIII-D [143]. Real-time lithium powder injection has also been applied to long-pulse (> 30 s) H-mode plasmas in EAST with an ITER-like tungsten upper divertor. That allowed to suppress impurity influx and control recycling effectively [144].

Pure boron and boron nitride powders introduced gravitationally in H-mode plasma discharges of ASDEX Upgrade appeared to improve wall conditions similarly to boronization [145, 146]. The experience of DIII-D tokamak also shows the improvement of wall conditions similarly to GD boronization, with indications of reduced wall fueling, reduced recycling at the outer strike point and reduced impurity content at break-down [141]. Continuous boron powder injection enabled a robust suppression of edge-localized modes (ELMs) in EAST [147]. First experiments dedicated to boron and boron nitride powder injection were also performed in LHD [148].

It should be noticed that the powder dropper technique is only suitable to create good conditions in present devices. However, it is not acceptable in a fusion reactor where recycling and impurity control have to be fully achieved via the exhaust systems.

Another promising solution is to use a controlled high temperature of PFCs, allowing controlling fuel recycling in a steady-state regime. For example, the experience of the spherical tokamak QUEST exploitation shows that the hot wall (120 °C) plays an essential role in reducing the amount of wall-stored H and facilitating H recycling during long pulse operation [149].

Chapter 3

Application of wall conditioning on W7 - X

Progress in science comes when experiments contradict theory.
Richard P. Feynman

It is necessary to consider the device's construction peculiarities, technical capabilities, and operational limitations to adapt and optimize specific wall conditioning techniques for the superconducting stellarator Wendelstein 7-X. The detailed studies of each wall conditioning technique application are essential for identifying the best parameters to achieve a maximum conditioning outcome. The combination of both allows defining the most suitable procedure to prepare the device for plasma operation and maintain a good level of wall conditions throughout the plasma operation.

This chapter presents the most important results of the PhD project. The first part of the chapter gives the main technical details of W7-X. The systems and diagnostics relevant for wall conditioning studies are briefly described. Additionally, a short overview of the past operational phase is given. This overview contains the list of the most critical device upgrades made prior to each experimental campaign. The second part of the chapter is dedicated to the results of the wall conditioning studies in W7-X. It gives a review of wall conditioning in the limiter operation phase OP1.1 and an analysis of wall conditions in two experimental campaigns of the test divertor operation phase OP1.2. The influence of the plasma vessel baking on the residual gas content is discussed. The results of GDC optimization, its cleaning efficiency and break-down studies are given. The peculiarities of the boronization procedure and its impact on the impurity sources and

Table 3.1: Major parameters of the superconducting stellarator W7-X.

Quantity	Number	Unit
Major radius	5.5	m
Minor radius	0.5	m
Magnetic field on axis	2.5	T
Plasma volume	30	m^2
Rotational transform	5/6 ... 5/4	2π

plasma performance of boronization are described. The first boron dropper experiments, dedicated to real-time wall conditioning, finalize the device boronization studies in OP1.2b. The determination of the most suitable type of ECWC for W7-X in OP1.2a and its further optimization in OP1.2b make the final point of the chapter.

3.1 The superconducting stellarator W7-X

The superconducting stellarator Wendelstein 7-X (W7-X) is the largest comprehensively optimized stellarator, located at the Max Planck Institute for Plasma Physics (IPP), Greifswald, Germany, which was designed to have low neoclassical transport, small bootstrap current, robust magnetic-field equilibrium, and reasonably simple modular field coils [30]. W7-X is built to demonstrate a steady-state operation of a magnetic field generated by modular superconducting coils with a low error field, control plasma density and impurity content, and achieve quasi-steady-state operation in a reactor-relevant parameter range [150]. Table 3.1 contains the main parameters of the stellarator.

3.1.1 Technical description

W7-X is based on a five-fold-periodic Helias configuration and, therefore, the device comprises five nearly identical magnet modules [152]. Each of the modules is 180 °rotationally symmetric, making the device consisting of 10 so-called half modules. In each of the modules, the flux surface cross-section varies strongly from a bean to a triangular shape resulting in the fivefold toroidal symmetry (see also Fig. 3.3). The schematic diagram of W7-X is shown in Fig. 3.1. The main components of the device, which are relevant to the wall conditioning studies, are briefly described in this section.

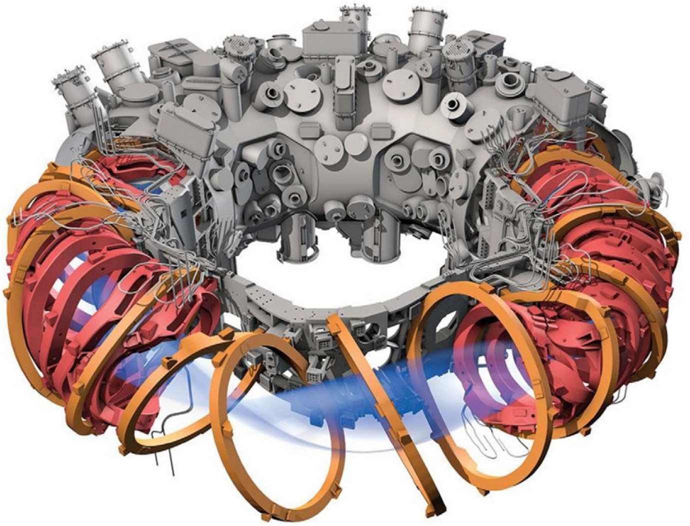

Figure 3.1: Schematic diagram of the superconducting stellarator device Wendelstein 7-X. The last closed magnetic flux surface is indicated in light blue. The 50 non-planar (red) and the 20 planar (orange) superconducting coils are operated in an evacuated cryostat volume between the plasma vessel and the outer vessel [151].

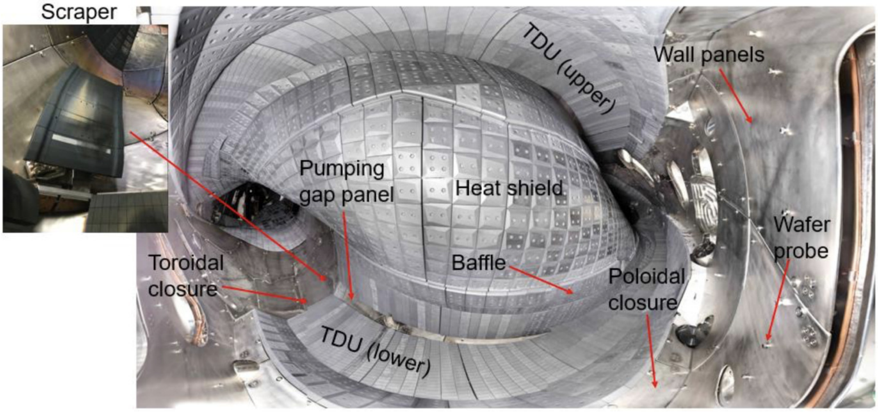

Figure 3.2: Location of in-vessel components in the W7-X plasma vessel [156].

3.1.1.1 Cryostat

The main task of the cryostat system is to provide an insulating vacuum for the cryogenic magnet system, ultra-high vacuum conditions within the plasma vessel, and give an external access to the in-vessel components [153].

The cryostat of W7-X consists of an inner and an outer stainless steel vessel. The inner vessel is a plasma vessel and encloses the hot plasma. The plasma vessel has a complex 3D contour repeating the plasma shape and varies from a triangular to a bean shape within each half-module. The water-cooling/heating tubes are welded on the plasma vessel external surface [154].

The outer vessel, functioning as an external boundary of the cryostat, contains the superconducting magnet system that confines the hot plasma in a magnetic cage, the dedicated support structure, the plasma vessel and the 254 ports. The ports that connect the outside of the cryostat with the insides of the plasma vessel are used for diagnostics, plasma heating, water and power supply, and maintenance access. Plasma vessel, outer vessel and the ports are covered with thermal insulation based on multilayer foil, and a thermal shield actively cooled to 70 K [155].

3.1.1.2 In-vessel components

The in-vessel components of W7-X consist of the divertor components and the wall protection with its internal cooling supply (Fig. 3.2) [157]. The plasma vessel wall has two types of wall protection elements. The inboard wall side, close to the plasma surface, is covered by graphite-protected heat shields.

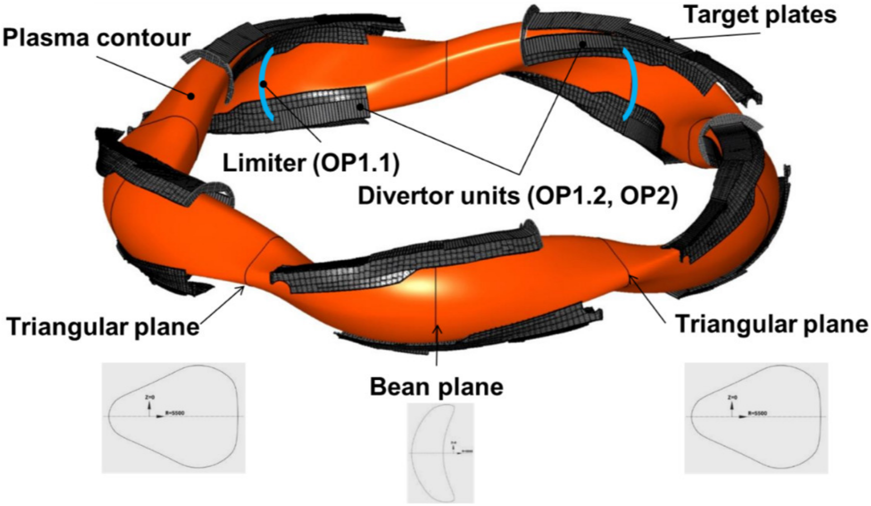

Figure 3.3: The drawing of the ten Test Divertor Units and the last closed flux surface [158].

The tiles are screwed onto the heat shields made of CuCrZr cooling structures.

The stainless steel wall panels cover the vessel wall's low loaded areas (< 100 kW/m^2). Each panel is made from a sandwich of two stainless steel sheets welded together to form a meander of cooling channels.

W7-X has ten separate Test Divertor Units (TDUs) [159], which are placed in equivalent positions, five on the bottom of the machine and five on the top, following the plasma symmetry along the helical edge of the plasma contour (Fig. 3.3). As shown in Fig. 3.4, each TDU has a long horizontal target and a shorter vertical target forming the pumping gap. The horizontal target is continued by the low heat-flux region and the high heat-flux high iota tail. The 3-D shape of the targets allows operating the device in different magnetic field configurations. These elements are covered by monolithic graphite tiles mounted onto stainless steel frames with simple springs. Additionally, baffles made of CuCrZr cooling structures and covered by graphite tiles are placed adjacent to the target plates to prevent the neutral gas from streaming back to the main chamber. Two scraper elements (TDU–SEs), also equipped with graphite tiles, protect the divertor pumping gap and the edges of the primary plasma-facing components during the bootstrap current evolution [160].

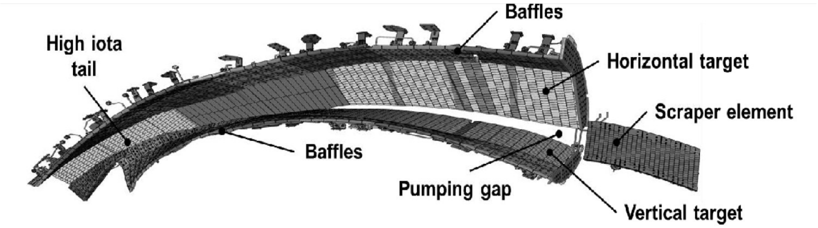

Figure 3.4: Test Divertor Unit.

3.1.1.3 Magnetic field coils

The magnet system of W7-X is composed of three different groups of coil systems. The main one is the superconducting W7-X coil system which consists of 50 non-planar and 20 planar coils. The coils are located in the cryostat, between the plasma vessel and the outer vessel wall, being attached to a central support ring (Fig. 3.1). The coils are equally arranged in 10 half modules. Each half module contains five different non-planar and two different planar coils. The design and technical details are described in [161].

The coils can produce a magnetic field strength of 2.5 T on the magnetic axis. The coils current can be independently controlled for all different types of non-planar and planar coils. It allows changing the magnetic field configuration according to various stellarator optimization criteria. The 50 non-planar coils by themselves are sufficient to generate a confining magnetic field [150]. Natural magnetic islands form at the plasma boundary depending on the magnetic configuration, given by the rotational transform $\iota/2\pi = n/m$, which is the number of poloidal revolutions around the plasma column a field line takes per toroidal revolution. If the current is equal in all non-planar coils and there is 0 current in the planar coils, the reference magnetic field configurations of W7-X is standard (EJM, $\iota/2\pi = 5/5$). The toroidal field component can be increased or reduced by driving non-zero currents in the planar coils, thus, modifying the rotational transform. In this case, one can have high iota (FTM, $\iota/2\pi = 5/4$) or low iota (DBM, $\iota/2\pi = 5/6$) configurations. With different coil currents in the five non-planar coil types, the magnetic mirror can be varied. Thus, when the current of planar coils is 0, one of the references magnetic field configurations is a high mirror ratio (KJM). The heat flux patterns (strike lines footprints) on the divertor targets for the reference magnetic field configurations are shown in Fig. ??. More details of the reference magnetic field configurations and other configurations, including limiter ones, are given in [162]. It should be noticed that Wendelstein 7-X is optimized to be a high-iota low-shear device.

The superconducting magnet system is accompanied by the Trim Coils

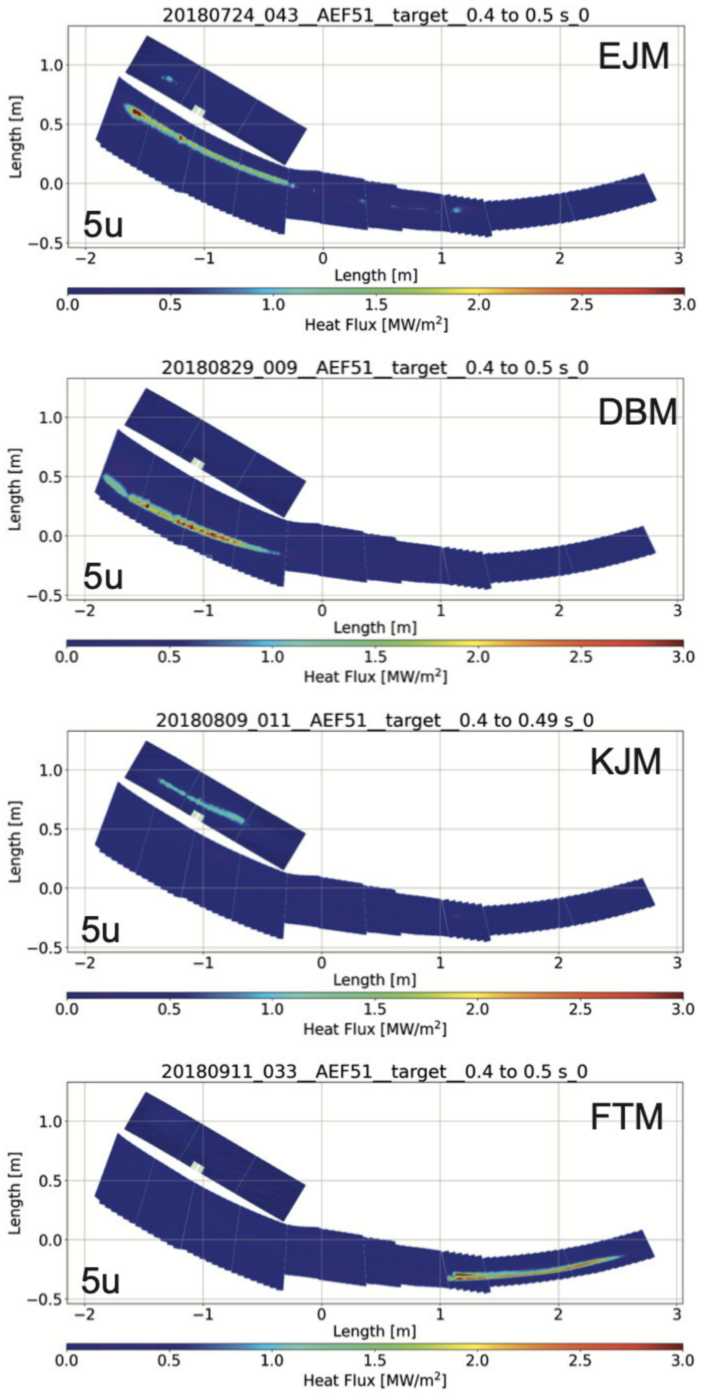

Figure 3.5: Examples of Infra-Red thermography footprint of main magnetic divertor configurations used in W7- X. Measurements were taken under ionization conditions in half Module 5u [163].

and Control Coil systems. The first system includes five normal conducting trim coils located outside of the cryostat [164]. Each Trim coil has an individual power supply allowing for the reduction of the leading error field components.

The control coil system contains ten identical 3-D shaped control coils located behind the baffle plates of corresponding divertor units. It is designated to rectify the error field and sweep hot spots (strike lines) on the divertor target plates [165]. The currents in the island control coils can also be adjusted individually. The shift of strike lines across the target surface of the divertor or, in other words, the manipulation of the poloidal position and the behaviour of the strike lines can be carried out in different ways. One way is to apply an AC (alternating current) with an amplitude of up to 625 A and frequency of 20 Hz (AC sweep, during a plasma discharge) [166]. The other way is to set up to $\pm$ 2500 A of DC (direct current) to change the strike line position from discharge to discharge, the so-called DC sweep [166]. The strike line sweeps can also be combined (DC + AC sweep), simultaneously applying AC and DC currents.

3.1.1.4 Vacuum system

The main vacuum is provided by 30 turbomolecular pumps (TMPs) with a maximum effective pumping speed in the vessel of about 30 m^3/s for H_2 [167]. The gas evacuation is done via two ports for pumping located behind each divertor. Three TMPs are connected via approximately 3.6 m (1 port $\rightarrow$ 2 pumps) and 4.3 m (1 port $\rightarrow$ 1 pump) long tubes of 400 mm diameter to the pumping ports of each divertor forming so-called pumping stations. In order to stationary handle high gas loads and remove TMP exhaust gases, roots and rotary pumps are connected in series with pumping stations.

Two out of ten pumping stations (upper Module 1 and lower Module 4) are equipped with thermal diborane decomposers and diborane sensors, allowing for the use of the boronization procedure.

Besides the main pumping units, some of the diagnostics have a differential pumping. However, due to the low pumping speed of its differential pumping and the separation from the main volume by the small apertures, its contribution to the total pumping speed is negligible. The Neutral Beam Injection (NBI) is equipped with a small TMP and large titanium getter pumps [168]. The pumping speed of an NBI pumping unit is estimated to be $\sim$ 0.5 m^3/s which is sufficient to influence the total particle removal rate [169].

3.1.1.5 Gas injection system

The gas supply system and the gas inlet system are two important technical systems of the W7-X device, providing a broad spectrum of functions for plasma vessel conditioning and plasma operation [170]. The gas supply system aims for a controlled supply of the gases for plasma operation (H_2, He), injection of impurities in the plasma edge (Ne, Ar, N_2, CH_4), injection into the plasma for diagnostic purposes (H_2, He, N_2, inert gases), wall conditioning (H_2, He) and for a coating of the plasma vessel wall (B_2H_6).

The gas inlet system of W7-X is capable of a fast switch of the gas species for every inlet position of the W7-X plasma vessel for operational gases. The gas injection into the plasma vessel takes place in different locations via dedicated ports by two groups of gas inlets. The first group of the gas injectors contains 11 Fast Piezo Valves feeding the gas injection for plasma operation in the range of $1 - 200$ mbar $\cdot$ l/s with a response time of less than 2 ms. Fast Piezo Valves are also used for feedback density control. In total, eight mass flow controllers with an injection range of up to 500 mbar $\cdot$ l/s belong to the second group providing functions more related to experiment preparation. Three of them are used for wall conditioning by Glow Discharge Cleaning. The use of others is dedicated to the boronization procedure.

Besides the main gas injection system, the part of the diagnostics such as He/Ne beam [171], neutral alkali beam [172], gas-puff imaging [173] and injection systems such as neutral beam injection (NBI) [168], hydrogen pellet injection [174], tracer-encapsulated solid pellet injection (TESPEL) [175] also contribute to the total amount of injected gases. Leaks have a negative influence on the residual gas content and the base pressure level of the device.

3.1.1.6 Bake out system

The baking system has two different types of inner vessel heating. The plasma vessel and some ports are heated by pressurized hot water at 150 $^\circ$C via cooling/heating pipes attached to the outer side of the plasma vessel and ports. The diagnostic ports, connecting the plasma vessel to the torus hall, are heated electrically to about 160 $^\circ$C by $\sim$ 90 heating mats [153]. Due to the non-uniform heat distribution of the plasma vessel, some ports have temperatures only between 100 and 150 $^\circ$C during the baking procedure [29]. The superconducting coils are protected by a thermal insulation shield on the cryostat walls, covering $\sim$ 150 ports and $\sim$ 60 extensions [153]. During the baking, the superconducting coils are kept cool by liquid helium down to - 265 $^\circ$C.

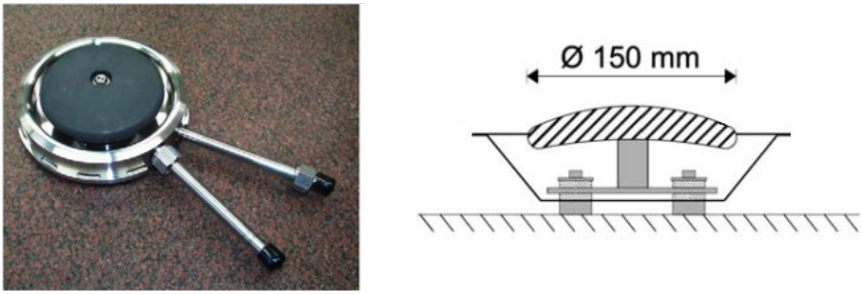

Figure 3.6: a) Glow discharge anode, b) schematic cross-section of GD anode [178].

3.1.1.7 Glow discharge system

The GDC system of W7-X consists of 10 calotte-shaped graphite anodes with a diameter of 150 mm [176]. Each anode is thermally connected to a cooled stainless steel base via a ceramic stand-off structure. The prototype anode and its schematic cross-section are shown in Fig. 3.6. One anode is located in each half module and individually power supplied with maximum ratings of 3 kV and 3 A [177]. The anodes are integrated within the wall panels on the outboard plasma vessel wall. The output power of the GDC system is limited by 4.5 kW, while the recommended anode current should not exceed 1.5 A [178]. Unlike the similar system on ASDEX Upgrade [84], the GDC system of W7-X is not equipped with a separate starting device. Thus, a break-down of glow discharge cannot be achieved at operational pressures.

3.1.1.8 Electron Cyclotron Resonance Heating system

The Electron Cyclotron Resonance Heating (ECRH) system is designed to be the main W7-X plasma heating system [179]. ECRH is routinely used for plasma start-up. The system is currently based on ten gyrotrons operating at 140 GHz, corresponding to the 2nd harmonic of the electron cyclotron resonance frequency for the nominal magnetic field of W7-X. Each gyrotron is capable to produce up to 1 MW in continuous wave (CW) operation. The power is delivered to the plasma vessel via a low-loss quasi-optical transmission system and a versatile in-vessel launching system. The launching ports are schematically shown in Fig. 3.7.

The power levels of stray radiation in the vacuum vessel of W7-X are controlled using calibrated sniffer probes equidistantly distributed around the stellarator [180]. Their location in the device is shown in Fig. 3.7.

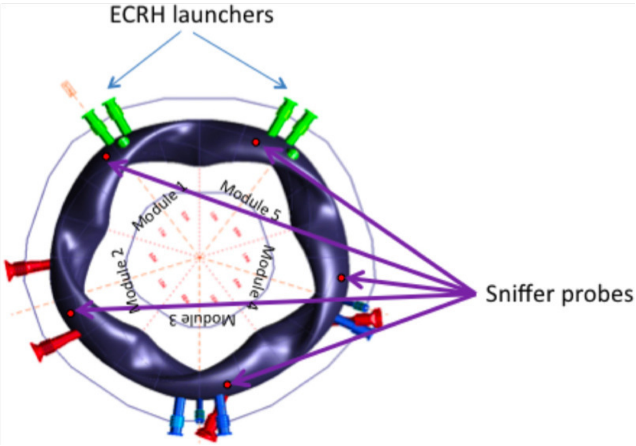

Figure 3.7: Schematic positions of the ECRH launchers (green ports) and locations of sniffer probes (red dots) [181].

All ECRH-based conditioning discharges are carried out at the extraordinary mode (X2). The microwave absorption coefficient fluctuates around $98.0{\pm}1.5\,\%$ [181]. The break-down time is less than 10 ms for input power 1.5 - 2.3 MW at neutral gas pressure (He) of $3 \cdot 10^{-5} - 5 \cdot 10^{-5}$ mbar [182]. After breakdown near to full microwaves absorption is achieved quasi immediately [183].

3.1.1.9 Relevant diagnostics for wall conditioning studies

The superconducting stellarator W7-X has numerous diagnostics to measure plasma parameters, monitor the conditions of PFC and other in-vessel components, and control the device parameters to ensure safe and reliable operation. The overview of W7-X diagnostics is given in [184–186]. The diagnostics which are most relevant to wall conditioning studies and, in particular, gas content and PWI processes monitoring are listed in this section.

The central long-term monitoring of vacuum conditions is done by commercial Penning and Pirani gauges located in the pumping ducts [167]. Neutral pressure is calculated as an average of the multiple Penning gauges, or Pirani gauges depending on the operational pressure range. The average pressure is calibrated according to the dominating gas in the residual gas content. Additionally, W7-X uses hot cathode ionization gauges suited for a long-pulse operation to measure neutral pressure with high time resolution [187]. A set of Wisconsin in-situ Penning gauges (WISP) is also used to measure partial pressures in strong magnetic fields [188].

The composition of W7-X exhaust gases is observed by two Pfeiffer Prisma Plus QMG 220 quadrupole mass spectrometers (QMS). The mass spectrometers are located in the pumping ducts of modules 2 and 4, approximately 3 m away from the vacuum vessel. Both devices are differentially pumped, and measurements are done at room temperature. The QMS spectra are not absolutely calibrated to the different gas partial pressures because, even though they are shielded, QMS still suffer from external magnetic stray fields. The data is recorded with a systematic error of 2 % – 4 % depending on the magnetic field. The decomposition of QMS signal intensities into partial impurity pressures related to the same mass-to-charge ratios are extracted according to the cracking patterns and methods are given in [201]. The ITER diagnostic residual gas analyzer (DRGA) prototype has been successfully commissioned and is additionally used to monitor partial pressures of plasma exhaust gases with a time resolution of seconds [202].

The line-integrated electron density is measured with real-time dispersion interferometry, providing the input for density feedback control [189].

Impurity content in the plasma is monitored by charge exchange recombination spectroscopy (CXRS) [190], extreme ultraviolet overview spectroscopy (HEXOS) [191] and soft-x-ray pulse height analysis (PHA) [192, 193]. The effective plasma charge Z_{eff} is calculated using measurements of visible Bremsstrahlung [194, 195]. To characterize impurity sources at the divertor, the ultraviolet-visible-near-infrared (UV-VIS-NIR) overview spectroscopy system [196] installed in the endoscope [197] is used. Impurity sources at the heat shields, baffles and wall panels are monitored by the filterscope system [198].

A ten-channel overview video diagnostic (EDICAM) system covering the whole torus interior is used to observe the plasma and detect rare operational events [199]. Infrared imaging systems are exploited to monitor all main plasma-facing components, i.e. the TDU target elements, and to identify areas of excessive temperature rise due to PWI processes [200].

3.1.2 Operational phases

Between 2015 and 2018, the first three experimental campaigns (operational phases) OP1.1, OP1.2a and OP1.2b of the W7-X stellarator have been successfully completed [203]. A complete overview of the first three Operation Phases is given in [150, 203].

The first phase, called OP 1.1, was performed in the so-called limiter configuration between December 2015 and March 2016. Five inertially cooled graphite limiters with a total surface area of 0.86 m^2 were installed on the

Table 3.2: Overview of main magnetic field configuration families in OP1.2a [163].

Configuration Family (OP1.2a)	Plasma species	Plasma time, s	Fraction, %
Standard configuration (EJM)	H + He	2481	65.6
High Mirror Configuration (KJM)	H + He	714	18.9
High Iota Configuration (FTM)	H + He	434	11.5
Diverse	H + He	147	3.9
Total	H + He	3776	99.9

inner side of the plasma vessel wall defining the Last Closed Flux Surface (LCFS) [204]. The first wall consisting of stainless steel protection panels ($\sim$ 70 m^2) and CuCrZr heat sink structures ($\sim$ 45 m^2), was almost not protected by the carbon tiles (less than 20 %) [205]. Thus, the energy limit was set to 4 MJ per discharge. A total amount of 776 discharges were performed, containing the total He plasma time of $\sim$ 69 s and 242 s of H_2 plasma [38, 203].

To prepare the device for OP1.2a (August 2017 – December 2017), the limiters were replaced by a temporary graphite test divertor unit (TDU) and baffles covered by graphite tiles [159]. The installation of graphite tiles on the heat shield was completed. The total TDU surface area was 25 m^2. The total area of wall elements covered by graphite became 114.9 m^2, while stainless steel elements covered 77.1 m^2 [156]. Thus, the device was transformed to be operated in the divertor configuration. This experimental campaign successfully commissioned additional plasma fueling via hydrogen pellet injection with up to $\sim$ 40 pellets per discharge [174]. The energy limit was increased to 80 MJ per discharge. The maximum ECRH heating power was 7.5 MW. In total, 1156 discharges were performed in OP1.2a [203]. The overview of plasma time distribution among the reference magnetic field configuration is given in Table 3.2.

OP1.2b was performed from June 2018 to October 2018. For this operational phase, two graphite scraper elements with an area of 0.5 m^2 were installed to test a potential divertor pumping gap protection [160]. Boronization of the in-vessel components became available via the GD procedure. NBI system containing two ion sources brought an additional 3 MW of power for plasma heating [168]. At the end of this stage, the operation was determined by maximum heating energy of 200 MJ and pulse length of up to 100 s [151]. The total amount of successful discharges was 1120 [203]. Table 3.3 contains the OP1.2b plasma time distribution.

Table 3.3: Overview of main magnetic field configuration families in OP1.2b [163].

Configuration Family (OP1.2b)	Plasma species	Plasma time, s	Fraction, %
Standard configuration (EJM)	H	4809	53.1
High Mirror Configuration (KJM)	H	1392	15.3
High Iota Configuration (FTM)	H	1673	18.5
Low Iota Configuration (DBM)	H	1180	13.0
Total	H	9054	99.9

3.2 Overview of wall conditioning in the limiter operation phase OP1.1

As noticed earlier, the experiments of operation phase OP1.1 (2016) were performed in the limiter magnetic field configuration. Despite that, the author did not personally participate in this experimental campaign, he has significantly contributed to the data analysis and interpretation of the experimental results, which are shown below in this section.

Before plasma operation, the device underwent the baking procedure after the vacuum vessel pump down. The bakeout was performed for one week at an average temperature of 150 $^{\circ}\mathrm{C}$. After the baking and some leak repairs, a plasma vessel pressure of $2 \cdot 10^{-8}$ mbar was achieved compared to $7 \cdot 10^{-7}$ mbar before the baking [29]. The procedure allowed to reduce mainly water as well as other impurities such as hydrocarbons and carbon oxides. No other wall conditioning techniques were used to prepare for initial plasma operation. GDC was used between experimental days during the plasma operation phase, and ECWC was employed during experimental days. A detailed analysis of these wall conditioning techniques application in OP1.1 is given in [70].

GDC was operated with the de-energized magnetic field coils. Due to a technical problem with one of the vacuum feedthroughs, only 9 out of 10 GD anodes were used. GDC was performed only in helium, and its total duration was 10.9 hours. The usage of He-GDC was limited to avoid erosion of the unprotected area of the PFCs. The operational time was not longer than 40 minutes (often no longer than 20 minutes). The parameters of the GD were as follows. The working pressure was kept at $\sim 3.9 \cdot 10^{-3}$ mbar and the current did not exceed 1.2 A per anode. To characterize the efficiency of He-GDC and its influence on the plasma performance in OP1.1, the function of normalized outgassing, considered to be proportional to the PFC gas release

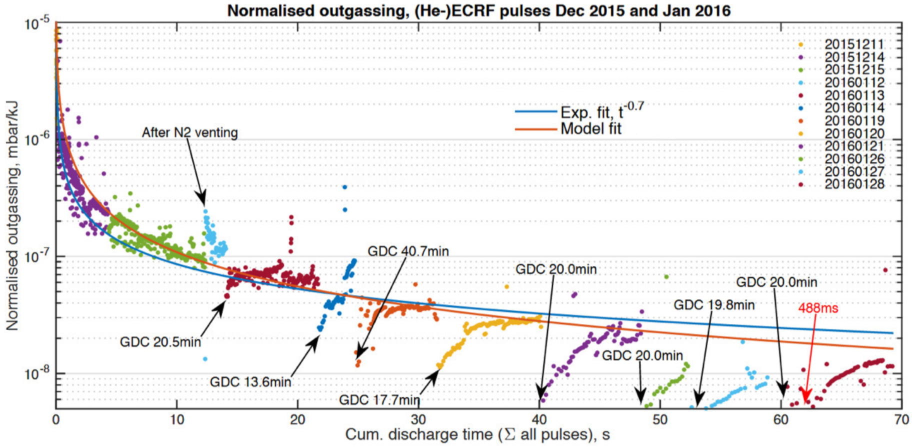

Figure 3.8: Normalized outgassing in the initial He-phase of the experimental campaign. Dots represent individual discharges. Different data colours correspond to the experiments on certain days. Arrows indicate the trend interruptions caused by He-GDC and nitrogen venting. A typical experimental $t^{-0.7}$ and Andrew's model fits are shown by blue and red lines, correspondingly [206].

rate, is evaluated in [206]. Here, normalized outgassing is calculated as an outgassing pressure peak at the end of a plasma discharge normalized to the total injected ECRH energy in that discharge. Fig. 3.8 shows the normalized outgassing as a function of the cumulated ECRH plasma time (sum of all previous discharge lengths) in the He-phase of OP1.1.

One can see that the application of He-GDC forces the ion-induced desorption of impurities and hydrogenic species. It results in a temporal decrease of the normalized outgassing at the start of an operational day, after He-GDC, and consequent improvement of the plasma performance. At the end of the He phase, the application of He-GDC allowed achieving 0.5 s 2 MJ plasmas.

The value of normalized outgassing in the He phase dropped down to $\sim 1 \cdot 10^{-8}$ mbar $\cdot$ kJ^{-1} while the initial value was $5 \cdot 10^{-6}$ mbar $\cdot$ kJ^{-1}. It indicates the gradual improvement of wall conditions by the additional cleaning effect of helium ECRH plasma. According to the mass spectroscopy measurements, the outgassing impurities were dominated by CO and H_2. The release of water and hydrocarbons was significantly lower.

To understand the outgassing behaviour, the normalized outgassing trend given in Fig. 3.8 can be explained by the typical $t^{-0.7}$ dependence (see

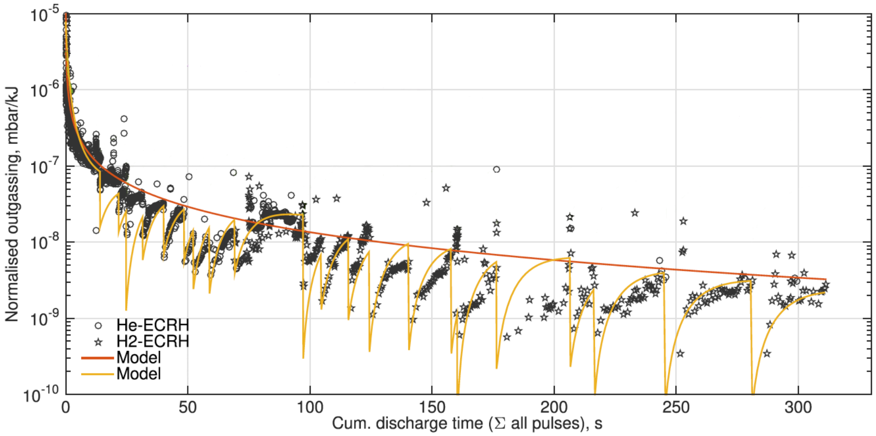

Figure 3.9: Normalized outgassing throughout OP1.1: experimental data ECRH discharges, Andrew's model fit used in Fig. 3.8 (red line) and the model fit including the conditioning contribution by GDC (yellow line) [70].

Eq. 2.9 and Eq. 2.16), which was also used for some other devices [72–74]. However, Andrew's model, described in Sec 2.2 (Eq. 2.24), with $Kc_0 = 10^{-2}$ s^{-1} and $c(t = 0) = 0.95c_0$ provides a better fit (according to a comparison of the R^2 coefficients of determination) for the given data [70].

ECWC applied in OP1.1 had similar heating power and gas fueling and were conducted in the same magnetic field configuration as the main ECRH plasmas. A typical ECRH recovery discharge was performed at ~ 2 MW of heating power at the neutral pressure range of $1.1 - 1.5 \cdot 10^{-5}$ mbar. Helium recovery discharges were used to recover from radiative collapses and improve the recycling conditions. A recovery discharge in helium allowed to deplete the PFCs from hydrogen and impurities, keeping helium recycling close to 1. Thus, the subsequent hydrogen plasma discharge duration could be significantly extended (up to 1 s).

As shown in Fig. 3.9, most hydrogen discharges in the second part of OP1.1 followed the same normalized outgassing trend given by Andrew's model. The strong outgassing from PFCs remained a major issue in the second part. More details about normalized outgassing modelling for OP1.1 are given in [70].

Overall, the total cumulated plasma time in OP1.1 is 311 s. The normalized outgassing trend reached the level of $\sim 3 \cdot 10^{-8}$ mbar $\cdot$ kJ^{-1} at the end of the experimental campaign making available 6 s 4 MJ discharges. CO remained dominating impurity throughout the whole plasma operation phase indicating the abundance of the O impurity.

Another tool allowing to estimate the status of wall conditions is the gas balance, the comparison of the injected and pumped amount of gas. In OP1.1, the gas balance calculation was done by the following scheme.

- The injected amount of gas is given by

  $$Q_{inj} = \sum_i C_i \int f_i dt,$$

  where i is the number of gas injectors in use, C_i is a gas type correction coefficient (H_2, He or Ar) for each gas injector, and f_i is the calibrated gas flow. The integration is done over the gas injection time.

- The pumped amount of gas is estimated as

  $$Q_{pumped} = \int_{t_0}^{t_{end}} pdt \sum_n S_n,$$

  where p is average neutral pressure (calculated in Sec. 3.1.1.4) in the vacuum vessel, n is the number of turbopumps in use, t_0 is the start of a discharge execution, t_{end} is a post-discharge time ($\sim$ 60 s) when the sufficient amount of gas is pumped. S_n is an effective pumping speed of each pump calculated as

  $$\frac{1}{S_n} = \frac{1}{c_{smm} g_t S_p} + \frac{1}{C'},$$

  where S_p is a variable pumping speed of a turbopump, c_{ssm} is the conductance coefficient of splinter safety mesh ($\sim$ 0.9) connected to each pump, g_t is gas type correction coefficient for pumping speed and $C^{'}$ is the conductance of the pumping duct for a certain gas type [167]. The total amount of the pumped gas can be assumed as a sum of the pumped amount of dominated gases (H_2, He, Ar and CO). The average pressure value should be corrected by a gas type correction coefficient proportional to the ionization gauge sensitivity factor to calculate the pumped amount for a certain gas. The conductance of the pumping duct should be converted according to the gas type as inversely proportional to the square root of the molecular mass.

The complete analysis of the residual gas composition was not available in OP1.1. The pumped amount calculation was based on the assumption

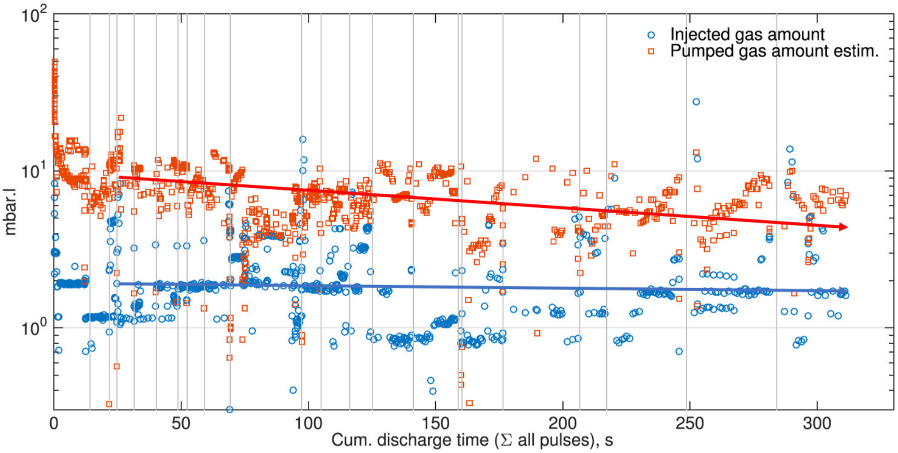

Figure 3.10: OP1.1 gas balance as a function of the cumulated ECRH pulse time. Blue circles indicate the injected amount of gas, and red squares correspond to the gas pumped. Blue and red arrows show the behaviour trends of injected and pumped gas amounts throughout the operation phase. Vertical grey lines indicate the events after the He-GDC application where the recycling is close to 1 (similar amounts of injected and pumped gas) [70].

that partial gas pressures are proportional to the amount of injected gases for multi-gas injection discharges. In most discharges, the outgassed species are assumed to be mainly hydrogen, considering that CO is the dominating impurity. The results of the gas balance calculation are illustrated in Fig. 3.10.

The analysis of the gas balance shows that the total amount of injected gas is $\sim$ 4.4 bar · l while the total amount of pumped gas is equal to 22.0 ± 0.2 bar · l [70]. The calculation uncertainty of the pumped amount of gas is related to the variation of the effective pumping speed for hydrogen at lower pressures. The behaviour trends of the injected and pumped amounts of the gas show a slight improvement in recycling. The average pumped amount of gas dropped by a factor of $\sim$ 3 during OP1.1.

Both tools, normalized outgassing trend and the gas balance have shown that the wall conditions continuously improved throughout the operation phase but were still far from ideal. To achieve good wall conditions, defined by normalized outgassing values below $1 \cdot 10^{-9}$ mbar · kJ^{-1}, the device requires a set of initial wall conditioning procedures applied before the start of plasma operation. The results of the experimental campaign show that He-GDC in combination with ECRH - based wall conditioning alone is not well suited for initial wall conditioning techniques.

3.3 Wall conditioning in the divertor operation phase OP1.2

Based on the experience of OP1.1, the combination of different cleaning techniques turned out to be essential to get to good wall conditions. The available conditioning techniques in OP1.2a were baking, GDC and ECWC. Complete protection of the wall elements by carbon tiles in OP1.2 allowed for a long GDC in hydrogen, significantly reducing the amount of impurities such as H_2O, CH_4, CO and CO_2. Following GDC in helium allowed depleting the walls from remaining hydrogen. In OP1.2b, the application of boronization also became accessible. These wall conditioning techniques have been applied to achieve high plasma performance in the divertor operational phase forming the wall conditioning strategy. Before the first plasma, the initial conditioning included baking the vacuum vessels and GDC to provide the minimum conditions for starting physics experiments. Boronisation and ECWC were used during the plasma operation period to reduce the amount of oxygen and control the hydrogen recycling, respectively.

The PhD thesis author was directly involved in two experimental campaigns. As a contribution to wall conditioning studies and optimization, the activity was dedicated to planning, preparing, leading experiments, and analyzing and interpreting results for GDC and ECWC. In the case of boronization, an optimization of GD was performed for boronization support, and the part of data analysis was done. The author has also analyzed overall wall conditions throughout OP1.2a and OP1.2b.

An overview of the gas balance, outgassing mechanisms and main impurities in OP1.2 is given in this section. The details of the application and optimization of these wall conditioning techniques and the results of wall conditioning efficiency and plasma performance improvement are described in the following part of this chapter.

3.3.1 Outgassing and gas balance overview of OP1.2a

Changing the limiter configuration to the divertor configuration has a clear advantage for impurity shielding and fuel recycling in W7-X. The difference related to the different plasma geometry and the pumping capability of the divertor allowed the device to be more resilient to particle release from the PFC's.

Indeed, the impurity release from the PFC's in the first pulse of OP1.2a was less severe than in the case of the first pulses in the limiter configuration. The latter was also due to an application of GDC as initial wall conditioning (see Sec. 3.3.5). No significant outgassing trend was observed. Instead, the normalized outgassing was reduced to values around $1 \cdot 10^{-9}$ mbar $\cdot$ kJ^{-1} within three days after the beginning of OP1.2a (Fig. 3.11). Afterwards, its level mostly fluctuated around this value for the rest of the experimental campaign. There was not any obvious relation to the progress of the wall conditions. It means that the discharge length was no longer determined by outgassing, causing eventually a radiative collapse.

Due to the commissioning of the new tools and diagnostics, including pellet injection, additional fuel and impurity injection, and NBI heating, the calculation of the gas balance became more complicated in OP1.2. Thus, the method of analysis used for OP1.1 had to be modified. A new simplified method includes inboard and outboard launched pellets to calculate the injected amount of gas. The calculation of the pumped gas amount is obtained by integrating an average gas pressure multiplied by the effective pumping speed for helium and hydrogen. However, for simplicity, the pumped gas for hydrogen and helium pulses is assumed to be only hydrogen and helium, respectively, which was more justified in OP1.2a than OP1.1. The downside of the simplified method is that it overestimates the pumped amount of gas in hydrogen discharges in case of impurities outgassing because impurities are

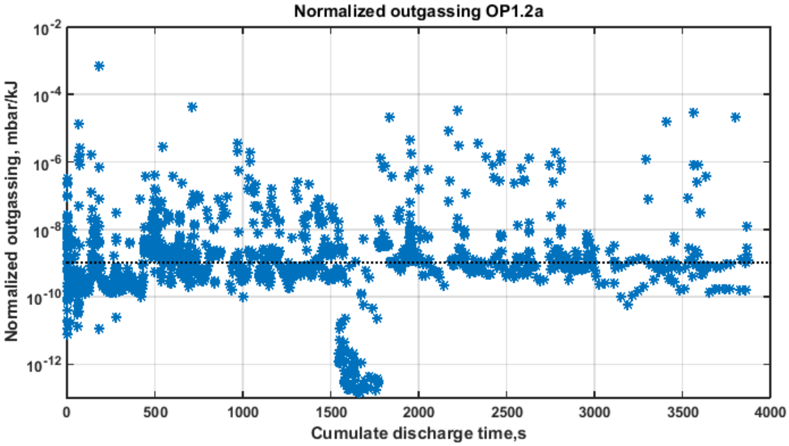

Figure 3.11: Normalized outgassing as a function of the cumulated discharge time in OP1.2a. The horizontal black dotted line corresponds to the normalized outgassing level of $1 \cdot 10^{-9}$ mbar · kJ^{-1}.

pumped at a lower rate than hydrogen. In the case of helium discharges, the method slightly overestimates the pumped amount of gas when hydrogen outgassing is strong.

Nevertheless, the OP1.2a gas balance analysis results, shown in Fig. 3.12, clearly illustrate the following. In general, hydrogen discharges have net retention. It can be explained by the hydrogen trapping in He-conditioned walls, its co-deposition with eroded material and implantation in the PFC.

At the same time, helium discharges demonstrate net removal, which is understood from the complete recycling of helium and additional plasma-induced desorption of hydrogen. Being typical for carbon PFC this type of fuel recycling behaviour makes controlling the hydrogen content in the PFC's throughout an operation day rather challenging [207].

3.3.2 Outgassing and gas balance overview of OP1.2b

The same set of wall conditioning techniques were used to prepare the first plasma operation in OP1.2b. However, the total duration of GDC was significantly larger (see Sec. 3.3.5) based on the OP1.2a experience. A similar situation with normalized outgassing was observed at the beginning of OP1.2b before the first boronization procedure (Fig. 3.13). The first boronization procedure did not significantly change the trend. Most of the values stayed below $1 \cdot 10^{-9}$ mbar · kJ^{-1}. However, the scattering of the normalized

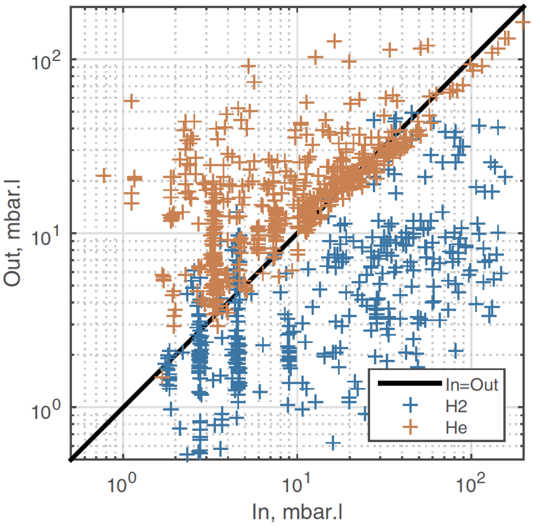

Figure 3.12: Gas balance for all ECRH experiments of OP1.2a. Hydrogen and helium discharges are shown as blue and red crosses, respectively [207].

outgassing values above this level was decreased by ~ 2 orders of magnitude. Further analysis (see Sec. 3.3.6) proves that it is correlated with a significant improvement of the wall conditions and plasma performance. The consequent boronizations did not have a visible contribution to the picture of normalized outgassing. It should be noticed that after the first boronization, all plasma discharges were in hydrogen except for the conditioning discharges conducted in helium.

In OP1.2b, new diagnostics contributed to the total amount and the composition of the injected gas (see Sec. 3.1.1.5). Thus, calculation of the gas balance required a more sophisticated and accurate approach to the gas balance analysis. This method is given in [169, 208]. It allows estimating the wall inventory and the effect of fueling and heating on the wall inventory, helping to develop the operation scenarios for the long-pulse physics program. The analysis shows that auxiliary fueling on low heated walls leads to strong fuel (hydrogen) absorption [208]. At the same time, an increase of the graphite PFC surface temperature allows mobilizing retained gas in the carbon structures [208]. A single-reservoir particle balance for the main plasma species, such as hydrogen, has been established, enabling the quantitative characterization of the particle sources and analyzing fueling, recycling, and particle confinement in the standard configuration [188].

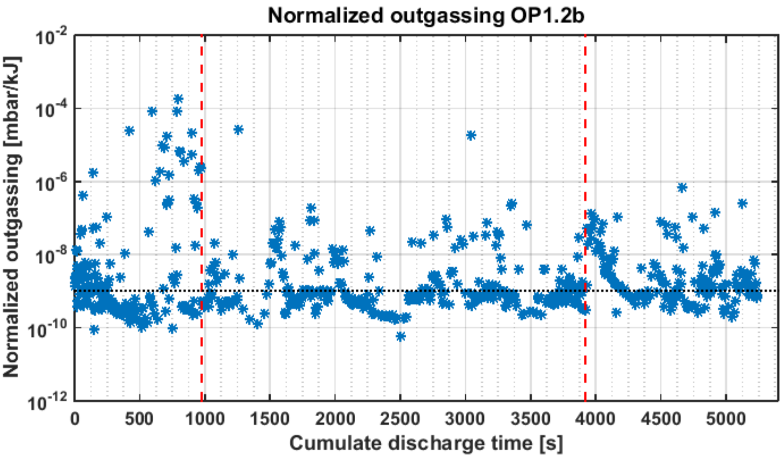

Figure 3.13: Normalized outgassing as a function of the cumulated discharge time in OP1.2b. The horizontal black dotted line corresponds to the normalized outgassing level of $1 \cdot 10^{-9}$ mbar $\cdot$ kJ^{-1}. The vertical dashed lines indicate the 1stand 2nd boronization events.

3.3.3 Comparison of residual gas content and its temperature dependence in OP1.2a and OP1.2b

During the divertor operational phase, He, C and O were the principal impurities in hydrogen plasmas according to the divertor spectrometer measurements [209]. In OP1.2b, helium mainly originated from the application of He-GDC and He-ECWC. In the case of oxygen, its primary source was a vapour contained in the fine grain graphite. The existence of He and O in plasma made a significant contribution to the overall carbon erosion through enhanced physical and chemical sputtering [209]. The latter resulted in the domination of CO and H_2O in the outgassing content, both OP1.2a and OP1.2b (before boronization). However, the residual gas content after boronization has significant changes. For comparison, one example is given for the end of OP1.2a (Fig. 3.14a), while another one shows the data from OP1.2b after boronization (Fig. 3.14b). Both examples contain the mass-spectra recorded at the same magnetic field configuration (standard) to make QMS spectra comparable.

The average level of water is $\sim$ 3 times lower in OP1.2b while carbon oxide level is reduced by a factor of $\sim 2 - 2.5$. The QMS signal of CO is slightly higher than one of H_2O in OP1.2b (after boronization). The signal of the molecular oxygen remains almost at the same level, indicating that its source is most probably outside of the vacuum vessel (in the pumping ducts).

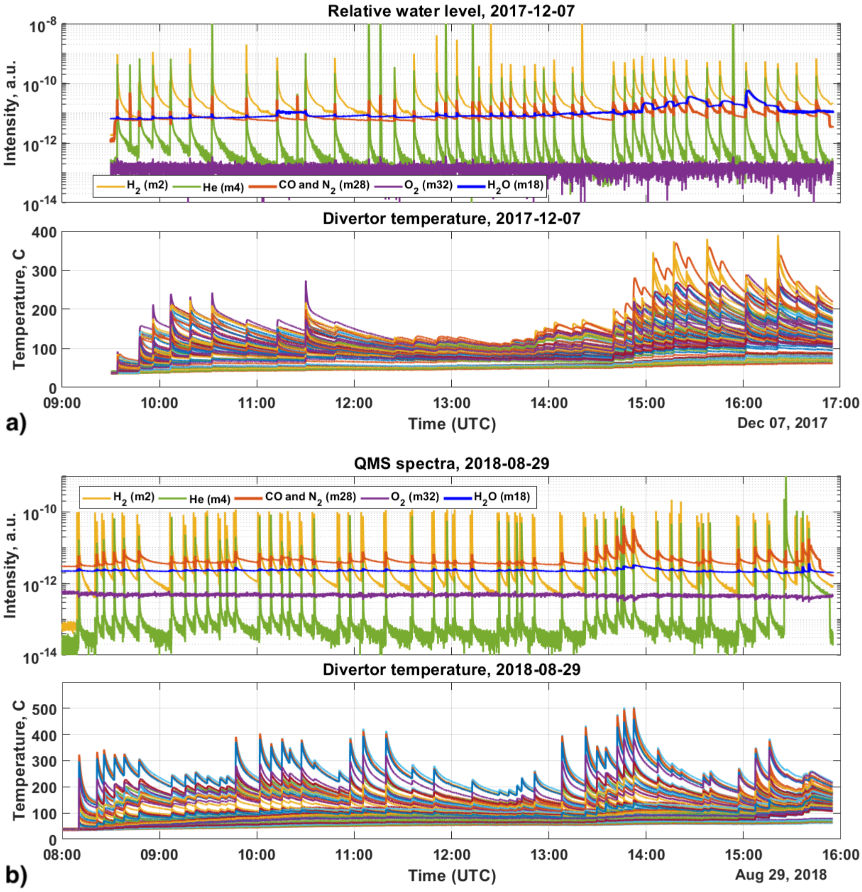

Figure 3.14: Dominating impurity (H_2, He, CO, O_2 and H_2O) outgassing given by QMS versus divertor temperatures measured by divertor thermocouples in the different locations throughout an experimental day. a) 7th of December 2017 (OP1.2a), b) 29th of August 2018 (OP1.2b). The QMS spectra peaks and temperature peaks correspond to discharge execution. The increase of the divertor temperature correlates with discharge outgassing (each discharge causes the steep rise of the impurity outgassing and divertor temperatures). Black arrows and numbers indicate the discharges caused an extra release of water and carbon oxide.

The operation of the device in the divertor configuration shows that some PFC parts, mainly divertor parts, are heated up strongly during an ECRH discharge. Other locations experience a temperature rise due to heat diffusion through the materials. There are significant temperature gradients along the components, as shown in Fig. 3.14. This figure also shows the influence of the selected divertor location temperatures on the outgassing of different species from the residual gas content. It should be noticed that the actual temperature of the PFC surfaces is higher than the one given by thermocouples because most of the thermocouples are located inside the support structure of PFCs.

Additionally, there can also be significant variations in the PFC temperature throughout an operation day. The temperature of these locations can increase by up to 100 $^{\circ}\mathrm{C}$ from the initial value after only one discharge execution with the energy limit of 80 MJ per discharge. The average temperature of the divertor can slowly rise by up to $\sim$ 60 $^{\circ}\mathrm{C}$ throughout an experimental day.

The PFC temperature strongly affects an impurity release from the PFC and hydrogen recycling during a plasma discharge and the continued outgassing after a discharge [207]. The average level of water outgassing also correlates with the average PFC temperature. The partial water pressure drops during an ECRH discharge. However, it quickly recovers in the post-discharge period. In some cases, the intense heating (more than 200 $^{\circ}\mathrm{C}$) of some divertor areas may release the extra water stored in graphite microcavities in the deep material layers. Examples of such events that happened in OP1.2a and OP1.2b are also shown in Fig. 3.14. The rise of the H_2O outgassing can reach a factor of 5. Both CH_4 and CO are also strongly released during a discharge. Methane is pumped quickly in a post-discharge phase while the carbon oxide signal decays slowly over about one order of magnitude in $\sim$ 20 min. The outgassing of CO is also correlated to the passive cooling rate of the hottest PFC locations. It can result in a CO background pressure increase of about one order of magnitude during an operation day if the discharge repetition rate is higher than a characteristic pumping time. In the case of hydrogen discharges, the signal outgassing tail increases with increasing wall temperature, which is better pronounced in the total pressure measurements than in hydrogen partial pressure given by QMS. More details about hydrogen outgassing studies and outgassing modelling results can be found in [207].

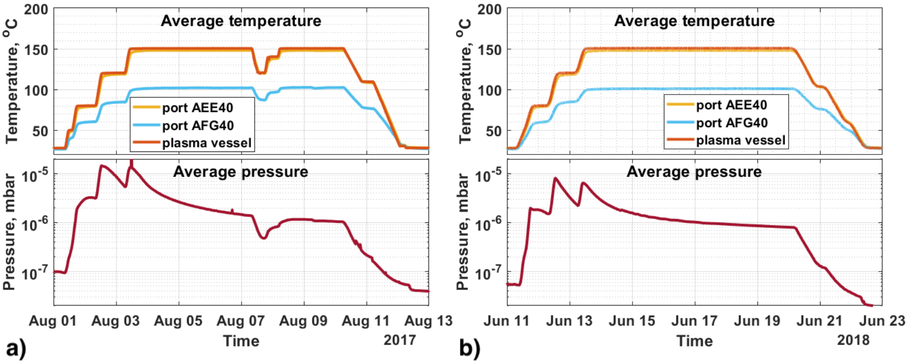

Figure 3.15: Overview of the baking procedure. a) OP1.2a (the drop of the average temperature and the corresponding pressure drop on 8th of August 2017 due to a leak in one of the water-cooling circuits), b) OP1.2b.

3.3.4 Baking

The baking of the plasma vessel walls was performed in each part of operation phase OP1.2 after the vessel pump down. The procedure of the bake out took 11 days in total. The first phase contained a stepwise temperature increase. The flat-top phase was carried out during 7 days at the average wall temperature of 150 $^{\circ}\mathrm{C}$. However, it should be noticed that maximum baking temperatures varied for different elements of the plasma vessel. For example, the baking temperatures along the ports range between about 100 to 160 $^{\circ}\mathrm{C}$ [29]. Finally, the termination of the procedure was also performed as a step by step temperature decrease. The overview of the baking procedures of OP1.2a and OP1.2b is shown in Fig. 3.15.

The trend of the residual gas pressure during the flat-top phase show the same behaviour for two experimental campaigns. At each temperature increase, a sharp thermal outgassing peak is observed in the total vessel pressure. In both cases, at the flat-top phase, the pressure curve follows a $\sim t^{-0.7}$ dependence (Fig. 3.16a) typical for temperature-induced particles' desorption, as discussed in Sec. 2.1. The total duration of the bake out is found to be satisfactory. Following this outgassing power law means that a further extension of the baking time can cause only a minor improvement of the residual gas content and a further decrease of base pressure becomes increasingly difficult. For example, after 7 days of bake-out, the relative pressure decrease rate ($\Delta p/\Delta t/p$) becomes less than 10 %.

The analysis of the QMS spectra shows that water is the main compo-

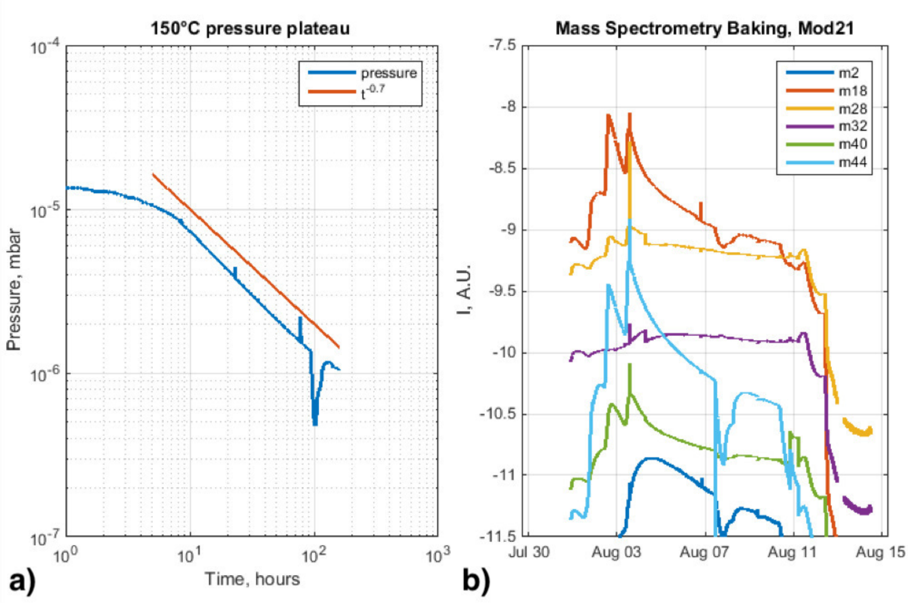

Figure 3.16: Evolution of pressure and residual gas content throughout OP1.2a baking. a) average neutral pressure (blue) in the flat-top phase and $t^{-0.7}$ trend curve (red),), b) QMS spectra recorded by mass spectrometer located in Module 21, mass-to-charge ratio signals (m/q) have the following relations: H_2 (m2), H_2O (m18), CO (m28), Ar (m40), and CO_2 (m44).

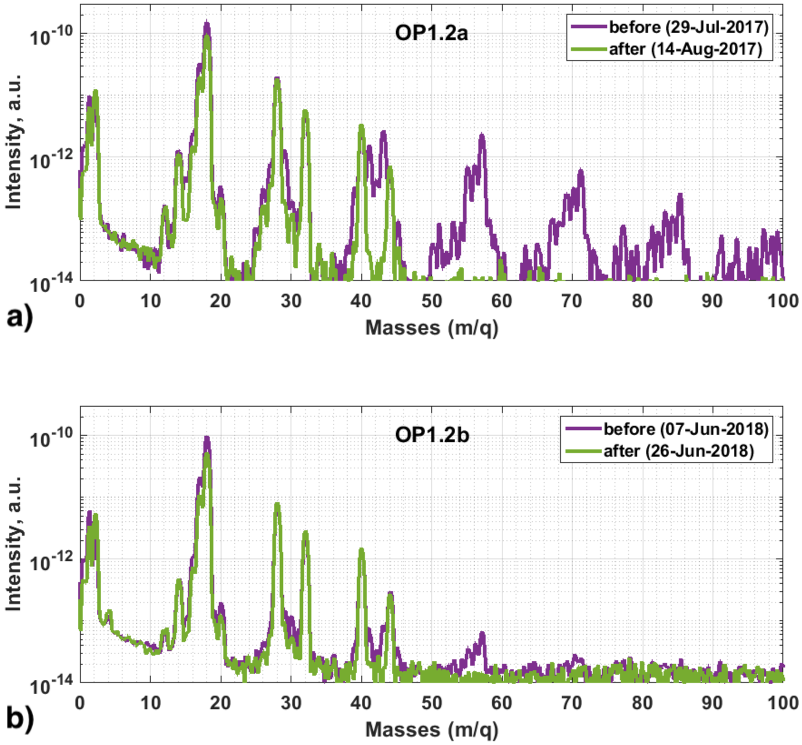

Figure 3.17: Residual gas content before (magenta) and after (green) baking. a) OP1.2a (1st of August 2017 – 12th of August 2017), b) OP1.2b (11th of July 2018 – 23d of July 2018) [210].

nent in the outgassing content (Fig. 3.16b). Carbon oxide and carbon dioxide are the following prominent species. However, these species are released at lower rates, by one order of magnitude compared to water.

The application of baking decreased a base pressure level in the torus at room temperature from $(8.1 \pm 0.6) \cdot 10^{-8}$ mbar to $(3.9 \pm 0.4) \cdot 10^{-8}$ mbar prior OP1.2a and from $(5.4 \pm 0.8) \cdot 10^{-8}$ mbar to $(2.1 \pm 0.4) \cdot 10^{-8}$ mbar prior OP1.2b. The comparison of the residual gas content before and after the baking for both experimental campaigns is shown in Fig. 3.17. According to the given data, more extensive removal of impurities was observed in OP1.2a. In this case, the outgassing of heavy species, mostly high hydrocarbons, with a mass-to-charge ratio above 50 was suppressed.

Water outgassing was reduced by a factor of 1.6 ± 0.4 resulting in the removal of about 10^{25} molecules. The QMS signals of air-related species like molecular oxygen (O_2), carbon oxide (CO), carbon dioxide (CO_2), argon

(Ar) and molecular nitrogen (N_2) had almost no changes. Partial pressures of methane and ethane, being approximately two orders of magnitude lower than the partial water pressure, dropped by 1.6 ± 0.1 and 2.1 ± 0.2, respectively.

Contrary to the OP1.2a, the second divertor campaign baking did not dramatically change the residual gas content at higher masses after baking. The better wall conditions after the pump down in OP1.2b correlate with the lesser in-vessel assembly and vessel venting times ($\sim$ 14 months before OP1.2a and $\sim$ 4 months before OP1.2b). For the lower masses, the outgassing of water was reduced by a factor of 1.9 ± 0.1 and the level of methane had a $\sim$ 1.5 times decrease while being only about 1.3 % compared to the water concentration. Similar to OP1.2a, the level of air-related species did not experience any changes indicating a potential presence of small continuous air leaks. Thus, the bakeout before OP1.2b mainly resulted in water removal.

3.3.5 GDC

To further deplete the contamination layer at the surface of in-vessel components after the baking, OP1.2 employed GDC in hydrogen at room temperature. Apart from the initial conditioning, hydrogen GDC was used weekly throughout the experimental campaign to further improve the wall conditions for plasma operations until the application of boronization allowed to suspend further GDC operation. GDC in helium was executed either daily after hydrogen plasma experiments or application of H_2-GDC to desaturate walls from hydrogen.

3.3.5.1 GDC optimization

In OP1.2a, the execution session time for the GDC application was limited due to a dense commissioning and physics program together with the requirement of restricted torus hall access during GDC execution. Following these limitations, the duration of the weekly applied H_2-GDC did not exceed 90 minutes in total for OP1.2a. In comparison, He-GDC was conducted in separate procedures of 20 – 25 minutes each only before plasma operation. Thus, the challenge was to remove a maximum of impurities in the given time by improving the stability and homogeneity of the glow discharge while minimizing spurious PFC erosion.

The application of H_2-GDC did not lead to any noticeable erosion during plasma operation. The latter allowed to operate H_2-GDC at the upper anode current limit of 1.5 A. The ten anodes available in OP1.2 correspond to an average current density at the wall of about 50 mA/m^2. The maximization of the available flux of the high-energetic ions towards PFC contributed to higher cleaning efficiency. Fig. 3.18 shows an increase of the outgassed impurity partial pressure (QMS) at the rise of the anode current from 1 A to 1.5 A. Lowering the hydrogen operation pressure leads to an improved discharge homogeneity which could only be observed visually in the overview video diagnostic (EDICAM) system. The minimum working pressure for stable GDC operation was defined in the range of $(4.4 - 4.5) \cdot 10^{-3}$ mbar. The average voltage is $\sim$ 305 V at these parameters of current and pressure. A pressure decrease below this value leads to the unstable work of some glow anodes (Fig. 3.19a), which is seen by the increasing deviation of individual anode voltages from the average voltage values. Decreasing the pressure further causes the termination of the glow discharge. At the same time, an increase in the average voltage is not significant (only $\sim$ 3 V).

In contrast to H_2-GDC, indications of in-vessel components erosion caused by He-GDC application were found at the beginning of OP1.2a [211]. For example, the PHA diagnostic clearly showed that eroded and further redeposited material mainly consisted of stainless steel components such as Fe, Ni and Cr, released during the subsequent ECRH plasma discharges. Fig. 3.20 demonstrates that PHA spectra of discharges before He-GDC application did not have any evident traces of the metallic PFC components appearing in the plasma. The presence of the eroded and redistributed material appeared only after the glow discharge. The characteristic line intensities are lower in the following similar discharges, indicating that Cr, Ni, and Fe concentrations are reduced.

The voltage in OP1.2 was reduced to its minimum value corresponding to the operational pressure of $\sim 3.8 \cdot 10^{-3}$ mbar (Fig. 3.19b) to minimize the influence of physical sputtering by He-GDC. To reduce the amount of eroded material, the anode current decrease reduced the He ion flux. While reducing the erosion rate, the reduction of the ion current also reduces the hydrogen removal rate. Thus, a compromise needs to be found between getting satisfactory wall conditions, e.g. entirely suppressed wall fueling after He-GDC application and keeping the minimum impact on PFC erosion. Due to limited time, it could not be established experimentally. Moreover, it is seen that decreasing the current to its minimum value of 0.5 A, a limit to keep sustaining the discharge, has a minor influence on the anode voltage and the related ion impact energy on the surfaces. In this case, the reduction of the anode voltage is less than 1 %. Considering all the above-mentioned arguments, the anode current of glow discharge in helium was kept at 1 A. Together with chosen value of working pressure, it corresponds to an average voltage of $\sim$ 210 V.

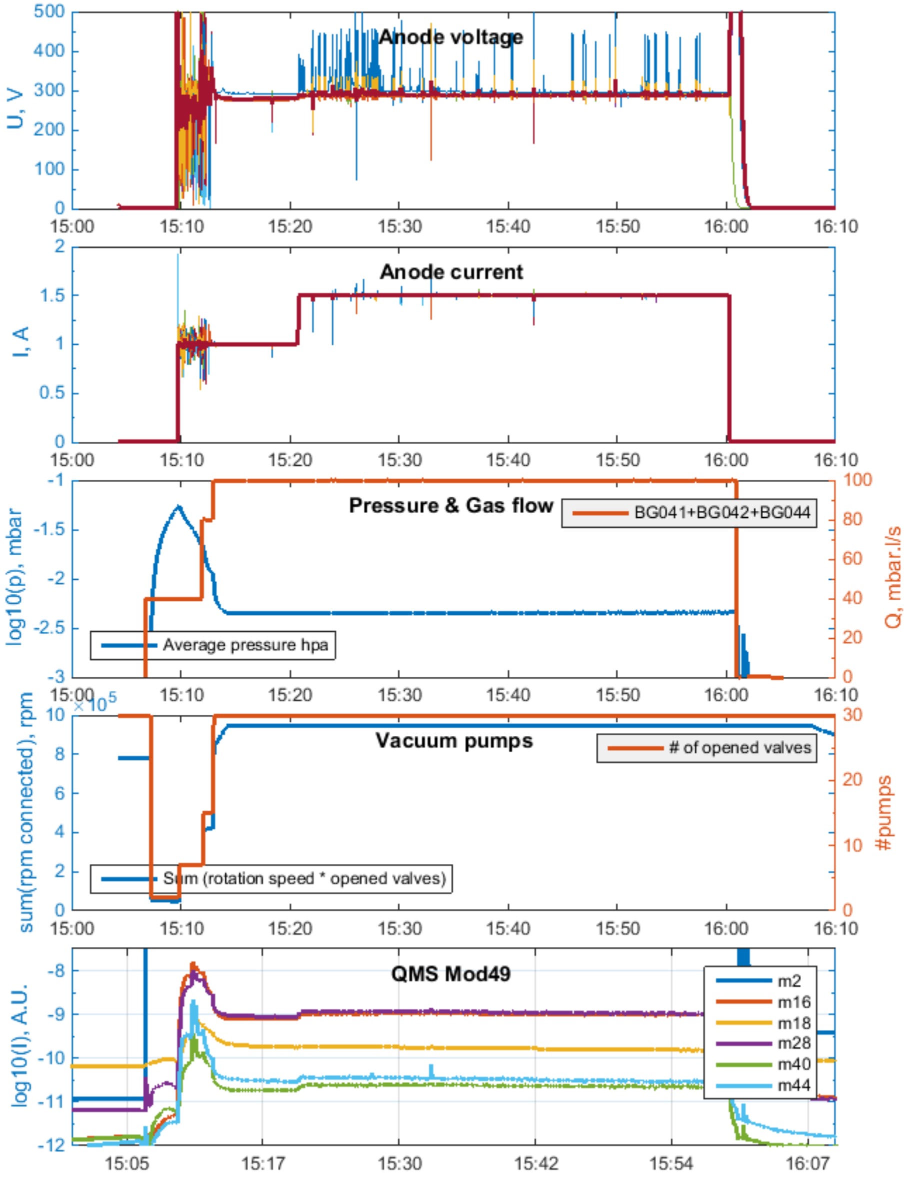

Figure 3.18: Overview of H_2-GDC operation 20170830: anode voltage, anode currents, gas flow, pressure, total pumping speed and partial pressures of dominating impurities.

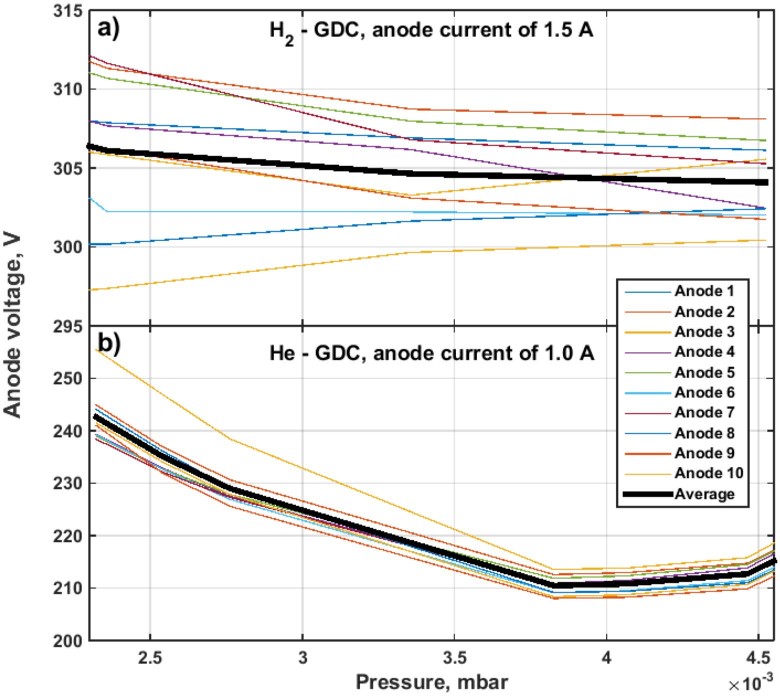

Figure 3.19: Glow discharge anode voltage dependence on neutral gas pressure a) hydrogen GD at anode current of 1.5 A, b) helium GD at anode current of 1 A.

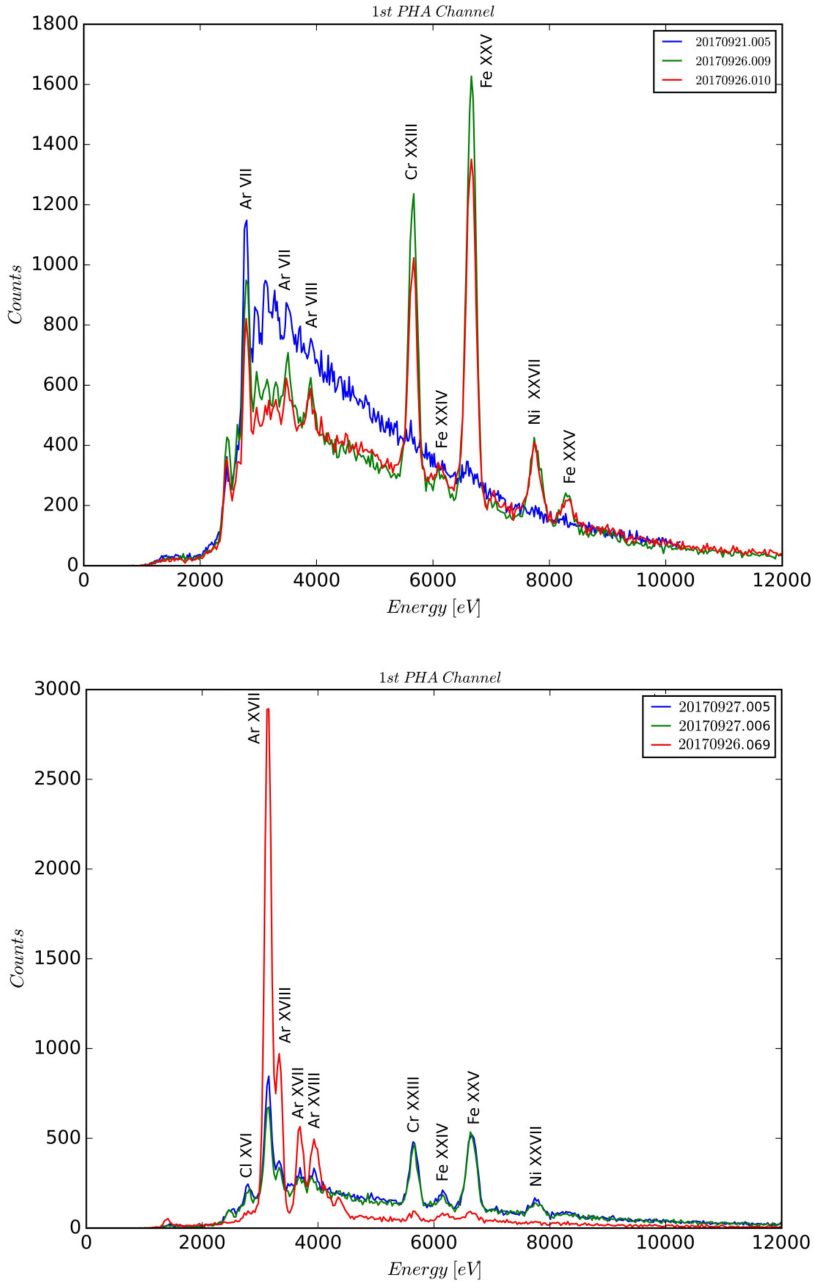

Figure 3.20: PHA spectra of similar hydrogen plasma discharges. a) before (20170921.005) and after (20170926.009 and 20170926.010) He-GDC on 25th of September 2017, b) before (20170926.069) and after (20170927.005 and 20170927.006) He-GDC on 26th of September 2017.

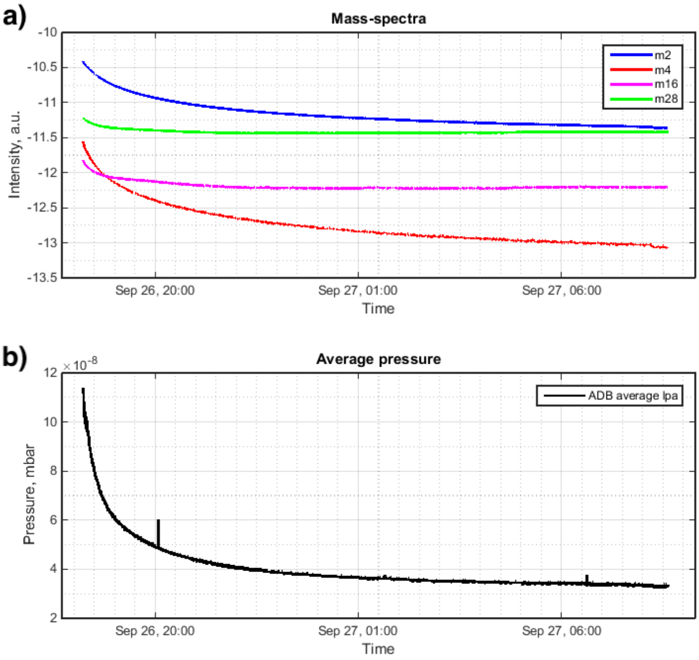

Figure 3.21: The outgassing trend after H_2-GDC operation ($\sim$ 20 minutes) on 26th of September 2017. a) QMS spectra (m2 – H_2, m4 – He, m16 – CH_4, m28 - CO), b) average neutral gas pressure. The glow discharge was terminated at around 18:00 Sep 26.

Besides the cleaning effect, GDC operation causes post-discharge outgassing. The example of the outgassing trend is given in Fig. 3.21. Even in the case of 20 minutes H_2-GDC, due to the strong post-discharge outgassing dominated by hydrogen, $\sim$ 4 hours of pumping time is needed to decrease average pressure by a factor of $\sim$ 3. Thus, to avoid any influence of the outgassing on the following plasma operation, it is recommended to use GDC at the end of the experimental day providing enough time for the pump down.

3.3.5.2 GD break-down

Another challenge of GDC optimization is related to the achievement of a reliable and fast break-down. Glow discharge break-down could not be achieved at operational pressure using the current GD system (see Sec. 3.1.1.7). In the case of H_2-GDC, the break-down could be achieved at neutral gas pressures above $2.9 \cdot 10^{-2}$ mbar. H_2-GDC is strongly inhomogeneous in this

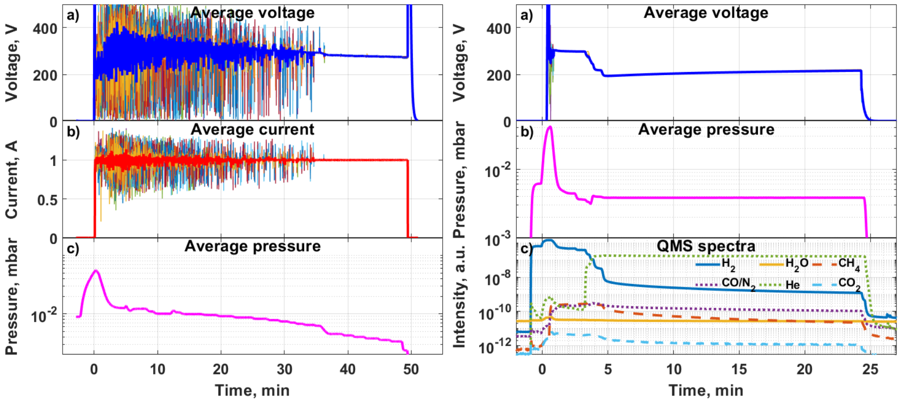

Figure 3.22: (left) The evolution of the main H_2 – GDC (20170823) parameters: anode voltage (a), anode current (b) and neutral gas pressure (c). The working pressure range corresponding to GDC stability and reliable homogeneity is below $5 \cdot 10^{-3}$ mbar. (right) He – GDC overview (20171109): averaged anode voltage (a), neutral gas pressure (b), QMS time traces of wall released molecules (c). The discharge break-down was done in hydrogen, which after $\sim$ 5 min was changed by helium [211].

pressure range, being localized in the anode vicinity and vacuum vessel cavities. It corresponds to the hollow cathode effect [212]. At the beginning of OP1.2a, when glow anodes were not yet conditioned, the glow discharge current-voltage characteristics had strong fluctuations at pressures above $\sim 9 \cdot 10^{-3}$ mbar (Fig. 3.22a). This effect may lead to arcing, potentially causing severe damages of in-vessel components as discussed later in Section 3.3.5.4.

A discharge ignition procedure that includes a fast pressure decrease while avoiding discharge termination was developed to minimize the spurious effects at higher pressure. The break-down is achieved at a hydrogen flow of 40 mbar · l/s with only two turbopumps connected. While pressure is rising above $1 \cdot 10^{-2}$ mbar a simultaneous voltage ramp is done up to 3 kV setting the anode current to 1 A. The fast pressure decrease could be reliably achieved by combining a stepwise increase of the total pumping speed by connecting more pumps and variation of gas flow. The following scheme is found to be optimal (e.g. in Fig. 3.18). The number of connected pumps is increased $(2 \rightarrow 7 \rightarrow 15 \rightarrow 30)$ and the gas flow is also increased $(40 \rightarrow 80 \rightarrow 100$ mbar · l/s). The rapid increase of the pumping speed and gas flow while maintaining working pressure allows faster gas exchange in the vessel, reducing impurity and fuel redeposition rates. Thus, the operation pressure can be achieved in less than 2 minutes after break-down following the developed scheme after this procedure optimization. Right after that, the anode current is increased to 1.5 A. Moreover, the first procedure automatization tests have been successfully done, reducing the workforce needed for glow discharge execution in future experimental campaigns.

The break-down of He-GDC could not be made reliable in OP1.2a even at the maximum voltage of 3 kV and pressures up to $\sim 8 \cdot 10^{-2}$ mbar. A robust workaround was to ignite the glow discharge in hydrogen using the procedures described above. Then, after the discharge stabilization, one could gradually exchange the working gas for helium. The entire gas exchange procedure took 5 – 7 minutes. The typical He-GDC execution is shown in Fig. 3.22b. Despite the introduction of hydrogen at the start of the glow and the extension of the total GDC execution time, it is found more effective than spending time on several attempts of direct ignition in helium. A downside is that the gas exchange procedure makes the quantification of the hydrogen removal by He-GDC impossible. The ignition pressure is $\sim$ 4 orders of magnitude above the typical hydrogen outgassing pressure, and even a short H_2-GDC would load the PFC with some amount of hydrogen. Nevertheless, QMS data given in Fig. 3.22b shows that He-GDC also induces CH_4, CO and CO_2 removal from W7-X PFCs.

The most interesting point is that this problem did not remain in OP1.2b. It is connected to the fact that the anode conditions were worse in the first divertor campaign. The latter is also proved by the lack of current-voltage characteristics fluctuation in the break-down phase.

To better understand the peculiarities of glow discharge ignition, the data containing all successful glow discharge break-downs in OP1.2 has been summarized in Fig. 3.23. The figure presents the dependence of the break-down voltage on neutral gas pressures.

Fig. 3.23a shows the parameters of hydrogen GD break-down events. The data points are grouped along with a trend that corresponds to Paschen's law (see Eq. 2.28). It is clear that to achieve a break down in hydrogen at a minimum pressure of $\sim 2.9 \cdot 10^{-2}$ mbar the anode voltage should be set to its maximum possible value of 3 kV. However, in the case of break-down in helium, the dependence is not straightforward. The data is scattered and can't be easily fitted using a Paschen curve (Fig. 3.23b). Anyway, further reducing the helium and hydrogen break-down pressure requires looking for alternative ways to assist the GD break-down in W7-X.

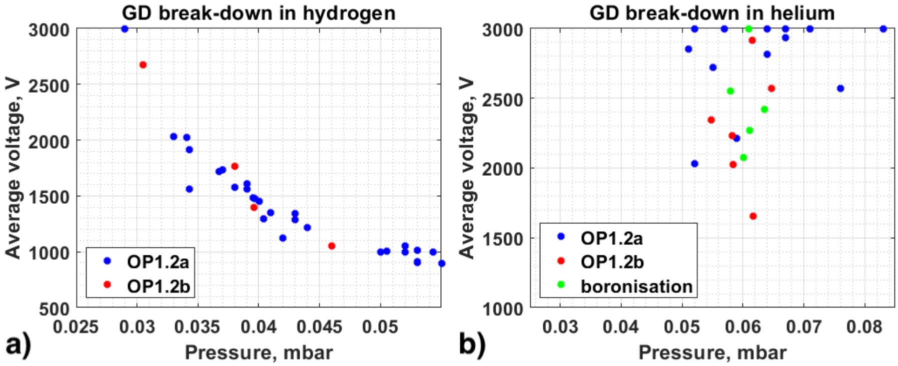

Figure 3.23: Summary of the glow discharge break-down characteristics (anode voltage vs neutral gas pressure) in the passively cooled divertor operation phases a) hydrogen GD b) helium GD. Blue asterisks correspond to glow discharge break-down events in OP1.2a. Red asterisks represent OP1.2b. Green asterisks are helium glow discharge break-downs during boronization procedures in OP1.2b.

3.3.5.3 Cleaning efficiency and cumulative effect of H_2-GDC

The application of H_2-GDC as an initial wall conditioning was short in OP1.2a (Table 3.4). Most of the H_2-GDC sessions were weekly performed throughout the experimental campaign. Fig. 3.24a gives an overview of the impurity removal by subsequent H_2-GDC sessions as a function of the cumulated H_2-GDC time in OP1.2a [207].

The given mass over charge ratio (m/q) intensities correspond to the following impurities. The vertical red dashed lines indicate the ECRH experimental sessions, including hydrogen and helium plasmas and the daily application of He-GDC. The signals discontinuity after the first H_2-GDC session is due to the optimization procedure leading to the gas flow increase by a factor of 2. The temporal increase of partial impurity pressures after $\sim$ 650 minutes of the cumulated glow discharge is due to an air leak. This air leak, causing an average pressure increase of up to $\sim 5 \cdot 10^{-5}$ mbar (within $\sim$ 5 hours), happened before the corresponding GDC application. The strong signals decay in the first 50 - 100 seconds in every GDC procedure result from the glow discharge ignition procedure discussed in the previous section. The same behavior is observed throughout the first H_2-GDC session due to a slow stepwise decrease of the gas flow and a simultaneous stepwise increase of the pumping speed. As one can see, the impurity signals form continuous

Table 3.4: GDC throughout the inertially cooled divertor operational phase [210].

Operational phase	**OP1.2a**	**OP1.2b**
	Prior to plasma operation	
H_2 – GDC	2:58 h	9:35 h
He – GDC	0:36 h	0:36 h
	Prior to plasma operation	
H_2 – GDC	13:46 h	1:03 h*
He – GDC	14:48 h	2:24 h*

* before boronization, excluding GDC in He/diborane mixture

envelope curves from session to session. For most of the impurities, these curves follow $\sim t^{-0.7}$ time dependence. The exception for CH_4 and CO_2 partial pressures is due to the dominating chemical sputtering processes making its signal saturated in time. Application of He-GDC and ECRH plasma operation has almost no effect on the impurity removal trends. The first is the lack of strong chemical processes between fuel, impurities and PFC material during He-GDC. In the second case, ECRH plasma in W7-X, being diverted plasma, reveals weak interaction with the main wall compared to the strong interaction in the divertor [38]. Even though the diverted plasmas are weakly interacting with the main wall, the large reservoir of impurities (O) at the main wall is thought to contribute significantly to the impurity influx in these plasmas. The partial pressures behaviour means that GDC in hydrogen has a cumulative effect on the impurity removal. Thus, according to Fig. 3.24a, a minimum of 9 to 10 hours of the initial H_2-GDC must be performed to achieve the impurity level reduction by more than one order of magnitude. The latter ensures reliable plasma operation conditions.

Based on this finding, the initial H_2-GDC in OP1.2b was $\sim$ 9.2 hours. The procedure was split into two parts, separated by one week of device commissioning. The results show the same cumulative effect (Fig. 3.24b) as for OP1.2a. The initial conditioning by H_2-GDC allowed to reduce the amount of H_2O by a factor of $\sim$ 12, CH_4 by $\sim$ 5, CO by $\sim$ 13, O_2 by $\sim$ 5, Ar by $\sim$ 6 and CO_2 by $\sim$ 36 [213]. He-GDC followed the last H_2-GDC session with a duration of 1.83 hours. It provided the required hydrogen outgassing level for a reliable start of the physics program. The time of GDC operation throughout the divertor operation phase (OP1.2a and OP1.2b) is summarized in Table 3.4.

GDC was routinely applied only in the first month of OP1.2b leading to

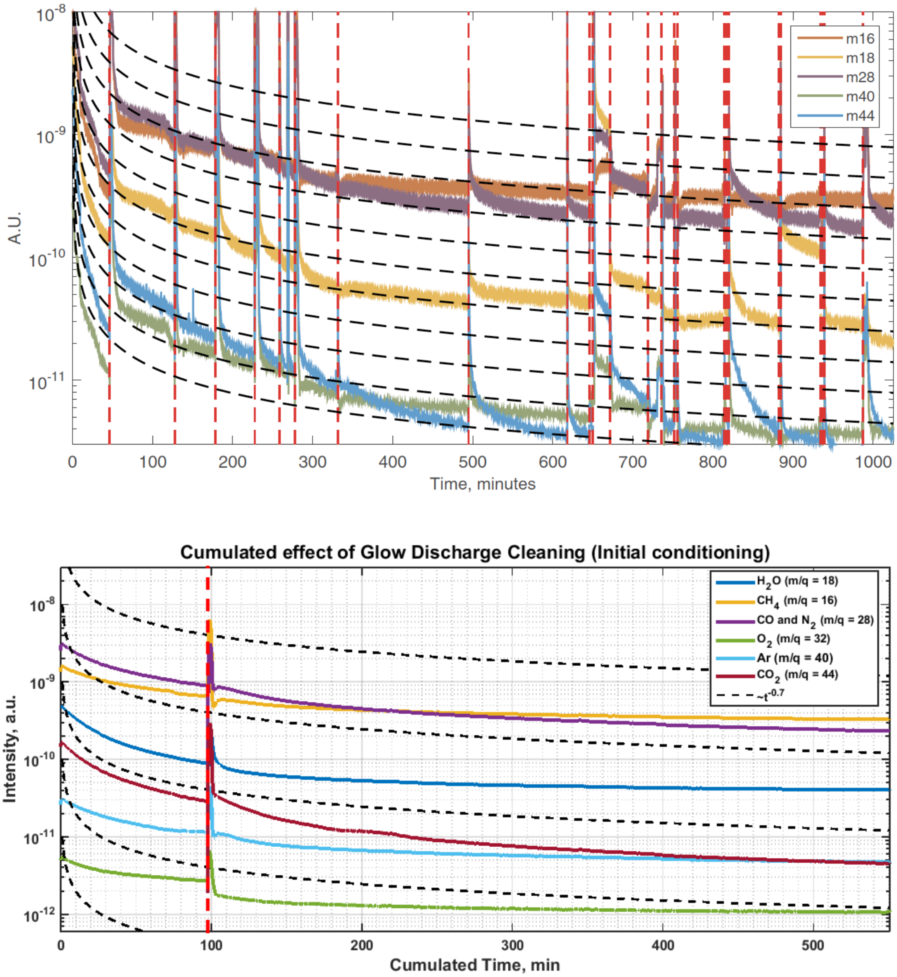

Figure 3.24: QMS signal intensities for subsequent H_2-GDC's procedures as a function of cumulated H_2-GDC time (CH_4 - m16, H_2O – m18, CO – m28, Ar – m40 and CO_2 – m44). a) for subsequent H_2-GDC's procedures from OP1.2a campaign start to end [207], b) for subsequent H_2-GDC's initial conditioning procedures of OP1.2b. The QMS signals are normalized to the glow anode current. The black dashed grid lines show time dependencies ($\sim t^{-0.7}$), the red dashed lines indicate ECRH operation days (OP1.2a) and break between sessions (OP1.2b).

a short total time compared to OP1.2a. It was due to the decision to suspend this type of wall conditioning after the first boronization. The decision was motivated by the significant improvement of the wall conditioning owing to boronization (see Sec. 3.3.6) and the consideration that further application of GDC might cause erosion of the boron layer. The latter must be further proved and investigated in detail, including additional experiments on the TOMAS device (see Chapter 4).

3.3.5.4 Adverse effects of GDC

The post-mortem analysis of different PFC component surfaces and inspection of the in-vessel components show that carbon erosion had also occurred during GDC operations [156]. According to the calculation based on the physical sputtering process, the amounts of eroded carbon were $\sim 4.98 \cdot 10^{22}$ during H_2-GDC and $\sim 2.12 \cdot 10^{23}$ during He-GDC operations. These amounts correspond to the total material eroded weight of 5.2 g [156].

A small part of the eroded material was found redeposited in the form of stripes on the plasma vessel wall behind the Cu–Cr– Zr support plates for carbon tiles of the heat shield (Fig. 3.25). The edges of the stripes are relatively sharp, with widths of less than 1 mm, and its total area is $\sim$ 3.23 m^2. It is a clear indication of the erosion and redeposition processes during GDC application (see Sec. 4.2.4.2). The possibilities of migration at this location by ECRH plasma ions and the impact of neutrals are almost negligible [156]. The analysis of the redeposited material on one of the tag number plates (Fig. 3.25a) shows that the total carbon deposition in the stripes behind the tiles is 0.1 – 0.3 g [214].

Another problem is related to the damage of the metallic surfaces. Around 300 arc traces were found on various metal PFCs after OP1.2b [156, 214, 215]. A considerable number of the trails appeared in the non-plasma exposed region. Broad arc trails appeared on the surfaces of diagnostic ports and mirrors (Fig. 3.26). Most trails had no clear linearity expected in the presence of a magnetic field, indicating that arcing initiated during the glow discharge cleaning phase operated without a magnetic field [215].

Similar problems were observed in LHD, where helium GD caused microscopic damage in metallic PFCs exposed to GD, leading to redeposition of impurities that originated from the sputtering of the first wall [216].

Both issues require to be mitigated by the further development of the GDC procedures. It includes optimizing glow discharge parameters and durations and studies of assisted break-down igniting the discharge at lower pressures.

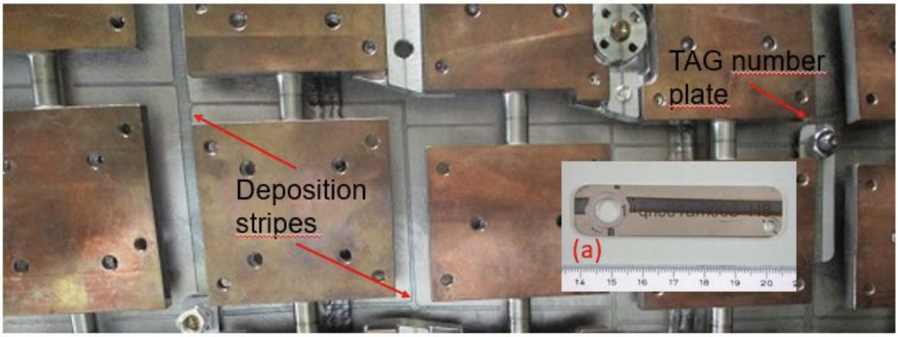

Figure 3.25: Deposition stripes formed the plasma vessel wall by material deposition through the gap between the graphite tiles. Inset a) shows a tag number plate mounted on the wall, removed for the analysis [156].

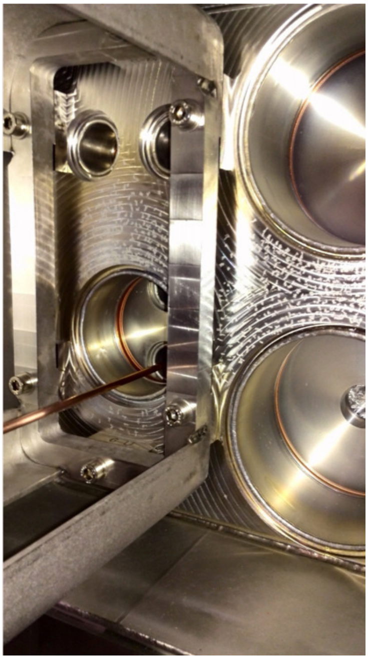

Figure 3.26: The traces of arcs in the Port AEE41 found during the post-operation W7-X in-vessel components inspection after OP1.2a.

Table 3.5: Overview of boronization procedures in OP1.2b.

Parameters	$\mathbf{1^{st}}$	$\mathbf{2^{nd}}$	$\mathbf{3^{d}}$
Active coating phase	3.5 h	5.5 h	5.0 h
Amount of gas	45 mbar · l	84 mbar · l	68 mbar · l
Estimated thickness of boron layer*	10.5 nm	24.1 nm	18.3 nm

* the thickness is estimated (Eq. 2.34), assuming that all injected boron ends up on the PFCs and forms a pure amorphous boron layer with a density of 2.4 g · cm^{-3}.

3.3.6 Boronization

The main aim of boronization in W7-X was to reduce oxygen radiative and sputtering activity by minimizing its amount in plasma. Due to the complexity of the procedure, the application of boronization became available only in OP1.2b.

3.3.6.1 The boronization procedure

The boron coating in W7-X is applied by a GD in the mixture of diborane and helium with a proportion of 10:90. According to technical and safety constraints, only 2 pumping stations (6 turbopumps in total) are available during boronization (see Sec. 3.1.1.4). The dry GD (anode current of 1 A) test in helium (without diborane) has defined that the average pressure level of $\sim 4 \cdot 10^{-3}$ mbar at the maximum available pumping speed allows achieving the maximum coating efficiency and the speed of the boronization procedure in the used system configuration (see Sec. 3.1.1.5).

The first boronization procedure was carried out three weeks after the beginning of the plasma operation. After the first boronization, W7-X was exclusively operated with hydrogen. Helium GDC was no longer applied to avoid enhanced sputtering of the boron layer.

In total, three boronizations with time intervals of one month were applied in OP1.2b. The details of the boronization procedures are summarized in Table 3.5.

The glow discharge for each boronization was ignited in pure helium with a current of 1 A. The parameters of the break-down are given in Fig. 3.23b. When the pressure level reached $\sim 4 \cdot 10^{-3}$ mbar and the discharge was stabilized, helium was gradually changed by diborane. Each procedure was followed by $\sim$ 20 - 30 minutes He-GDC to crack the remaining diborane molecules and desaturate the wall from hydrogen.

The process of boronization was optimized from session to session. During the first boronization, the diborane alarm, caused by the signal saturation of the diborane sensors behind the diborane crackers in the gas exhaust system, led to a halt of diborane injection (Fig. 3.27a). The glow discharge had to be terminated. It caused a delay before the subsequent continuation procedure with a reduction of the active coating phase. Later on, it was found that hydrogen, which is also produced during the diborane decomposition in the GD, also triggers the sensors by saturating the received signal.

Based on the first boronization experience, the process of the second boronization was organizationally modified (Fig. 3.27b). To avoid reaching the alarm threshold, only one pumping station (three TMPs) was used while the other could recover from the diborane exposure. Switching between the pumping stations could only be done manually via the local control. This strategy allowed to avoid triggering an alarm and, thus, the process to be aborted.

For the third boronization, new sensors were installed that are insensitive to hydrogen. It helped to mitigate the problem and helped to accelerate the process significantly allowing to use two pumping stations simultaneously. However, another challenge took over, which related to the glow discharge instability. The reason for the unstable behaviour is the high flow resistance of the thermal diborane decomposers in the exhaust air of the vacuum pumping stations. As a result, pressure behind the turbopumps rises, leading to a backflow of hydrogen exhaust gas into the plasma vessel and destabilizing the glow discharge as an additional gas source.

As a countermeasure, for the third boronization, the number of active TMPs was reduced from a possible six to two (one per pumping station). It allowed to stabilize the process, but at the expense of the efficiency of the coating, since the diborane throughput was significantly lower with a coating duration comparable to that of the 2nd boronization (Fig. 3.27c).

Thus, the troubleshooting and different procedure optimizations led to the different durations and average boron coating thickness (Table 3.5).

To conclude, the higher efficiency of the process requires an increase in the pumping capacity of the vacuum system, i.e. equipping additional pumping stations with the corresponding diborane decomposers.

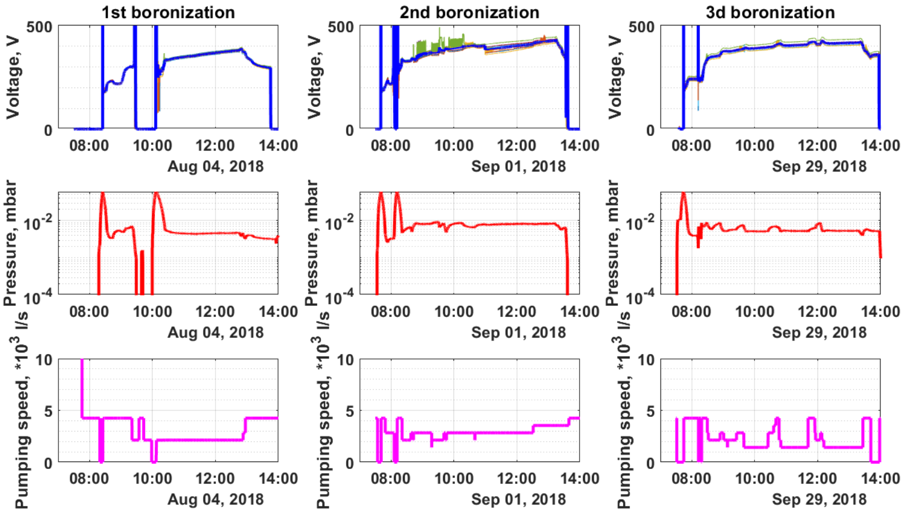

Figure 3.27: Overview of the boronization procedure. a) 1st boronization (04-Aug-2018), b) 2nd boronization (01-Sep-2018), c) 3d boronization (29-Sep-2018).

3.3.6.2 Impact of boronization on impurity sources and plasma performance

The major part of the boronization impact on wall conditions and plasma performance is amply described in [217, 218]. However, to provide a comprehensive picture of the boronization influence on the overall wall conditioning studies on W7-X, the most important results of boronization outcome are also presented in this section.

The comparison of the residual gas content before and after the first boronization is shown in Fig. 3.28. The recording of the QMS spectra was done one day prior and two days after the boronization procedure. The most noticeable change is a significant suppression of helium outgassing. The intensity of the helium signal dropped by ~ 2 orders of magnitude, remaining as a barely noticeable peak slightly above the noise level. At the same time, the partial pressures of water, carbon oxide and methane had only a slight decrease. The rest of the dominating outgassing species did not undergo any changes. The latter indicates that the pumping duct and other remote areas mainly contribute to the remaining impurity outgassing after applying the initial and regular wall conditioning procedures and cannot be a subject of further impurity removal.

To properly evaluate the impact of boronization on plasma performance, a series of hydrogen reference discharges were executed before and after

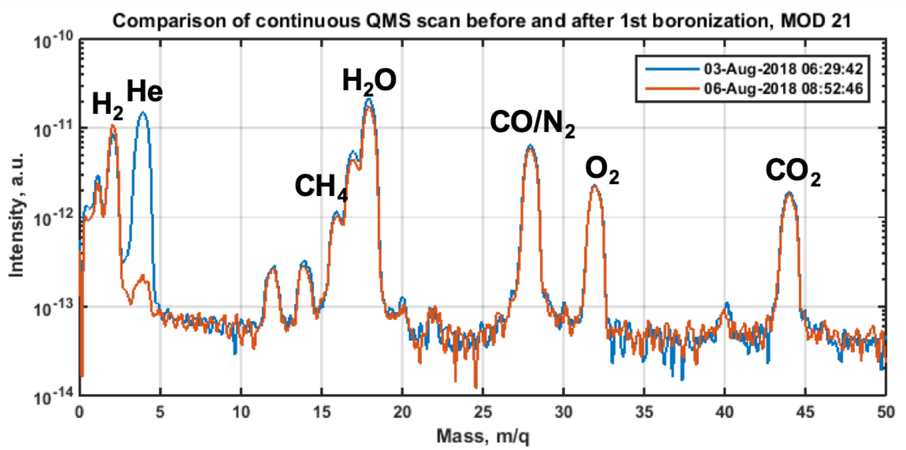

Figure 3.28: Comparison of the residual gas content (by QMS) before (solid blue line) and after (solid red line) the first boronization procedure.

the boronization procedure. There were two types of reference discharges, schematically shown in Fig. 3.29. Both types of reference discharges were initially performed in the standard magnetic field configuration.

The "Power steps" reference discharges were also used daily at the beginning of plasma operation. However, the magnetic field configuration for these discharges was the same as for the experimental program of that day.

To estimate the achievable density limit, the "Density ramp" discharges were explored. The comparison of these discharges before and after the first

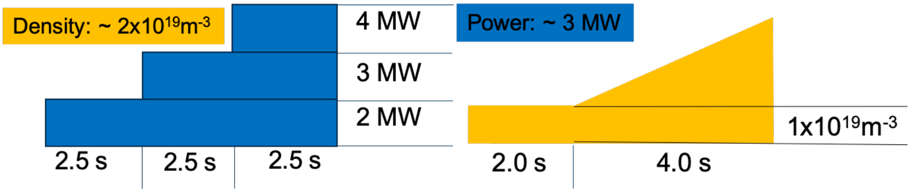

Figure 3.29: Schematic representation of the boronization reference discharges. a) "Power steps" reference discharges with constant density and a stepwise increase of the ECRH power, b) "Density ramp" reference discharges with the constant ECRH power and gradually raising density until the plasma collapse.

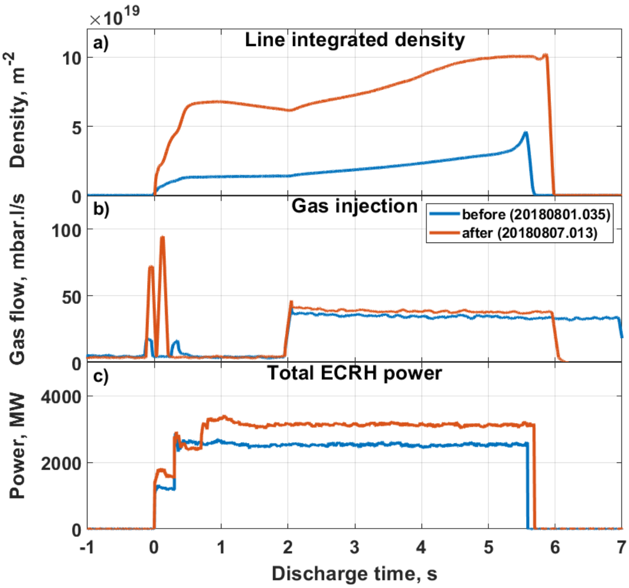

Figure 3.30: "Density ramp" reference discharges before and after the first boronization [213].

boronization is presented in Fig. 3.30.

The reference discharge performed before the boronization was terminated by a radiative collapse reaching an average density value of $2.3 \cdot 10^{19}$ m^{-3}. The corresponding discharge after the first boronization successfully passed, achieving an average density of about 10^{20} m^{-3}. Thus, as seen in the following physics program, boronization significantly extends the plasma operation window. It made it possible to perform stable hydrogen discharges in the density range from $1 \cdot 10^{19}$ m^{-3} to more than $1 \cdot 10^{20}$ m^{-3}, determined mainly by the density limit defined by a plasma heating scheme in use.

The significant improvement of the plasma performance is due to reduction of oxygen, the primary energy radiator, and, subsequently, oxygen-based impurities. The outgassing QMS spectra of the same reference discharges show that carbon oxides and water production was significantly decreased by the first boronisation (Fig. 3.31). The comparison of the outgassing curves was made by taking an average ratio between integrals of the outgassing curves after the discharge termination and the outgassing peak values. Thus, according to the calculations, the amount of CO was decreased by a factor of 9.3 ± 0.9 while the CO_2 outgassing dropped by a factor of 2.7 ± 0.7. The water outgassing was only reduced by a factor of 1.7 ± 0.2. It should be noticed that, in the case of partial water pressure

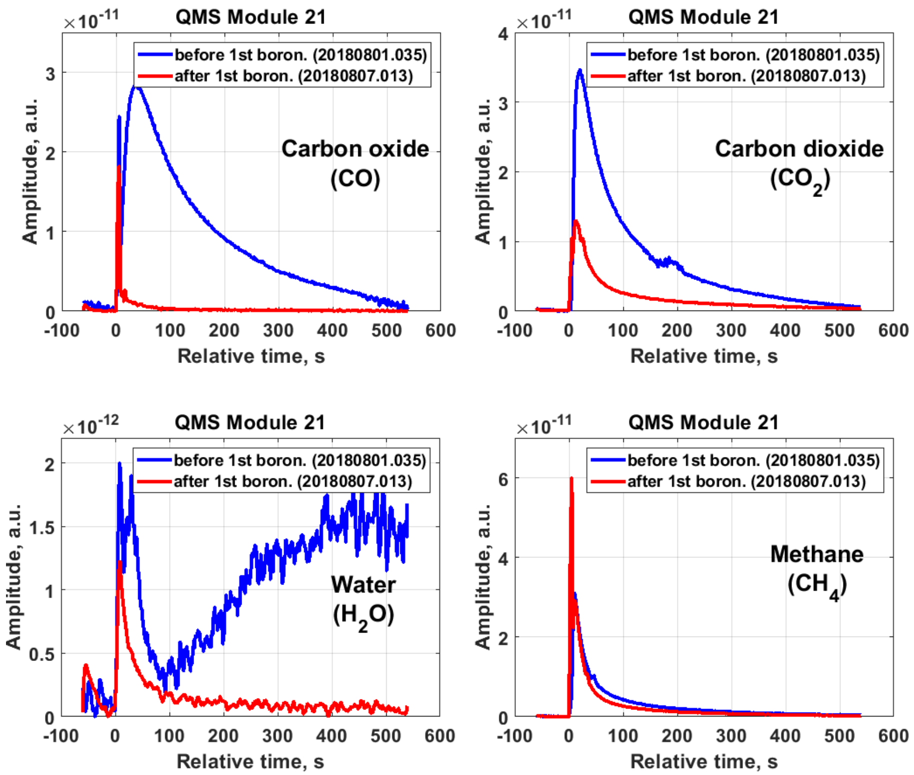

Figure 3.31: Partial pressures of carbon- and oxygen-based impurities before (blue lines) and after (red lines) the first boronization calculated from QMS recorded data [210].

in the pre-boronization reference discharge, the strong water release at the relative time of ∼ 100 s was due to a high temperature of some divertor plates. According to the divertor thermocouple measurements, the maximum temperature exceeded a value of ∼ 650 °C. It led to the water release from the deep layers of fine-grain graphite [209]. The same effect was also observed at specific conditions in OP1.2a (see Sec. 3.3.3).

A different situation can be observed for CH_4 partial pressure. Methane outgassing has almost no changes due to the wall coating by boron, meaning that methane production has an origin insusceptible to boronization-relevant processes. It should be kept in mind that the intrinsic CH_4 was mainly produced at the strike line and deposition region even after boronization in W7-X [209]. In contrast, the formation of carbon oxides during plasma discharges is mainly a result of the graphite PFC erosion caused by oxygen chemical sputtering [219]. The latter means that boronization, by reducing oxygen

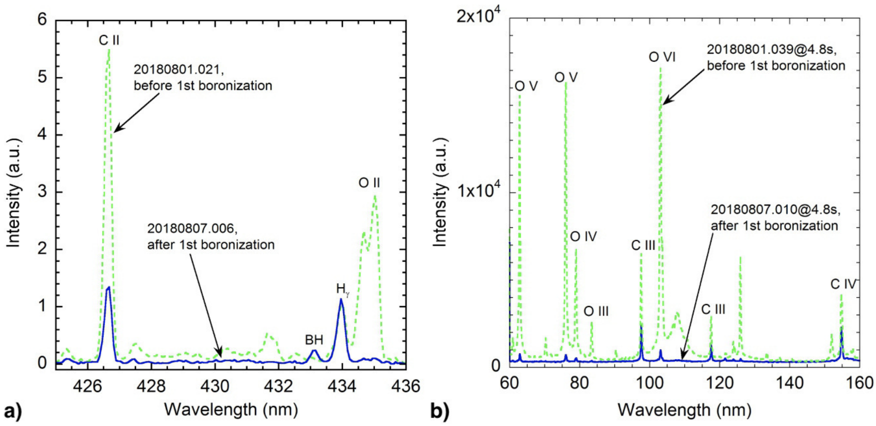

Figure 3.32: Impact of a boronization on the impurity content in (a) the divertor (divertor overview spectrometer), normalized to H-gamma emission, and (b) core plasma (HEXOS) [163, 209].

content, also helps to decrease the amount of carbon in the plasma and mitigate subsequent self-erosion of graphite PFCs by released carbon. It can be proven by the dramatic drop of oxygen and carbon levels observed in the divertor region and the plasma core after the first boronization. Fig. 3.32a shows the emission spectra of singly ionized oxygen and carbon, representing the divertor impurity sources, for reference discharges with similar plasma conditions and magnetic configuration. The corresponding oxygen characteristic line almost disappeared in the post-boronization discharge while the intensity of the carbon line was reduced by $\sim$ 75 % [209]. The carbon and oxygen content in the plasma core, recorded in another couple of reference discharges by HEXOS (Fig. 3.32b), also experienced a dramatic reduction showing similar behaviour of the impurity concentration. According to the spectra comparison, one can see a significant suppression of the oxygen ion emission in the plasma core. The line radiation produced by carbon ions in the core dropped by 2 - 3 times.

The overall boronization effect in the second divertor campaign can be presented as 2D maps of several discharge parameters (Fig. 3.33) [38]. The figure contains the summary of all OP1.2b discharges in the standard magnetic field configuration. Fig. 3.33a shows the oxygen emission plotted versus carbon radiation normalized by hydrogen radiation of the corresponding discharges recorded by CXRS.

The first boronization decreased the oxygen influx at the divertor by a factor of 8. Corresponding carbon influx was reduced by order of magnitude.

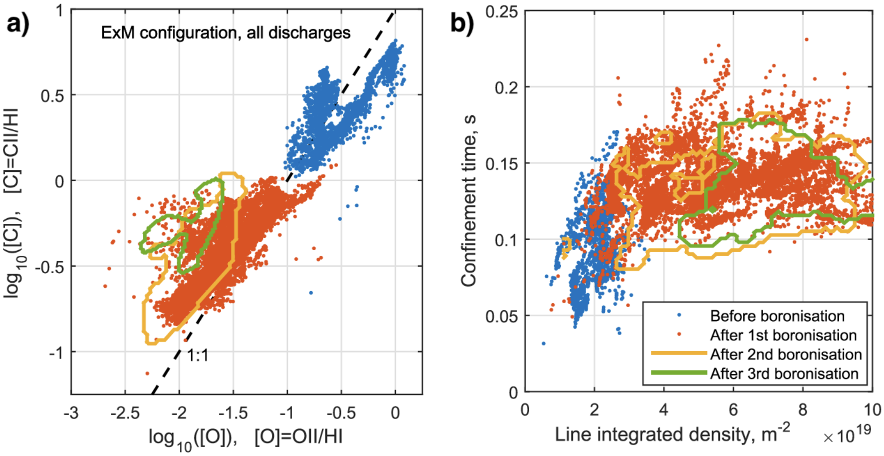

Figure 3.33: W7-X data samples from all discharges in the standard configuration (E×M) of the second divertor campaign OP1.2b, separated by three boronizations. a) oxygen and carbon radiation normalized by hydrogen radiation from passive spectroscopy viewing the W7-X divertor, b) line integrated plasma density and confinement time [38].

Subsequent boronizations facilitated further oxygen content decrease.

Fig. 3.33b contains the information about correlations of the density and plasma confinement times connected to the boronization events. According to this figure, the operational density range increased by a factor of 4. As a result of the higher density, plasmas also exhibited increased confinement times by a factor of 2 [158]. The overall changes also led to the plasma purity improvement. Thus, the values of Z_{eff} decreased from values of around 4.5 for all densities down to low values of approximately 1.2 [217].

In contrast to the rough calculation of the pure boron layer thickness given in Table 3.5, the deposited layer is a B/C-H layer, and its average thickness could reach 100 nm. This assumption is based on the experience of TEXTOR and W7-AS with similar boronization conditions in [137, 220]. Moreover, the deposited boron layer is always subject to erosion and redeposition processes during the plasma operation. For example, post-mortem analysis of a sample taken from the divertor target element TM2h6 located in a net-deposition zone shows carbon, oxygen, boron and iron content in the deposits, with a maximum observed layer thickness of 8 μm [163, 217]. Thus, the B deposition results from multiple erosion/deposition processes and intense net deposition at the analyzed location.

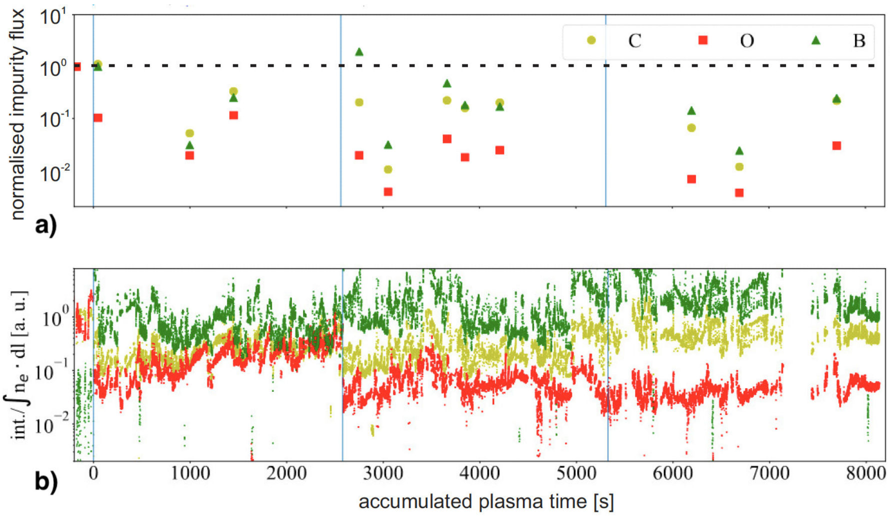

Figure 3.34: Time evolution of oxygen (*OI* at 844.5 nm), carbon (*CII* at 426.7 nm) and boron (*BII* at 703.1 nm) over the plasma time in OP1.2b: a) normalized influx from a divertor source deduced from divertor spectroscopy ("Power steps" reference discharges), b) Long-term evolution of C (*CVI* at 3.374 nm), B (*BV* at 4.859 nm), O (*OVI*at 103.221 nm) core content (HEXOS) normalized to the line integrated density [217]. Blue vertical lines indicate boronization events.

The boronization has a temporal effect on the plasma performance improvement in the majority of the fusion devices. The PFC region most prone to erosion corresponds to the plasma-wetted areas. In the case of W7-X, the study shows that the boron layer at the strike lines on the divertor target is eroded within $\sim$ 59 s of the total plasma exposure time, which corresponds to the $\sim$ 15 discharges with 7.5 s duration, 2 – 4 MW of the ECRH heating power and a plasma density of $\sim 2 \cdot 10^{19}$ m^{-3} [38, 217]. Thus, the boron layer is eroded with an erosion rate of about 0.25 nm/s until a relatively low level which is further kept by a balance between erosion and redeposition processes. The latter was deduced from the divertor spectroscopy observation (Fig. 3.34).

The erosion rate at the main wall is much lower. That can be deduced from the temporal evolution of the B, C and O edge and plasma core emissions, as shown in Fig. 3.34. According to the given data, every subsequent boronization decreased the oxygen level even further due to the appearance of new boron layers. O and C plasma core concentrations did not show a significant increase between boronization events. Moreover, the oxygen level did not reach pre-boronization values meaning that the boronization effect has not deteriorated even after the protective boron layer was eroded from the divertor at the locations of strike lines. Thus, the long-lasting impact of boronization is provided by the gettering of oxygen on the recessed PFC areas.

To conclude, the positive impact of boronizations on the wall conditions in W7-X can be separated (i) in a short-term effect related to the strike-line location and limited due to fast re-erosion of the B layer under high ion flux impact, and (ii) a long-lasting effect related to the first wall and limited by re-erosion due to the low impinging ion and charge-exchange flux [163]. The second point means that extending the inter-boronization period (> 2400 s) may be possible without compromising the high plasma performance at similar plasma operation conditions.

3.3.7 Boron powder injection experiments

The results of boronization studies conclude that there was no significant degradation of plasma performance between subsequent boronizations indicating an effective coating lifetime being more than 2400 s of total plasma time. Aiming to perform regular discharges with a discharge length of 1800 s in future experimental campaigns create a new challenge for maintaining high plasma performance. This duration is indeed similar to the demonstrated coating lifetime. An extensive physics program containing long-pulse discharges may hence wear off the effect of boronization over one or two operation days.

Thus, it is proposed to introduce boron particulates into W7-X discharges to extend the coating lifetime and maintain overall plasma performance. Boron dropper experiments in OP1.2b were intended to provide a first estimation of the effectiveness of an Impurity Powder Dropper (IPD), discussed in 2.3.2, as an alternate means of wall conditioning for W7-X. Indeed, a boronization, performed via glow discharge, provides the ability to getter oxygen over the entire internal volume of the plasma vessel. In contrast, the injection of boron-containing powder in the plasma edge is anticipated to replenish only the boron coating at high fluence plasma surfaces such as limiters and divertors due to preferential transport in plasmas.

An installation of a full powder dropper on Wendelstein 7-X stellarator (W7-X) turned out to be impossible in OP1.2 due to a series of technical and time constraints. As an alternative to IPD, a periodic particle injection source named the Probe Mounted Particle Injector (PMPI) [221] was installed on the W7-X Multi-Purpose Manipulator (MPM) [222]. The major difference between the operation principle of the IPD and PMPI is to provide a horizontal injection instead of a gravitational one. At regular operation, this can provide a pulsed injection with every 350 ms allowing the majority of the powder delivered within 12 - 18 cm from the vessel wall with a maximum horizontal throw of 25 cm. Boron carbide (B_4C) was selected as an injection medium because the carbon atoms within the crystalline lattice act like a graphite lubricant maintaining the particulate flow without clump formation.

To evaluate plasma response to the powder injection and any effects on plasma performance, a series of 100 μm diameter B_4C granules were injected into several plasma discharges [221]. The powder quantities varied from approximately 1 mg/pulse to 30 mg/pulse. The total boron amount of about 2.0 g was introduced via the PMPI. The front face of the PMPI was located between 20 and 5 cm from the nearest island scrape-off layer. To provide the powder's longest horizontal throw, the injection frequency of 2.8 Hz was maintained throughout plasma discharges. Thus, a radially injected granule could penetrate $\sim$ 5 cm into the discharge.

The full description of the boron powder injection experiment and its influence on the plasma performance were reported in [223]. The most representative example of the boron powder injection experiment was 20180927.047. The ECRH power was set at 4 MW starting from the plasma density level of $\sim 5 \cdot 10^{19}$ m^{-3}. The discharge length of 6.5 s allowed a direct comparison of the effects of multiple injection quantities on plasma behaviour within the same discharge. There were three groupings of injection covering the ranges of 1- 10 mg/injection in the period of 2.5 - 3.5 s, 10 - 20 mg/injection between 3.5 s and 5 s and more than 20 mg/injection from 5 s to 6.5 s.

Overall, injected impurities are observed to enter the confined region of the discharge. It is evidenced by an increase in overall radiated power as well as increases in plasma density. Effective plasma charge (Z_{eff}) and HEXOS spectroscopic data were used to determine a wall conditioning effect and plasma response, as shown in Fig. 3.35.

For the small injections between 2.5 s and 3.5 s, the plasma parameters can return to an initial state between injections because the introduced impurity flushing is mainly completed in this interval. The period of medium quantities injection is characterized by the increase of Z_{eff} from $\sim$ 1.3 at the beginning of the discharge to a value of $\sim$ 2. For injections larger than 20 mg/pulse, the value of Z_{eff} is increased to an average of 3.5 with oscillations caused by fast-subsequent flushing of a large amount of impurities. The oscillations continue throughout the injection sequence until the final injection triggers a radiative collapse at 6.2 s. The latter indicates a limit of the injected material amounts by the PMPI.

The observation of the boron, carbon and oxygen levels in the plasma

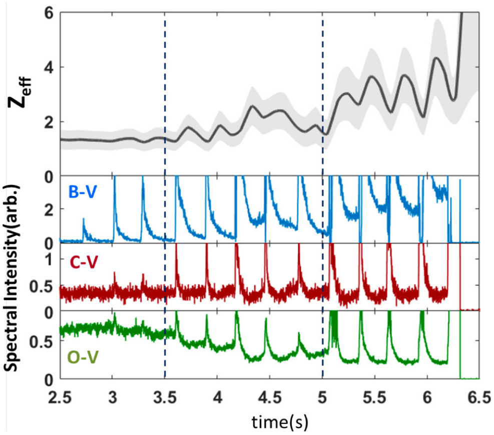

Figure 3.35: Evolution of effective nuclear charge (Z_{eff}) and boron, carbon and oxygen concentrations, shown by characteristic ion emission lines (BV at 4.859 nm, CV at 4.027 nm and OV at 62.977 nm), in the plasma core during 20180927.047 [223]. Vertical dark blue dashed lines separate injection groupings.

core gives the following. There is an expectable general increase in the boron signal correlating to the injection quantity increases. However, there is no corresponding increase in the carbon baseline level, which is also a part of the powder. A decrease is observed in the overall oxygen signal intensity once the pulsed impurity injections begin. The oxygen level at the end of the discharge (before the radiative collapse) is less than its original value by a factor of ~ 2. It indicates a positive effect of the wall conditioning effect.

Nevertheless, according to [223], a determined positive impact of the boron-containing powder injection on wall conditions is inconclusive. Only the fact that the operation of the PMPI did not have any adverse influence neither on the overall wall conditioning nor on subsequent plasma discharges can be certainty stated. It can be explained by the fact that the effect of standard boronization did not degrade significantly during experimental operations. It means that an effective deposition layer on the plasma-facing components limits the visibility of the impact of any additional material deposition.

In conclusion, a dedicated set of experiments in a previously un-boronized device is needed to adequately assess powder injection effects by the PMPI on wall conditioning.

3.3.8 Electron Cyclotron Wall Conditioning

First ECWC experiments in OP1.1 showed that single ECRH discharges could not replace the GDC for initial wall conditioning [70]. However, in OP1.2, ECWC turned out to be the only available technique that worked in the presence of the magnetic field. This fact urged further development and optimization of this technique for fuel recycling control. As a result, ECWC became a suitable tool for wall conditioning in W7-X during the experimental days when the magnetic field was ramped up.

Unlike in tokamaks, the W7-X ECRH conditioning plasmas are fully-ionized diverted plasmas due to magnetic field islands with nested surfaces intersected by the divertor targets. In contrast to the strong interaction in the divertor, ECRH plasma in W7-X reveals weak interaction with the main wall [38]. Thus, the main conditioning effect of ECWC in W7-X is related to the cleaning of the divertor area. It is particularly suitable for recycling control from the divertor but less appropriate for controlling impurity and fuel influx from the main wall.

The development, study and main parameter optimization of the ECWC started in OP1.2a. Due to boronization applied in OP1.2b, the technique could be more refined for the particular needs of plasma density control by extending the operational parameter window and applying additional mechanisms for a conditioning efficiency improvement.

3.3.8.1 Study and development of ECWC in OP1.2a

Initial exploration of ECWC in W7-X

Due to a dense experimental program in OP1.2a, the lack of time to ramp down the magnetic field for GDC, and the absence of other wall conditioning methods that could be applied in the presence of the magnetic field, the development of He ECWC methods was a necessity. As part of this PhD, the technique was optimized into a routine tool for density control, impurity release reduction and recovery of the plasma conditions after radiative collapses. At first, two competitive types of He ECWC were developed during OP1.2a: (i) so-called “single He recovery discharges”, single long (up to 10 s) discharges in helium at low density and medium heating power (up to 3 MW) and (ii) so-called ”pulse trains”, sequences of short low to moderate power (up to 2.5 MW) discharges (up to 3.5 s) with a fixed duty cycle. The scheme of a typical pulse train is shown in Fig. 3.36 for better representation.

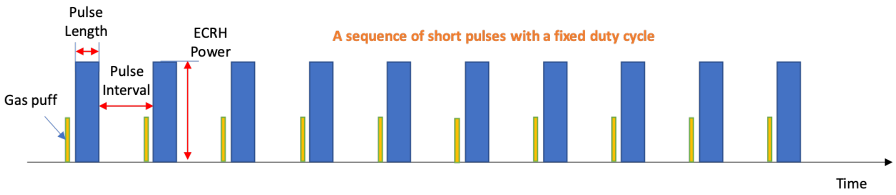

Figure 3.36: Scheme of a pulse train. The main parameters of the pulse train are the pulse length, the pulse interval, the ECRH input power, and the gas prefill.

Recovery discharges

In the case of the first ECWC type, recovery discharges, these were often piggy-backed for physics experiments in helium. The typical discharge length was from 2 s to 10 s, and its energy could reach 30 MJ. A comparative analysis of fuel removal has been done to optimize the cleaning efficiency of the recovery discharges. In order to compare the ECWC cleaning efficiency, the cumulated amount of removed fuel (hydrogen partial pressure) is used as a primary criterion. Additionally, the outgassing curve of the average neutral pressure is used to show the difference in the total amount of released gas. The most successful examples of removal by recovery discharges are given in Fig. 3.37.

According to the results of fuel removal analysis, the most effective recovery discharges applied for wall desaturation from hydrogen and density control are 10 s recovery discharges with a heating power of 3 MW. Another critical point of the comparison is that the recovery efficiency of this type of ECWC depends not only on discharge duration and input power. The fuel removal is also strongly correlated with the wall loading and the temperature of PFCs. It is also demonstrated in Fig. 3.37. Here, a 3 s recovery discharge with input energy of ~ 9 MJ removes three times more hydrogen than a 5 s discharge with more than three times more input energy which is unexpected based on results that will be shown later. According to the OP1.2a operation experience, the single He recovery discharges using high power of more than 3 MW are more prone to a radiative collapse.

Pulse trains

The main idea behind the pulse train concept is to reduce the probability for the migration and redeposition of released fuel and impurities during the conditioning discharge, as described in Sec. 2.2.3. The ratio between removal

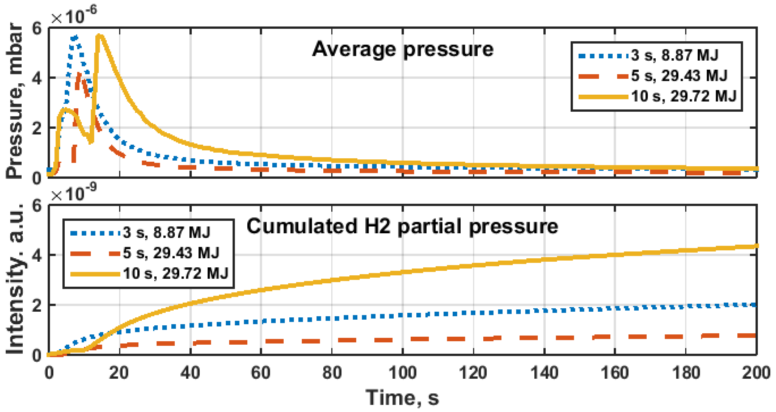

Figure 3.37: Comparison of average neutral gas pressure and cumulated hydrogen partial pressure (QMS) for 3 s recovery discharge 20171121.033(dotted blue line), 5 s recovery discharge 20171109.053 (red dashed line) and 10 s recovery discharge 20171121.013 (solid yellow line) [211].

and redeposition is usually higher for long pulses at the same plasma parameters (see Eq. 2.32). The short pulse length, together with the pulse interval time, which is sufficient to evacuate the outgassed species from the vessel (up to three times longer than the characteristic pumping time), allow to pump down more released fuel and other species, making the subsequent plasma discharge less contaminated. Thus, the conditioning efficiency increases.

The typical pulse train has ten discharges in the pulse sequence. It was found that this number of discharges is optimal time-wise, keeping a balance between pulse train program loading (by the central control system), execution and the necessity to repeat the same cleaning routine several times. As shown in Fig. 3.36, pulse trains can be characterized by the pulse length, pulse interval, ECRH input power, and gas prefill. The latter is the amount of gas injected at a defined duration and constant gas flow of 75 mbar · l/s. For all discharges in a pulse train, the gas prefill is started 100 ms prior to the discharge ignition.

The first experiments dedicated to pulse train optimization were carried out at the beginning of OP1.2a. Following the main experimental program, the experiment was done in the High Mirror (KJM) magnetic field configuration. Three gyrotrons were constantly used at reduced power to produce and heat the conditioning plasma to obtain a reliable execution. The optimization range of the discharge input power was chosen between

1.5 MW and 2.2 MW. Firstly, these power levels provided a reliable discharge breakdown. Secondly, the power increase allowed to achieve more significant particle and heat fluxes towards the divertor. Moreover, it was done for a proof of principle for the divertor conditioning by ECWC in stellarators. The latter was considered for future application in other fusion devices.

The optimization compared the hydrogen removal for different He pulse train scenarios. Only one parameter was varied between several pairs of pulse trains. The hydrogen partial pressures were normalized to the removal of the first pulse in the sequences to correct for the varying wall loading throughout the experiment. The results of this comparison are shown in Fig. 3.38, plotting the integrated hydrogen pressure for each procedure.

The first part of the parameter optimization was dedicated to the discharge power. Two helium pulse trains with discharge input power of 2.1 MW and 1.6 MW were compared. Both pulse trains had the same pulse length of 1.5 s, a pulse interval of 30 s and a gas prefill of 25 ms. Fig. 3.38a shows the corresponding cumulated hydrogen removal. The hydrogen removal is higher in the case of the pulse train with higher input power. It is understood from the increased plasma density and divertor fluxes at higher power causing higher fuel release.

The second optimization parameter was the pulse length. The fuel removal efficiency comparison of pulse trains with the pulse length of 0.75 s and 1.5 s is given in Fig. 3.38b. The result demonstrates that the extension of the pulse length increases the fuel removal rate by a factor of 1.6. The dependence of the fuel removal on the pulse length is supposed to be non-linear due to the re-ionization and the released fuel redeposition. This assumption required additional studies. It must be noted that a further extension beyond $\sim$ 2 s of the pulse lengths in OP1.2a increased the risk of a radiative collapse during the pulse train execution and its subsequent abortion.

The results of experiments dedicated to the gas prefill variation are shown in Fig. 3.38c. A reduction of the injected amount of helium, corresponding to the change of the injection time from 25 ms to 15 ms, results in a slight improvement of hydrogen removal. Further decrease of the gas prefill down to 10 ms leads to the problem of achieving a reliable discharge break down because the injected amount of gas is not sufficient.

To complete the first pulse train optimization experiments, the variation of the pulse interval was also studied. Two pulse trains with pulse intervals of 30 s and 60 s were compared (Fig. 3.38d). The pulse train with the 60 s pulse interval was applied before one with the pulse interval of 30 s. No additional wall loading by hydrogen was done between these two pulse trains. Reducing the pulse interval down to 30 s allows increasing

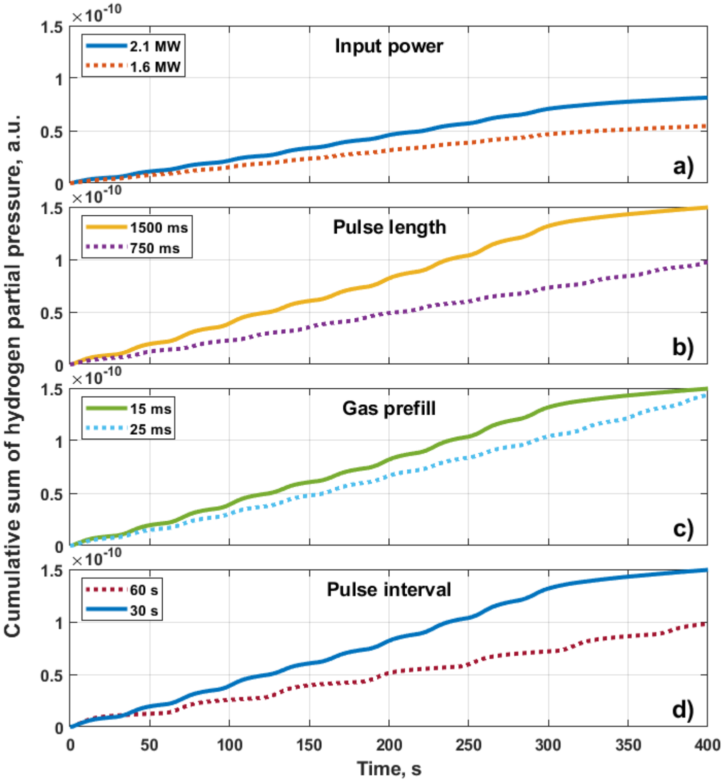

Figure 3.38: Comparison of pulse train cleaning efficiency represented by the removed amount of fuel (integrated QMS hydrogen partial pressure) by variation of: a) input power, 20170913.50 (2.1 MW) – solid line and 20170913.51 (1.6 MW) – dashed line, for both experiments the following parameters: pulse length is 1.5 s, pulse interval is 30 s, gas prefill is 15 ms. b) pulse length, 20170919.8 (1500 ms) – solid line and 20170919.9 (750 ms) – dashed line, for both experiments the following parameters: input power is 2100 kW, pulse interval is 30 s, gas prefill is 15 ms. c) gas prefill, 20170919.8 (15 ms) – solid line and 20170919.10 (25 ms) – dashed line, for both experiments the following parameters: input power is 2100 kW, pulse interval is 30 s, the pulse length is 1.5 s. d) pulse interval, 20170919.6 (60 s) – solid line and 20170919.8 (30 s) – dashed line, for both experiments the following parameters: input power is 2100 kW, the pulse length is 1.5 s, gas prefill is 15 ms [211].

the removal rate by a factor of $\sim$ 1.6. The analysis shows that a 30 s pulse interval is enough to pump down the major part of the released hydrogen and other light impurities (m/q <16). Moreover, the extension of the discharge sequence by adding more discharges will not suffer from the accumulation of the released product mentioned above. In the case of heavy impurities, its accumulation can be compensated by the pump down in the post pulse train period. The usual interval between the program execution is more than 5 minutes. The main advantage of the pulse interval reduction is a corresponding decrease of the total pulse train execution time attaining a given fuel removal efficiency. Further pulse interval reduction studies were continued in OP1.2b (see Sec. 3.3.8.2).

To summarize the results of the first optimization studies, the optimum pulse train scheme for OP1.2a was pulse length of 1.5 s, a pulse interval of 30 s and an input discharge power of 2.1 MW. Moreover, to support discharge break down, the input power was slightly higher (up to 2.5 MW) for the first 50 ms of each pulse. The gas prefill with a duration of 15 ms should start 100 ms prior to the discharge initiation with the constant gas flow of $\sim$ 75 mbar $\cdot$ l/s. An example of the successful application of the optimized pulse trains during the high-density hydrogen plasma studies in OP1.2a is shown in Fig. 3.39. According to the data, the plasma density, hydrogen partial pressure, divertor hydrogen, oxygen and carbon fluxes decrease from discharge to discharge, showing the progress of wall conditioning directly.

Comparison between recovery discharges and pulse trains

The concluding step of the ECWC development in OP1.2a was a comparison of the most efficient single recovery discharges and the optimized pulse trains. Average neutral pressure and the cumulated hydrogen removal of two 3 MW 10 s recovery discharges and one optimized pulse train are shown in Fig. 3.40. In order to make a proper comparison of these ECWC methods, all experiments were carried out in similar operation conditions (the standard magnetic field configuration).

The efficiency comparison shows that the most efficient 10 s single recovery discharge with an input power of 3 MW could remove only 50 % to 75 % of hydrogen compared to the optimized pulse train. These single recovery discharges required a longer time to prepare the gyrotrons in use for the subsequent discharge. Even if one could use different gyrotrons in every subsequent discharge, the high probability of a radiative collapse during the discharge execution remained a severe problem. To achieve the required fuel removal result, it was necessary to perform 2 - 3 single recovery discharges in a row making these types of ECWC operational time consuming due to the

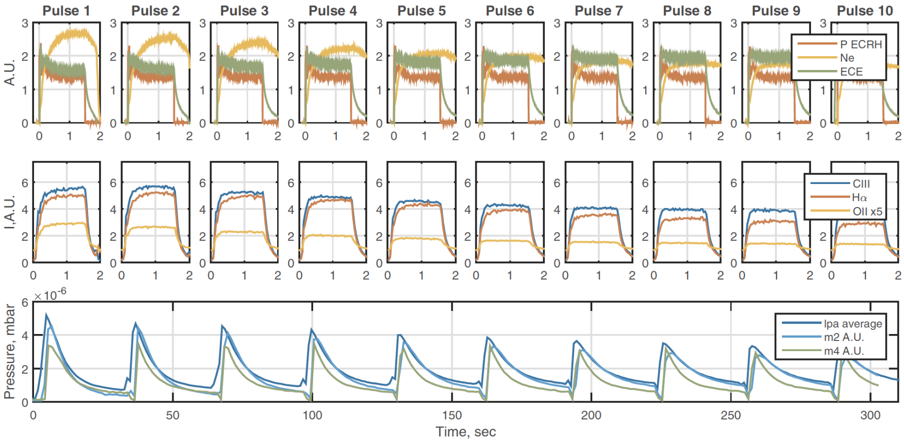

Figure 3.39: ECWC pulse train 20171121.39 consisting of 10 pulses of 1.5 s at an input power of 2.1 MW with 30 s pulse interval. Ongoing recovery is apparent from interferometry density, ECE temperature, CXRS for hydrogen (H_α), carbon (*CIII*) and oxygen (*OII*) characteristic lines intensity, average neutral pressure and partial hydrogen (m2) and helium pressures (m4) (QMS) [207].

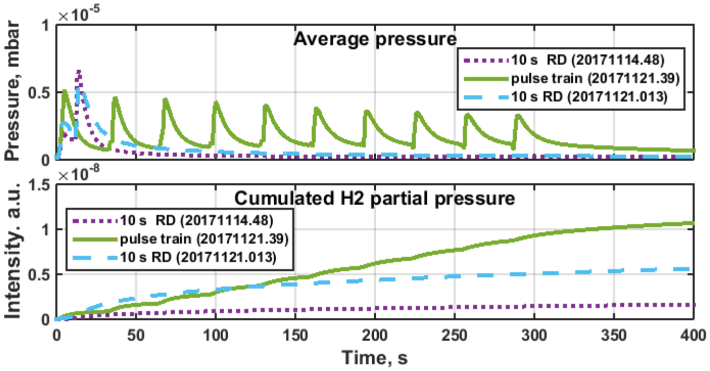

Figure 3.40: Comparison of average neutral gas pressure and cumulated hydrogen partial pressure (QMS) for 10 s single recovery discharge (RD) 20171114.048 (purple dotted line), pulse train 20171121.039 (solid green line) and 3 MW 10 s single recovery discharge 20171121.013 (blue dashed line) [211].

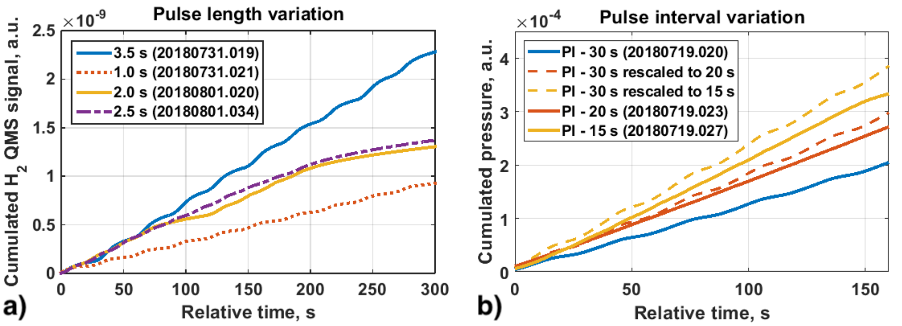

Figure 3.41: He pulse train optimization by variation of the pulse length (a) and pulse interval (b) in OP1.2b. The cleaning efficiency is shown by cumulated hydrogen removal calculated from the partial pressure measurements of the QMS. Relative time equal to 0 indicates the beginning of the first pulses. The dashed lines on the right figure show the predicted hydrogen removal for 30 s pulse intervals rescaled to pulse intervals of 20 s and 15 s [210].

increase of the discharge preparation, execution and post-discharge procedures. It can easily exceed the time required for an optimized pulse train execution by a factor of 1.5 - 2. In other words, the application of the optimized pulse train uses the W7-X experimental time more effectively, in general.

3.3.8.2 Optimization of ECWC in OP1.2b

Duty cycle optimization, part 2

ECWC was applied in OP1.2b with better overall wall conditions, which further stretched its parameter range such as pulse length and pulse interval without risking a radiative collapse during the pulse train execution. Additional experiments dedicated to optimizing the pulse length and interval were still carried out before the first boronization. The first pulses of each pulse train were made identical (2 s) to get a reference for the wall conditions for each pulse train. With this information, one could rescale each pulse train's measured cumulated hydrogen removal with the respective removal of the first pulse and post-pulse. All pulse trains had the same gas prefill (15 ms at 75 mbar · l/s) and input power (2.1 MW). The comparison of hydrogen removal efficiency by pulse trains with different discharge lengths and pulse intervals is shown in Fig. 3.41.

Fig. 3.41a shows the results of a pulse length variation from 1 s to 3.5 s. The compared pulse trains in this experimental set had the sum of pulse length and pulse interval equal to 20 s. One can see that the fuel removal rate increases with the pulse length extension, but this dependence is not linear. Small variations, such as an increase from 2 s to 2.5 s, do not give a noticeable improvement in these results, which may attribute to a lower or different wall loading by hydrogen prior to the pulse train with 2.5 s. Thus, while longer pulses generally remove more, $\sim$ 35 % more for 3.5 s pulses than 2 s pulses, the removal is dependent on wall history, even though the results are tentatively corrected for this using the first pulse which is identical in each pulse train as reference.

Another experimental set investigated a further reduction of the pulse interval (Fig. 3.41b). All examined pulse trains had a pulse length of 2 s. Reducing the pulse interval down to 15 s slightly increases the experimental time-averaged removal rates. However, this increase is again not linear. Due to hydrogen re-ionization and redeposition, the experimental improvement is lower than expected. The latter is illustrated by rescaling the outgassing curve of the pulse train (20180719.020) with a pulse interval of 30 s to the outgassing traces of the pulse trains with 20 s and 15 s pulse intervals. The rescaling factor is a ratio

$$f_r = \frac{PI + PL}{PI_r + PL},$$

where PL is the pulse length of 2 s, PI is the pulse interval of 30 s, and PI_r is a rescaled pulse interval of 20 s or 15 s. While the characteristic hydrogen pumping time in W7-X is $\sim$ 3.3 s, the observed pressure decay time after a pulse train discharge is $\sim$ 7 s, primarily due to continued hydrogen outgassing in the post-discharge phase. It is less than the pulse interval of 15 s, allowing to evacuate most of the released fuel between the discharges. However, as heavier impurities are evacuated more slowly, as discussed in the Sec. 3.3.8.1, a further reduction of the pulse interval will cause an impurity accumulation with a minor benefit to fuel removal.

Nevertheless, an essential point of the pulse train execution is the reliability of the ECRH system operation. To manually restart a gyrotron after an aborted discharge before the subsequent discharge execution, the pulse interval should be kept above 30 s. Considering only the minor advantage of the reduced pulse interval compared to the reliability of the pulse train execution, it was decided to keep the pulse interval at $\sim$ 30 s.

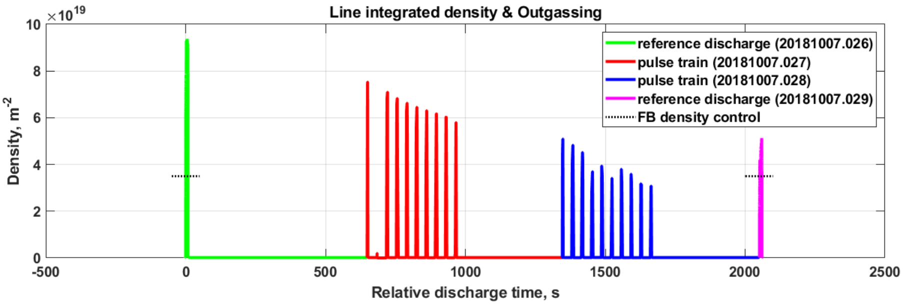

Figure 3.42: An example of two optimized pulse train (pulse length of 3 s, pulse interval of 35 s and input power of 2.1 MW) applications to achieve the density control. Green and purple lines show the line integrated density of the reference discharges with a density feedback control aiming to maintain the line integrated density level at $3.8 \cdot 10^{19}$ m^{-2}. Red and blue lines correspond to the density changes during pulse trains. The second pulse of the first pulse train was aborted.

Application of helium ECWC conditioning for density control

Boronization almost mitigated the risk of radiative collapse and significantly improved the plasma performance. However, the issue with the plasma density control became more critical. After boronization, it was challenging to control wall fueling at densities below $\sim 6 \cdot 10^{19}$ m^{-3}, especially when the preceding experiments operated at high density or fueling. In the case of strong fueling, to desaturate the graphite divertor targets from hydrogen and achieve stable low-density operation with boronized walls, an application of one optimized pulse train can be insufficient and can require repeating the cleaning sequence. An example of such an event is given in Fig. 3.42.

Two reference discharges, performed before and after the pulse trains, are compared to evaluate the improved density control. Each discharge had a length of 8 s and a stepwise input power increase (Fig. 3.43). Both discharges aimed to be conducted at a line integrated density level of $3.8 \cdot 10^{19}$ m^{-2}. However, due to the remaining strong wall fueling, the density of the first discharge reached the values of $\sim 9.3 \cdot 10^{19}$ m^{-2}. After the two pulse trains (19 discharges in total), the plasma density in the reference hydrogen discharge decreased by a factor of $\sim$ 2, approaching the feedback control value.

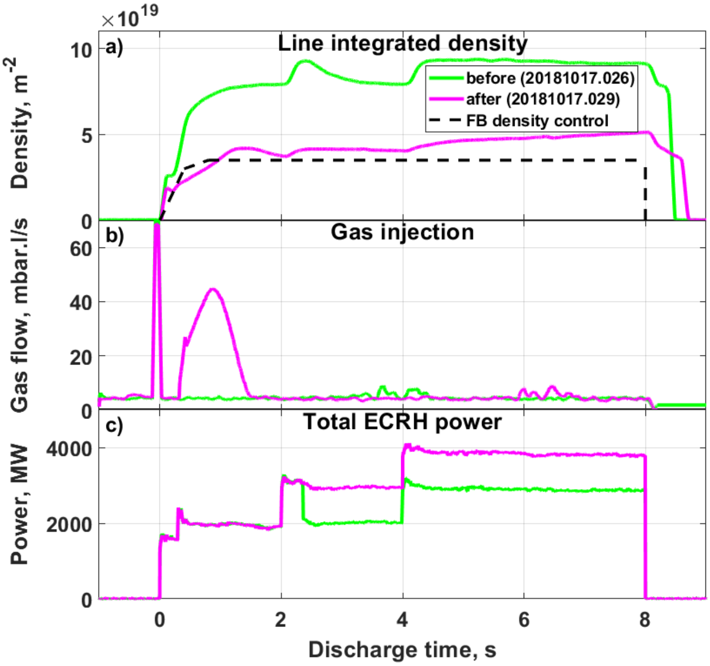

Figure 3.43: Reference discharges on W7-X before (20181017.026) and after (20181017.029) application of ECWC. (a) line integrated density and density feedback control, (b) total gas injection, (c) ECRH input power [38]. One of the gyrotrons failed after 2.4 s of the first reference discharge execution causing a 1 MW power decrease.

Gas balance

The detailed analysis of the gas balance of these reference discharges shows different wall content behaviour before and after wall conditioning (Fig. 3.44). In this approach, the particle content can be split up into different reservoirs: free neutral particles, plasma molecular equivalent representing the corrected electron density for the additional electrons from impurities and giving the number of hydrogen ions and particles bound in the wall [224]. The latter can change significantly, determining the release or retention of the fuel depending on material properties and wall conditioning. The estimation of the W7-X particle reservoirs is given in [208].

No external fueling besides the prefill was required for the reference discharge before conditioning, indicating the density control's absence. Due to heavy wall loading remaining after preceding high-density plasma operations, the given amount of ECRH power was enough to mobilize more particles than needed to sustain plasma density. The negative values of the net wall content during the plasma phase (Fig. 3.44a) indicate net outgassing of the wall of about $8 \cdot 10^{20}$ particles at the end of ECRH heating.

In contrast, the reference discharge after conditioning reached the target density only via additional gas injection. Low wall recycling on the walls leads to a net retention of gas. It corresponds to the high positive values of the black curve representing the net wall content in Fig. 3.44b. After a strong additional injection, the net wall content reaches its maximum at $\sim 14 \cdot 10^{20}$ particles. By the end of heating, the total amount of retained molecules decreases to $\sim 12 \cdot 10^{20}$ particles due to the partial release.

It should also be noticed that in both cases, the wall gas uptake increases drastically at the end of the plasma. As the direct plasma heating on the tiles disappears much faster than the plasma, the surfaces cool and outgassing less abruptly. In contrast, the decaying plasma is present around the target plates for longer.

During the pulse train application (Fig. 3.42), the density decreased from pulse to pulse due to a decreasing contribution of wall fueling. It indicated a successive depletion of particle reservoirs in the divertor targets and was understood as a conditioning effect on the divertor. However, even after the last pulse train discharges, the density trend did not have any saturation attribute. The latter means that another pulse train could have been applied for a further reduction of wall fueling.

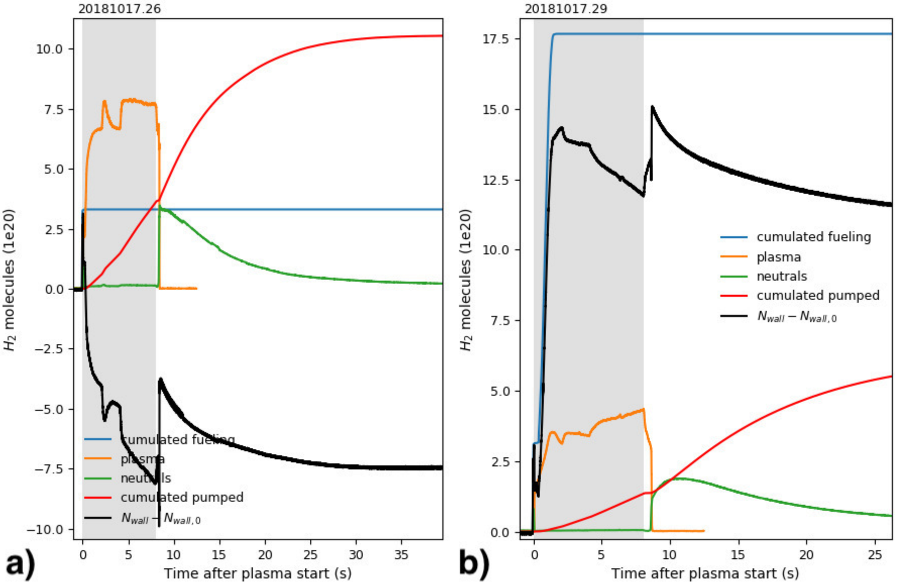

Figure 3.44: Gas balance of the hydrogen reference discharges (a) before and (b) after pulse trains application. Cumulated fueling (blue) and total pumped particles (red) are shown along with the plasma molecular equivalent(orange) and the total neutral inventory (green). Net wall content (black) is calculated according to [208].

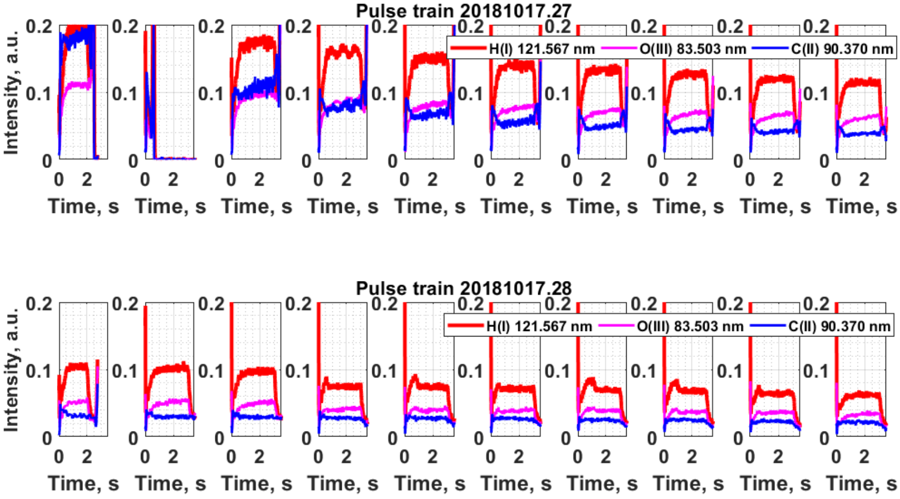

Figure 3.45: Hydrogen, oxygen and carbon concentrations (given by HEXOS) in the plasma core during the application of pulse trains 20181017.27 (top) and 20181017.27 (bottom).

Effect on core fueling and impurity content

As shown in Fig. 3.45. , the oxygen and carbon decrease is also observed as the hydrogen reduction in the plasma core. There is a clear correlation between the oxygen and carbon concentration trends. In the graphite PFC, the fuel can be absorbed as a compound in the form of water. After boronization, oxygen is efficiently captured, and water is released as hydrogen only [208]. However, due to a fast boron layer erosion in the divertor area, the part of oxygen can be still released from the divertor into the plasma core. Thus, by the fuel removal, the pulse trains also reduce the amount of oxygen release, which in turn causes a reduction of the plasma carbon content via a decrease of the erosion rate caused by released oxygen.

Extending the plasma wetted area by strike line sweeps

The previous section discussed that in conditions with strong wall fueling, an application of more than one pulse train is needed. It requires either increasing the number of pulses at the cost of experimental time or improving the pulse train's efficiency.

According to the observation in [225], the strike lines positions are sensitive to the net toroidal current. Strong toroidal currents up to 5 kA

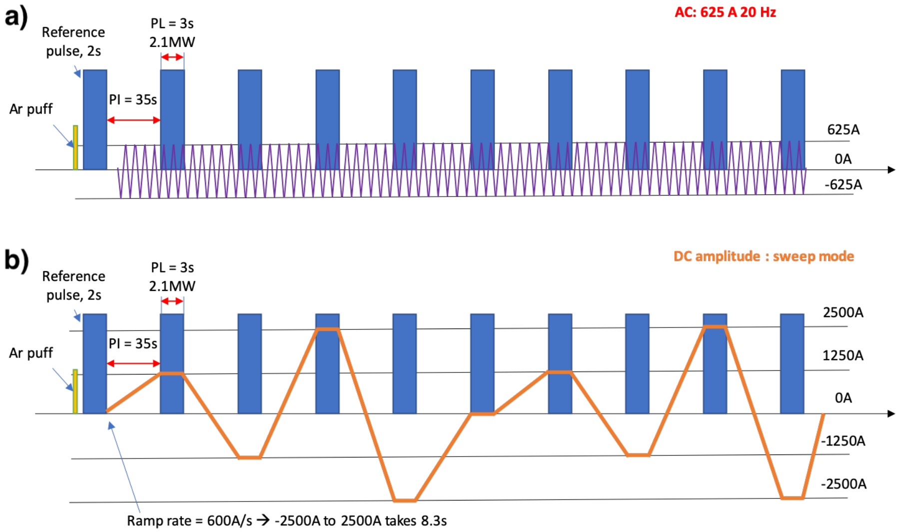

Figure 3.46: Scheme of a pulse train with strike lines sweeping: a) AC sweep, b) DC sweep.

can develop slowly, in order of 10 s, causing a strike line shift of up to 3 cm poloidally along the target surface [226]. It naturally changes the location of the subsurface fuel reservoirs with which the plasma exchanges. To compensate for this, in the short pulse train pulses, the effect of strike lines sweep during the pulse train execution was investigated. The position of the strike lines can be moved across the divertor target by using control. As is described in the previous section, the system of control coils can perform AC sweep and DC sweep, as illustrated in Fig. 3.46.

The AC sweep leads to the rapid oscillation of the strike lines around their standard positions, while DC sweep shifts strike lines to new positions depending on the amplitude and polarity of the applied current [224]. The latter is applied from pulse to pulse. Both types of sweep increase the total plasma wetted area [227]. The mentioned sweeps can also be combined in a DC+AC sweep.

Effect on fuel removal

Three pulse trains with a pulse length of 3 s, a pulse interval of 35 s and input power of 2.1 MW were used to explore the influence of different strike line sweeps on fuel removal. The first discharges of these pulse trains were again used as the reference pulses, with a length of 2 s. A small argon puff prior to

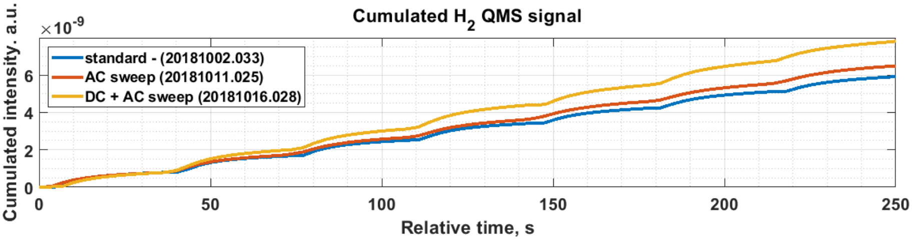

Figure 3.47: The cumulated removal of hydrogen by three He pulse trains with identical main parameters: standard (blue line), AC sweep (red line), DC+AC sweep (yellow line) [210]

the first discharges was used for diagnostic purposes. The first pulse train, called standard, was without strike line sweeping. The second pulse train was performed with AC sweep at a frequency of 20 Hz and an amplitude of 625 A. The last pulse train was equipped with a combined DC+AC sweep. The DC bias amplitude was changed in steps between − 2500 A and 2500 A from pulse to pulse with the ramp rate of 600 A/s between pulses, as shown in Fig. 3.46b. Fig. 3.47 shows the cumulated hydrogen removal for the three experiments.

The application of the pulse train with AC sweep gives only a minor improvement to the hydrogen removal compared to the standard pulse train. In the case of DC+AC sweep, up to 30 % of additional hydrogen removal can be gained. Thus, the fuel removal depends on the total plasma wetted area of the divertor target surface.

The application of pulse trains with DC+AC sweep requires a better understanding of the fuel removal correlation with plasma wetted area and plasma fuel and impurity content.

Analysis of the plasma wetted area

Here, the extension of the plasma wetted area is assessed by analyzing the IR camera images of the divertor targets. It should be noticed that the plasma wetted area is firstly dependent on the magnetic field configurations (as shown in the previous section). Moreover, the wetted areas increase generally with a rise of the divertor power loads [227]. Thus, the estimation of the plasma wetted area extended due to strike lines sweeping is not necessarily straightforward. To simplify this task, only experiments carried out in the standard magnetic field configuration were taken into account because 53.1% of total plasma time in OP1.2b was conducted in this configuration. Moreover, the heat flux distribution data provided by infrared cameras is partially avail-

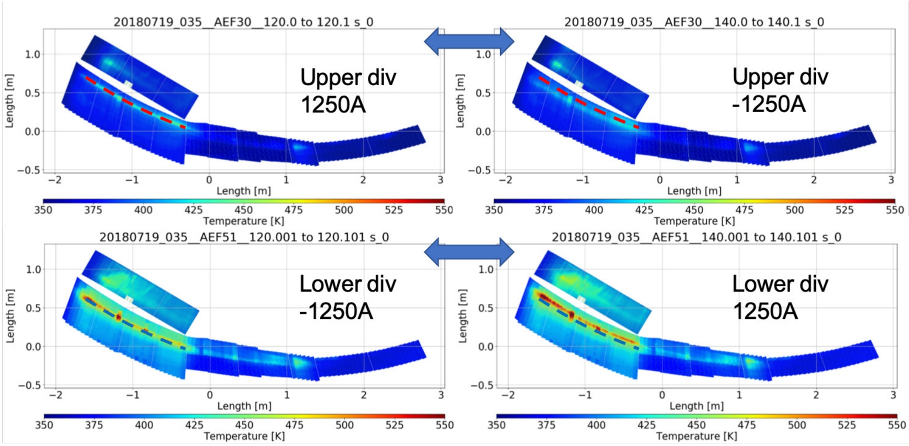

Position of the strike lines at DC **1250 A** (upper) and DC **-1250 A** (lower)

Position of the strike lines at DC **-1250 A** (upper) and DC **1250 A** (lower)

Figure 3.48: Comparison of the heat flux distribution on the upper divertor surface in Module 3 (top figures) and the lower divertor surface in Module 5 (bottom figures) at different current values in the corresponding control coils. Red and blue dashed lines indicate the position of strike lines (120 s) before the current change on the upper and lower divertor targets, respectively.

able for one pulse train with AC+DC sweep (20180719.035) conducted in the standard magnetic field configuration. A particular case of the strike lines position on the horizontal and vertical target plates is shown in Fig. 3.48. The change of the heat flux distribution is analyzed for one of the lower and one of the upper divertor modules for two DC values in the corresponding control coils, +/- 1250 A and -/+ 1250 A at times 120.0 – 121.1 s and 140.0 – 140.1 s, respectively.

One can see that the heat flux pattern on the horizontal target of the lower divertor shifts while the size of the pattern on the vertical target increases. In the case of the upper module, there are no dramatic changes in the heat flux pattern size observed. To better evaluate the heat flux changes on the divertor target surfaces, the temperature profiles corresponding to the strike lines position given in Fig. 3.48 and the current in the control coils are shown in Fig. 3.48. The peaks of the temperature profiles on the horizontal targets of the lower and upper divertors had a shift of $\sim$ 5 cm corresponding to the current change of 2500 A. Moreover, the comparison of the temperature profile peaks shows that the heat flux is not equally distributed between upper and lower modules. A rough approximation shows that the whole sweep of the strike lines from – 2500 A to 2500 A should be $\sim$ 10 cm, while

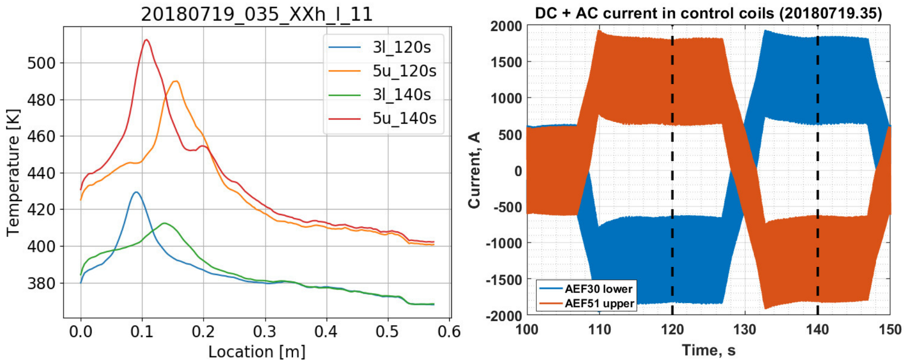

Figure 3.49: Analysis of the pulse train with DC+AC sweep (20180719.035): a) Temperature profile (IR-thermography) on the divertor finger 11 of the horizontal target at 120 s and 140 s after the pulse train start for lower divertor in Module 3 and upper divertor in Module 5, b) corresponding current in the control coils (red line corresponds to the current of the control coil located below the lower divertor in Module 3, blue line corresponds to the current of the control coil located below the upper divertor in Module 5), vertical black dashed lines indicate the time (120 s and 140 s) of the temperature measurements.

the one of the AC sweeps is expected to be rather $\sim$ 2.5 cm based on the maximum current amplitude ratio between AC and DC sweeps [224].

IR camera images are generally not stored for the long pulse trains due to its huge size. Unfortunately, the data for some strike line positions is not available. Thus, the total plasma wetted area can be only roughly extrapolated based on profile changes presented above, taking into account the peculiarities of the changes in full width half maximum (FWHM) of the temperature profiles. The estimation of the total plasma wetted area changes is based on a method of the divertor wetted area calculation given in [227]. Without going further into details about these calculations, the following result is obtained. The total plasma wetted area can be increased by a factor of $\sim$ 8 in the case of the DC+AC sweep in the standard magnetic field configuration at a discharge input power of 2.1 MW. As discussed earlier, it can give up to 30 % of the fuel removal rate improvement, but from a much larger area. However, it is also strongly dependent on the divertor surface fuel loads.

Effect on core fueling and impurity content

Another interesting point of the detailed analysis is to understand how the sweeping of the strike lines affects the impurity and fuel concentration in the plasma core compared to its concentrations in the residual gas content. In order to do this, two pulse trains with (20181016.032) and without DC+AC sweep (20181017.034) have been examined. Both pulse trains had identical parameters of the pulse length (3 s), pulse interval (35 s) and input power (2.1 MW). Due to the failure of the last discharges, only the first five discharges are taken into account in this analysis. The corresponding changes of the hydrogen and oxygen content in the core during these pulse train executions and the cumulated hydrogen removal are shown in Fig. 3.50.

According to the presented data (Fig. 3.50a top), adding the strike lines sweeping does not affect the hydrogen concentration in the plasma core. The hydrogen characteristic emission intensity trends are almost the same for both pulse trains. At the same time, the outgassing hydrogen partial pressure shows an increase of the fuel removal in the case of the pulse train with the sweep (Fig. 3.50b). An additional fuel release occurs in the post-discharge phase due to the interaction with a larger divertor area. Thus, heating a larger divertor surface can stimulate an increase in the fuel removal rate.

As it was mentioned earlier, the application of pulse trains is also practical for oxygen reduction. However, sweeping the strike lines has an inverse effect on the main radiator impurity concentration in the plasma core (Fig. 3.50a bottom). The most pronounced difference is visible during the fourth discharge. There is an evident rise of the oxygen content resulting in an increase by a factor of 2 at the end of the discharge. The subsequent discharge has an oscillating oxygen signal increasing only by $\sim$ 50 %. The oscillation frequency does not match the AC sweep frequency, meaning that a different process causes these oscillations.

Thus, sweeping can increase the oxygen release from the divertor and its concentration in the plasma core during some discharges of the pulse train supposedly due to the erosion of the boron layer in the previously untouched divertor area. However, the rise of the oxygen in the plasma core during the pulse train with strike line sweep does not influence the overall wall conditions and plasma performance in the consecutive physics program discharges.

Role of PFC temperature on fuel and impurity removal

In order to meticulously study the temperature effect on the impurity release and fuel removal during a pulse train, it is necessary to consider the case

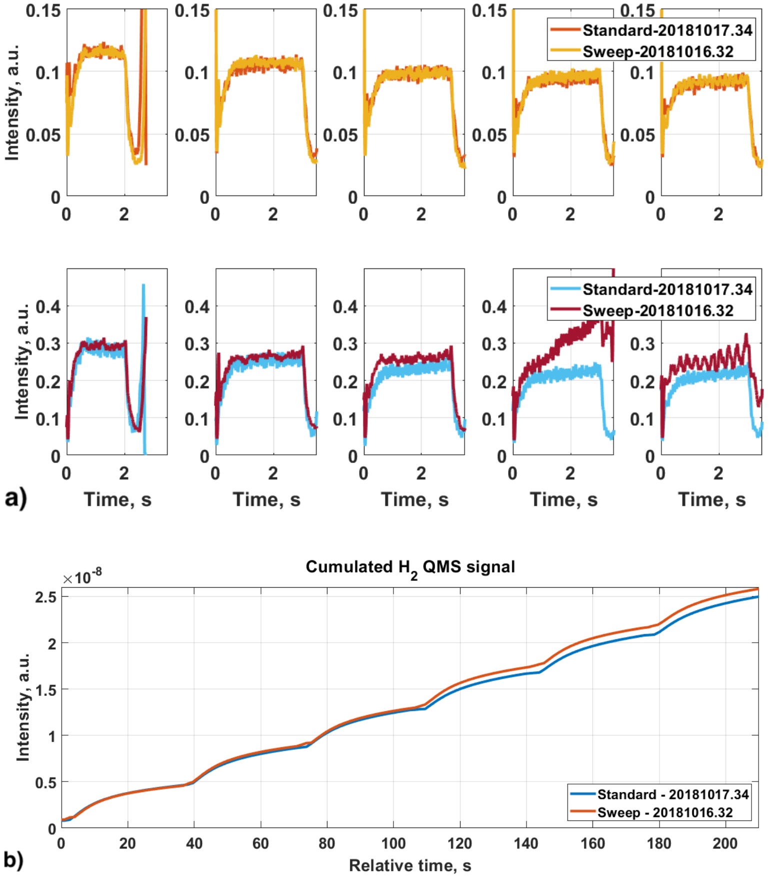

Figure 3.50: Analysis of fuel and impurity removal by the pulse trains (only first five pulses) with (201810170.34) and without (20181016.032) strike line sweep: a) concentrations of hydrogen (top, *HI* 121.567 nm) and oxygen (bottom, *OIV* 55.426 nm) in the plasma core given by HEXOS, b) cumulated hydrogen removal given by QMS.

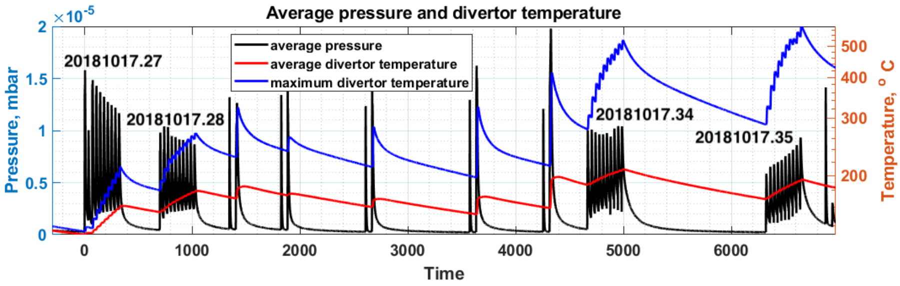

Figure 3.51: Outgassing given by the average neutral pressure measurements and maximum and average divertor temperatures given by divertor thermocouples for pulse trains 20181017.027, -.028, -.034 and -.035 with identical parameters.

when the divertor temperatures are high enough to demonstrate outstanding behaviour of fuel and impurity release. An application of 4 identical pulse trains (pulse length of 3 s, pulse interval of 35 s and input power of 2.1 MW) in similar device conditions allowed to study a temperature influence on the outgassing. The first two pulse trains (20181017.027 and 20181017.028) were already analyzed in Sec. 3.3.8.2. Another two pulse trains (20181017.034 and 20181017.035) were applied after five hydrogen discharges. Their execution caused a significant increase in the divertor temperatures in different locations. The outgassing and its correlation to the divertor maximum and average temperatures are given in Fig. 3.51.

The outgassing trend for the first two pulse trains shows the apparent effect of the wall desaturation. The pressure peak after each pulse decreases from pulse to pulse. However, a pressure peaks increase is observed in the last discharges of the third pulse train and all the discharges of the last pulse train. In this case, the maximum temperature raised above $\sim$ 300 - 400 $^{\circ}\mathrm{C}$ while the average temperature increased by $\sim$ 20 $^{\circ}\mathrm{C}$. The temperature rise activates release from different trapping sites. It is evident in the last pulse train with lower wall loading, where the temperature effect dominates.

Fuel removal

More details of the last pulse train 20181017.035 are given in Fig. 3.52. No significant changes of the line integrated density are observed. The maximum density values vary from $2.2 \cdot 10^{19}$ m^{-2} to $2.4 \cdot 10^{19}$ m^{-2}, mainly in the precision range of the gas injection and density measurements. The same behaviour is observed for the hydrogen concentration in the plasma core. However, the amount of the outgassed hydrogen rises from discharge to dis-

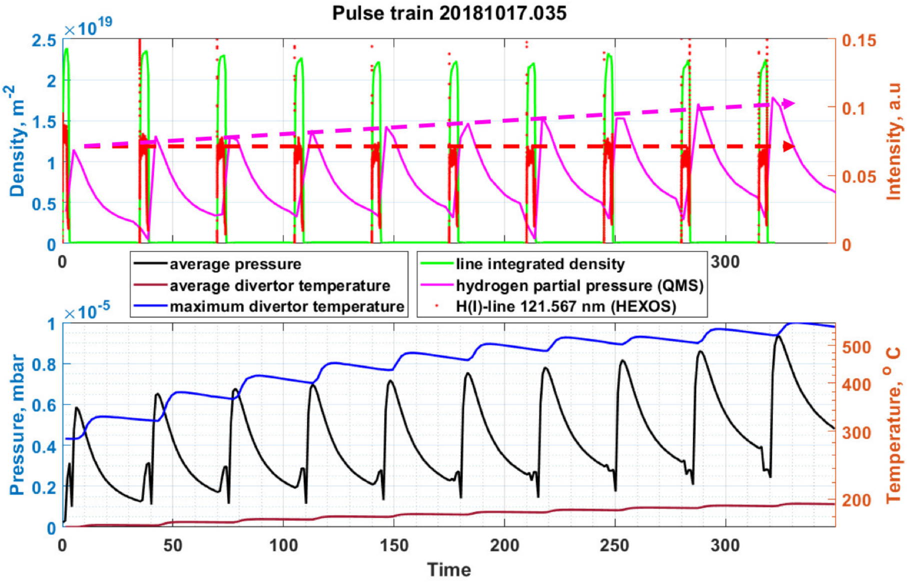

Figure 3.52: Comparison of the hydrogen release behaviour in plasma core with the post-discharge phase, line integrated density and maximum and average divertor temperatures influence the outgassing during pulse train 20171017.035 execution.

charge, visible in the increasing pressure peaks after each pulse, correlating with the divertor temperature increase. The total increase of the hydrogen outgassing peak measured by mass spectrometry is from $6.9 \cdot 10^{-11}$ a.u. to $1.1 \cdot 10^{-10}$ a.u. (by a factor of $\sim$1.59) while the average neutral pressure outgassing peaks rise from $\sim 5.9 \cdot 10^{-6}$ mbar to $\sim 9.3 \cdot 10^{-6}$ mbar (by a factor of $\sim$ 1.58). Thus, the outgassing is dominated by the post-discharge released fuel.

Based on the analysis results, one can say that the temperature effect does not seem to influence core fueling during discharge execution. The cleaning efficiency of the pulse depends mostly on post-discharge outgassing in case of high divertor temperatures. As the divertor temperature increases stepwise throughout the experiment, more trapping sites with higher activation energies can be depleted. The PFCs desaturate from pulse to pulse. Thus, even in a well-conditioned machine, the extra fuel release can be achieved due to a "temperature-dependent wall source”. Particle reservoirs inside the graphite tiles are increasingly depleted, and the outgassing happens only at higher surface temperatures. A plausible explanation is the spread of heat into the full divertor tile and even its holding structure [208].

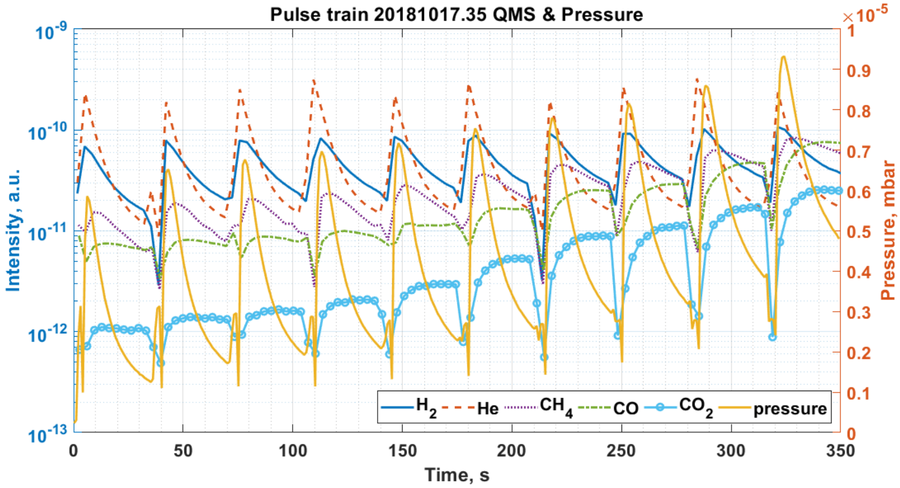

Figure 3.53: Impurity partial pressure in the residual gas content and average neutral pressure during the pulse train 20171017.035 execution.

Impurity removal

The influence of temperature increase on the hydrogen and dominating impurity outgassing and helium post-discharge release are shown in Fig. 3.53.

The signals of impurities such as methane and carbon oxides also show their concentration increase in the outgassing content. It means that the divertor temperature increase leads to the extra formation of these impurity species. The highest increase rate belongs to CO_2. Its signal rises by a factor of 12 during the pulse train application. The shape of the CO_2 spectrum shows that its concentration slowly increases in the post-discharge phase. The maximum divertor temperature increase leads to a thermal outgassing increase between pulses. Even with longer intervals, the base pressure level will rise. In this case, the chosen pulse interval should correspond to the outgassing at a maximum achievable temperature for the sufficient impurity pumping preventing a considerable accumulation of this impurity species. For example, the pulse interval of 35 s (Fig. 3.53) seems sufficient to remove the significant amount of outgassed fuel, CH_4 and CO at the maximum divertor temperature of $\sim 400\ ^\circ\mathrm{C}$.

A similar effect is observed for CO. Its concentration is increased by one order of magnitude. However, due to a higher pumping speed for this species, accumulation is less pronounced.

The concentration of the carbon and oxygen in the core are not signif-

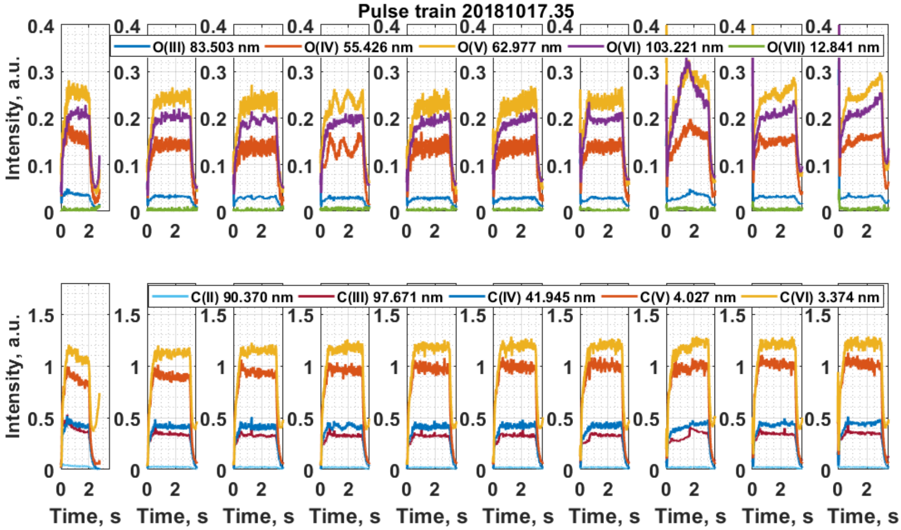

Figure 3.54: The oxygen and carbon concentration represented by the intensities of the characteristic lines (HEXOS) of different ionization states during the pulse train 20171017.035 execution.

icantly affected by the divertor temperature increase (Fig. 3.54). Only some characteristic line intensities show a slight increase of the corresponding ion concentration at the end of the pulse train execution. Considering the previous cases (Fig. 3.45), it can be confirmed that the changes of the carbon and oxygen concentrations given by HEXOS correlate with the released hydrogen amount in the plasma core. It also indicates that methane and carbon oxides production may occur mainly in the post-discharge phase. Moreover, the accumulation of carbon oxides has only a minor influence on the concentration of their components in the plasma core. The latter can mean that the amount of the accumulated carbon oxides in the residual gas content is relatively small. The plasma screen effect almost prevents its penetration and further dissociation from the plasma edge.

To evaluate the behaviour of outgassing in the case of intensive divertor target heating, one can compare the growth of the maximum outgassing with respect to the divertor temperature increase. The outgassing peaks versus the corresponding peaks of the maximum and average divertor temperature, as shown in Fig. 3.52, are presented in Fig. 3.55.

The increase of the outgassing shows a clear non-linear dependence on local temperatures of carbon PFCs. The increased temperature of the divertor leads clearly to increased outgassing after each subsequent pulse despite the significant wall desaturation during the previous pulse trains.

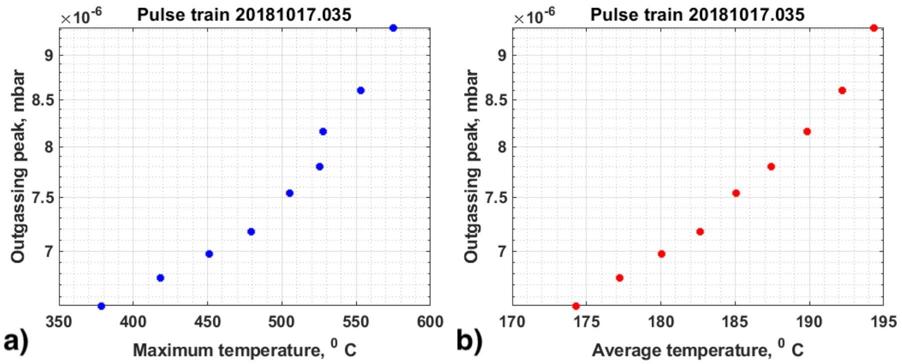

Figure 3.55: Dependence of the total outgassing (outgassing peak of each subsequent discharge shown in Fig. 3.52) according to (a) average and (b) maximum divertor temperatures.

While temperature mobilizes more gas trapped in the deeper layers of the graphite, graphite's relatively high thermal conductivity allows increasing hydrogen outgassing from previously untouched divertor areas. The outgassing trend has attributes of an exponential dependence. Nevertheless, the detailed analysis requires involving more sophisticated modelling and further experiments.

Besides a strong hydrogen release at high divertor temperatures, the water outgassing is also enchanted, as discussed in the previous sections.

Chapter 4

The TOMAS device: a plasma facility for wall conditioning studies

I tried so hard and got so far
But in the end, it doesn't even matter …
Linking Park, "In the end."

The study and optimization of the wall conditioning techniques applied in the superconducting stellarator W7-X require extensive operation time and hence competes for experimental time with other physics topics. Conditioning experiments need many tests under various experimental conditions that call for device flexibility and the availability of adapted diagnostics. Large fusion devices as W7-X can provide these conditions only partially. Therefore, it was decided that it would be essential to put in place an experimental set-up dedicated to wall conditioning studies to get better insight into the complex multi-physics picture of the wall conditioning techniques and prepare them for further applications on a specific fusion device. For this purpose, the TOMAS (TOroidal MAgnetized System) device [40] has been significantly upgraded.

The author strongly contributed to the engineering and design of device components, installation and commissioning of the device systems and diagnostics, planning and carrying out wall conditioning experiments, and interpreting their results. Moreover, the author has prepared the device for the PSI studies and technically supported colleagues during the first characterization of RF plasmas. The device allows complementing wall condition-

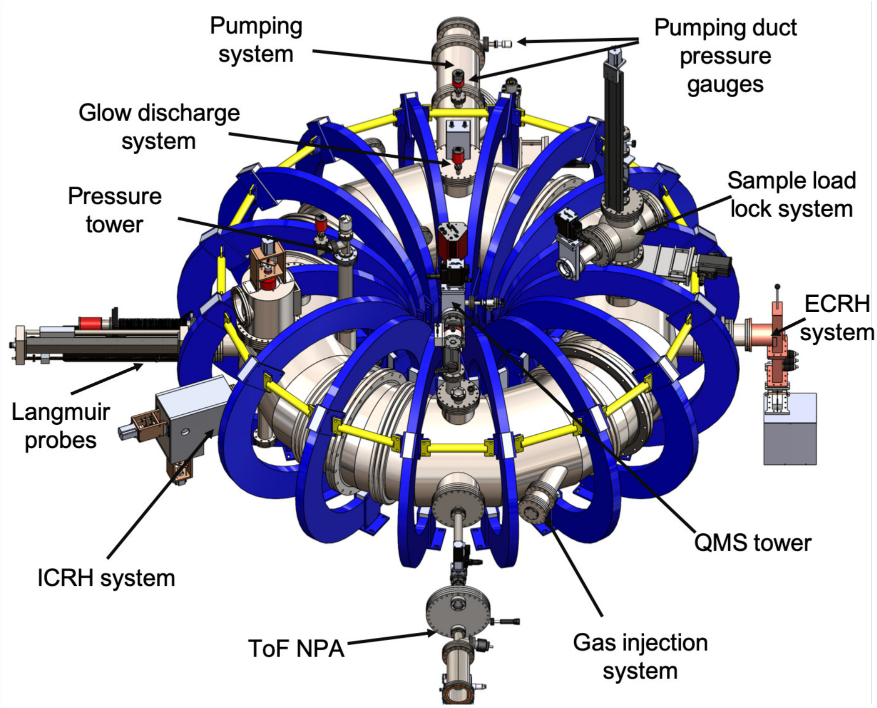

Figure 4.1: The 3D model of the upgraded TOMAS device [40] .

ing, plasma production and plasma-surface interaction studies not only for W7-X but for other large fusion devices such as JT-60SA and ITER, too.

4.1 The TOMAS device

The TOMAS device is located in the IEK-4 Forschungszentrum Jülich. It was built at the Kurchatov Institute in Moscow to systematically study wall conditioning plasmas in a toroidal geometry [228]. The first experiments on TOMAS were dedicated to investigations of electron cyclotron resonance plasmas [101, 229]. The device was also used in experiments related to fuel removal by Glow Discharge Cleaning [230, 231]. Compared to the previous operation experience, TOMAS was significantly upgraded in the course of this PhD work between 2016 and 2020. The model of the upgraded TOMAS device with its main systems at present is shown in Fig. 4.1.

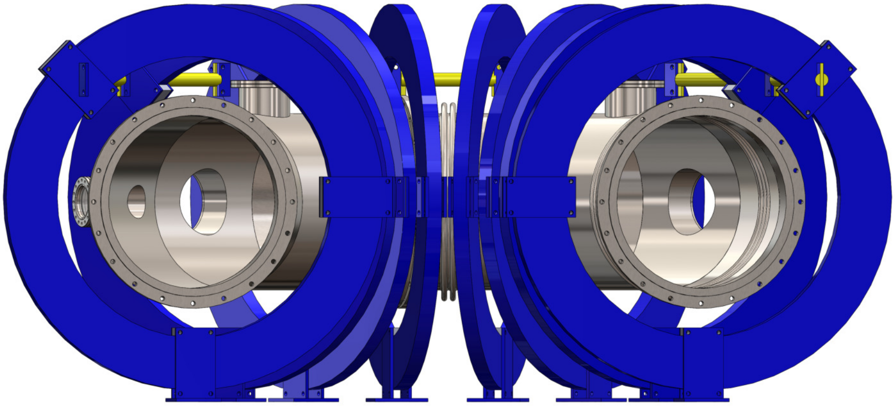

Figure 4.2: The 3D model of the TOMAS vacuum vessel and magnetic field coils [40] .

4.1.1 The vacuum vessel and the magnetic field system

The TOMAS device is based on a quasi toroidal vacuum vessel consisting of 4 sectors. Each sector is made of cylindrical stainless steel elements with a wall thickness of 5 mm. A major radius of the vessel is 0.78 m, while its minor radius is 0.26 m. The inner surface of the vacuum vessel has an area of $\sim$ 8.5 m^2. Its volume is $\sim$ 1.1 m^3. The vessel has 22 different vertical and horizontal DN ports. The vacuum vessel is also equipped with a bake-out system consisting of 16 heating tapes wrapped around the cylindrical sections, including thermocouples for temperature monitoring. Each tape provides 750 W of heating power, allowing it to reach the maximum average vessel temperature of 80 $^\circ\mathrm{C}$ within $\sim$ 45 minutes.

The magnetic field system is based on 16 toroidal magnetic field coils. Each coil has a circular shape with an inner radius of 0.422 m and an outer radius of 0.581 m. The geometrical centres of the coils are aligned with the vacuum vessel central axis. A 3D model of the vacuum vessel and magnetic field coils is shown in Fig. 4.2. The coils are actively cooled by water. The main characteristics of the magnetic field system are summarized in Table 4.1.

The following formula approximates the value of the magnetic field.

$$B(r)[T] = 5.7 \times 10^{-5} \times I_c[A] \times \frac{R_0}{R_0 + \Delta r} \tag{4.1}$$

where I_c is the coil current, R_0 is major radius and Δr is the radial position relative to the major radius. The more detailed model [232] of magnetic field

Table 4.1: The main parameters of the TOMAS magnetic field system.

Parameter	Value
Toroidal coils	16
Coil material	Copper
Maximum voltage	80 V
Maximum current	2.2 kA
Maximum field on the axis	125 mT
Coil resistance	2 mΩ
Current frequency ripple	300 Hz
Maximum spatial ripple	6 %

distribution is shown in Fig. 4.3, indicating a toroidal ripple in the magnetic field strength of a maximum of 6 % at the low field side (LFS).

4.1.2 The vacuum system

The vacuum system of TOMAS includes the pumping system, the gas injection system and pressure monitoring. The vacuum system is schematically depicted in Fig.4.

The vacuum in the vessel is provided by the main pumping unit based on a Pfeiffer 1201P C turbomolecular pump which is installed in series with a Pfeiffer DUO 35 rotary vane pump. The turbopump is connected to the vacuum vessel by a 200 mm diameter "Γ-shaped" pumping duct with a length of 1.33 m. The variable pumping speed of the turbopump can reach 1250 l/s, while the conductance of the pumping duct is $\sim$ 728 l/s at room temperature for air/nitrogen. The vacuum for some diagnostics, such as the mass spectrometer (see Sec. 4.1.5.2), is provided differentially by independent pumping units.

The gas injection system of TOMAS has two parts, the main and the auxiliary one. The main part contains three Bronkhorst F-201CV-200-VGD-88-V mass flow controllers. Each mass flow controller is individually calibrated for hydrogen, helium and argon and injects a working gas in the range of 4–400 sccm. The controllers are installed in parallel. The venting of the vacuum vessel can be performed via a valve installed in the main gas injection system. The system is evacuated by the Leybold TRIVAC D4B rotary vane vacuum pump via multiple manual valves. The auxiliary gas injection system consists of two MKS Instruments 1259CC-00500RU multi-gas mass flow controllers. These controllers can inject different working gases with

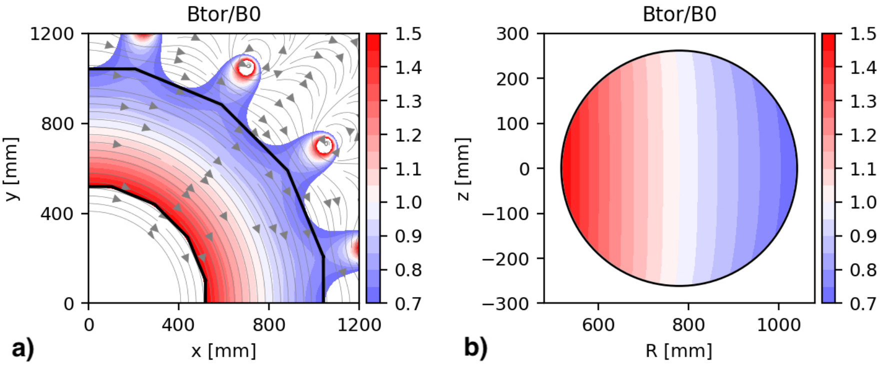

Figure 4.3: The magnetic field intensity distribution model given as a ratio between magnetic field values and the magnetic field value on the toroidal axis. Black solid lines indicate the area inside the vacuum vessel: (a) the toroidal cross-section and (b) the poloidal cross-section (in the x–z plane) [40].

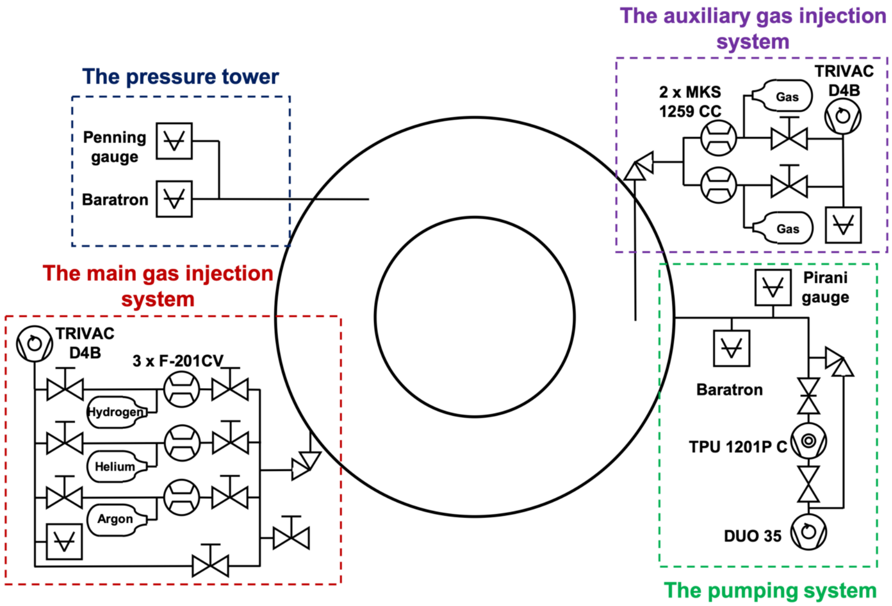

Figure 4.4: The Piping and Instrumental Diagram (P&ID) of the vacuum system of TOMAS [40] .

flow rates up to 500 sccm. The auxiliary gas injection system is mainly used for local gas injection in the vicinity of the glow discharge anode.

The pressure monitoring inside the vacuum vessel is done by the Pfeiffer CMR 375 capacitance gauge (Baratron) and the Pfeiffer IKR 270 cold cathode gauge (Penning gauge). Both pressure gauges are installed in the so-called pressure tower (Fig. 4.10) to minimize the influence of the magnetic field on the pressure reading. The Baratron measurement is independent of the gas type and can be used in the range of $1.0 \cdot 10^{-5}$ mbar - $1.1 \cdot 10^{-1}$ mbar. The Penning gauge measurements are gas dependent and are sensitive in the range from $1 \cdot 10^{-9}$ to $1 \cdot 10^{-3}$ mbar. Additionally, a Baratron is installed in the pumping duct together with a Pfeiffer TPR 270 Pirani gauge operating between $1 \cdot 10^{-4}$ and $1 \cdot 10^{3}$ mbar. A third Baratron is located in the vicinity of the glow anode. Some of the diagnostics have an individual pressure control which is independent of the main units.

4.1.3 The systems of plasma production

The TOMAS device has been equipped with a new Glow Discharge system, a modified Electron Cyclotron Resonance Heating system and a new Ion Cyclotron Range of Frequency system.

4.1.3.1 Glow Discharge system

The Glow Discharge system of TOMAS is based on a prototype W7-X glow discharge anode [176] and is hence similar to anodes used on W7-X [178] and ASDEX-Upgrade [84]. The anode is made of graphite and has a spherical calotte shape with a diameter of 0.15 m (Fig. 4.5). The anode is passively cooled, allowing it to keep its maximum surface temperature below 390 $^{\circ}\mathrm{C}$ at the anode current of 3 A. The glow discharge system shows good thermal and discharge stability in the pressure range of $2 \cdot 10^{-3}$– $2 \cdot 10^{-2}$ mbar. The anode is connected to the power line in the vertical port via a single copper pin with a diameter of 0.12 m, as is shown in Fig. 4.5.

The power supply of the Glow Discharge system is based on the modular Fug MYN 60000M–1500. It delivers up to 1.5 kV for break-down and is operated well below 6 A to avoid feedthrough and cables overheating. Thus, the characteristic current densities of GD are 0.1– 0.7 A/m^2.

4.1.3.2 Electron Cyclotron Resonance Heating system

The main element of the Electron Cyclotron Resonance Heating system is a MUEGGE MH6000-213BF magnetron. The system provides a 2.45 GHz con-

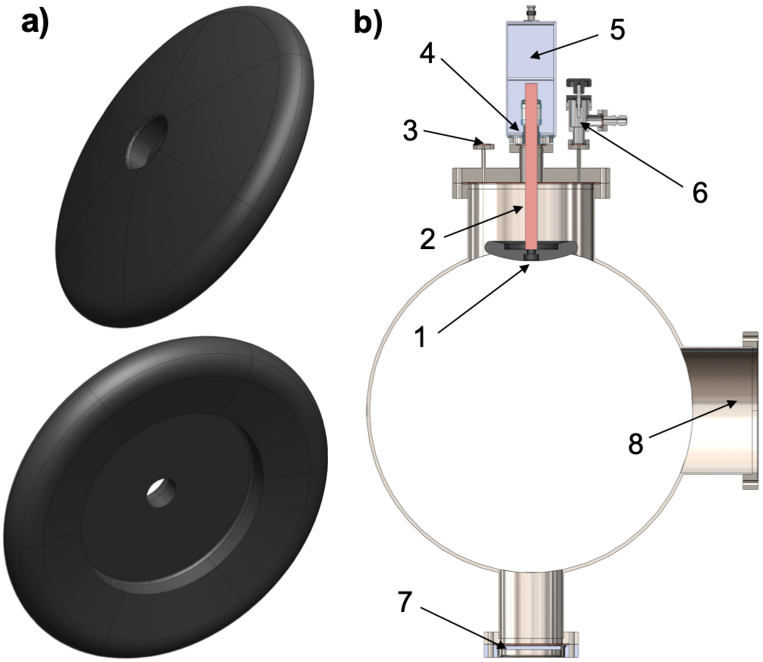

Figure 4.5: a) the model of the W7-X – like GD anode b) the model of the glow discharge system: 1 – glow discharge anode, 2 – a feedthrough connection pin, 3 – DN16 port for an optional connection of the baratron, 4 – DN40 anode feedthrough, 5 – electronics box, 6 – DN16 manual angle valve, 7 – DN100 viewport, 8 – DN200 port for the pumping system connection [40].

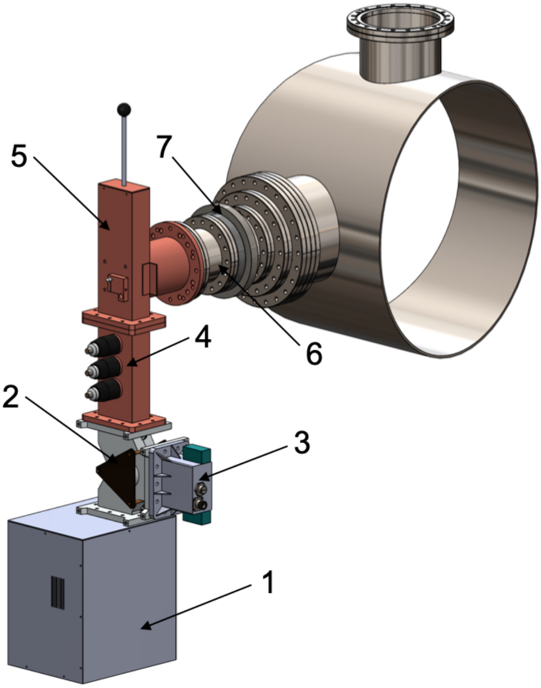

Figure 4.6: The ECRH system of TOMAS. 1 – magnetron MUEGGE MH6000-213BF, 2 - circulator Philips 2722 163 02004, 3 – dummy load Philips 2722 163 02004, 4 - 3-stub tuner, 5 - transition element MUEGGE MW5002B-120YD, 6 – 100 mm DN100 pipe, 7 - Fused Silica UV window [40] .

tinuous wave (CW) in the power range of 0.6 – 6 kW. However, the MUEGGE MW-PPEE3327-6K - 016 magnetron power supply also allows operating the ECRH system in a pulsed regime with a minimum pulse length of $\sim$ 1 s. The power supply is externally controlled by a Tektronix AFG 3252 Dual Channel Arbitrary/Function Generator. The 3D model of the TOMAS ECRH system is shown in Fig. 4.6.

The magnetron head is equipped with the Philips 2722 163 02004 isolator, which circulates the reflected power to a water-cooled power (dummy) load. The level of the reflected power is controlled by a MUEGGE TD 2450-01-N zero-bias Schottky diode. The elements of the transition line are based on a WR340 waveguide. The isolator is followed by a 200 mm 3-stub tuner containing non-contacting stubs spaced along the centerline by a quarter of the wavelength. The MUEGGE MW5002B-120YD transition element trans-

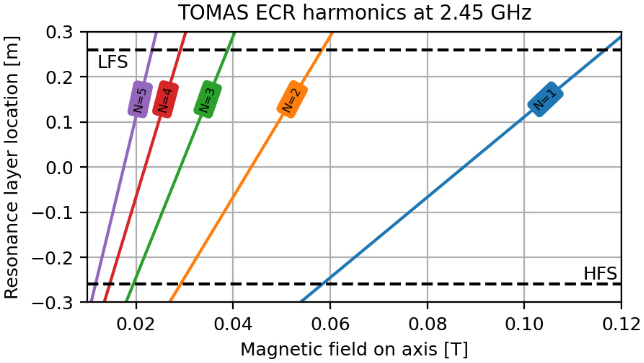

Figure 4.7: Location of the cyclotron harmonic layers for the ECR as a function of the available toroidal magnetic field B_0 on-axis (HFS – High Field Side, LFS – Low Field Side, N – harmonic number) [40] .

forms the vertical WR340 waveguide to a horizontal circular part with an inner diameter of 100 mm. It converts the excited propagating TE10 mode in the WR340 waveguide to a TE11 mode propagating in the circular part. The transition element contains an active tuning element and an integrated adjustable short to tune the launching system. The microwave power is transmitted to the vacuum vessel through a low absorption fused silica UV window.

The microwave power at 2.45 GHz can be absorbed in the Electron Cyclotron Resonance or its harmonics depending on the applied magnetic field (Fig. 4.7). Other absorption mechanisms may play a dominant role depending on the plasma parameters, e.g. the appearance of wave cut-offs or resonances such as the upper-hybrid resonance. Low single-pass absorption leads to multiple microwave reflections at the vessel boundaries causing a microwave propagation and polarization mixture.

4.1.3.3 Ion Cyclotron Range of Frequency system

The Ion Cyclotron Range of Frequency (ICRF) system is built around a single poloidal strap antenna in an antenna box marked by lateral limiters [233] and uses a matching system similar to the W7-X antenna [41]. The antenna system was dimensioned to operate in the frequency range of 10 - 50 MHz with a power load of up to 6 kW. The antenna is shown in Fig. 4.8. The width of the strap is 90 mm, while its thickness is 5 mm. The shape of the antenna box repeats the circular curvature of the vacuum vessel inner wall.

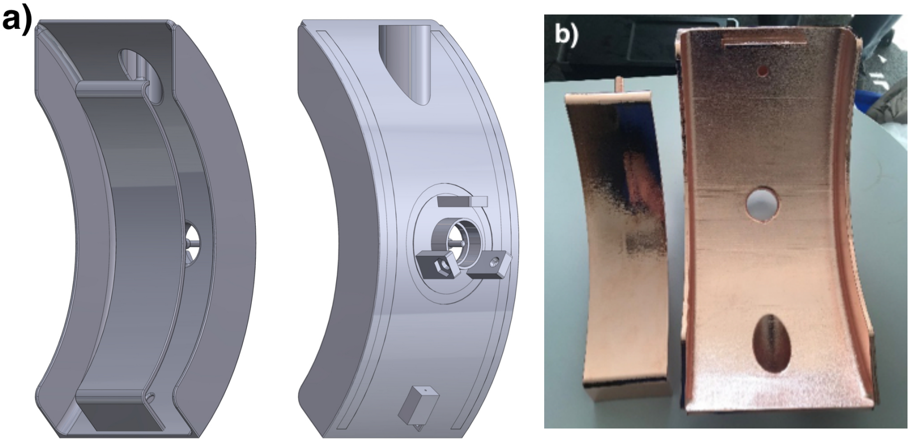

Figure 4.8: The ICRF antenna for the TOMAS device: a) the originally designed 3D model, b) the last modified version of the antenna currently installed in the device [40].

The antenna box has an inner width of 180 mm. The thickness of the side limiters is 4 mm. The front face of the antenna strap resides 5 mm behind the limiters. The antenna box and the antenna strap are separately 3D printed in Inconel 718. The decision of 3D printing technology usage was made to test new technology for antenna production. Thus, it allowed simplifying the manufacturing process of the metallic components with complex geometry. Both components are coated by a 0.2 – 0.3 mm thick copper layer.

The matching scheme of the ICRF system is shown in Fig. 4.9. First, the antenna is tuned by the pre-matching Comet CV2C 1000 variable capacitor (C_A), which is connected to the antenna strap via a top tap. The central tap of the antenna is fed via the L-matching circuit containing a CVDD-1000-10S variable capacitor (C_S) connected in series and a Jennings CVCH-1000-5 variable capacitor (C_P) connected in parallel. The operation characteristics of the capacitors are given in Table 4.2. Both circuits are enclosed in the matching box, as is shown in Fig. 4.10. The matching circuits are connected to the antenna ports by 50 Ω 1 5/8" rigid transmission lines.

The RF signal is generated by a Tektronix AFG 3252 dual-channel function generator and then amplified by a BONN Elektronik BLWA 0105-6000P solid-state amplifier working in a frequency range from 10 MHz to 50 MHz with the CW output power of up to 6 kW. The RF signals in the matching boxes and feeding lines captured by voltage and current probes and the amplifier forward and the reflected power are read by high-speed RF logarithmic

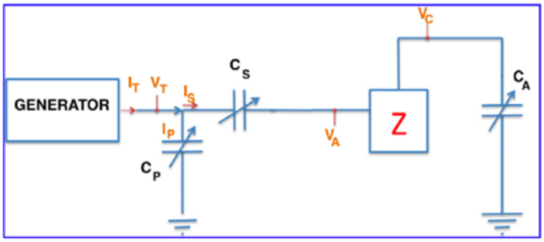

Figure 4.9: The matching scheme of the ICRF system (Z is the antenna, V and I are voltage and current probes, respectively) [233] .

Table 4.2: Matching system capacitor characteristics [40].

Capacitor	**Capacitance, range, pF**	**Peak voltage, kV**	**Maximum continuous operation voltage, kV**
C_A	35 - 1000	30	18
C_S	25 - 1000	10	6
C_P	7 - 1000	5	5

detector power meters (AD8310 0.1 MHz – 440 MHz). Based on the obtained signals, each capacitor is envisaged to be automatically tuned by a matching algorithm based on the TEXTOR matching scheme [234–236].

The ICRF system is operated in a pulsed regime with a pulse length of up to 4 s. The minimum discharge dwell time depends on the plasma load and the heat dissipation in the system because the system components are passively cooled.

The main ICRF plasma operation mode in TOMAS is the high cyclotron harmonics (HCH) regime. The electrons absorb a significant amount of the power of the RF fields via electron–neutron collisions. Thus, a typical frequency corresponds to the tenth harmonics of the hydrogen proton [233].

4.1.4 The load-lock system for PSI studies

The TOMAS device has been equipped with a sample load lock system specially built to expose material samples to a wide variety of plasma conditions relevant to wall conditioning plasmas and fusion edge plasmas.

The system consists of a differentially pumped sample chamber that allows the relatively fast sample exchange via a quick-access door. The individual pumping unit is based on the Pfeiffer Vacuum TSU 260 D turbomolecular pump system with a maximum pumping speed of 210 l/s. A Leybold

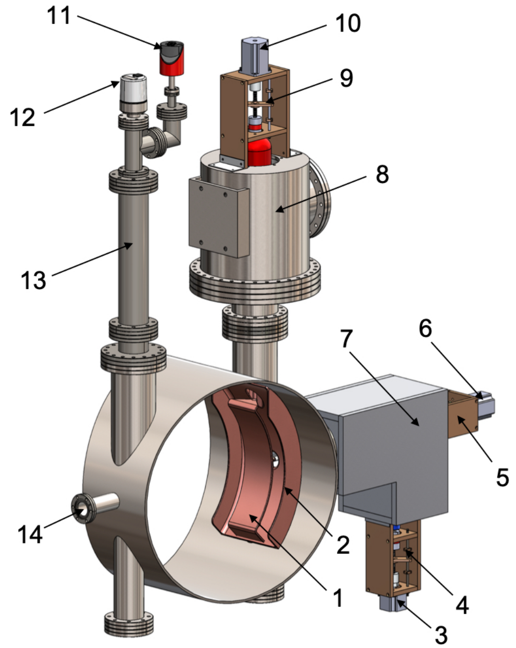

Figure 4.10: The ICRF system and the pressure tower. 1 – antenna strep, 2 - antenna box, 3 – step motor, 4,5 – automatic tuning system, 6 – step motor, 7 – pre-matching (L) box, 8 – matching (top) box, 9 – automatic tuning system, 10 – step motor, 11 – capacitance gauge Pfeiffer CMR 375 (Baratron), 12 - cold cathode gauge Pfeiffer IKR 270 (Penning gauge), 13 – pressure tower, 14 – camera endoscope [40] .

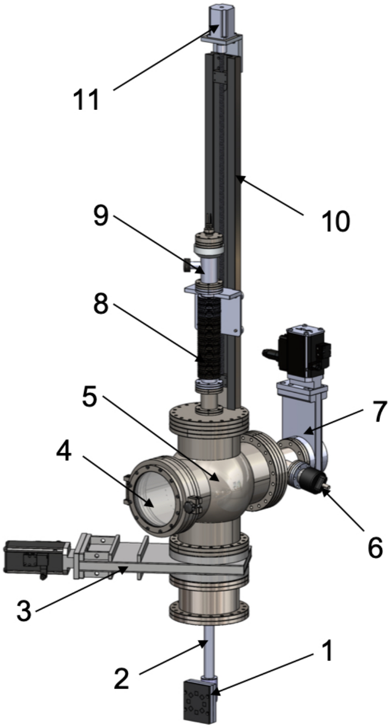

Figure 4.11: The load lock system. 1 – PSI-2 – like sample holder, 2 – vacuum manipulator shaft, 3 – DN160 gate valve, 4 - DN160 Quick-Access Door with a Borosilicate Sight Glass, 5 – sample chamber, 6 – pressure gauge, 7 – DN63 gate valve, 8 – vacuum manipulator, 9 - rotary feedthrough DN40, 10 – manipulator base (rail), 11 – automated linear drive (step motor) [40] .

PENNINGVAC PR27 pressure gauge ($1 \cdot 10^{-9}$ mbar – $1 \cdot 10^{-2}$ mbar) monitors the pressure in the sample chamber. The samples can be exchanged within $\sim$ 2 hours.

A vertical vacuum manipulator mounted on the top of the sample chamber is used to insert and position probes in the TOMAS vessel. The manipulator shaft has a length of 1190 mm to move a sample holder down to the plasma centre. The model of the sample load lock system is shown in Fig. 4.11.

The sample holder attached to the manipulator shaft consists of an adjustable adapter and an exchangeable target holder. The geometry of the samples and exchangeable target holder are identical to the parameters of a sample holder used in the linear plasma device PSI-2 [237]. The target holder

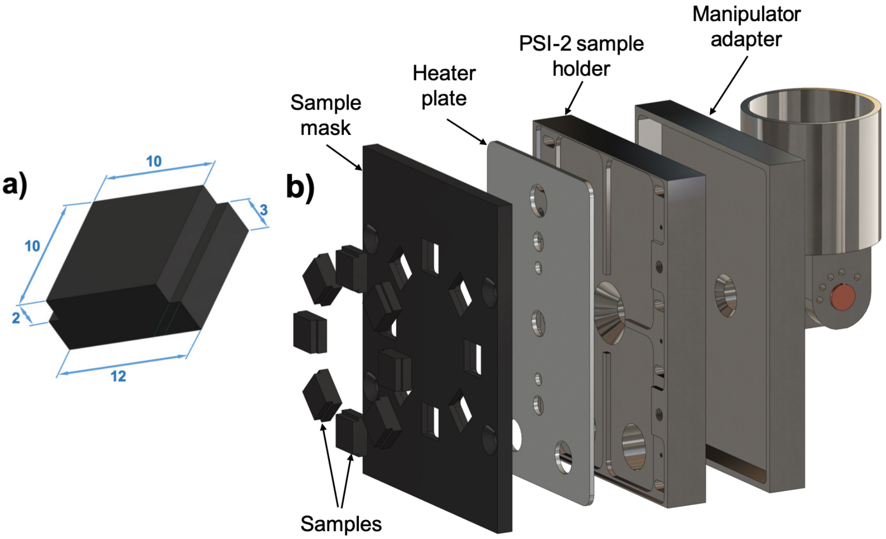

Figure 4.12: a) The sample (with dimensions), b) The 3D model of the sample holder [40].

consists of a holder base, an active heating element, and a mask (a fixing plate), which holds sample probes (Fig. 4.12). The holder base (PSI-2 sample holder) made of stainless steel has a 100 mm × 80 mm rectangular profile. The heating element (Heater plate) combines an electrically conductive pyrolytic graphite and a dielectric pyrolytic boron nitride. The temperature monitoring of the exposed material is done by a thermocouple attached to the backside of the sample mask. The sample mask has the same profile as the holder plate. Its thickness is 5 mm. Eight samples are located around the centre of the mask in a circle with a diameter of 50 mm. Mask and samples are available in stainless steel and graphite for relevant W7-X studies.

The heater plate allows heating of the samples to 600 °C. The sample can be exposed with a chosen surface orientation concerning the magnetic field lines. The angular positioning of the samples can be done with 360 degrees of freedom around the vertical axes and with an angle of 0°, 30°, 45°, 60° or 90° to the vertical plane. The samples can be placed at the desired radial distance up from the plasma center.

4.1.5 Diagnostics

Several relevant diagnostics, including movable Langmuir probes, a Quadrupole Mass Spectrometer (QMS), a Time-of-Flight Neutral Particle Analyzer (ToF

NPA), and video cameras have been installed for plasma characterization.

4.1.5.1 Movable Langmuir probes

The TOMAS device is equipped with a single and a triple Langmuir probe. Both probes are installed on vacuum manipulators at the low field side, allowing for a radial scan in the toroidal mid-plane. Thus, these diagnostics provide measurements of the radial electron density and temperature profiles as well as the plasma and floating potentials. The toroidal distance between the probe axes is 138 mm, as is shown in Fig. 4.13. The parameters measurement difference of both probes does not exceed 25 % [238, 239].

Impedans Ltd commercially makes the single Langmuir probe. The probe has a tungsten tip with the shape of the right circular cylinder with a height of 1.4 mm surmounted by a 1.5 mm diameter hemisphere. The tip is embodied in a ceramic with a diameter of 10 mm. The single probe uses RF and DC compensation schemes to minimize the influence of plasma perturbations on the measurement's quality. The system can provide reliable measurements of the electron temperature between 1 eV and 20 eV, plasma densities range from $1 \cdot 10^{11}$ m^{-3} to $1 \cdot 10^{18}$ m^{-3}, when the plasma potential is between -100 V and 145 V and the floating potential between - 145 V and 145 V.

The other Langmuir probe is the triple probe, which allows the determination of instantaneous plasma parameters without frequency or voltage sweeps [240]. The head of this probe embodies three cylindrical tungsten tips with a diameter of 0.8 mm and a length of 4 mm. The data collection and acquisition via an electrical circuit is shown in Fig. 4.14. The data acquisition system defines the parameter range measurement limitation.

4.1.5.2 Residual Gas Analyzer

The Residual Gas Analyzer (RGA) is an essential diagnostic for wall conditioning studies on TOMAS. It is based on the Pfeiffer PrismaPlus QMG 220 M2 Quadrupole Mass Spectrometer (QMS). The QMS has a grid ion source with two tungsten filaments and a Faraday cup as a detector. The operation range of the QMS is 1 u – 200 u (where u is a single atomic mass unit) with a resolution of 0.5. The QMS scan speed is 100 ms/u to 1 s/u in analogue and multi-ion detection modes.

The QMS is installed in the RGA tower, as shown in Fig. 4.15. It is done to minimize the influence of the magnetic field on the measurements. The QMS can be reliably operated in the pressure range of $1 \cdot 10^{-8}$ mbar

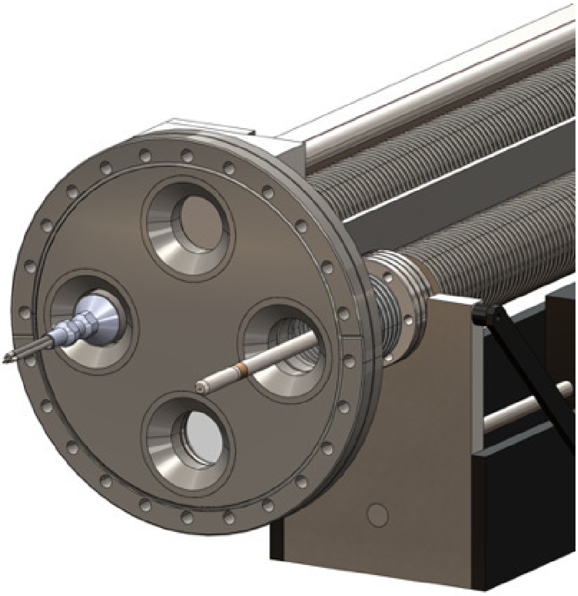

Figure 4.13: The 3D model of single and triple probes installed in the horizontal port of TOMAS.

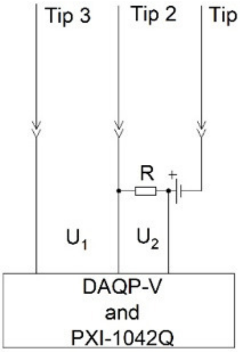

Figure 4.14: The triple probe connection circuit [239].

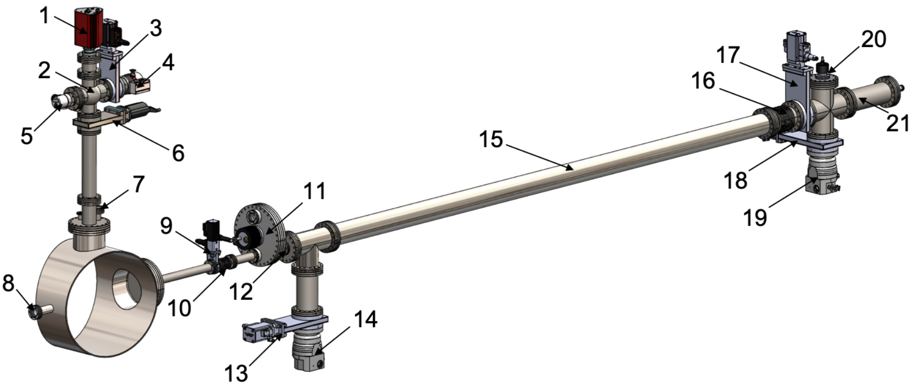

Figure 4.15: Time-of-Flight Neutral Particle Analyzer and Residual Gas Analyzer. 1 – Quadrupole Mass-Spectrometer (QMS), 2 – by-pass DN16 angle valve, 3 – DN63 electro-pneumatic gate valve, 4 – turbomolecular pump Pfeiffer HiPace 80, 5 - cold cathode gauge Pfeiffer IKR 270 (Penning gauge), 6 – DN63 manual gate valve, 7 – DN40 viewport, 8 - DN40 viewport, 9 – DN40 electro-pneumatic gate valve, 10 – DN40 bellow, 11 – chopper, 12 – pressure gauge Leybold PENNINGVAC PR 27, 13 – DN100 electro-pneumatic gate valve, 14 – turbomolecular pump Pfeiffer HiPace 300 H, 15 – DN100 flight distance pipe, 16 – DN100 bellow, 17 - DN100 electro-pneumatic gate valve, 18 - DN100 electro-pneumatic gate valve, 19 – turbomolecular pump Pfeiffer HiPace 300 H, 20 – pressure gauge Leybold PENNINGVAC PR 27, 21 – detector pipe [40].

– $1 \cdot 10^{-5}$ mbar. That is why the Pfeiffer HiPace 80 turbomolecular pump differentially pumps the RGA with a maximum pumping speed of 67 l/s (for nitrogen/air). The Penning gauge does the pressure monitoring for comparison with the RGA signals. The whole system works reliably at main vacuum vessel pressures below $6 \cdot 10^{-2}$ mbar.

4.1.5.3 Time-of-Flight Neutral Particle Analyzer

The Time-of-Flight Neutral Particle Analyzer (ToF NPA) is used in the TOMAS device to determine and study energy spectra of charge-exchange neutral fluxes from plasmas. Being previously installed on the reversed field pinch fusion device EXTRAP–T2R [241, 242], the ToF NPA has been modified and adapted to be integrated and operated on TOMAS. The working principle

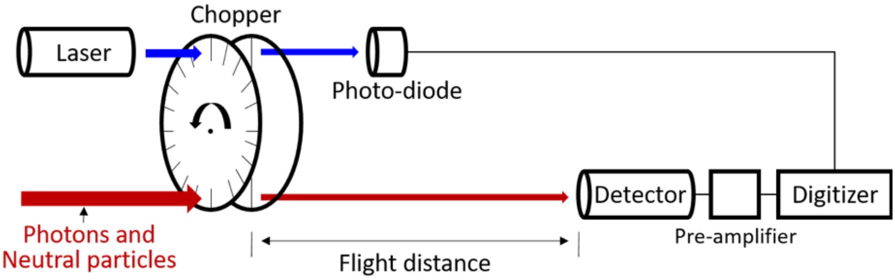

Figure 4.16: The scheme of the ToF NPA system [243].

of ToF NPA is schematically given in Fig. 4.16, while the 3D model of the diagnostic is shown in Fig. 4.15.

The ToF NPA system consists of a chopper tower, a flight path, and a detector tower. Together with the flight pass, the chopper tower is separated from the vacuum vessel and the detector tower. Both parts are differentially pumped by the Pfeiffer HiPace 300 H turbopump with a maximum pumping speed of 260 l/s. Leybold PENNINGVAC PR 27 pressure gauges monitor the pressure in the chopper and detector towers.

The chopper containing two aluminium coaxial disks is the main element of the corresponding tower. The rotating disk has 20 equidistantly separated radial rectangular slits with a size of 0.15 × 40 mm^2. It can achieve a rotation speed of up to 20 000 rpm. The second disk is fixed and has only two radial rectangular slits of the same size as the rotating disk. Thus, the slit opening time is about 1.8 μs for particles to pass through and the interval for consecutive particle passages is about 150 μs at the maximum rotation speed. One side of the chopper is used to separate the particle flux. The other serves as a port for trigger signal generation by the combination of a laser and a photo-diode. The flight pass has a length of 3 m and contains collimator plates with a central circular aperture of 35 mm diameter.

The detector tower which follows the flight distance pipe contains the Hamamatsu R595 head-on electron multiplier detector with the sensor active area of 10×12 mm^2. The powering of the detector, the detector signal output collection and the trigger signal collection are done using the CAEN DT5790 dual digital acquisition system based on a 2×250 MS/s and 12-bit waveform digitizer.

ToF NPA is aligned in the radial direction to the centre of the TOMAS device. The particles travel a total distance of 4.07 m after the chopper. The solid angle under which the detector is seen from the slits is 8.2 μSr. The neutral particle energy range of the ToF NPA is 10 eV - 1000 eV.

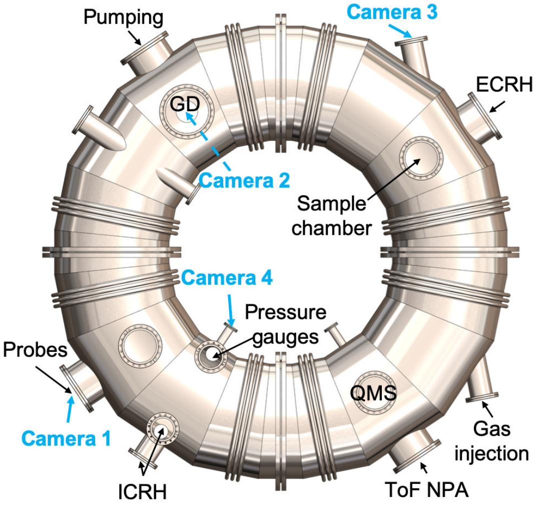

Figure 4.17: The scheme of the video diagnostic locations in the TOMAS vacuum vessel (Cameras 1, 2 and 3 are Logitech C615, Camera 4 is Arducam) [40].

4.1.5.4 Video diagnostics

TOMAS has two types of video diagnostics to monitor plasma operation and record different plasma events. The first type is used to observe the plasma from different positions. Three Logitech C615 USB HD video cameras are installed to view the tangential, radial and vertical (in front of the GD anode) direction of the vacuum vessel, as is shown in Fig. 4.17. These cameras are attached to viewports which are protected by a metal mesh. Each camera has a maximum image resolution of 8 MP, a maximum video resolution of 1920 × 1080 pixels with a frame rate of 30 fps and a Field of View of 78°.

The other type of video diagnostics is the Arducam 8MP wide-angle drop-in replacement video camera for Raspberry Pi Camera Module V2. The camera module is based on an 8 MP 1/4" SONY IMX219 CMOS image sensor with an image resolution of up to 3280 × 2464 pixel and a video resolution of 1920 × 1080 pixels with a frame rate of 30 fps. The camera is equipped with a 175°(D) ×145°(H) ×77°(W) wide-angle M12 lens with a f-number of 2.8 and a focal length of 2.5 mm. The camera module is mounted inside an endoscope placed inside a horizontal port of the vacuum vessel in front of the ICRH antenna. This camera is mainly used for the observation of plasma events in the antenna vicinity.

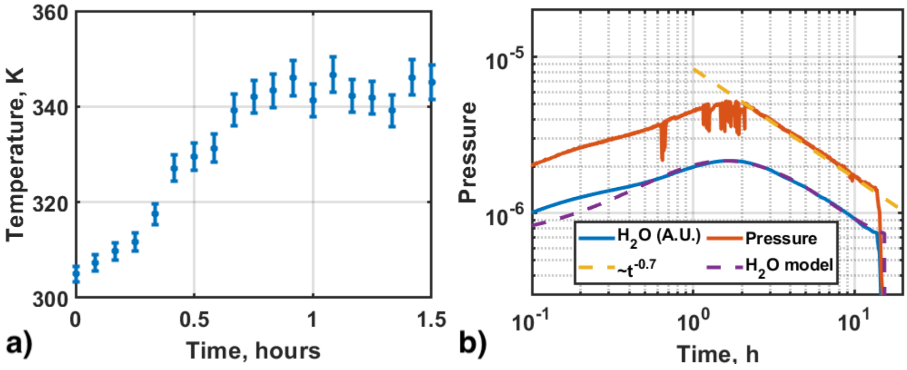

Figure 4.18: The experimental results of the first baking: a) average temperature of TOMAS vacuum vessel as a function of baking time during first 1.5 hours, b) the temporal evolution of pressure and the water release within the whole procedure of baking [102].

4.2 TOMAS studies aimed at W7-X wall conditioning optimization

The first results of TOMAS experiments relevant to W7-X conditioning procedures like baking and Glow Discharge Cleaning were discussed in [102]. After refurbishing the ECRH system and installing the new ICRF system, the EC and IC plasmas were partially characterized using the Langmuir probes [238, 239] and ToF NPA [243]. As the last step, the device has been prepared for the PSI studies related to the lasting effect of W7-X boronization.

4.2.1 Baking

One of the first experimental tests of the baking system was performed for $\sim$ 10 hours. The whole procedure can be split into the temperature rise phase and the temperature plateau phase. The maximum average temperature of the vessel wall did not exceed 80 $^{\circ}\mathrm{C}$ (the plateau phase) and was achieved after $\sim$ 45 - 50 minutes of the operation. The evolution of the vacuum vessel temperature is shown in Fig. 4.18a. The total pressure raised from $2 \cdot 10^{-6}$ mbar to $5 \cdot 10^{-6}$ mbar during 1.5 – 1.6 hours. Then, the outgassing started decreasing (Fig. 4.18b).

The QMS spectra clearly show that water ($m18$) is the most dominant outgassing impurity species (Fig. 4.19). Moreover, the signal of water repeats the common trend of the total neutral pressure. It should be noticed that

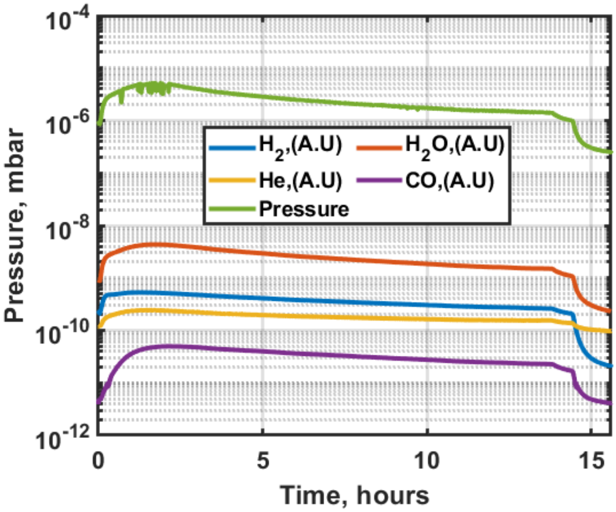

Figure 4.19: Time evolution of neutral gas pressure and the residual gas content obtained from QMS measurements.

the QMS signals are not calibrated, and the analysis is done by looking at changes of each impurity species separately. Nevertheless, according to the QMS data and its correlation to the penning pressure, water release can be considered the main contributor to the total pressure.

The baking experiments on TOMAS have shown that Andrew's model described in Sec. 2.2 is also suitable to characterize the water outgassing from the metallic PFC surface stimulated by thermal desorption. In this case, the model gives the change in the water concentration on the wall and hence it is equivalent to the net wall release rate, which is then balanced by vacuum pumping.

The result of the data fitting is shown in Fig. 4.18b. The fit of the partial water pressure is obtained by using Andrew's model (Sec. 2.2 Eq. 2.25). In this case, Andrew's model is chosen among other models (introduced in Sec. 2.1) because it allows to reproduce the outgassing behaviour during all stages of the baking procedure quite well. It is considered the average flat-top phase temperature of $T \approx 74\ ^{\circ}\mathrm{C}$(Fig. 4.18a) and $E = 26$ kJ $\cdot$ mol^{-1}, the desorption activation energy for water on stainless steel [244]. The results of the fitting give $K_p\beta_0$ equal to $1.8 \cdot 10^3$. This coefficient represents the balance between thermal desorption from the wall and reabsorption. C_{adj} is an additional source of impurities that represents the process on the PFC surfaces and leaks. The reabsorption is dependent on the vessel pressure. In this case, it is negligible at pressures below 10^{-5} mbar. Moreover, C_{adj} is comparable with $K_p\beta_0$. That leads to the outgassing rates of water and total pressure

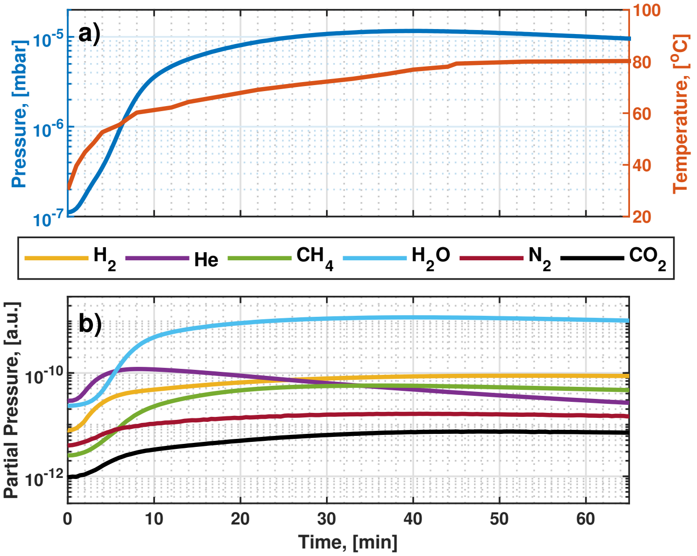

Figure 4.20: Results of the TOMAS vacuum vessel baking. a) time evolution of the average temperature of the vacuum vessel walls and neutral gas pressure (base pressure), b) time evolution of the residual gas content obtained from QMS measurements [40].

following the typical $\sim t^{-0.7}$ dependence when the average wall temperature reaches its maximum, as shown in Fig. 4.18b.

The results of the TOMAS baking test show that the outgassing during the flat-top phase follows the same power law corresponding to the literature overview given in Sec. 2.1(e.g. [50, 52]). It is also in good agreement with the W7-X baking results discussed in Sec. 3.3.4. In both cases, for TOMAS and W7-X (OP1.2a and OP1.2b), the outgassing content is dominated by water.

An additional bake-out of the vacuum vessel containing small graphite (e.g. GD anode) and ceramic elements was performed after the complete device upgrade to understand the outgassing behaviour of helium. The short bake-out was done for 65 minutes after an intensive ($\sim$ 2 hours) helium plasma (GD) operation with a pressure of $\sim 4 \cdot 10^{-3}$ mbar, anode current of 1 A and GD voltage of 260 - 280 V. The results of the experiment are given in Fig. 4.20.

As it was for the previous test, there were the same temperature phases. However, the plateau phase was achieved already after $\sim$ 45 min of baking. The pressure maximum of $\sim 1.1 \cdot 10^{-5}$ mbar occurred about 5 min before the average temperature achieved its maximum. Similar to the previous experiments, the QMS spectra shows that water is the most prominent outgassing species. The behaviour of the helium outgassing trend is entirely different from all other dominating impurities. The released helium concentration achieves its highest point in the residual gas after 6 – 7 min of baking. Then, it strongly decreases. This behaviour is also confirmed by experience in LHD [245, 246], showing the remarkable thermal outgassing of He from the metallic surface even at room temperatures. In the case of low wall temperature (below 175 $^{\circ}\mathrm{C}$), this desorption likely occurs by the de-trapping of helium weakly trapped in the distorted lattice around defects [246].

It means that an increase of the wall temperature at the level of the device baking can be employed for fast removal of retained helium after wall conditioning in helium. For example, it can significantly contribute to the minimization of helium dilution into consequent hydrogen plasmas. The same idea can be implemented in W7-X.

4.2.2 Glow Discharge studies on TOMAS

The installation of W7-X – like Glow Discharge system in TOMAS has given an opportunity to study some particular aspects of Glow Discharge, namely the plasma break-down and the erosion of PFCs. These studies aim to complement the results of W7-X OP1.2a and OP1.2b.

As for W7-X, the GD pressure operation window in TOMAS is also limited by the following factors. The high-pressure limit is determined by GD homogeneity, meaning how discharge spreads in the vacuum vessel, and reliability, avoiding large oscillations of the current and voltage. The lower-pressure limit is the level at which the discharge terminates. Moreover, a substantial increase of the discharge voltage causing an increase of the PFC erosion rate is observed at lower pressures close to this limit. The TOMAS GD system can be reliably operated in the pressure range of $2 \cdot 10^{-3}$ – $2 \cdot 10^{-2}$ mbar for hydrogen and helium considering these limitations. That means that the discharge is rather sustainable in the given pressure ranges and does not suffer from perturbation of voltage-current characteristics.

4.2.2.1 Hydrogen glow discharge

The discharge break-down in hydrogen can be achieved at the maximum possible anode voltage of 1.5 kV for pressures of $4 \cdot 10^{-2}$ – $6 \cdot 10^{-2}$ mbar, depending on how well the anode is conditioned. The discharge is ignited in the vicinity of the anode and stays localized when pressure is close to the break-down pressure values. The GD can also be localized in the vessel port

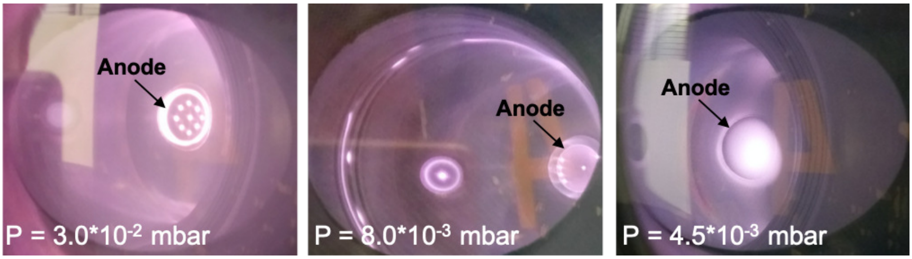

Figure 4.21: The homogeneity of H_2 -GDC and fireball formation according to pressure at the anode current of 1.5 A.

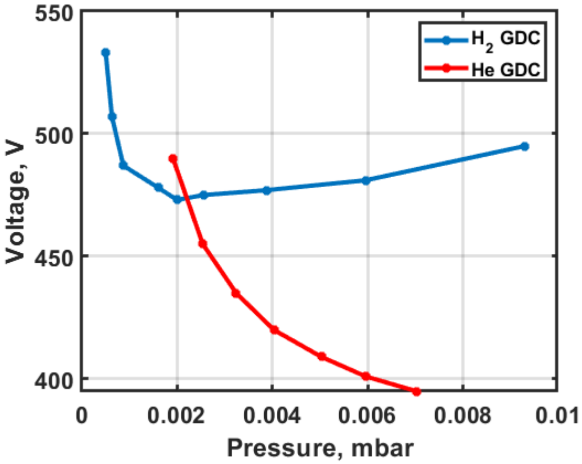

Figure 4.22: Operation voltage as a function of the pressure (measured by the Baratron) of H_2- and He-GDC at the current of 3 A.

cavities and sharp edges of in-vessel components at high pressures, as shown in Fig. 4.21. The voltage slowly decreases, and GD becomes more homogeneous when going from the break-down pressure to the lower pressure range optimal for steady operation ($2 \cdot 10^{-3}$ – $5 \cdot 10^{-3}$ mbar). The hydrogen GD voltage reaches its minimum at $\sim 2 \cdot 10^{-3}$ mbar at the discharge current of 3 A (Fig. 4.22) and $\sim 4 \cdot 10^{-3}$ mbar at the discharge current of 1.5 A. A strong voltage rise is observed when the pressure is further decreased. As mentioned earlier, a more uniform glow in the hollow cathode regime is due to the longer mean free paths of the secondary electrons are at low pressures. However, if the neutral gas pressure is too low, the anode voltage rises to maintain the requested current, as the secondary electrons have fewer ionizing collisions [85].

It should be noted that the location of the GD anode, low field side horizontal port vs top vertical port, has a minor influence on the obtained discharge parameters and plasma behaviour, as also found in [75]. However, high-pressure GD operation and the location of the anode in the horizontal port at the low field side could cause some rare events like fireballs (glow phenomena appearing as bright spheres and cylinders on the anode surface) formation (Fig. 4.21) described in detail in [247]. Besides the interesting physics behind these events, they also lead to potential damage to the anode surface.

4.2.2.2 Helium glow discharge

The dependence of the helium GD operation voltage on gas pressure is different in comparison to hydrogen GD. GD operation voltages as a function of helium pressures are given in Fig. 4.22. The minimum voltage cannot be reached without losing discharge homogeneity. It is necessary to increase the pressure to reduce the voltage further. However, it leads to a non-uniform discharge. When the pressure decreases, the voltage has a gradual growth.

In the case of helium GD, the discharge break-down is almost impossible to achieve at the maximum available power supply voltage of 1.5 kV and the maximum pressure (< $8 \cdot 10^{-2}$ mbar), which the pumping unit can safely maintain. According to the Paschen law (Eq. 2.28), for helium at a maximum voltage of 1.5 kV and a minimum distance of 2.5 cm between the anode and the wall, the break-down pressure should be above $8.1 \cdot 10^{-1}$ mbar.

4.2.2.3 Assisted GD break-down tests

The localization of the GD in the anode vicinity, vessel cavities and ports lead to more substantial erosion of the PFCs and possible damage of other in-vessel components by arcing. It is preferred to facilitate the break-down at low working gas pressures, meaning to assist the break-down, to prevent these spurious conditions. A known way is to use a special starting electrode like in the similar GD system of ASDEX-Upgrade [84]. There are other two solutions for the break-down achievement. The first one is a break-down in hydrogen and, then, a smooth gas exchange into helium, like it was for W7-X He-GDC break-downs in OP1.2a (Sec. 3.3.5.2). Another solution is an additional injection of an auxiliary gas with lower ionization potential, such as argon, available in TOMAS. The latter has been investigated in TOMAS using a localized short-time injection of gas with low ionization energy.

The auxiliary gas injection system allows making local argon injections behind the GD anode. The aim is to take advantage of a temporary pressure gradient in the torus during the gas puff and volume pumping after break-down. The parameters of the experiment are shown in Fig. 4.23. Helium was

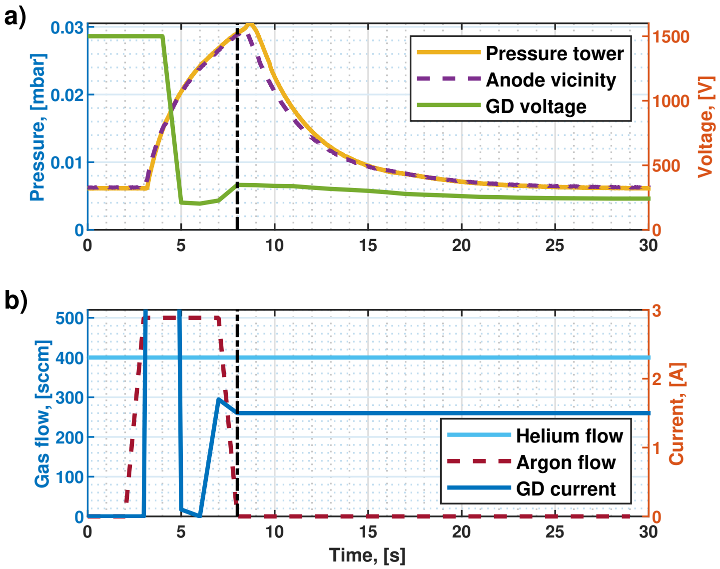

Figure 4.23: The He GD assisted break-down experiment (black dashed line indicates the event of the break-down): a) Vacuum vessel neutral gas pressure, the neutral gas pressure in the vicinity of the glow anode, and glow discharge voltage; (b) gas (He) flow from the main gas injection system, gas (Ar) flow from the auxiliary gas injection system, and glow discharge current [40].

injected at the constant flow of 400 sccm via the main valves. The anode is powered at the maximum available voltage of 1.5 kV, and the current was limited to 1.5 A. A short argon injection with a flow of 500 sccm was done in the anode vicinity until the break-down was achieved, which happened within $\sim$ 5 s after the start of argon injection. The break-down neutral pressure reached the level of $\sim 2.9 \cdot 10^{-2}$ mbar.

Due to the limited gas flow at the anode and the small dimensions of TOMAS, it has been found that the difference between the pressure measured in the anode vicinity and the pressure measured in the torus is negligible. A slight delay in the pressure response in the torus compared to the glow anode port is found. Nevertheless, the separate local injection of argon provides better control of the discharge ignition process. Overall, it lowers the break-down pressure and the pressure peak's duration, minimizing the discharge's localization and avoiding spurious events.

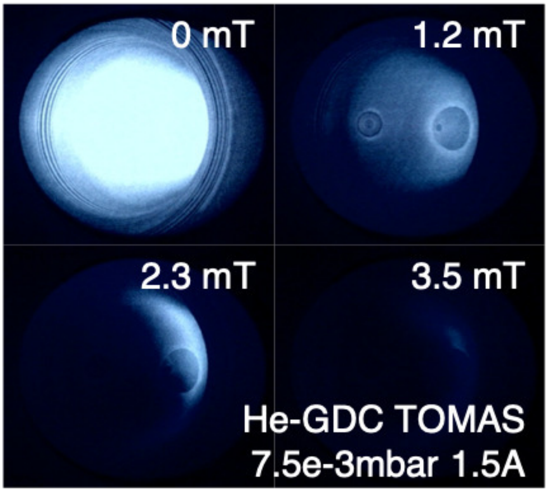

Figure 4.24: The localization and homogeneity of He-GDC at the various values of the toroidal magnetic field. The neutral gas pressure is $7.5 \cdot 10^{-3}$ mbar, and the discharge current is 1.5 A [94].

4.2.2.4 Influence of the magnetic field on glow discharge operation

Another exciting experiment illustrates the influence of the magnetic field on glow discharge homogeneity. As shown in Fig. 4.24, the glow discharge becomes strongly localized even at a small magnetic field value of 3 – 4 mT. While the GDC is incompatible with a toroidal field, poloidal fields may be employed to attract flux to specific wall areas. At magnetic field values above 4 mT, the glow discharge vanishes.

4.2.3 EC and IC plasma characterization

It is necessary to characterize these plasma types as part of the experiments that study wall conditioning or PSI aspects of ECWC and ICWC plasmas on TOMAS. This requires identifying the operation ranges of the parameters such as temperature, density and particle fluxes and understanding their dependence on the experimental conditions (magnetic field, input power, neutral gas pressure, etc.).

The first pre-characterization of EC, IC and mixed (EC+IC) plasmas on TOMAS has been done using the Langmuir Probes (in collaboration with KIPT Kharkiv Institute of Physics and Technology, Ukraine) and ToF NPA (in collaboration with KTH Royal Institute of Technology, Sweden). An example of TOMAS EC plasma images is shown in Fig. 4.25.

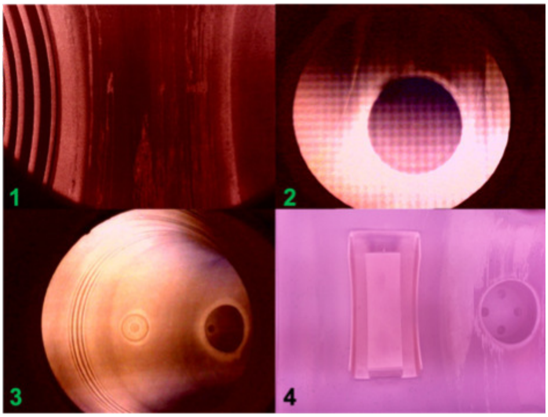

Figure 4.25: An overview of helium EC plasma (pressure of $1.2 \cdot 10^{-4}$ mbar, input power of 1.5 kW) from the location of 4 cameras as given in Fig. 4.17.

The Langmuir probe measurements deliver radial profiles of the electron temperature and density in the poloidal plane. The comparison of the single probe and triple probe measurements was presented in [238, 239]. Essential aspects of the Langmuir theory, data interpretation and corrections for the magnetized plasmas and their application on TOMAS are described in detail in [238].

4.2.3.1 Pre-characterization of IC plasma

The first electron density and temperature measurements were done for IC plasmas in hydrogen [238]. Two IC plasma profiles for relatively low ($2.1 \cdot 10^{-4}$ mbar) and high ($8.1 \cdot 10^{-4}$ mbar) neutral hydrogen pressures are shown in Fig. 4.26. The scans are done by moving the probes pulse by pulse, with 2 s long IC discharges with an input IC power of 3 kW at 14 MHz and a corresponding current of 1750 A in the magnetic field coils.

The highest electron temperature and density are located close to the low field side, at $r = 18$ cm and $r = 15$ cm, respectively, for both pressure values (Fig. 4.26). Specific temperature and density peaks at these locations are probably due to RF absorption physics, requiring further investigation. Both density profiles have a steep decrease towards the high field side. The temperature at the low field side is higher at higher pressure. The opposite is true for the high field side of the plasma. The plasma density and temperature show pronounced secondary peaks in the lower pressure pulse, hinting at further ICRF absorption physics effects. While more detailed studies are

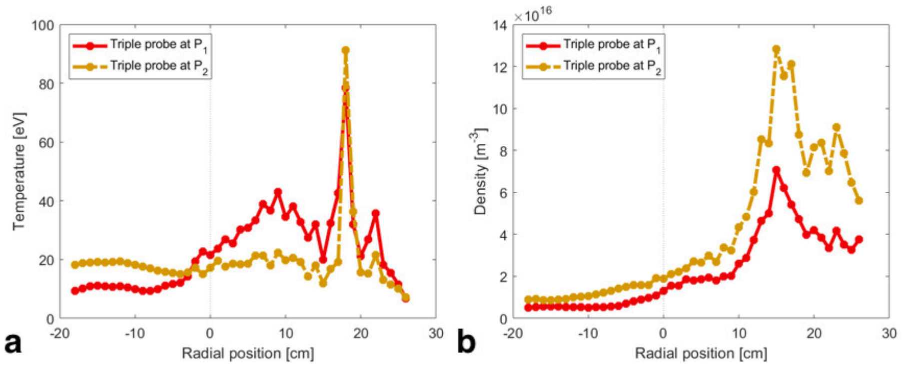

Figure 4.26: IC hydrogen discharge radial profiles of a) the electron temperature and b) the electron density for $P_1 = 2.1 \cdot 10^{-4}$ mbar, $P_2 = 8.1 \cdot 10^{-4}$ mbar, magnetic field coil current is 1750 A, IC input power is 3000 W, IC frequency is 14 MHz [238].

needed, these results already clearly illustrate the interest of the TOMAS set-up for fundamental ICWC studies.

To look further into the pressure dependency of the hydrogen IC discharges, pressure scans were done at two fixed radial probe positions ($r_1 = 22$ cm, $r_2 = 12$ cm). The results are shown in Fig. 4.27. The discharge parameters were the same as in the previous experiment. For both radial positions, the electron temperature decreases while the density increases with the increase in neutral gas pressure, as concluded from the previous example. In the given experimental configuration, the decrease of the electron temperature becomes more gradual, going from the low field side to the center of the plasma vessel. Similar to the electron temperature behaviour, the density trend steepness depends on the radial position. The current operation window of the ICRF system allows achieving plasma densities of up to $5 \cdot 10^{17}$ m^{-3} and temperatures of 10 eV – 90 eV [40].

4.2.3.2 Pre-characterization of EC plasma

The pre-characterization of EC plasmas using the triple probe was done for two input powers and two neutral gas pressures in [239]. In the case of the first studies of EC plasmas, 2 s EC discharges were conducted in helium with a magnetic field corresponding to the coils' current of 1400 A.

As an example, the comparison of two EC discharges with 1 kW and 2 kW of input power at the same neutral gas pressure of $3.8 \cdot 10^{-4}$ mbar

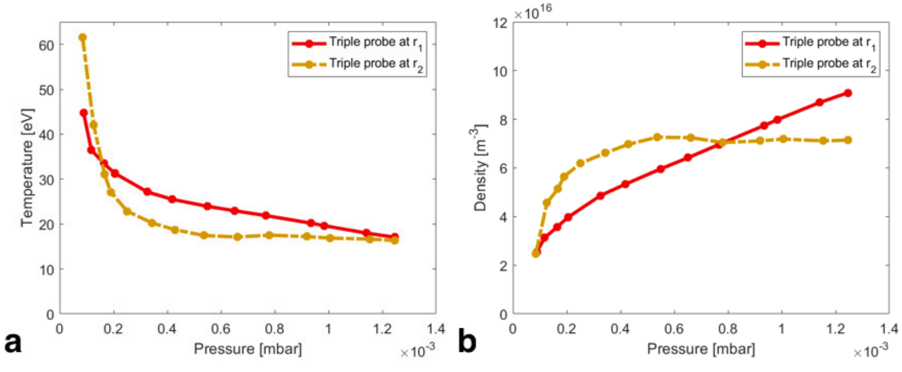

Figure 4.27: IC hydrogen discharge pressure scan of a) the electron temperature and b) the electron density for the radial positions $r_1 = 22$ cm, $r_2 = 12$ cm, the magnetic field coil current is 1750 A, the IC input power is 3000 W, the IC frequency is 14 MHz [238].

and two discharges at two different neutral gas pressures ($3.8 \cdot 10^{-4}$ mbar and $2.7 \cdot 10^{-4}$ mbar) with the same EC input power of 2 kW are shown in Fig. 4.28.

The increase of EC input power has almost no influence on the electron temperature along with the radial measurements in the equatorial plane. However, a slight difference can be seen close to the high field side (at $r = 17.8$ cm), where the maximum temperature change occurs from $\sim$ 7.8 eV to $\sim$ 9.5 eV. At the same time, the electron density increases by a maximum factor of 1.6. The peak of the plasma density shifts towards the low field side by $\sim$ 4.5 cm. The pressure decrease leads to the electron temperature increase by a factor of 1.1 - 1.5 in 2 kW discharges. The edge region behind the antenna box at the low field side is not considered in this comparison. The electron density is generally lower at lower pressure except for the region from $r = -14$ cm to the high field side and $r \approx 8.2 - 10.2$ cm, where the density reaches its maximum value. The density peak at lower pressure is shifted towards the high field side at lower pressure.

These plasma parameters behaviour at power and pressure variation is typical for a low-temperature and weakly ionized EC plasma. The obtained results also correlate with the previous EC plasma studies on TOMAS [101, 229].

Overall, the TOMAS ECRH system allows generating discharges with electron densities of $1.8 \cdot 10^{17}$ m^{-3} – $6.6 \cdot 10^{17}$ m^{-3} and electron temperatures of 8 – 15 eV for helium plasmas and $4 \cdot 10^{16}$ m^{-3}– $3 \cdot 10^{17}$ m^{-3} and 1 – 23 eV

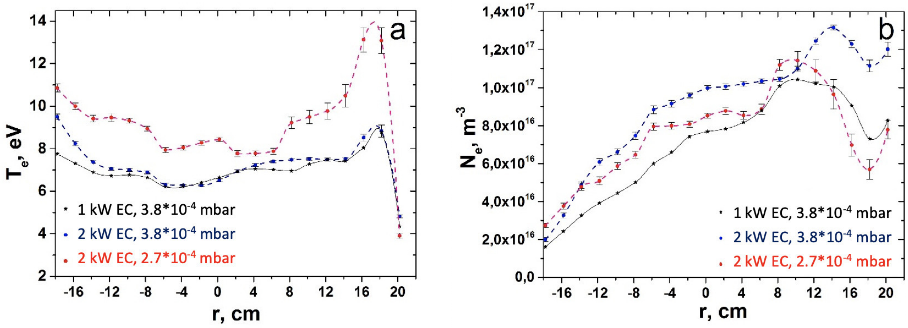

Figure 4.28: Radial distributions of a) the electron temperature and b) the electron density for helium EC discharges at two input power values and two pressure levels [239].

for hydrogen plasmas, respectively.

4.2.3.3 Pre-characterization of EC+IC plasma

The studies of mixed EC+IC plasmas were based on adding IC power at 25 MHz to the EC discharges described above. Thus, the parameters of the magnetic field, working gas and discharge duration are the same as in the previous example. The first experiment compares different IC input powers added to 1 kW of EC power at a neutral gas pressure of $3.8 \cdot 10^{-4}$ mbar shown in Fig. 4.28. The studies show that adding more IC power to the EC discharge increases the electron temperature while the electron density decreases. The most pronounced changes are in the area with peaked temperature. The dependence of plasma parameters on the IC input power in mixed plasmas at a constant gas flow and EC input power has different behaviour than the EC plasma characteristics described above. These differences can be associated with a seemingly strong relation between power absorption, plasma temperature and density, and particle sources and losses in different plasma areas. However, it requires a self-consistent description of these plasmas using modelling, e.g. TOMATOR [97].

Another interesting example of EC+IC plasma characterization is related to the comparison of plasma parameters with the similar amount of IC input power (0.65 – 0.79 kW) and variation of neutral gas pressure (from $3.8 \cdot 10^{-4}$ mbar to $2.7 \cdot 10^{-4}$ mbar) and EC input power (from 1 kW to 2 kW). The result of these experiments is presented in Fig. 4.29.

Increasing the EC input at constant pressure power in mixed plasmas leads to a density increase and small changes in the electron temperature.

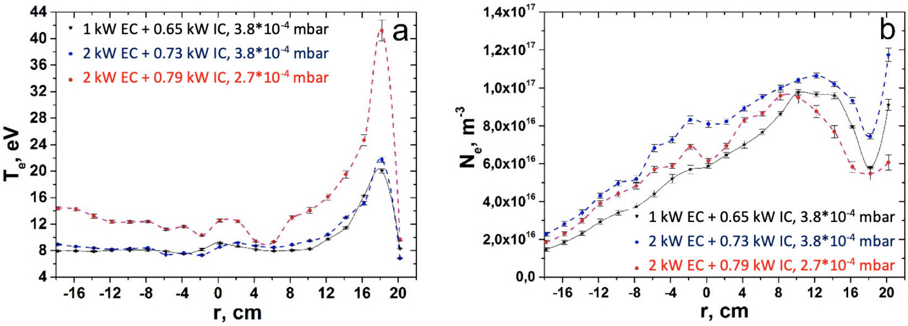

Figure 4.29: Radial distributions of a) the electron temperature and b) the electron density for helium EC+IC discharges at two EC input power values, two pressure levels and almost the same IC input power [239].

The peak temperature has a slight growth in this case. However, by decreasing the neutral gas pressure, one can see a rise in the electron temperature. The maximum temperature has increased by a factor of ~ 2. At the same time, the electron density has a slight decrease and shift of its maximum value towards the high field side by ~ 3 cm.

The current studies show that changing the plasma parameters independently from the EC discharge is possible by adding IC power to the EC discharge. Determining EC and IC operational ranges (e.g. power and neutral pressure) can create an additional tool for controlling plasma parameters, such as flux and energy of neutral particles. It can have a direct impact on the conditioning efficiency of RF mixed plasmas. For example, under the longer time sequence, the EC+IC conditioning plasma significantly decreased the wall hydrogen compared with the conventional ICWC applied in LHD [103]. This experience is of particular interest in developing a new wall conditioning technique relevant for W7-X.

The operational ranges of plasma density and temperature using EC and IC will be analyzed in more detail in future.

4.2.3.4 Neutral particle flux determination

The determination of low energy neutral particle flux and the assessment of the neutral distribution under the different experimental conditions for EC, EC+IC and IC plasmas significantly contribute to the understanding of wall conditioning mechanisms under permanent magnetic field [243].

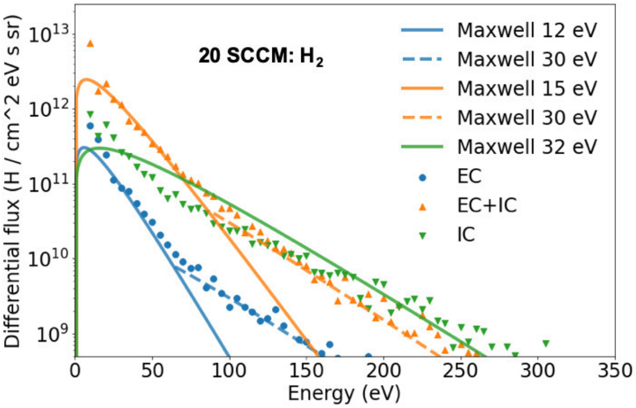

Figure 4.30: Differential flux spectra of neutrals (scatters) of the three different phases in the integrated set with a pressure of $2.4 \cdot 10^{-4}$ mbar and the calculated Maxwell energy distribution fitting.

The ToF NPA measurements were done in plasma pulses with three 2 s long phases; the first series with only EC heating, the following series with mixed EC + IC plasma, and the last series with 2 s of IC plasma. Two sets of experiments were carried out. Each set consisted of 20 pulses repeated under the same experimental conditions: corresponding magnetic field coil current of 1400 A, the EC input power of 2 kW, the IC input power of 1 kW at 25 MHz. The first set had neutral hydrogen pressure of $\sim 6.0 \cdot 10^{-4}$ mbar. The pressure of another experimental set was $\sim 2.4 \cdot 10^{-4}$ mbar.

The differential monoatomic hydrogen neutral fluxes for each phase of the experimental set with a neutral gas pressure of $2.4 \cdot 10^{-4}$ mbar is presented in Fig. 4.30. The differential fluxes are fitted to the Maxwellian energy distribution [243]. The complex picture of experimental results containing integrated differential fluxes in the 10 - 725 eV energy range and 4π geometry is given in Table 4.3.

The highest neutral particle flux is observed in the EC+EC plasma phase for both values of neutral gas pressure. In the EC phase, the fluxes are almost one order of magnitude lower. The IC plasma phase is characterized by a higher mean neutral particle energy than the EC+IC plasma phase. The latest can be explained by the higher electron density of EC+IC plasma making available less power per charged particle. The increase of neutral gas pressure leads to the reduction of the higher energy neutrals' fraction. It also causes the increase of the electron density and decreases the mean neutral particle energy.

The characterization of the neutral particle fluxes will significantly

Table 4.3: Experimental results in each phase [243].

Pressure	**Phase**	**Neutral flux** $(H^0 cm^{-2} s^{-1})$	$\mathbf{n_e}$ $(\cdot 10^{15}\mathrm{m}^{-3})$	**Energy of neutrals** (eV)	$\mathbf{T_e}$ (eV)
$2.4 \cdot 10^{-4}$ mbar	EC	$0.11 \cdot 10^{15}$	5.5 - 40	12	2 – 9
	EC+IC	$1.11 \cdot 10^{15}$	8.1 - 40	15	4 – 18
	IC	$0.24 \cdot 10^{15}$	1.4 - 10	32	7 – 36
$6.0 \cdot 10^{-4}$ mbar	EC	$0.06 \cdot 10^{15}$	1.0 - 27	7	1 – 7
	EC+IC	$0.50 \cdot 10^{15}$	7.5 - 28	16	3 – 17
	IC	$0.23 \cdot 10^{15}$	2.0 - 12	28	5 – 23

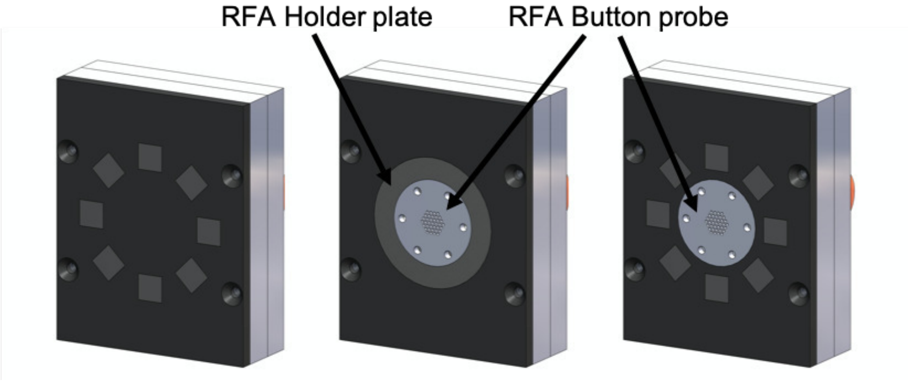

Figure 4.31: Sample holder modifications including integration of RFA: only samples (left), only RFA (centre), samples and RFA (right).

contribute to the interpretation of further experiments related to exposure of pre-characterized samples made of W7-X wall material (graphite) to different types of wall conditioning plasmas.

4.2.4 Further upgrades and experimental contribution

The next step of the TOMAS experimental activity contributing to some aspects of W7-X wall conditioning and PSI studies is to

- Study of boron coating lifetime by exposure of boron-coated W7-X graphite samples (contribution to boronization studies) to GDC and ICWC,
- Reproduce and mitigate spurious conditions observed to produce damage in W7-X during GDC in a similar environment of TOMAS.

4.2.4.1 Preparation for boron coating lifetime studies

First experiments on removing boron from coated polished graphite samples made from W7-X tiles by helium glow discharge are supposed to be in the scope of a contribution to W7-X boronization studies. The graphite samples have a geometry shown in Fig. 4.12a. The coatings are applied via magnetron sputtering to a thickness of 40 nm due to limits of delamination. The coating thickness is pre-analyzed by 3 MeV protons via the particle-induced gamma-ray emission (PIGE) technique. The erosion rates will be studied at different glow discharge conditions (helium pressure of $\sim 4 \cdot 10^{-3}$ mbar and current of 0.5 – 1.6 A) and surface temperatures (20 – 600 $^{\circ}\mathrm{C}$).

Exposure of the boron coated graphite samples to ICWC requires additional device modifications and further characterization of IC plasmas. The first modification requires assembly and installation of the second triple probe in the vertical plane. The triple probe is similar to the one already exploited on TOMAS (described in Sec. 4.1.5.1). It is supposed to be installed in the vertical port available in the same section of the vacuum vessel. The first characterization of electron density and temperature in two dimensions of ICWC plasmas with different experimental parameters should follow the installation. In parallel, the neutral particle spectra (from 10 to 725 eV) will be further explored to identify the best parameters of ICWC (frequency, power level, discharge duration and duty cycle) used in the boron erosion experiments.

The modification of the sample holder is also essential for this type of experiment. A significant improvement is installing a Retarding Field Analyzer (RFA), mountable on the sample manipulator, to characterize the ion flux and ion energy distribution at the surface substrates in real-time. The preliminary system design based on Semion Retarding Field Energy Analyzer (Impedans Ltd.) is shown in Fig. 4.31. The design of the sample holder modification and the RFA integration includes an option of RFA - only installation using a button holder plate as well as a combination of samples and an RFA button. The last option allows having simultaneous measurements during sample exposure experiments. However, it may be subject to contamination by an eroded mask material redeposition. The operational parameters of the RFA system are given in Table 4.4.

4.2.4.2 Reproduce of spurious conditions caused by GDC

Tests that reproduce the spurious conditions observed during GDC in W7-X were done while exposing W7-X like in-vessel components in TOMAS. A simple PFC construction containing W7-X heat shield graphite tiles was built

Table 4.4: Technical and operation parameters of RFA.

Parameters	Values	Units
Holder plate radius	25	mm
Button probe radius	16.5	mm
Pressure Range	< 0.4	mbar
Ion Flux	0.001-700	A/m^2
Ion Energy Range	0 - 2000	eV
Ion Density Range	$10^{12} - 10^{20}$	m^{-3}
Operating temperature	< 150	$^\circ$C
Energy Resolution	± 1	eV

to mimic a part of the W7-X first wall component. The construction was based on the 1 mm thick 200 mm × 300 mm copper plate. Four graphite tiles were mounted on the top of the copper plate and fixated by hexagonal screws, as shown in Fig. 4.32. The average width of the gap between tiles edges was $\sim$ 1.5 mm. The construction was put at the bottom of the vacuum vessel. It was observed by one of the cameras from the top port (Fig. 4.33).

This first test aimed to observe any arcing or discharge localization events in the vicinity of the exposed construction at the GD break-down regime (neutral gas pressures above $4 \cdot 10^{-2}$ mbar) and explore the influence of long exposure on the construction elements at regular operation regime ($2 \cdot 10^{-3}$ - $5 \cdot 10^{-3}$ mbar). The construction was exposed to hydrogen and helium GD at the current of 1.5 A.

An example of the pressure rise during the tiles exposure to hydrogen GD is given in Fig. 4.33. As in the previous GD experiments, the increase of neutral gas pressure leads to GD localization in the ports and vacuum vessel cavities. The GD localization in the port, in front of the PFC construction, is shown as a bright spot on the camera images. The spot brightness increases with the pressure increase. Other cameras have not shown any extraordinary events.

During the exposure at the pressures corresponding to the break-down regime, both in hydrogen and helium, events like arcing or discharge localization on the construction were not observed. However, some small traces of arcing have been found on the back side of the copper plate, which was in close contact with the vacuum vessel wall (Fig. 4.34a).

Besides the high-pressure experiments, the PFC construction was exposed to $\sim$ 4 hours of hydrogen GD at $\sim 4 \cdot 10^{-3}$ mbar and $\sim$ 4 hours of helium GD at $\sim 3 \cdot 10^{-3}$ mbar with some breaks between experiments. All this time, the construction remained in the vacuum vessel. After the exposure

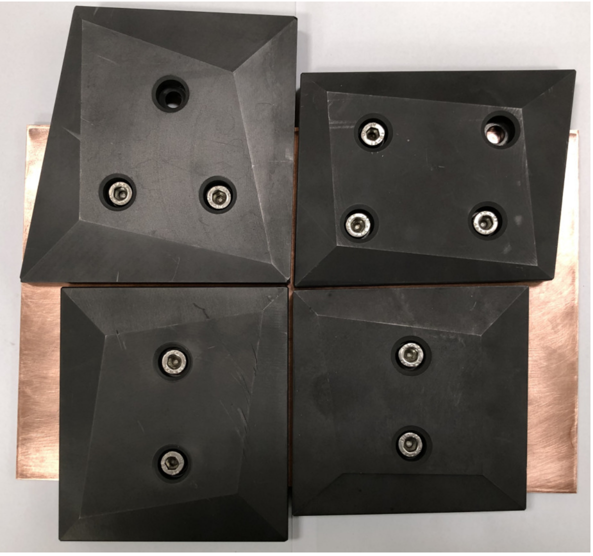

Figure 4.32: The PFC construction for first tests of GDC spurious conditions. Four spare W7-X heat shield graphite baffle tiles are mounted by stainless steel hexagonal screws on top of the copper plate to imitate a small part of the W7-X first wall.

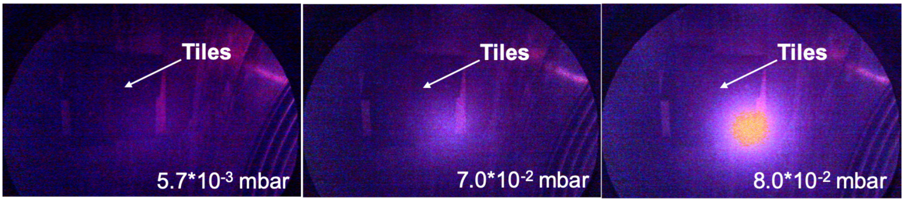

Figure 4.33: An example of PFC construction exposure to hydrogen GD at the current of 1.5 A.

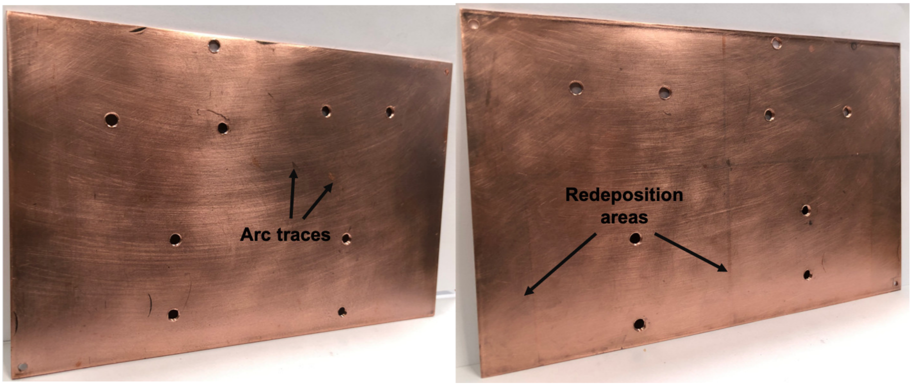

Figure 4.34: Two sides of the base copper plate after the exposure: a) back side, b) front side (the side where the graphite tiles were attached).

experiments, all parts of the construction have been visually examined. The most noticeable changes have been found on the front side of the copper plate (Fig. 4.34b). The surface of the back side has not experienced any significant modification, not taking into account minor traces of arcs. The surface difference between the back and front sides after the exposure is shown in Fig. 4.34.

The front side has areas covered by a layer of redeposited graphite. The redeposition areas repeat the contour of the tiles attached during the experiment. It indicates that the material (graphite) redeposition and arc traces seen on remote W7-X surfaces (discussed in Sec. 3.3.5.4) is due to GDC. The redeposition pattern is similar to one given by the W7-X first wall elements examination. The next step will be distinguishing between the impact of H_2-GDC and He-GDC on the damage of in-vessel components. Moreover, further detailed analysis is required to determine the layer thickness and structure of the redeposited graphite and its correlation with exposure time.

Unfortunately, the extensive studies dedicated to reproduction and mitigation of GDC spurious conditions in TOMAS and complete characterization of exposed samples in GDC and ICWC plasmas were delayed due to the COVID-19 pandemic. Thus, the detailed analysis of the experimental results could not be included in this PhD thesis.

Chapter 5

Wall Conditioning strategy at W7-X operating with graphite divertor and conclusion for future operations

> *Things are always obvious after the fact.*
> Nassim Nicholas Taleb, Fooled by Randomness

This chapter takes the lessons learned from the previous chapters and summarizes these into a strategy for wall conditioning in the upcoming W7-X campaign. The author looks forward to the commissioning of the ICRH system of W7-X, developed jointly at ERM and FZJ. It partly aims at wall conditioning and plasma production applications, in addition to plasma heating and fast particle generation. Supplementary studies to be performed in other devices are proposed to prepare the operation of the first ICRF conditioning plasmas in W7-X. Finally, an overview of further possible wall conditioning studies is given for future device operation.

5.1 Synopsis of wall conditioning strategy

Different wall conditioning techniques were optimized and combined into a wall conditioning strategy to achieve high plasma performance throughout W7-X campaigns. The current wall conditioning strategy comprises two phases (Fig. 5.1). The first phase, the so-called initial wall conditioning phase, is performed prior to the first plasma to provide the minimum conditions for the operation. The initial wall conditioning set starts with 11 days of vacuum vessel bake-out (Sec. 3.3.4). The baking has a flat top phase of a minimum of 7 days at the average PFC temperature of 150 $^\circ$C, while other days are reserved for the steady temperature rise of the vessel and the cool down. The baking suppresses higher hydrocarbons in the residual gas content and removes most of the water retained at the PFC surfaces. The following step of the initial wall conditioning set is GDC (Sec. 3.3.5). This step consists of two parts. First, at least 9 -10 hours of GDC in hydrogen should be performed to further reduce water, methane and carbon oxides from the main wall and divertor surfaces by an almost uniform ion flux in the glow discharge. The optimal parameters of H_2-GDC are a pressure of $\sim 4.5 \cdot 10^{-3}$ mbar and an anode current of 1.5 A. The glow discharge is performed at the maximum available pumping speed in order to minimize the impurity redepositing. The entire duration can be achieved in one continuous discharge or multiple shorter discharges. The next and final step is He-GDC applied with a minimum duration of 2 hours to desaturate the walls from the hydrogen retained by the H_2-GDC application. He-GDC is operated at a neutral gas pressure of $\sim 3.8 \cdot 10^{-3}$ mbar and an anode current of 1 A. The current of He-GDC is lower compared to H_2-GDC to mitigate PFC erosion.

The second phase of the wall conditioning strategy is a set of wall conditioning techniques routinely applied during plasma operation. Before the first boronization, it is recommended to apply H_2-GDC weekly to avoid the accumulation of impurities produced by the physical and chemical sputtering during plasma operation and leaks. Also, 15 – 20 minutes of He-GDC should be applied daily to start each experimental day with good hydrogen recycling conditions. Both GDC procedures have the same operating parameters as those used in the initial wall conditioning. After the first boronization, GDC should be skipped to avoid a potential boron layer erosion.

The boronization procedure based on GD application (anode current of 1 A) in the mixture of diborane and helium with a proportion of 10:90 should be applied monthly to maintain high plasma performance (Sec. 3.3.6). A revision of this frequency may be needed when the operations programme goes towards significantly longer integrated plasma durations than those achieved in OP1.2b. The steady boronization glow (coating phase) has to be done with the neutral gas pressure below $5 \cdot 10^{-3}$ mbar to have a more homogeneous coating. A sufficient boron layer is deposited within 3.5 - 4 hours, keeping the pumping speed about 2000 l/s. An increase in the pumping speed will lead to the shortening of the coating procedure. However, it should be done only by equipping additional pumping stations with diborane processing equipment.

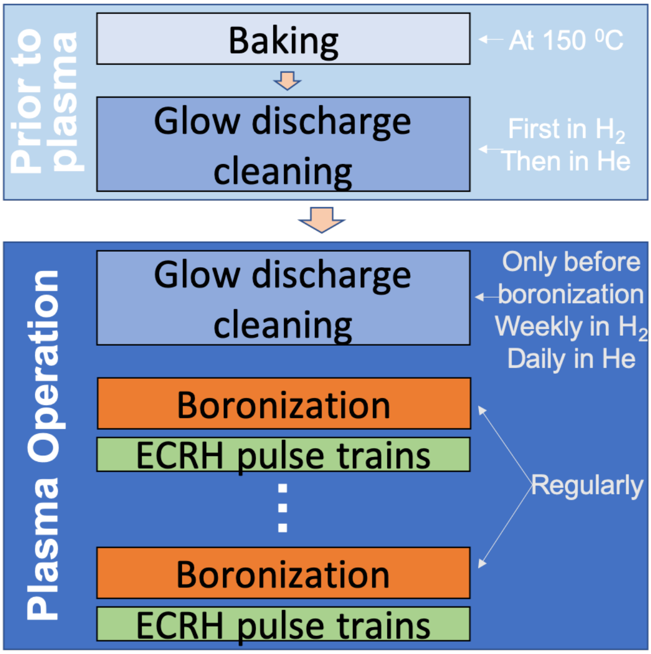

Figure 5.1: Scheme of the wall conditioning strategy.

Further development of the boron powder dropper or its analogue (PMPI) should be envisaged to extend the boron coating lifetime, e.g. at high fluence plasma surfaces (Sec. 3.3.7). When using the PMPI in ECRH heated plasmas, the amount of injected material should not exceed 20 mg/injection with the injection frequency of 2.8 Hz [223].

ECWC is a time-efficient manner to control the fuel recycling throughout an experimental day, e.g. when switching from pulses with high fueling to ones with low fueling (Sec. 3.3.8). Indeed, when strong wall fueling interferes with the device operation at the density range below $\sim 6 \cdot 10^{19}$ m^{-3}, conditioning is recommended. ECWC is performed using ECRH pulse trains in He and in presence of the magnetic field. The optimized He pulse train for application in the boronized device has the following parameters: the pulse length is 3 s, the pulse interval is about 30 – 35 s, the input power is 2.1 MW using three gyrotrons (for the first 50 ms of each discharge the input power is recommended to be slightly higher for a quick and robust break-down), gas prefill should be done 100 ms prior to each discharge with a duration of 15 ms at the constant gas flow of 75 mbar · l/s. When possible, one should apply DC+AC strike lines sweeping in the pulse trains (from discharge to discharge, the DC in the control coils is changed between – 2500 A and 2500 A while the

AC is kept at 625 A with a frequency of 20 Hz) to increase the removal and maximize the affected area. It is especially beneficial for the density control recovery after applying longer pulses where the strike lines move due to the slow ramping of the plasma self-produced currents.

Moreover, maintaining divertor temperatures above 400 °C during the pulse train application enhances the fuel removal rate. Pulse trains are launched as one experimental programme via the central control system. As such, they are experimental programmes rather than technical procedures placed between programmes. Increasing the efficiency of a pulse train, by the means mentioned above, allows making the best use of the allocated time for the pulse train execution. The conditioning action, nevertheless, increases the likelihood of success for the subsequent programme. Hence the time allotted to conditioning must be seen as favourable for the experimental outcomes.

5.2 Ion Cyclotron Wall Conditioning for future W7-X operation

The upcoming operational phase, OP2, is expected to start at the end of 2022. The planned stepwise extension of plasma discharge durations up to 30 minutes and a dense experimental program will require continuous improvement of the current wall conditioning techniques. OP2 is characterized by the first usage of the water-cooled High Heat Flux divertor units and other actively cooled PFCs [248]. Additionally, cryopumps are planned to be installed behind the new divertor targets [249]. Both temperature control of a significant part of the in-vessel components and a significantly increased maximum pumping speed will affect the conditioning needs. Besides the further upgrades of the ECRH and NBI systems, increasing its deliverable power, an ICRH system capable of delivering $\sim$ 1.5 MW of RF power at frequencies between 25-38 MHz in discharges up to 10 s will be installed [250]. The latter opens a new opportunity for the development and studies of ICWC in W7-X.

The efficiency of ICWC can be much higher for density control than in the case of the currently used ECWC [251]. Moreover, ICWC studies in JET showed that ICWC features a comparable fluence per energy unit and particle-material-interaction as in GDC [252]. Thus, ICWC is expected to be a powerful tool that can be used as an alternative to the currently employed wall conditioning techniques in the presence of a magnetic field.

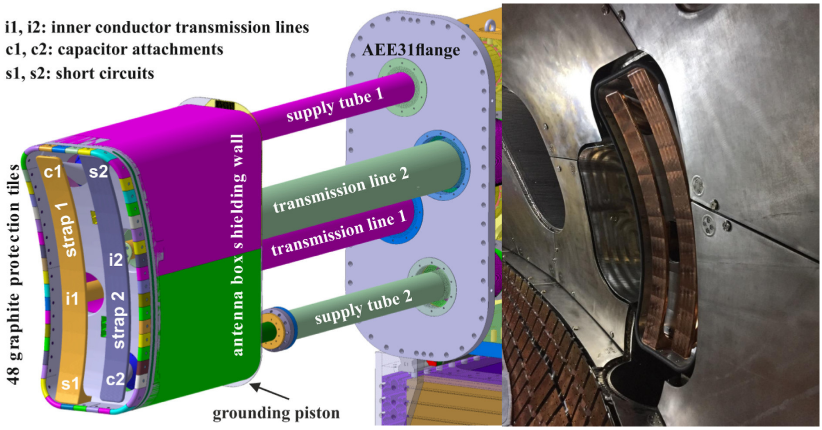

Figure 5.2: The ICRH antenna system: a) model of the antenna box (outer height of 924 mm, outer width of 378 mm), antenna straps (height of 866 mm, width of 90 mm, depth of 15 mm), and feeding lines [41], b) picture of the installed antenna in W7-X(view from the vacuum vessel).

5.2.1 ICRH system of W7-X

The ICRH system of W7-X is built for plasma heating, generating high-energetic ion tails (up to 200 keV) for fast particle confinement studies, target plasma production and ICWC with low power operation (up to a few hundred kW) [41].

The ICRH system is based on a two-strap antenna with the same 3D surface shape as the Last Closed Flux Surface (LCFS) of the plasma in the standard magnetic field configuration. The antenna head consists of the antenna box made of stainless steel and antenna straps recessed inside the box by 10 mm (Fig. 5.2). Graphite tiles cover the front surface of the antenna box. Each strap is connected to a tuning capacitor (pre-matching system) on one end and grounded to the antenna box on the other end. The power is fed to the straps via a central feeding tap almost in the middle of its poloidal dimension. The antenna head can be radially moved as a whole with a speed of 3 mm/s over 350 mm during plasma operations. Between the RF heating pulses, up to 10 s long and applied to NBI or ECRH target plasma, the antenna will be retracted into the port.

The antenna is planned to be powered by two 25 - 38 MHz RF generators allowing to operate the system at any strap phasing flexibly. The maximum power of $\sim$ 1 MW can be delivered for dipole $(0, \pi)$ phasing and

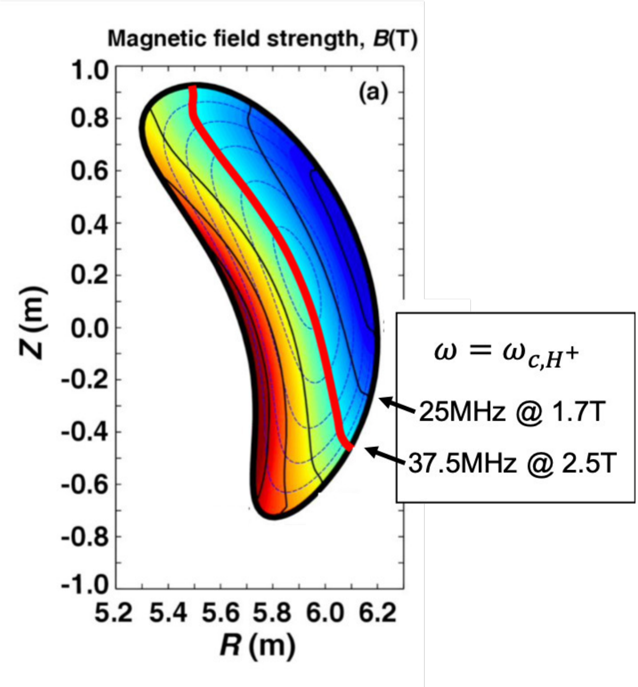

Figure 5.3: Locations of the IC resonance layers corresponding to the different ICRH frequencies and toroidal magnetic field values.

$\sim$ 2 MW for monopole (0,0) phasing. One generator is available at the start of OP2, effectively limiting the phasing to monopole or dipole only.

The antenna box is equipped with two Piezo valves that provide short hydrogen or deuterium puffing in the scape-off-layer for coupling improvement. However, these valves should not be used to assist the IC breakdown avoiding high pressures in the vicinity of the antenna. Microwave interferometers will also be installed in the antenna box for electron density and plasma turbulence characteristics measurements. Most of the antenna head components are water-cooled. The cooling system can also provide 150 $^{\circ}\mathrm{C}$ for initial wall conditioning and keep $\sim$ 100 $^{\circ}\mathrm{C}$ for regular conditioning to minimize the absorption and redeposition of the impurities released from the PFCs.

5.2.2 ICWC scenarios

As already mentioned, the ICRH system will also be used for plasma production, namely for the wall conditioning application and target plasma production. The latter is needed for operation at the reduced toroidal magnetic field of 1.7 T for the ECRH X3 heating scenario [253]. As the X3 waves are effectively absorbed only in sufficiently hot plasmas, a preheating stage that does not use ECRH is needed. Thus, ICRH target plasmas will need to be used for this type of operation. ICRF plasma production is shown to work at any typical toroidal magnetic field and frequency ranges in present tokamaks. For target plasma production, it may be advantageous to operate in helium with the cyclotron resonance frequency of the hydrogen ion close to the vessel axis, which is the case at 25 MHz at 1.7 T, and as well at 37.5 MHz at the standard field of 2.5 T (Fig. 5.3). Thus, RF plasma parameters may vary depending on the chosen frequency and toroidal magnetic field, besides other parameters such as pressure and power. The optimal values need to be explored concerning the envisaged application. ICWC and IC target plasma production have similar plasma production aspects but different optimization indeed. While the purpose of IC target plasma is to reach the maximum electron temperature and density in the core and is ideally fully ionized, the partially ionized ICWC discharge aims to increase fluxes of neutrals to the PFCs.

Potential applications of ICWC in W7-X are impurity removal by hydrogen ICWC, wall desaturation by ICWC in helium and boron coating during ICWC by using the boron powder dropper or its analogues. For each of these applications, the task is to find the optimal discharge parameters. The main parameters to scan are neutral gas pressure, power and antenna phasing (monopole vs dipole) at two magnetic field values and two frequencies, as shown in Fig. 5.3.

5.2.3 Contribution to W7-X ICWC development by studies on other relevant fusion devices

5.2.3.1 Uragan-2M

To support the ICWC development for W7-X first experiments dedicated to the ICRF plasma production have been carried out in the Uragan-2M stellarator with a W7-X – like antenna [254]. U-2M has a topologically similar plasma column. The antenna in use almost repeats a W7-X antenna shape and has a similar $k_{\parallel}$ spectrum. The similarities are also found in gas types. The experiments of plasma production were carried out in the monopole phasing, input power of $\sim$ 0.1 MW at 5.15 MHz and 0.347 T and helium pressure range of $5.0 \cdot 10^{-4}$ mbar – $1.4 \cdot 10^{-3}$ mbar. It should be noted that this pressure range is too high for IC plasma production in W7-X. For operational safety reasons, the highest pressure value should not rise above the lower end of the studied pressure range. The PFCs were pre-loaded by hydrogen to mimic the minority of hydrogen in the helium atmosphere typical for wall conditioning in helium. The plasma production was achieved at frequencies close to the hydrogen ion fundamental harmonic frequency at densities above 10^{17} m^{-3}. Plasma average densities were in the range of $2.0 \cdot 10^{18} - 2.6 \cdot 10^{18}$ m^{-3}. Moreover, the density is saturated with an increase in the RF input power. The experimental results have shown that the plasma production rate does not depend on the RF input power at an initial discharge phase (first 2-5 ms during the power ramp-up). RF field strongly contributes to the electron heating during the plasma production phase resulting in a short plasma production time (less than 5 ms).

5.2.3.2 LHD

The application of the RF conditioning in LHD allowed to successfully extend the high ion temperature operation regime and improve the efficiency of the high-performance plasma production [103]. In order to prepare the first ICWC operation in W7-X further experiments, dedicated to exploring the operational window for IC plasma production in LHD are proposed. The task is to identify the discharge parameters and phase that are optimum for wall conditioning and target plasma using LHD antennas at 38 MHz and a toroidal magnetic field of 2.8 T. It is planned to be achieved by varying the helium pressures between $1 \cdot 10^{-5}$ mbar to $5 \cdot 10^{-4}$ mbar, the CW power between 0.1 MW and 0.5 MW and try changing the antenna phasing.

5.2.3.3 TOMAS

Neutral particle fluxes are thought to be responsible for the high conditioning efficiency of ICWC in W7-X. The highest fluxes can be expected in the low energy range of 10 - 100 eV. This energy region is ideally suited for wall conditioning. The characterization of these particle fluxes cannot be achieved within W7-X due to the absence of diagnostic flexibility for the low-temperature low-density conditioning plasmas. The TOMAS device is suitable to help the development of ICWC for W7-X. Moreover, the device can research aspects of IC plasma production, providing detailed experimental data to ensure good and safe ICRF antenna performance and benchmark codes, e.g. RFdinity1D [255].

The ICWC experimental programme on TOMAS aims at characterizing the conditioning particle flux to the plasma-facing components as a function of discharge parameters (pressure, RF voltage, RF frequency, etc.). Moreover, a large flexibility for exposing surface samples allows studying the impact of these fluxes on materials. The latter will be done by plasma-induced material modification and optimization of the wall conditioning efficiency via exposure of probes made of W7-X spare PFC materials (graphite and stainless steel).

Besides the studies of boron coating lifetime under high fluxes of low-energy particles produced by ICWC plasmas, the following PWI aspects of ICWC, such as (i) the impact on fuel retention and removal, (ii) the impact of helium on PFC materials at these relevant fluences, (iii) material migration and its impact on surface morphology, (iv) the removal of (seeding) impurities from PFC materials in W7-X – like environment and (v) real-time conditioning techniques such as wall boron coating by plasma-enhanced vapour deposition (boron dropper) with ICWC can be investigated.

5.3 Future work

The work done in the scope of this PhD project should be continued by studies, which can further modify and complement the proposed wall conditioning strategy of W7-X.

First of all, the benefits of the cryo-pumps installation (significant increase of the effective pumping speed) should be investigated for all developed plasma-assisted wall conditioning techniques in W7-X.

The GD assisted break-down studies have to be proceeded to minimize the PFCs erosion and mitigate the potential damage of in-vessel components. One should complete an investigation of the GD influence on the boron coating lifetime to prove or refute the necessity of He-GDC application after the W7-X boronization. An application of GDC with the hot walls (combination with baking) could increase the conditioning efficiency and reduce the procedure execution time, e.g. in the initial wall conditioning phase.

Further optimization of ECWC is necessary for the practical application of this technique with an actively cooled PFCs. The influence of the divertor temperature control on ECWC efficiency should be analyzed, including strike lines sweeping effect in different magnetic field configurations.

The comparison of optimized ICWC with GDC by means of impurity and fuel removal will clarify whether ICWC can be used as a promising alternative to GDC in W7-X. It is worth developing possible scenarios combining ECWC and ICWC application to cover all possible needs of wall conditioning in the presence of a magnetic field. The RF-mixed plasma effect on wall conditioning might be a new tool for effective density control.

Since long-pulse operation is expected to be available with the commissioning of the high heat flux divertor, the investigation of the boron layer lifetime will become a crucial point for maintaining high plasma performance. Moreover, estimating the boronization frequency at different operational scenarios is necessary for an effective device operation.

Boron dropper experiments with the unboronized device should be completed to support the "classic" boronization procedure, considering its limitations. Additionally, studies of the differences between real-time boronization applications in EC, IC and EC+IC discharges can be proposed to reveal the best coating efficiency and the largest boron deposition areas.

An operation of the device with hot walls during the long-pulse plasma can play an essential role in facilitating hydrogen recycling. In this case, keeping the wall temperature above 100 $^\circ\mathrm{C}$ might be sufficient for reducing the amount of wall-stored hydrogen. Investigating this effect in W7-X can benefit to maintaining better density control during long discharge execution.

Chapter 6

Conclusion

The total energy consumption in the world is increasing for numerous economic and social reasons. Most of this energy comes from burning fossil fuels, leading to tremendous greenhouse gas emissions. To phase out these sources whilst avoiding an unprecedented global energy crisis, alternative energy sources must be developed.

A promising long-term solution is nuclear fusion. It can be employed to build a steady and sustainable energy source based on the most favourable reaction between deuterium and tritium. One of the main options how to confine the reactants is magnetic confinement. It retains plasma via the collective behaviour of its free charge carriers and their interaction with magnetic fields. Among many different types of magnetic configurations for plasma confinement, devices with helical magnetic field lines going around in the torus are most promising for a reactor. The two most advanced toroidal confinement concepts are the tokamak and the stellarator.

All fusion devices in operation today are experimental machines. ITER is the world's largest tokamak experiment that aims at demonstrating and studying how a burning plasma is created and sustained. Its planned successor, DEMO, will be a magnetic confinement path to a fully integrated science and technology demonstration of fusion.

The EUROfusion consortium, coordinating magnetic confinement fusion research in Europe, guides early conceptual designs of a European DEMO. The stellarator is herein considered as a possible long-term alternative to a tokamak fusion power plant, including DEMO. The European stellarator programme primarily focuses on the scientific exploitation of the superconducting stellarator Wendelstein 7-X, which is designed to work under steady-state conditions and to demonstrate high-performance plasma scenarios. The superconducting stellarator Wendelstein 7-X (W7-X) is based on a five-field-period Helias configuration. Its major radius is 5.5 m, while a minor radius is 0.5 m. The maximum magnetic field on-axis is 2.5 T. The in-vessel components of W7-X consist of the divertor components and the wall protection (stainless steel wall panels and graphite tiles). Ten separate Test Divertor Units (TDUs) made of graphite are placed in equivalent positions following the plasma symmetry along the edge of the plasma contour. The magnet system of W7-X is composed of three different groups of coil systems. The main one delivers the stellarator magnetic field configuration. Two others are there to rectify the error field and sweep hot spots (strike lines) on the divertor target plates. The baking system allows heating of the plasma vessel and some ports by pressurized hot water at 150 $^\circ$C and the diagnostic ports electrically to about 160 $^\circ$C. The glow discharge (GD) system of W7-X consists of 10 calotte-shaped graphite anodes located in each half module and individually power supplied with maximum ratings of 3 kV and 1.5 A. The Electron Cyclotron Heating (ECRH) system is the primary plasma heating system based on ten gyrotrons producing up to 1 MW each in continuous wave operation and operating at 140 GHz, corresponding to the 2nd harmonic of the resonance frequency for the nominal magnetic field. W7-X has numerous diagnostics to measure plasma parameters, monitor the conditions of PFC and other in-vessel components, and control the device parameters.

Wall conditioning

One of the W7-X challenges is about edge plasma physics and Plasma - Surface Interaction (PSI) studies that are responsible for two critical elements of high-performance operation: plasma impurities and fuel recycling. Impurities cool the plasma by radiation and dilute the hydrogenic species. Fuel recycling, the repeated interchange of hydrogen isotopes between the plasma and the wall, is crucial for plasma density control. Wall conditioning in fusion devices is a standard tool to influence fuel and impurity recycling, improving both plasma performance and discharge reproducibility.

Operating W7-X, today and in the future, requires a wall conditioning strategy, which is the topic of this PhD manuscript. The strategy is developed by analyzing the conditioning effect of selected wall conditioning techniques in terms of removed gas, minimization of impurity content and subsequent W7-X plasma performance. It includes performing conditioning optimization experimentally and follow up of the implemented wall conditioning strategy in each of the operation phases of W7-X.

A detailed review of the wall conditioning methods presented in this work has shown that the following techniques are relevant for application in W7-X operating in the divertor configuration with graphite plasma-facing components (PFC)s.

Baking is the process of using high temperatures to remove by thermal desorption the volatile species from the walls of a vacuum vessel to prevent its further migration and contamination of plasmas. Baking is a forced acceleration of the outgassing process, meaning that previously adsorbed molecules diffuse through the bulk of material of in-vessel components, arrive at its surface layer and desorb from it. Baking is the most common technique to reduce the amount of water.

Plasma-assisted wall conditioning is a method based on the mechanisms of particle-induced desorption to remove impurities and fuel from PFCs. Glow Discharge Cleaning (GDC) is one of the most established techniques, historically in fusion devices with normal conducting magnetic field coils. In fusion devices, Glow Discharge (GD) is weakly ionized ($n_e < 10^{16}$ m^{-3}) low temperature (T_e < 10 eV) plasma which is created by applying a voltage difference between one or more small electrodes inside the vacuum vessel (anode) and vacuum vessel walls (cathode). It allows further impurity removal by reducing metal oxides or hydrogenation of carbon-based surfaces, for example after baking, and reset the wall conditions between operation cycles.

Radiofrequency (RF) - based techniques are to be compatible with magnetic fields unlike GDC and even need it to couple energy into the plasma. Therefore, they are particularly relevant for fusion devices with superconducting coils. Conditioning by ECRH plasma, or Electron Cyclotron Wall Conditioning (ECWC), relies on a currentless discharge, typically partially ionized, produced by localized power absorption at the fundamental EC resonance or its second harmonic. In stellarators, ECRH plasma is fully ionized (T_e > 100 eV) with electron density above 10^{19} m^{-3}. ECWC in a stellarator is efficient for cleaning the divertor area given that the nominal confining magnetic flux surfaces with its divertor configuration are present in the ECRH conditioning plasmas.

Ion Cyclotron Wall Conditioning (ICWC) discharges couple RF power in the ion cyclotron range of frequencies to both electrons and ions, by collisional absorption mostly. ICWC plasmas are characterized by densities in the range of $10^{16} - 10^{18}$ m^{-3} and low temperatures (1 - 10 eV). As other discharge conditioning techniques it aims to induce a known and optimal flux of particles to the plasma-facing components, but here in particular the low energetic neutrals (10's of eV to a few keV) contribute strongly to the PSI.

Wall conditioning aims, of course, to pump away the desorbed species, preventing their redeposition on the vessel walls by the conditioning plasmas. Pulsed discharge conditioning with an optimized duty cycle can achieve maximum removal while minimizing retention or redeposition of both the injected and wall released gas.

Low-Z (beryllium, lithium and boron) wall coating is a fast and efficient way to significantly reduce oxygen recycling by chemically binding it to stable solid oxides. Additional effects are the suppression of metal release from the vessel wall, overall reduction of the low-Z impurity concentrations in the plasma and a positive influence on fuel recycling. Boronization is the most common low-Z coating method. Boronization is typically applied through plasma-assisted chemical vapour deposition using a GD in a mixture with helium to deposit amorphous boron or carbon-boron hydrogenated thin films with a thickness of up to $\sim$ 100 nm.

An alternative method that is studied to apply low-Z wall coatings in real-time and in the presence of the magnetic field is based on low-Z powder (with grain sizes less than 1 mm) injections. The coating occurs preferentially in the areas in contact with the Last Closed Flux Surface (LCFS). The distribution of the coating layer across the machine wall depends on the plasma scenario.

Application of wall conditioning on W7-X

Between 2015 and 2018, the first three experimental campaigns (operational phases) OP1.1, OP1.2a, and OP1.2b of the W7-X stellarator have been completed. The first phase, called OP 1.1, was performed in the limiter configuration with five inertially cooled graphite limiters. In OP1.2a, the limiters were replaced by 10 TDUs, and the installation of graphite tiles on the heat shield was completed. In OP1.2b, two graphite scraper elements were installed. Boronization of the in-vessel components became available via the GD procedure. Throughout this PhD project the author has analyzed data of OP1.1 and had an active participation in OP1.2.

In OP1.1, baking was performed for one week at an average temperature of 150 °C. It allowed reducing a plasma vessel pressure from $7 \cdot 10^{-7}$ mbar to $2 \cdot 10^{-8}$ mbar. GDC was used between experimental days during the plasma operation phase, and ECWC was employed during experimental days. At the end of the experimental campaign, the value of normalized outgassing, an outgassing pressure peak at the end of a plasma discharge normalized to the total injected ECRH energy, reached the level of $3 \cdot 10^{-8}$ mbar $\cdot$ kJ^{-1}. CO remained dominating impurity throughout the whole plasma operation phase. The analysis of the gas balance shows that the temporal trends of the injected and pumped amounts of the gas have a slight improvement in recycling. The average pumped amount of gas dropped by a factor of $\sim$3. To achieve good wall conditions, defined by normalized outgassing values below $1 \cdot 10^{-9}$ mbar · kJ^{-1}, the device requires a set of initial wall conditioning procedures applied before the start of plasma operation.

The available conditioning techniques in OP1.2a were baking, GDC and ECWC. OP1.2 allowed for a long GDC in hydrogen, significantly reducing the amount of impurities such as H_2O, CH_4, CO and CO_2. Following GDC in helium allowed depleting the walls from remaining hydrogen. In OP1.2b, the application of boronization also became accessible. Before the first plasma, the baking and GDC provided the minimum required conditions for starting physics experiments. Boronisation and ECWC were used during the plasma operation period to reduce the amount of oxygen and control the hydrogen recycling, respectively. The normalized outgassing was reduced to values around $1 \cdot 10^{-9}$ mbar · kJ^{-1} within three days after the beginning of OP1.2a. The results of the gas balance analysis clearly illustrate that hydrogen discharges have net retention while helium discharges demonstrate net removal. A similar situation with normalized outgassing was observed at the beginning of OP1.2b before the first boronization procedure. The gas balance analysis shows that auxiliary fueling on low heated walls leads to strong fuel absorption. At the same time, an increase of the graphite PFC surface temperature allows mobilizing retained gas in the carbon structures.

During OP1.2, He, C and O were the principal impurities in hydrogen plasmas. The existence of He and O in plasma made a significant contribution to the overall carbon erosion through enhanced sputtering. The latter resulted in the domination of CO and H_2O in the outgassing content, both in OP1.2a and OP1.2b (before boronization). The operation of the device shows that mainly the divertor parts are heated up strongly during an ECRH discharge. That strongly affects an impurity release from the PFC and hydrogen recycling during a plasma discharge and the continued outgassing after a discharge.

The baking of the plasma vessel walls was performed in each part of OP1.2 after the vessel pump down. The procedure of the bake out took 11 days in total with the flat-top phase of 7 days at the average wall temperature of 150 °C. In both cases, at the flat-top phase, the pressure curve follows a $\sim t^{-0.7}$ dependence. Water is the main component in the outgassing content. Carbon oxide and carbon dioxide are the following prominent species. The baking application decreased a base pressure level from $8.1 \cdot 10^{-8}$ mbar to $3.9 \cdot 10^{-8}$ mbar prior to OP1.2a and from $5.4 \cdot 10^{-8}$ mbar to $2.1 \cdot 10^{-8}$ mbar prior to OP1.2b. More extensive removal of impurities was observed in OP1.2a. The outgassing of heavy species, mostly high hydrocarbons, with a mass-to-charge ratio above 50 was suppressed. The OP1.2b baking did not dramatically change the residual gas content at higher masses after baking.

Apart from the initial conditioning in OP1.2, hydrogen GDC was used weekly throughout the experimental campaign to further improve the wall conditions for plasma operations until the first boronization. GDC in helium was executed either daily after hydrogen plasma experiments or application of H_2-GDC to desaturate walls from hydrogen. The duration of the weekly applied H_2-GDC did not exceed 90 minutes. H_2-GDC was operated at an upper anode current limit of 1.5 A, working pressure of $4.4 \cdot 10^{-3}$ - $4.5 \cdot 10^{-3}$ mbar and an average voltage of $\sim$ 305 V to achieve homogeneity. He-GDC was conducted in separate procedures of 20 − 25 minutes each only before plasma operation. The operational pressure of $\sim 3.8 \cdot 10^{-3}$ mbar and the current of 1 A, corresponding to a voltage of $\sim$ 210 V. Due to the long post-discharge outgassing, it is recommended to use GDC at the end of the experimental day.

In the case of H_2-GDC, a reliable break-down could be achieved at neutral gas pressures above $2.9 \cdot 10^{-2}$ mbar. The fast pressure decrease could be reached by combining a stepwise increase of the total pumping speed and variation of gas flow. The break-down of He-GDC could not be made reliable in OP1.2a even at the maximum voltage of 3 kV and pressures up to $\sim 8 \cdot 10^{-2}$ mbar. A robust workaround was to ignite the glow discharge in hydrogen and gradually exchange the working gas for helium. Further reducing the helium and hydrogen break-down pressure requires looking for alternative ways to assist the GD break-down in W7-X.

GDC in hydrogen has a cumulative effect on impurity removal. A minimum of 9 to 10 hours of the initial H_2-GDC must be performed to ensure reliable plasma operation conditions. The following He-GDC should have a duration of 2 hours to provide the required hydrogen outgassing level for a reliable start of the physics program.

The post-mortem analysis of different PFC component surfaces and inspection of the in-vessel components show that carbon erosion and the damage of the metallic surfaces creating arc traces on various metal PFCs also occurred during GDC operations. Both issues require to be mitigated by the further development of the GDC procedures by optimizing GD parameters and durations and studying of assisted break-down at lower pressures.

Boronization aimed to reduce oxygen radiation and sputtering. A GD applies the boron coating in W7-X in the mixture of diborane (10 %) and helium (90 %). Three boronizations with time intervals of one month were applied. The process of boronization was optimized from session to session due to the different technical issues. The higher efficiency of the process requires an increase in the pumping capacity of the vacuum system.

The first boronization suppressed helium outgassing and significantly extended the plasma operation window in the density range from a few times 10^{19} m^{-3} to more than $1 \cdot 10^{20}$ m^{-3}. The improvement of the plasma performance was due to the reduction of oxygen and oxygen-based impurities. The amounts of CO, CO_2 and H_2O were decreased by 9.3, 2.7 and 1.7, respectively. Methane outgassing has almost no changes because its origin is insusceptible to boronization - relevant processes. The first boronization decreased the oxygen influx at the divertor by a factor of 8. Consequently, the carbon influx was reduced as well by order of magnitude. Subsequent boronizations facilitated further oxygen content decrease. The values of Z_{eff} decreased from values of 4.5 down to 1.2. Plasmas exhibited increased confinement times by a factor of 2.

The boron layer at the strike lines on the divertor target is eroded quickly with an erosion rate of about 0.25 nm/s until a relatively low level. A long-lasting effect is related to the low impinging ion and charge-exchange flux to the main wall. Extending the inter-boronization period (> 2400 s) may be possible without compromising the high plasma performance at similar plasma operation conditions. Boron dropper experiments in OP1.2b were intended to estimate the effectiveness of the Probe Mounted Particle Injector (PMPI). The injection of boron-containing powder (100 µm diameter B_4C granules) in the plasma edge with the frequency of 2.8 Hz is anticipated to replenish only the boron coating at divertors. The powder quantities varied from approximately 1 mg/pulse to 30 mg/pulse. Injections larger than 20 mg/pulse increase an average Z_{eff} value to 3.5 and trigger a radiative collapse. A decrease by a factor of $\sim$ 2 is observed in the overall oxygen content. The impact of the boron-containing powder injection on wall conditions is inconclusive because previously deposited layer on the PFCs by regular boronization limits the visibility of the effect of any additional material deposition. A dedicated set of experiments in an un-boronized device is needed to assess powder injection effects on wall conditioning adequately.

The main conditioning effect of He ECWC in W7-X is related to the cleaning of the divertor area. The development, study and main parameter optimization of the ECWC started in OP1.2a. The technique was optimized into a routine tool for density control and recovery of the plasma conditions after radiative collapses. Two types of He ECWC were developed: (i) so-called "single He recovery discharges", single discharges at low density and moderate heating power and (ii) so-called "pulse trains", sequences of short, low to medium power discharges with a fixed duty cycle. The most effective recovery discharges are 10 s discharges with a heating power of 3 MW. The optimum pulse train scheme for OP1.2a had a pulse length of 1.5 s, a pulse interval of 30 s and an input power of 2.1 MW. The most efficient recovery discharge could remove only 50 % to 75 % of hydrogen compared to the optimized pulse train. Moreover, the application of the optimized pulse train uses the W7-X experimental time more effectively. The pulse trains also reduce the oxygen release, which causes a reduction of the carbon content via a decrease of the erosion rate caused by released oxygen.

In OP1.2b, better overall wall conditions allowed to increase the pulse length and pulse interval ranges in pulse trains. While longer pulses (3.5 s) generally remove more, the removal is non-linear and dependent on wall loading by hydrogen. Reducing the pulse interval down to 15 s slightly increases the experimental time-averaged removal rates. However, this increase is not linear. While it still allows evacuating most of the released fuel between the discharges, heavier impurities are evacuated more slowly and hence need more time. Considering only the minor advantage of the reduced pulse interval at the cost of a lower reliability of the pulse train execution, the pulse interval should be kept at $\sim$ 30 s.

Due to boronization applied in OP1.2b, conditioning requirements changed, and ECWC could be more refined for particular needs, such as fuel recycling control. To desaturate the graphite divertor targets from hydrogen and achieve stable low-density operation, an application of one optimized pulse train can be insufficient and can require repeating the cleaning sequence. To further improve the efficiency of the pulse train, the effect of strike line sweeps during the pulse train execution was investigated. The total plasma wetted area can be increased by a factor of $\sim$ 8 in the case of the most efficient sweep at a discharge input power of 2.1 MW. It improves the fuel removal by 30 %, while depleting a much larger surface area. However, it is also strongly dependent on the divertor surface fuel loads. Sweeping can also increase the oxygen release from the divertor and its concentration in the plasma core during the pulse train due to the erosion of the boron layer in the previously untouched divertor area.

The increase of the outgassing (mainly fuel release) shows a clear nonlinear dependence on local temperatures of carbon PFCs. The increased temperature of the divertor leads clearly to increased outgassing after each subsequent pulse. The temperature effect does not seem to influence core fueling during discharge execution. The cleaning efficiency of the pulse depends mostly on post-discharge outgassing in case of high divertor temperatures. Even in a well-conditioned machine, the extra release of the fuel can be achieved when the temperature rises. Together with fuel, as well impurity outgassing increases at higher temperatures. Nevertheless, the carbon and oxygen concentration in the core of the conditioning plasma seem not significantly affected by the divertor temperature increase due to their small concentration and the plasma screen effect.

Contribution of the TOMAS device to wall conditioning studies

The study and optimization of the wall conditioning techniques applied in W7-X require extensive operation time and hence competes for experimental time with other physics topics. It was decided to put in place an experimental set-up dedicated to wall conditioning studies to get better insight into the complex multi-physics picture of the wall conditioning techniques and prepare them for further applications on W7-X. For this purpose, the TOMAS (TOroidal Magnetized System) device has been significantly upgraded, having the following specifications. The toroidal magnetic field can reach its maximum of 125 mT on the axis. The EC system is operated at 2.45 GHz with up to 6 kW forward power. The IC system can couple up to 6 kW in the frequency range of 10 – 50 MHz. The DC GD system is based on a graphite anode (similar to W7-X). It produces a voltage of up to 1.5 kV and a current of up to 6 A. A load-lock system with a vertical manipulator allows exposure of material samples. A number of diagnostics have been installed: single and triple-pin Langmuir probes for radial plasma profiles, a time-of-flight neutral particle analyzer capable of detecting neutrals in the energy range of 10 - 1000 eV, and a quadrupole mass spectrometer and video systems for plasma imaging.

The first results of TOMAS experiments relevant to W7-X conditioning procedures were dedicated to baking and Glow Discharge Cleaning. The baking experiments showed that an increase of the wall temperature at the level of the device could be employed for fast removal of retained helium after wall conditioning in helium. The installation of W7-X – like Glow Discharge system in TOMAS allowed studying some particular aspects of GD. An attempt to perform assisted break-down has been investigated in TOMAS using a localized short-time injection of argon. The influence of the magnetic field on GD homogeneity shows GD becomes strongly localized even at the small magnetic field value of 3 – 4 mT and vanishes at higher values. An investigation of spurious events in GDC aimed at reproducing erosion at the GD break-down regime (W7-X like environment) and explore the influence of long exposure on the construction elements at regular operation regime. These studies confirmed that the material (graphite) redeposition and arc traces seen on remote W7-X surfaces is due to GDC.

The first pre-characterization of EC, IC and mixed (EC+IC) plasmas on TOMAS has been done using the Langmuir Probes and ToF NPA as part of the experiments that study wall conditioning or PSI aspects of ECWC and ICWC plasmas. ECRH system allows generating discharges with electron densities of $1.8 \cdot 10^{17}$ – $6.6 \cdot 10^{17}$ m^{-3} and electron temperatures of 1 – 23 eV. The ICRF operation window allows achieving plasma densities of up to $5 \cdot 10^{17}$ m^{-3} and temperatures of 10 – 90 eV.

First boron layer erosion studies using coated polished graphite samples made from W7-X tiles by He-GDC contribute to the understanding of the boron layer life-time in W7-X. Exposure of the boron coated graphite samples to ICWC requires additional device modifications. The installation of the second triple probe in the vertical plane and a Retarding Field Analyzer (RFA), mountable on the sample manipulator, is needed to characterize additional plasma parameters.

Wall conditioning strategy for W7-X

The studied conditioning techniques were optimized and combined into a wall conditioning strategy to achieve high plasma performance throughout W7-X campaigns. The current wall conditioning strategy comprises two phases.

The initial wall conditioning phase is performed before the first plasma to provide the minimum conditions for the operation. It starts with 11 days of vacuum vessel bake-out. The baking has a flat top phase of a minimum of 7 days at the average PFC temperature of 150 $^{\circ}\mathrm{C}$. The following step is GDC. First, at least 9-10 hours of GDC in hydrogen. The optimal parameters of H_2-GDC are pressure of $\sim 4.5 \cdot 10^{-3}$ mbar at the maximum pumping speed and anode current of 1.5 A. The final step is He-GDC applied with a minimum duration of 2 hours. He-GDC is operated at a neutral gas pressure of $\sim 3.8 \cdot 10^{-3}$ mbar and an anode current of 1 A.

The second phase of the wall conditioning strategy is a set of wall conditioning techniques routinely applied during the plasma operation. Before boronization, it is recommended to use H_2-GDC weekly. Also, 15 – 20 minutes of He-GDC should be applied daily. The boronization procedure based on a GD in the He:B_2H_6 mixture should be applied monthly to maintain high plasma performance. A revision of this frequency may be needed in future campaigns where much longer stellarator plasmas are envisaged. The steady boronization glow (coating phase) has to last 3.5 - 4 hours. Further development of the boron powder dropper or its analogue should be envisaged to extend the boron coating lifetime, e.g. at high fluence plasma surfaces.

To control the fuel recycling throughout an experimental day, the optimized He ECWC pulse train optimized for application in the boronized device has the following parameters: the pulse length is 3 s, the pulse interval is about 30 – 35 s, the input power is 2.1 MW using three gyrotrons, gas prefill should be done 100 ms before each discharge with a duration of 15 ms at the constant gas flow of 75 mbar · l/s. An application of strike lines sweeping in the pulse trains is recommended to increase the removal and maximize the affected area. Maintaining divertor temperatures above 400 °C during the pulse train application enhances the fuel removal rate.

Future work

The work done in this PhD project scope should be continued throughout future W7-X operation campaigns. For instance, one needs to study how the newly installed cryo-pumps and water-cooled High Heat Flux divertor units and other actively cooled PFCs can modify or complement the proposed wall conditioning strategy of W7-X.

An ICRH system capable of delivering $\sim$ 1.5 MW of RF power at frequencies between 25-38 MHz in discharges up to 10 s will be installed in OP2, making ICWC a powerful alternative to the currently employed wall conditioning techniques in the presence of a magnetic field. Potential applications of ICWC are impurity removal by H_2-ICWC, wall desaturation by He-ICWC and boron coating during ICWC using the boron powder dropper technique. To support the ICWC development for W7-X first experiments dedicated to the ICRF plasma production have been carried out in the Uragan-2M stellarator with a W7-X–like antenna. Additional experiments devoted to exploring the operational window for IC plasma production in LHD are proposed to prepare the first ICWC operation in W7-X. The TOMAS device will research aspects of ICWC plasma production, providing detailed experimental data to ensure good and safe ICRF antenna performance and benchmark codes by characterizing the conditioning particle flux to the plasma-facing components. Exposing surface samples allows studying the impact of these fluxes on materials in TOMAS.

Bibliography

[1] International Energy Agency, "World Energy Outlook 2020," (2020), report.

[2] R. B. Jackson *et al.*, "Global energy growth is outpacing decarbonization," *Environmental Research Letters* **13**, 120401 (2018).

[3] R. B. Jackson *et al.*, "Warning signs for stabilizing global CO_2 emissions," *Environmental Research Letters* **12**, 110202 (2017).

[4] M. Etminan *et al.*, "Radiative forcingof carbon dioxide, methane, and nitrousoxide: A significant revision of themethane radiative forcing," *Geophysical Research Letters* **43**, 12,614 (2016).

[5] C. Le Quéré *et al.*, "Temporary reduction in daily global CO_2 emissions during the COVID-19 forced confinement." *Nature Climate Change* **10**, 647 (2020).

[6] British Petrolium, "BP Statistical Review of World Energy 2020," (2020), report.

[7] J. Rogelj *et al.*, "Paris agreement climate proposals need a boost to keep warming well below 2 °C," *Nature* **534**, 631 (2016).

[8] European Commission, "National energy and climate plans," (2020), press release.

[9] Climate Transparency 2019, "Brown to green: The G20 transition towards a net-zero emissions economy," (2019), report.

[10] E. F. Moran *et al.*, "Sustainable hydropower in the 21st century," *Proceedings of the National Academy of Sciences* **115**, 11891 (2018).

[11] Q. Schiermeier *et al.*, "Energy alternatives: Electricity without carbon," *Nature* **454**, 816 (2008).

[12] J. D. Einkauf and J. D. Burns, "Recovery of oxidized actinides, Np(VI), Pu(VI), and Am(VI), from cocrystallized uranyl nitrate hexahydrate: A single technology approach to used nuclear fuel recycling," *Industrial & Engineering Chemistry Research* **59**, 4756 (2020).

[13] F. Diaz-Maurin and Z. Kovacic, "The unresolved controversy over nuclear power: A new approach from complexity theory," *Global Environmental Change* **31**, 207 (2015).

[14] IRENA (Internetional Renewable Energy Agency), "Reaching zero with renewables: Eliminating CO_2 emissions from industry and transport in line with the 1.5 $^\circ\mathrm{C}$ climate goal," (2020), report.

[15] G. McCracken and P. Stott, *Fusion: The Energy of the Universe* (Elsevier Academic Press, 2005).

[16] M. Rubel, "Fusion neutrons: Tritium breeding and impact on wall materials and components of diagnostic systems." *Journal of Fusion Energy* **38**, 315 (2019).

[17] T. Hamacher *et al.*, "Nuclear fusion and renewable energy forms: Are they compatible?" *Fusion Engineering and Design* **88**, 657 (2013).

[18] C. Bustreo *et al.*, "How fusion power can contribute to a fully decarbonized European power mix after 2050," *Fusion Engineering and Design* **146**, 2189 (2019).

[19] D. Maisonnier, "$RAMI$: The main challenge of fusion nuclear technologies," *Fusion Engineering and Design* **136**, 1202 (2018).

[20] T. C. Simonen, "Three game changing discoveries: A simpler fusion concept?" *Journal of Fusion Energy* **35**, 63 (2016).

[21] J. Proll, *Trapped-particle instabilities in quasi-isodynamic stellarators*, Ph.D. thesis, Ernst-Moritz-Arndt-Universität Greifswald (2014).

[22] A. Cardinali *et al.*, "Radio-frequency current drive for thermonuclear fusion reactors," *Scientific Reports* **8**, 10318 (2018).

[23] P. Politzer and G. Porter, "Power threshold for neutral beam current drive," *Nuclear Fusion* **30**, 1605 (1990).

[24] ITER Organization, "www.iter.org," (2022).

[25] G. Federici *et al.*, "DEMO design activity in Europe: Progress and updates," *Fusion Engineering and Design* **136**, 729 (2018).

[26] National Academy of Engineering and National Academies of Sciences, Engineering, and Medicine, *Bringing Fusion to the U.S. Grid* (The National Academies Press, Washington, DC, 2021).

[27] EUROfusion Consortium, "www.euro-fusion.org," (2022).

[28] G. Federici *et al.*, "European DEMO design strategy and consequences for materials," *Nuclear Fusion* **57**, 092002 (2017).

[29] H.-S. Bosch *et al.*, "Final integration, commissioning and start of the Wendelstein 7-X stellarator operation," *Nuclear Fusion* **57**, 16015 (2017).

[30] R. C. Wolf *et al.*, "Performance of Wendelstein 7-X stellarator plasmas during the first divertor operation phase," *Physics of Plasmas* **26**, 082504 (2019).

[31] T. Sunn Pedersen *et al.*, "Key results from the first plasma operation phase and outlook for future performance in Wendelstein 7-X," *Physics of Plasmas* **24**, 055503 (2017).

[32] A. J. H. Donné, "The European roadmap towards fusion electricity," *Philosophical Transactions of the Royal Society A: Mathematical, Physical and Engineering Sciences* **377**, 20170432 (2019).

[33] M. Rubel *et al.*, "Analysis of fuel retention in plasma-facing components from controlled fusion devices," *Nuclear Instruments and Methods in Physics Research Section B: Beam Interactions with Materials and Atoms* **267**, 711 (2009).

[34] J. Winter, "Wall conditioning in fusion devices and its influence on plasma performance," *Plasma Phys. Control. Fusion* **38**, 1503 (1996).

[35] M. Z. Tokar, "Role of impurities in fusion plasmas," *AIP Conference Proceedings* **1061**, 94 (2008).

[36] M. Greenwald, "Density limits in toroidal plasmas," *Plasma Physics and Controlled Fusion* **44**, R27 (2002).

[37] T. Loarer *et al.*, "Gas balance and fuel retention in fusion devices," *Nuclear Fusion* **47**, 1112 (2007).

[38] T. Wauters *et al.*, "Wall conditioning in fusion devices with superconducting coils," *Plasma Physics and Controlled Fusion* **62**, 034002 (2020).

[39] D. Douai *et al.*, "Wall conditioning for ITER: Current experimental and modeling activities," *Journal of Nuclear Materials* **463**, 150 (2015).

[40] A. Goriaev *et al.*, "The upgraded TOMAS device: A toroidal plasma facility for wall conditioning, plasma production, and plasma–surface interaction studies," *Review of Scientific Instruments* **92**, 023506 (2021).

[41] B. Schweer *et al.*, "Development of an ICRH antenna system at W7-X for plasma heating and wall conditioning," *Fusion Engineering and Design* **123**, 303 (2017).

[42] H. F. Dylla *et al.*, "Correlation of outgassing of stainless steel and aluminum with various surface treatments," *Journal of Vacuum Science & Technology A* **11**, 2623 (1993).

[43] P. Lazic, in *Physics of Surface, Interface and Cluster Catalysis*, 2053-2563 (IOP Publishing, 2016) pp. 2–1 to 2–25.

[44] J. R. Smith *et al.*, "Universal binding-energy relation in chemisorption," *Phys. Rev. B* **25**, 1419 (1982).

[45] K. Foo and B. Hameed, "Insights into the modeling of adsorption isotherm systems," *Chemical Engineering Journal* **156**, 2 (2010).

[46] P. A. Redhead, "Modeling the pump-down of a reversibly adsorbed phase. I. monolayer and submonolayer initial coverage," *Journal of Vacuum Science & Technology A* **13**, 467 (1995).

[47] H. Dylla, "A review of the wall problem and conditioning techniques for tokamaks," *Journal of Nuclear Materials* **93-94**, 61 (1980).

[48] P. A. Redhead, "Modeling the pump-down of a reversibly adsorbed phase. II. multilayer coverage," *Journal of Vacuum Science & Technology A* **13**, 2791 (1995).

[49] P. A. Redhead, "Effects of readsorption on outgassing rate measurements," *Journal of Vacuum Science & Technology A* **14**, 2599 (1996).

[50] M. Li and H. F. Dylla, "Model for the outgassing of water from metal surfaces," *Journal of Vacuum Science & Technology A* **11**, 1702 (1993).

[51] M. Li and H. F. Dylla, "Model for water outgassing from metal surfaces. II," *Journal of Vacuum Science & Technology A* **12**, 1772 (1994).

[52] R. Grinham and A. Chew, "A review of outgassing and methods for its reduction," *Applied Science and Convergence Technology* **26**, 95 (2017).

[53] C. Schlatter, *Turbulent Ion Heating in TCV Tokamak Plasmas*, Ph.D. thesis, École Polytechnique Fédérale de Lausanne (2009).

[54] V. Rohde *et al.*, "Recovery from a hot water leakage at the tokamak ASDEX Upgrade," *Fusion Engineering and Design* **157**, 111630 (2020).

[55] D. Douai *et al.*, "Wall conditioning of JET with the ITER-Like Wall," *Journal of Nuclear Materials* **438**, S1172 (2013).

[56] P. Moreau *et al.*, "The commissioning of the WEST tokamak: Experience and lessons learned," *IEEE Transactions on Plasma Science* **48**, 1376 (2020).

[57] Y. Nobuta *et al.*, "Effects of mild baking on hydrogen removal from the modified surface of the first wall in the LHD," *Plasma and Fusion Research* **12**, 1302048 (2017).

[58] S. Ishida *et al.*, "Status and prospect of the JT-60SA project," *Fusion Engineering and Design* **85**, 2070 (2010).

[59] K. P. Kim *et al.*, "Improvement of initial vacuum condition along 2008–2010 KSTAR campaign by vessel baking," *Fusion Engineering and Design* **86**, 671 (2011).

[60] S.-T. Kim *et al.*, "Design and operation results of nitrogen gas baking system for KSTAR plasma facing components," *Fusion Engineering and Design* **88**, 2967 (2013).

[61] Y. Li *et al.*, "An analysis method and primary calorimetry verification of tokamak plasma facing components (PFCs) baking from EAST," *Fusion Engineering and Design* **144**, 68 (2019).

[62] Z. Khan *et al.*, "Conditioning of SST-1 tokamak vacuum vessel by baking and glow discharge cleaning," *Fusion Engineering and Design* **103**, 69 (2016).

[63] P. M. Anderson and A. G. Kellman, in *18th IEEE/NPSS Symposium on Fusion Engineering. Symposium Proceedings (Cat. No.99CH37050)* (1999) pp. 535–538.

[64] I. A. Mironov *et al.*, "Design and design features of the T-15M tokamak vacuum vessel," *Plasma Devices and Operations* **12**, 19 (2004).

[65] P. Khvostenko *et al.*, "Experimental thermonuclear installation tokamak T-15MD," *Problems of Atomic Science and Technology, Ser. Thermonuclear Fusion* **42**, 15—38 (2019).

[66] R. Pitts *et al.*, "Physics basis and design of the ITER plasma-facing components," *Journal of Nuclear Materials* **415**, S957 (2011).

[67] E. de la Cal and E. Gauthier, "Review of radio frequency conditioning discharges with magnetic fields in superconducting fusion reactors," *Plasma Physics and Controlled Fusion* **47**, 197 (2005).

[68] T. Wauters *et al.*, "Isotope exchange experiments on TEXTOR and TORE SUPRA using Ion Cyclotron Wall Conditioning and Glow Discharge Conditioning," *Journal of Nuclear Materials* **415**, S1033 (2011).

[69] P. Andrew and M. Pick, "Hydrogen retention in the first wall," *Journal of Nuclear Materials* **220-222**, 601 (1995).

[70] T. Wauters *et al.*, "Wall conditioning by ECRH discharges and He-GDC in the limiter phase of Wendelstein 7-X," *Nuclear Fusion* **58**, 066013 (2018).

[71] V. Philipps and J. Ehrenberg, "Analysis of outgassing after Joint European Torus discharges under beryllium first wall conditions," *Journal of Vacuum Science & Technology A* **11**, 437 (1993).

[72] M. Mayer *et al.*, "Hydrogen inventories in nuclear fusion devices," *Journal of Nuclear Materials* **290-293**, 381 (2001).

[73] S. Panayotis *et al.*, "Deuterium inventory in Tore Supra: Contribution of carbon deposits outgassing," *Journal of Nuclear Materials* **438**, S1059 (2013).

[74] V. Philipps *et al.*, "Dynamic fuel retention and release under ITER like wall conditions in JET," *Journal of Nuclear Materials* **438**, S1067 (2013).

[75] A. Canton *et al.*, "Designing high efficiency glow discharge cleaning systems," *Nuclear Materials and Energy* **19**, 468 (2019).

[76] D. B. Go and D. A. Pohlman, "A mathematical model of the modified Paschen's curve for breakdown in microscale gaps," *Journal of Applied Physics* **107**, 103303 (2010).

[77] Y. P. Raizer, *Gas Discharge Physics* (Springer-Verlag Berlin Heidelberg, 1991).

[78] F. Diab *et al.*, "Influence of cathode material type on the electrical breakdown behaviors of DC discharge," *Canadian Journal of Physics* **98**, 726 (2020).

[79] D. Levko *et al.*, "Modified Paschen curves for pulsed breakdown," *Physics of Plasmas* **26**, 064502 (2019).

[80] H. Eichhorn *et al.*, "Paschen's law for a hollow cathode discharge," *Applied Physics Letters* **63**, 2481 (1993).

[81] J. Winter *et al.*, in *Fusion Technology 1982* (Pergamon, 1983) pp. 369–374.

[82] K. Kim *et al.*, "Wall conditioning of the KSTAR vacuum vessel," *Fusion Engineering and Design* **84**, 1026 (2009).

[83] K. M. Schaubel and G. L. Jackson, "Electron assisted glow discharges for conditioning fusion tokamak devices," *Journal of Vacuum Science & Technology A* **8**, 3063 (1990).

[84] T. Härtl *et al.*, "Optimization of the ASDEX Upgrade glow discharge," *Fusion Engineering and Design* **124**, 283 (2017).

[85] D. Kogut, *Study of wall conditioning in tokamaks with application to ITER*, Ph.D. thesis, Institut de Recherche sur la Fusion par connement Magnétique (2014).

[86] G. J. M. Hagelaar *et al.*, "Modelling of tokamak glow discharge cleaning I: physical principles," *Plasma Physics and Controlled Fusion* **57**, 025008 (2014).

[87] D. Kogut *et al.*, "Modelling of tokamak glow discharge cleaning II: comparison with experiment and application to ITER," *Plasma Physics and Controlled Fusion* **57**, 025009 (2014).

[88] S. Morita *et al.*, "Effect of ne glow discharge on ion density control in LHD," *Plasma Science and Technology* **6**, 2440 (2004).

[89] J. Hu *et al.*, "Vacuum and wall conditioning system on EAST," *Fusion Engineering and Design* **84**, 2167 (2009).

[90] S.-H. Hong *et al.*, "Initial phase wall conditioning in KSTAR," *Nuclear Fusion* **51**, 103027 (2011).

[91] W. R. Spears, in *2013 IEEE 25th Symposium on Fusion Engineering (SOFE)* (2013) pp. 1–8.

[92] M. Shimada and R. A. Pitts, "Wall conditioning on ITER," *Journal of Nuclear Materials* **415**, S1013 (2011).

[93] D. Kogut *et al.*, "Modelling the ITER glow discharge plasma," *Journal of Nuclear Materials* **463**, 1113 (2015).

[94] F. Tabares, ed., *Plasma Applications for Material Modification* (Jenny Stanford Publishing, 2021) p. 322.

[95] R. Prater, "Heating and current drive by electron cyclotron waves," *Physics of Plasmas* **11**, 2349 (2004).

[96] D. Douai *et al.*, "Development of helium electron cyclotron wall conditioning on TCV," *Nuclear Fusion* **58**, 026018 (2017).

[97] T. Wauters *et al.*, "RF plasma simulations using the TOMATOR 1D code: a case study for TCV helium ECRH plasmas," *Plasma Physics and Controlled Fusion* **62**, 105010 (2020).

[98] E. Gauthier *et al.*, in *28th EPS Conf. on Plasma Physics*, Vol. 25A, edited by C. Silva *et al.* (European Physical Society, 2001).

[99] K. Itami *et al.*, "RF heated wall conditioning discharges in JT-60U," *Journal of Nuclear Materials* **390-391**, 983 (2009).

[100] K. Itami *et al.*, "Wall-conditioning plasmas by ECRF heating in KSTAR," *Journal of Nuclear Materials* **438**, S930 (2013).

[101] J. Ihde *et al.*, "Wall conditioning by microwave generated plasmas in a toroidal magnetic field," *Journal of Nuclear Materials* **290-293**, 1180 (2001).

[102] A. Goriaev *et al.*, in *44th EPS Conf. on Plasma Physics*, Vol. 41F, edited by M. Fajardo *et al.* (European Physical Society, 2017).

[103] H. Takahashi *et al.*, "Effect of the RF wall conditioning on the high performance plasmas in the Large Helical Device," *Journal of Nuclear Materials* **463**, 1100 (2015).

[104] T. H. Stix, *Waves in Plasmas* (AIP, New York, 1992).

[105] J. Ongena *et al.*, "Recent advances in physics and technology of ion cyclotron resonance heating in view of future fusion reactors," *Plasma Physics and Controlled Fusion* **59**, 054002 (2017).

[106] P. Dumortier and A. M. Messiaen, "ICRH antenna design and matching," *Fusion Science and Technology* **57**, 230 (2010).

[107] M. Tripský, *Fundamentals of Discharge Initiation by ICRF Antennas in Fusion Devices*, Ph.D. thesis, Ghent University (2018).

[108] T. Wauters, *Study and Optimization of Magnetized ICRF Discharges*, Ph.D. thesis, LPP-ERM/KMS (2011).

[109] D. Douai *et al.*, "Recent results on Ion Cyclotron Wall Conditioning in mid and large size tokamaks," *Journal of Nuclear Materials* **415**, S1021 (2011).

[110] T. Wauters *et al.*, "Isotope exchange by ion cyclotron wall conditioning on JET," *Journal of Nuclear Materials* **463**, 1104 (2015).

[111] N. Nazarov *et al.*, "Cleaning of surfaces by plasma in the Uragan-3 torsatron," *Fizika Plazmy* **13**, 1511 (1987).

[112] H. Esser *et al.*, "ICRF wall conditioning at TEXTOR-94 in the presence of a 2.25 T magnetic field," *Journal of Nuclear Materials* **241-243**, 861 (1997).

[113] E. Gauthier *et al.*, "Wall conditioning technique development in Tore Supra with permanent magnetic field by ICRF wave injection," *Journal of Nuclear Materials* **241-243**, 553 (1997).

[114] Y. Yu *et al.*, "ICRF (ion cyclotron range of frequencies) discharge cleaning with toroidal and vertical fields on EAST," *Plasma Physics and Controlled Fusion* **53**, 015013 (2010).

[115] D. S. Lee *et al.*, "Ion cyclotron wall conditioning (ICWC) on KSTAR," *Fusion Science and Technology* **60**, 94 (2011).

[116] A. Hakola *et al.*, "Plasma-wall interaction studies in the full-W ASDEX upgrade during helium plasma discharges," *Nuclear Fusion* **57**, 066015 (2017).

[117] R. Brakel *et al.*, "ICRF wall conditioning experiments in the W7-AS stellarator," *Journal of Nuclear Materials* **290-293**, 1160 (2001).

[118] N. Ashikawa *et al.*, "Ion cyclotron conditioning with strong magnetic field in LHD," *Fusion Engineering and Design* **81**, 2831 (2006).

[119] H. TAKAHASHI *et al.*, "High ion temperature plasmas using an ICRF wall-conditioning technique in the Large Helical Device," *Plasma and Fusion Research* **9**, 1402050 (2014).

[120] J. Winter, "Tokamak wall coatings," *Plasma Physics and Controlled Fusion* **36**, B263 (1994).

[121] Malcolm W. Chase Jr., *NIST-JANAF Themochemical Tables, Fourth Edition*, International series of monographs on physics, Vol. 9 (American Institute of Physics, 1998).

[122] A. Refke *et al.*, "Interaction of energetic oxygen with different boron/-carbon materials," *Journal of Nuclear Materials* **212-215**, 1255 (1994).

[123] R. G. Castro *et al.*, "The structure, properties and performance of plasma-sprayed beryllium for fusion applications," *Physica Scripta* **T64**, 77 (1996).

[124] M. J. Rubel *et al.*, "Beryllium plasma-facing components for the ITER-like wall project at JET," *Journal of Physics: Conference Series* **100**, 062028 (2008).

[125] P. Tsavalas *et al.*, "Be ITER-like wall at the JET tokamak under plasma," *Physica Scripta* **T170**, 014049 (2017).

[126] A. Cardella *et al.*, "Application of beryllium as first wall armour for ITER primary, baffle, and limiter modules," *Fusion Technology* **38**, 326 (2000).

[127] P. Krstic *et al.*, "Unraveling the surface chemistry processes in lithiated and boronized plasma material interfaces under extreme conditions," *Matter and Radiation at Extremes* **3**, 165 (2018).

[128] F. L. Tabarés *et al.*, "Plasma performance and confinement in the TJ-II stellarator with lithium-coated walls," *Plasma Physics and Controlled Fusion* **50**, 124051 (2008).

[129] R. Maingi *et al.*, "The effect of progressively increasing lithium coatings on plasma discharge characteristics, transport, edge profiles and ELM stability in the National Spherical Torus Experiment," *Nuclear Fusion* **52**, 083001 (2012).

[130] D. Ruzic *et al.*, "Flowing liquid lithium plasma-facing components – physics, technology and system analysis of the LiMIT system," *Nuclear Materials and Energy* **12**, 1324 (2017).

[131] R. Goldston *et al.*, "Recent advances towards a lithium vapor box divertor," *Nuclear Materials and Energy* **12**, 1118 (2017).

[132] A. Devitre *et al.*, "Boron synergies in lithium film performance," *Nuclear Fusion* **60**, 106001 (2020).

[133] A. Annen *et al.*, "Stability of plasma-deposited amorphous hydrogenated boron films," *Thin Solid Films* **300**, 101 (1997).

[134] O. I. Buzhinskij and Y. M. Semenets, "Review of in situ boronization in contemporary tokamaks," *Fusion Technology* **32**, 1 (1997).

[135] D. Tafalla and F. Tabarés, “First boronization of the TJ-II stellarator,” *Vacuum* **67**, 393 (2002).

[136] J. Winter, “A comparison of tokamak operation with metallic getters (Ti, Cr, Be) and boronization,” *Journal of Nuclear Materials* **176-177**, 14 (1990).

[137] U. Schneider and J. Stadlbauer, in *Fusion Technology 1992*, edited by C. Ferro, M. Gasparotto, and H. Knoepfel (North-Holland, Oxford, 1993) pp. 376–380.

[138] U. Schneider *et al.*, “Boronization of ASDEX,” *Journal of Nuclear Materials* **176-177**, 350 (1990).

[139] K. Nishimura *et al.*, “Effects of boronization in LHD,” *Journal of Plasma and Fusion Research* **79**, 1216 (2003).

[140] E. Gauthier *et al.*, “Boronization in Tore Supra,” *Journal of Nuclear Materials* **196-198**, 637 (1992).

[141] A. Bortolon *et al.*, “Observations of wall conditioning by means of boron powder injection in DIII-D H-mode plasmas,” *Nuclear Fusion* **60**, 126010 (2020).

[142] A. Nagy *et al.*, “A multi-species powder dropper for magnetic fusion applications,” *Review of Scientific Instruments* **89**, 10K121 (2018).

[143] T. Osborne *et al.*, “Enhanced H-mode pedestals with lithium injection in DIII-D,” *Nuclear Fusion* **55**, 063018 (2015).

[144] Z. Sun *et al.*, “Real time wall conditioning with lithium powder injection in long pulse H-mode plasmas in EAST with tungsten divertor,” *Nuclear Materials and Energy* **19**, 124 (2019).

[145] A. Bortolon *et al.*, “Real-time wall conditioning by controlled injection of boron and boron nitride powder in full tungsten wall ASDEX Upgrade,” *Nuclear Materials and Energy* **19**, 384 (2019).

[146] R. Lunsford *et al.*, “Active conditioning of ASDEX Upgrade tungsten plasma-facing components and discharge enhancement through boron and boron nitride particulate injection,” *Nuclear Fusion* **59**, 126034 (2019).

[147] Z. Sun *et al.*, “Suppression of edge localized modes with real-time boron injection using the tungsten divertor in EAST,” *Nuclear Fusion* **61**, 014002 (2020).

[148] F. Nespoli *et al.*, "First impurity powder injection experiments in LHD," *Nuclear Materials and Energy* **25**, 100842 (2020).

[149] K. Hanada *et al.*, "Investigation of hydrogen recycling in long-duration discharges and its modification with a hot wall in the spherical tokamak QUEST," *Nuclear Fusion* **57**, 126061 (2017).

[150] M. Endler *et al.*, "Wendelstein 7-X on the path to long-pulse high-performance operation," *Fusion Engineering and Design* **167**, 112381 (2021).

[151] T. Klinger *et al.*, "Overview of first Wendelstein 7-X high-performance operation," *Nuclear Fusion* **59**, 112004 (2019).

[152] H.-S. Bosch *et al.*, "Experience with the commissioning of the superconducting stellarator Wendelstein 7-X," *Fusion Engineering and Design* **96-97**, 22 (2015).

[153] P. van Eeten *et al.*, "Monitoring of W7-X cryostat commissioning with cryostat system FE model," *Fusion Engineering and Design* **123**, 91 (2017).

[154] A. Cardella *et al.*, "Construction of the vacuum vessels and the magnet supporting structures of Wendelstein 7-X," *Fusion Engineering and Design* **82**, 1911 (2007).

[155] M. Nagel *et al.*, "Thermal and mechanical analysis of Wendelstein 7-X thermal shield," *Fusion Engineering and Design* **86**, 1830 (2011).

[156] C. P. Dhard *et al.*, "Plasma-wall interaction studies in W7-X: main results from the recent divertor operations," *Physica Scripta* **96**, 124059 (2021).

[157] R. Stadler *et al.*, "The in-vessel components of the experiment Wendelstein 7-X," *Fusion Engineering and Design* **84**, 305 (2009).

[158] T. S. Pedersen *et al.*, "First results from divertor operation in Wendelstein 7-X," *Plasma Physics and Controlled Fusion* **61**, 014035 (2019).

[159] A. Peacock *et al.*, "Progress in the design and development of a test divertor (TDU) for the start of W7-X operation," *Fusion Engineering and Design* **84**, 1475 (2009).

[160] J. D. Lore *et al.*, "Design and analysis of divertor scraper elements for the W7-X stellarator," *IEEE Transactions on Plasma Science* **42**, 539 (2014).

[161] L. Wegener *et al.*, “Final design and construction of the Wendelstein 7-X coils,” *Fusion Engineering and Design* **58-59**, 225 (2001).

[162] T. Andreeva *et al.*, “Magnetic configuration scans during divertor operation of Wendelstein 7-X,” *Nuclear Fusion* **62**, 026032 (2022).

[163] S. Brezinsek *et al.*, “Plasma-Surface Interaction in the stellarator W7-X: Conclusions drawn from operation with graphite Plasma-Facing Components,” *Nuclear Fusion* **62**, 016006 (2021).

[164] F. Füllenbach *et al.*, “The Wendelstein 7-X trim coil system commissioning and first operational results,” *Fusion Engineering and Design* **124**, 94 (2017).

[165] F. Füllenbach *et al.*, “Commissioning of the Wendelstein 7-X in vessel control coils,” *IEEE Transactions on Plasma Science* **48**, 2635 (2020).

[166] E. Jauregi *et al.*, “Turn-key supply for the power supplies of the control coils of Wendelstein 7-X experiment,” *Fusion Engineering and Design* **66-68**, 1125 (2003).

[167] H. Grote *et al.*, “Neutral particle modelling and particle exhaust in the Wendelstein 7-X stellarator,” *Journal of Nuclear Materials* **313-316**, 1298 (2003).

[168] P. McNeely *et al.*, “Current status of the neutral beam heating system of W7-X,” *Fusion Engineering and Design* **88**, 1034 (2013).

[169] G. Schlisio, *Analysis of the gas balance for Wendelstein 7-X*, Ph.D. thesis, Universität Greifswald (2021).

[170] J. Schacht *et al.*, “The gas supply and gas inlet control systems of the fusion experiment Wendelstein 7-X,” *Fusion Engineering and Design* **129**, 6 (2018).

[171] T. Barbui *et al.*, “The He/Ne beam diagnostic for line-ratio spectroscopy in the island divertor of Wendelstein 7-X,” *Journal of Instrumentation* (2019), 10.1088/1748-0221/14/07/c07014.

[172] S. Zoletnik *et al.*, “First results of the multi-purpose real-time processing video camera system on the Wendelstein 7-X stellarator and implications for future devices,” *Review of Scientific Instruments* **89**, 013502 (2018).

[173] K. Tang, *Design of the gas-puff imaging diagnostic for Wendelstein 7-X*, B.S. thesis, MIT (2019).

[174] M. Dibon *et al.*, "Blower gun pellet injection system for W7-X," *Fusion Engineering and Design* **98-99**, 1759 (2015).

[175] R. Bussiahn *et al.*, "Tracer-Encapsulated Solid Pellet (tespel) injection system for Wendelstein 7-X," *Review of Scientific Instruments* **89**, 10K112 (2018).

[176] A. Spring *et al.*, "Design, manufacture and testing of the glow discharge electrodes for Wendelstein 7-X," *Fusion Engineering and Design* **86**, 1933 (2011).

[177] T. Rummel *et al.*, "The power supplies for the glow discharge electrodes in Wendelstein 7-X," *Fusion Engineering and Design* **86**, 1562 (2011).

[178] A. Spring *et al.*, "Wall conditioning for Wendelstein 7-X by glow discharge," *Fusion Engineering and Design* **66-68**, 371 (2003).

[179] V. Erckmann *et al.*, "Electron cyclotron heating for W7-X: Physics and technology," *Fusion Science and Technology* **52**, 291 (2007).

[180] D. Moseev *et al.*, "Absolute calibration of sniffer probes on Wendelstein 7-X," *Review of Scientific Instruments* **87**, 083505 (2016).

[181] D. Moseev *et al.*, "Inference of the microwave absorption coefficient from stray radiation measurements in Wendelstein 7-X," *Nuclear Fusion* **57**, 036013 (2017).

[182] Moseev, Dmitry *et al.*, "Experimental investigation of the ECRH stray radiation during the start-up phase in Wendelstein 7-X," *EPJ Web Conf.* **147**, 03002 (2017).

[183] Stange, Torsten *et al.*, "Advanced electron cyclotron heating and current drive experiments on the stellarator Wendelstein 7-X," *EPJ Web Conf.* **157**, 02008 (2017).

[184] R. König *et al.*, "Diagnostics development for quasi-steady-state operation of the Wendelstein 7-X stellarator," *Review of Scientific Instruments* **83**, 10D730 (2012).

[185] R. König *et al.*, "The set of diagnostics for the first operation campaign of the Wendelstein 7-X stellarator," *Journal of Instrumentation* **10**, P10002 (2015).

[186] M. Krychowiak *et al.*, "Overview of diagnostic performance and results for the first operation phase in Wendelstein 7-X," *Review of Scientific Instruments* **87**, 11D304 (2016).

[187] U. Wenzel *et al.*, "Performance of new crystal cathode pressure gauges for long-pulse operation in the Wendelstein 7-X stellarator," *Review of Scientific Instruments* **90**, 123507 (2019).

[188] T. Kremeyer *et al.*, "Wisconsin In Situ Penning (WISP) gauge: A versatile neutral pressure gauge to measure partial pressures in strong magnetic fields," *Review of Scientific Instruments* **91**, 043504 (2020).

[189] K. Brunner *et al.*, "Real-time dispersion interferometry for density feedback in fusion devices," *Journal of Instrumentation* **13**, P09002 (2018).

[190] O. P. Ford *et al.*, "Charge exchange recombination spectroscopy at Wendelstein 7-X," *Review of Scientific Instruments* **91**, 023507 (2020).

[191] W. Biel *et al.*, "High efficiency extreme ultraviolet overview spectrometer: Construction and laboratory testing," *Review of Scientific Instruments* **77**, 10F305 (2006).

[192] N. Krawczyk *et al.*, "Commissioning and first operation of the pulse-height analysis diagnostic on Wendelstein 7-X stellarator," *Fusion Engineering and Design* **123**, 1006 (2017).

[193] M. Kubkowska *et al.*, "First results from the soft x-ray pulse height analysis system on Wendelstein 7-X stellarator," *Fusion Engineering and Design* **136**, 58 (2018).

[194] A. Pavone *et al.*, "Measurements of visible bremsstrahlung and automatic Bayesian inference of the effective plasma charge Z_{eff} at W7-X," *Journal of Instrumentation* **14**, C10003 (2019).

[195] S. Kwak *et al.*, "Bayesian inference of spatially resolved Zeff profiles from line integrated bremsstrahlung spectra," *Review of Scientific Instruments* **92**, 043505 (2021).

[196] Y. Wei *et al.*, "An ultraviolet-visible-near infrared overview spectroscopy for divertor plasma diagnosis on Wendelstein 7-X," *AIP Advances* **8**, 085011 (2018).

[197] O. Neubauer *et al.*, "Endoscopes for observation of plasma-wall interactions in the divertor of Wendelstein 7-X," *Fusion Engineering and Design* **146**, 19 (2019).

[198] L. Stephey *et al.*, "Spectroscopic imaging of limiter heat and particle fluxes and the resulting impurity sources during Wendelstein 7-X startup plasmas," *Review of Scientific Instruments* **87**, 11D606 (2016).

[199] G. Kocsis *et al.*, "Overview video diagnostics for the W7-X stellarator," *Fusion Engineering and Design* **96-97**, 808 (2015).

[200] M. Jakubowski *et al.*, "Infrared imaging systems for wall protection in the W7-X stellarator," *Review of Scientific Instruments* **89**, 10E116 (2018).

[201] J. H. Gross, *Mass Spectrometry*, 2nd ed. (Springer, 2011).

[202] G. Schlisio *et al.*, "First results from the implementation of the ITER diagnostic residual gas analyzer prototype at Wendelstein 7-X," *Review of Scientific Instruments* **90**, 093501 (2019).

[203] H.-S. Bosch *et al.*, "Operation of W7-X with an inertially cooled divertor - on the way to steady state operation," *IEEE Transactions on Plasma Science* **48**, 1369 (2020).

[204] T. S. Pedersen *et al.*, "Plans for the first plasma operation of Wendelstein 7-X," *Nuclear Fusion* **55**, 126001 (2015).

[205] J. Boscary *et al.*, "Design and technological solutions for the plasma facing components of Wendelstein 7-X," *Fusion Engineering and Design* **86**, 572 (2011).

[206] T. Wauters, in *43rd EPS Conference on Plasma Physics*, Vol. 40A, edited by M. Fajardo, E. Westerhof, C. Riconda, A. M. A. Bret, and B. Dromey (European Physical Society, 2016).

[207] T. Wauters *et al.*, "Wall conditioning throughout the first carbon divertor campaign on Wendelstein 7-X," *Nuclear Materials and Energy* **17**, 235 (2018).

[208] G. Schlisio *et al.*, "The evolution of the bound particle reservoir in Wendelstein 7-X and its influence on plasma control," *Nuclear Fusion* **61**, 036031 (2021).

[209] E. Wang *et al.*, "Impurity sources and fluxes in W7-X: from the plasma-facing components to the edge layer," *Physica Scripta* **T171**, 014040 (2020).

[210] A. Goriaev *et al.*, "Wall conditioning at the Wendelstein 7-X stellarator operating with a graphite divertor," *Physica Scripta* **T171**, 014063 (2020).

[211] A. Goriaev *et al.*, "Development of glow discharge and electron cyclotron resonance heating conditioning on W7-X," *Nuclear Materials and Energy* **18**, 227 (2019).

[212] D. Sturges and H. Oskam, “Hollow-cathode glow discharge in hydrogen and the noble gases,” *Journal of Applied Physics* **37**, 2405 (1966).

[213] R. Brakel *et al.*, in *Proc. 27th IAEA Fusion Energy Conf, India"* (IAEA, 2018).

[214] C. P. Dhard *et al.*, “Inspection of W 7-X plasma-facing components after the operation phase OP1.2b: observations and first assessments,” *Physica Scripta* **T171**, 014033 (2020).

[215] D. Hwangbo *et al.*, “Inspection of arc trails formed in stellarator/heliotron devices W7-X and LHD,” *Plasma and Fusion Research* **15**, 2402012 (2020).

[216] M. Miyamoto *et al.*, “Microscopic damage of materials exposed to glow discharge cleanings in LHD,” *Journal of Nuclear Materials* **329-333**, 742 (2004).

[217] S. Sereda *et al.*, “Impact of boronizations on impurity sources and performance in Wendelstein 7-X,” *Nuclear Fusion* **60**, 086007 (2020).

[218] S. Sereda, *Impact of boronizations on impurity sources and performance in Wendelstein 7-X*, Ph.D. thesis, Heinrich Heine University Düsseldorf (2021).

[219] V. Philipps, “Plasma wall interaction and its control by wall conditioning,” *Fusion Science and Technology* **45**, 237 (2004).

[220] J. Winter *et al.*, “Boronization in TEXTOR,” *Journal of Nuclear Materials* **162**, 713 (1989).

[221] A. Nagy *et al.*, “A horizontal powder injector for W7-X,” *Fusion Engineering and Design* **146**, 1403 (2019).

[222] D. Nicolai *et al.*, “A multi-purpose manipulator system for W7-X as user facility for plasma edge investigation,” *Fusion Engineering and Design* **123**, 960 (2017).

[223] R. Lunsford *et al.*, “Characterization of injection and confinement improvement through impurity induced profile modifications on the Wendelstein 7-X stellarator,” *Physics of Plasmas* **28**, 082506 (2021).

[224] M. Ŝleczka, in *43rd EPS Conference on Plasma Physics*, Vol. 42A, edited by S. Coda *et al.* (European Physical Society, 2018).

[225] R. C. Wolf *et al.*, "Electron-cyclotron-resonance heating in Wendelstein 7-X: A versatile heating and current-drive method and a tool for in-depth physics studies," *Plasma Physics and Controlled Fusion* **61**, 014037 (2018).

[226] Y. Gao *et al.*, "Methods for quantitative study of divertor heat loads on W7-X," *Nuclear Fusion* **59**, 066007 (2019).

[227] H. Niemann *et al.*, "Large wetted areas of divertor power loads at Wendelstein 7-X," *Nuclear Fusion* **60**, 084003 (2020).

[228] H. Störk *et al.*, "TOMAS - a toroidal magnetized plasma facility for studying wall conditioning of future fusion devices," *Fusion Science and Technology* **39**, 54 (2001).

[229] J. Ihde, *Untersuchung zur Wandkonditionierung mit mikrowellenerzeugten Plasmen in einem toroidalen Magnetfeld*, Ph.D. thesis, Ruhr-Universität Bochum (2001).

[230] P. Sundelin *et al.*, "Nitrogen-assisted removal of deuterated carbon layers," *Journal of Nuclear Materials* **390-391**, 647 (2009).

[231] C. Schulz *et al.*, "Fuel removal from castellated structures by plasma discharges in hydrogen and oxygen," *Journal of Nuclear Materials* **415**, S781 (2011).

[232] M. Ortner and L. Coliado Bandeira, "Magpylib: A free Python package for magnetic field computation," *SoftwareX* **11**, 100466 (2020).

[233] F. Louche *et al.*, "Design of an ICRF system for plasma–wall interactions and RF plasma production studies on TOMAS," *Fusion Engineering and Design* **123**, 317 (2017).

[234] F. Durodié and M. Vervier, in *Fusion Technology 1992*, edited by C. Ferro, M. Gasparotto, and H. Knoepfel (North-Holland, Oxford, 1993) pp. 477 – 480.

[235] F. Fasseur, *Study of an RF-system for plasma production on TOMAS*, M.S. thesis, ERM/KMS (2017).

[236] K. Elinck, *Implementation of an ICRF matching algorithm on TOMAS*, M.S. thesis, ERM/KMS (2019).

[237] A. Kreter *et al.*, "Linear plasma device PSI-2 for plasma-material interaction studies," *Fusion Science and Technology* **68**, 8 (2015).

[238] D. López-Rodríguez, *Characterisation of toroidal RF plasmas by Langmuir probe measurements on TOMAS*, M.S. thesis, Ghent University (2020).

[239] Y. Kovtun *et al.*, "Comparative analysis of the plasma parameters of ECR and combined ECR and RF discharges in the TOMAS plasma facility," *Plasma Physics and Controlled Fusion* **63**, 125023 (2021).

[240] S. Chen and T. Sekiguchi, "Instantaneous direct-display system of plasma parameters by means of triple probe," *Journal of Applied Physics* **36**, 2363 (1965).

[241] P. R. Brunsell *et al.*, "Initial results from the rebuilt EXTRAP T2R RFP device," *Plasma Physics and Controlled Fusion* **43**, 1457 (2001).

[242] M. Cecconello, "Neutral particle energy analyser based on time of flight technique for EXTRAP-T2R," Tech. Rep. KTH/ALF/R–01/3–SE (KTH, 2001).

[243] S. Moon *et al.*, "Characterization of neutral particle fluxes from ICWC and ECWC plasmas in the TOMAS facility," *Phisica Scripta* **96**, 124025 (2021).

[244] J. Joly *et al.*, "Temperature-programmed desorption (TPD) of water from iron, chromium, nickel and 304L stainless steel," *Vacuum* **59**, 854 (2000).

[245] M. Tokitani *et al.*, "Desorption of helium from austenitic stainless steel heavily bombarded by low energy He ions," *Journal of Nuclear Materials* **329**, 761 (2004).

[246] T. Hino *et al.*, "Retention and desorption of hydrogen and helium in stainless steel wall by glow discharge," *Fusion Engineering and Design* **72**, 339 (2005).

[247] R. Stenzel *et al.*, "Plasma fireballs," *IEEE Transactions on Plasma Science* **36**, 1000 (2008).

[248] J. Boscary *et al.*, "Actively water-cooled plasma facing components of the Wendelstein 7-X stellarator," *Fusion Science and Technology* **64**, 263 (2013).

[249] G. Ehrke *et al.*, "Design and manufacturing of the Wendelstein 7-X cryo-vacuum pump," *Fusion Engineering and Design* **146**, 2757 (2019).

[250] J. Ongena *et al.*, "The ICRH system for the stellarator Wendelstein 7-X," *AIP Conference Proceedings* **2254**, 070003 (2020).

[251] T. Wauters *et al.*, "Ion and electron cyclotron wall conditioning in stellarator and tokamak magnetic field configuration on WEGA," *AIP Conference Proceedings* **1580**, 187 (2014).

[252] T. Wauters *et al.*, "Isotope removal experiment in JET-ILW in view of t-removal after DTE2," *Physica Scripta* (2021 in press).

[253] Marushchenko, Nikolai B. *et al.*, "Reduced scenario with X3 heating in W7-X," *EPJ Web Conf.* **203**, 01006 (2019).

[254] V. E. Moiseenko *et al.*, "First experiments on ICRF discharge generation by a W7-X-like antenna in the Uragan-2M stellarator," *Journal of Plasma Physics* **86**, 905860517 (2020).

[255] M. Tripský *et al.*, "A PIC-MCC code RFdinity1d for simulation of discharge initiation by ICRF antenna," *Nuclear Fusion* **57**, 126043 (2017).

Plasma-Facing Components of the superconducting stellarator Wendelstein 7-X.